

UCLA

UCLA Electronic Theses and Dissertations

Title

Magnetic Field Characterization of a Diamagnetic Cavity Piston for Generation of Quasi-Perpendicular Collisionless Shocks

Permalink

<https://escholarship.org/uc/item/1b32088x>

Author

Everson, Erik Thomas

Publication Date

2016

Peer reviewed|Thesis/dissertation

UNIVERSITY OF CALIFORNIA
Los Angeles

Magnetic Field Characterization of a Diamagnetic Cavity Piston for
Generation of Quasi-Perpendicular Collisionless Shocks

A dissertation submitted in partial satisfaction
of the requirements for the degree
Doctor of Philosophy in Physics

by

Erik Thomas Everson

2016

© Copyright by
Erik Thomas Everson
2016

ABSTRACT OF THE DISSERTATION

Magnetic Field Characterization of a Diamagnetic Cavity Piston for Generation of Quasi-Perpendicular Collisionless Shocks

by

Erik Thomas Everson

Doctor of Philosophy in Physics

University of California, Los Angeles, 2016

Professor Christoph Niemann, Chair

Collisionless shocks are a common phenomena that occur in astrophysical and terrestrial space environments with a wide variety of physical characteristics, but are generally pre-formed, steady state when observed. This thesis studies the transient state that leads to the formation of a dissipation dominated, quasi-perpendicular, subcritical collisionless shock. To achieve this, two experimental platforms were conceived: (1) utilizing the Large Plasma Device (LaPD) at UCLA to produce a magnetized ambient-plasma and the Phoenix Laser System to create an expanding debris-plasma to shock the ambient-plasma and (2) installing a large ($\varnothing 56$ cm) pulsed Helmholtz Coil ($B_o \lesssim 1.25$ kG) into the target chamber at the Trident Laser Facility at Los Alamos National Laboratory (LANL) in which the ambient- and debris-plasma were created with two consecutive laser pulses. As the debris-plasma expands through the magnetized ambient-plasma a diamagnetic cavity is formed that expels the enclosed magnetic field and compresses the field upstream, outside the cavity. The formed magnetic compression acts as a piston to energize and shock the ambient-plasma, when conditions are suitable.

The goal of this dissertation is to produce, identify, and quantify the magnetic characteristics associated with coupling of energy and momentum from a LPP (debris-plasma)

into a magnetized ambient-plasma with the use of a driven magnetic piston (debris-ambient coupling). To achieve this goal a simple analytical model is developed to characterize the behavior of a “magnetic-only interacting cavity” (MOIC), that is, a diamagnetic cavity that only interacts with the background magnetic field. The MOIC model includes a scaling for the maximal cavity radius (§3.2), an equation-of-motion that predicts the trajectory of the cavity expansion (§3.3), as well as, the magnetic and electric field structure for a diamagnetic cavity with an infinitely thin diamagnetic current layer and a diamagnetic cavity with a radial distribution (§3.4). All these models are validated against experimental cases that satisfy the assumptions of the models and, thus, allowing for the development of benchmarks to quantify the behavior of all experimental cavities and the strength of their magnetic piston (§3.5). With these benchmarks a trifecta of characteristics is established to identify the advent of the debris-ambient coupling in the experiments: (1) a period of ‘enhanced’ deceleration in the expansion that is up to 8.8x stronger than a vacuum expansion, (2) a growth of the magnetic compression without additional expulsion that is up to $0.5B_o$ stronger than the best case vacuum cavity, and (3) a steepening of the compression ramp that is up to 3.5x narrower than a vacuum cavity. The development of these features indicate a driven cross-field electric current (perpendicular to \mathbf{B}_o and the expansion $\hat{\mathbf{n}}$) in the steepened portion of the compression ramp. The strength of this coupling behavior increases as the ratio of the local ambient-ion inertial length c/ω_{pi} to the length scale of the compression ramp $0.63r_{cav}$ decreases, with the only shock-like structure occurring when $(c/\omega_{pi})/r_{cav} = 0.5 < 0.63$.

The dissertation of Erik Thomas Everson is approved.

Christopher Russell

George Morales

Walter Gekelman

Christoph Niemann, Committee Chair

University of California, Los Angeles

2016

To my Aunt Carole

TABLE OF CONTENTS

1	Introduction	1
1.1	Collisionless Shocks: A Brief Review of Types	3
1.1.1	Shock Criticality and Dissipation	8
1.2	Experimental Concept for Driving Collisionless Shocks	10
1.3	Experimental Model	14
1.3.1	Stage 1: Setup of Diamagnetic Cavity	16
1.3.2	Stage 2: Coupling from Piston to the Ambient-Plasma	18
1.3.3	Stage 3: Shock Breakout	20
1.4	Scope of Dissertation	20
2	Experimental Platforms and Diagnostics	22
2.1	LaPD-Phoenix Platform	22
2.2	Trident Platform	28
2.2.1	As Compared to pre-2013 LaPD-Phoenix Experiments	36
2.3	Diagnostics	38
2.3.1	Magnetic Flux Probes (a.k.a. bdot probes)	38
2.3.2	Proton Radiography	43
3	Discussion of Results	49
3.1	Proton Radiography Results	53
3.2	Scalings of the Diamagnetic Cavity Size $2R_c$	55
3.3	Cavity Deceleration	71
3.4	Cavity Magnetic Field: Models versus Experiment	84

3.5	Cavity Compression Analysis & Debris-Ambient Coupling	101
3.6	Run17: A Shock-Like Event	115
4	Comparison to Recent Experiments	125
5	Conclusion	132
A	List of Key Terms/Variables	137
B	Magnetized Sphere Derivation	143
B.1	The Magnetic Field	143
B.2	The Inductive Electric Field	146
B.3	Energy of the Fields	148
B.4	$E \times B$ -Drifts	150

LIST OF FIGURES

1.1	A shock frame sketch depicting the basic geometry of a thin, planar collisionless shock of thickness Δ_{sh} . Represented is a special case where the upstream plasma flow \mathbf{v}_1 is anti-parallel to the shock normal $\hat{\mathbf{n}}$. The shock is moving from left to right and values denoted with 1 correspond to upstream, un-shocked conditions and 2 correspond to downstream, shocked conditions. The magnetic field is represented by \mathbf{B} and the plasma flow velocities are represented by \mathbf{v} . Diagram is adapted from <i>R. A. Treumann</i> [83].	5
1.2	Rankine-Hugoniot jump conditions for a strictly perpendicular ($\theta_{Bn} = \pi/2$), planar collisionless shock, equation 1.7, versus the Alfvénic Mach number M_A . Each plot shows traces for fixed $\beta_1 = n_1 k_B T_1 / (B_1^2 / (2\mu_o))$ of 0.001, 0.2, 0.5, 1.0, and 2.0. Plot (a) plots the jump conditions for an adiabatic index of $\gamma = 5/3$ and plot (b) plots the jump conditions for an adiabatic index of $\gamma = 2$	7
1.3	Schematic of an anomalous dissipation dominated, quasi-perpendicular, sub-critical, planar collisionless shock. The upstream plasma flow \mathbf{v}_1 is decelerated as it crosses the shock front to the downstream plasma flow \mathbf{v}_2 . The deceleration comes from the electric potential $U(x)$ setup over the shock of width Δ_{sh} . A shock width of $\sim c/\omega_{pi}$ implies the ions are unmagnetized, so only the electrons will experience guiding orbit drives. The electric field from the the electric potential within the shock front causes the electrons to drift within the shock front and perpendicular to the magnetic field. This electric current behaves as a free energy source for driving anomalous dissipation within the shock front. This figure is an adaption from figure 10 and §2.1 in <i>R. A. Treumann (2009)</i> . [83]	10

1.4	A cartoon for driving collisionless shocks in the laboratory. The background magnetic field is \mathbf{B}_o and the ambient-ion density is n_a . The piston, which is usually a strong magnetic compression, travels upstream, left to right in the figure, at a speed v_p and interacts with the ambient-plasma. As coupling occurs the piston ‘snow-plows’ the ambient-plasma creating an energized, ‘shocked,’ ambient-plasma distribution. Adapted from figure 1 in <i>R. P. Drake</i> (2000).[23]	11
1.5	This diagram depicts how a diamagnetic current is driven to create a diamagnetic cavity. As the debris-plasma expands the highly magnetized debris-electrons (really any local electrons) will experience the guiding orbit drifts, whereas the unmagnetized debris-ions will not. The setup $\mathbf{E} \times \mathbf{B}$ -drift and $\nabla \mathbf{P} \times \mathbf{B}$ -drift drive the diamagnetic current in the electrons.	17
2.1	Setup of the LaPD-Phoenix experiment. Figure (a) shows a side-view of the the experiment showing the port layout for the cathodes, target (port 19), and experimental region (port 18 to 38). Figure (b) shows a 3D rendering of the target, laser, and diagnostic arrangement at port 19. Figure (c) is a simplified view of the cross-section of port 19.	25
2.2	Figure (a) shows the Helmholtz Coil (HC) frame assembled in the Trident target chamber with the bottom coil being wound. The top right insert shows a 3D CAD rendering of the completely assembled HC. Figure (b) is an analytical solution of B_z (using the Biot-Savart Law) for a HC with the Trident experiment specifications. Figure (c) shows the measured time-dependent axial magnetic field $B_z(t)$ at the center of the HC for a typical discharge of the capacitor bank through the coil. The peak magnetic field occurs 22.3 ± 0.2 ms into the pulse.	31

2.3	Figure (a) is a SLR photo during Trident shot 21935 of the experimental setup. The photo is taken looking down through the top coil of the HC. The green hue is due to the light scattering of the green ‘diagnostic’ beam. Figure (b) is a 3D CAD render of the experimental setup with the ‘diagnostic’ beam in green and the ‘heater’/‘driver’ beam in red. Figure (c) is a 2D schematic of the experimental setup looking from atop.	34
2.4	Figure (a) illustrates the the wiring of a differentially wound magnetic flux probe where the thick (normal) line represents loop 2 (loop 1) of the probe. Figure (b) shows the circuit schematic for loop 1 of the probe, where r_1 is the internal resistance of the loop, C_1 is the internal capacitance of the loop, R_1 is the load resistance attached to the loop, and I_1 is the current through the loop generated by the total EMF \mathcal{E}_1 (external magnetic flux, self-inductance L_1 , and mutual-inductance M between the two loops).	39
2.5	Depicted is an over top, 2D schematic of the Trident experiment when the proton radiography diagnostic is configured. The bdot array is kept in place to provide reference positions for the proton radiography, but the bdot probes do not collect data. The chirp pulse amplified (CPA) beam comes in from the left to irradiate a Cu target and produce a proton beam off the target backside (right). The proton beam then passes through a Cu mesh, then the experimental volume, and finally deposits itself on the radiochromic film (RCF) stack.	44

2.6	Figure (a) is an example of a proton radiograph image captured on an EBT2 RCF (Trident shot number 21971, CPA energy 45 J) with no plasma and no background magnetic field. The film darkens upon absorption of protons so the white mesh is the shadow from the Cu mesh and the bdot shadows are seen as the thicker poles emerging from the bottom of the image. The graphite target is off to the left side of the image and the left most bdot probe is 6 cm from the target. Figure (b) is the same as (a) except with a vertical background magnetic field of 792 ± 6 G (Trident 21970, CPA 51 J). The magnetic field causes the proton beam and image to be shifted to the right by 1.43 ± 0.06 cm.	45
2.7	Figure (a) plots the tabulated energy deposition for a given proton energy into a layered RCF stack of 25 μm Al, 104 μm HD-810, 285 μm EBT2, and 283 μm MD-V2-55. The calculation is done using the SRIM software (www.SRIM.org)[94, 95]. Figure (b) shows the expected proton deflection Δ_p of a proton with energy E_p for various average magnetic field values over the distance $L = 49$ cm (see equation 2.11).	46
3.1	Plotted is an example of a formed diamagnetic cavity from data collected during Run04 of the 2013 January LaPD-Phoenix experiments (parameter details in table 3.1). Figure (a) shows a contour plot of the normalized magnetic field B_z/B_o ($\mathbf{B}_o = B_o\hat{\mathbf{z}}$) of the diamagnetic cavity versus time and distance from the target X_{TARGET} . The data was collected along the LaPD $\hat{\mathbf{x}}$ -axis for a line out directly in front of the target. Figure (b) represents the same dataset as a series of stack plots. Figure (c) shows the magnetic field profile (B_z/B_o versus X_{TARGET}) for a given time $t = 0.9 \mu\text{s}$ after ablation. Key cavity features (X_{cav} , X_{peak} , X_{ramp} , α , etc.) are identified and defined.	51

- 3.2 Figure (a) shows the proton energy deposition for the RCF stack used for Trident shot 21976. The RCF stack consists of five layers: 16 μm thick Al foil, 104 μm thick HD-810 film, and 3 consecutive sheets of 285 μm thick EBT2 film. Figure (b) shows horizontal proton deflection calculations made between the first and third sheet of EBT2 film. This imaged diamagnetic cavity is spherical and centered in a cavity with approximate radius of 8.1 cm and one edge still at the target surface. 54
- 3.3 The maximal diamagnetic cavity size ($2R_c$) versus the scaling of the magnetic-stopping radius (equation 3.6) for the entries in table 3.1 using graphite targets. Each data point is color coded to its respective campaign: (black) Trident, (red) 2011 LaPD-Phoenix, (blue) 2013 January LaPD-Phoenix, and (orange) 2013 June LaPD-Phoenix. The symbols represent the ambient conditions: (circle) H^+ , (square) He^+ , (triangle) vacuum. ‘Weak’ cavities, those with $B_{peak}/B_o < 1.4$, are highlighted with a firebrick colored dash-double dot circle. The ‘weak’ cavities are used for the linear least-squares fit. 61
- 3.4 Figures (a) and (b) show a normalized residual plot between the experimental cavity size and the empirically derived cavity size $(2R_c/2R_B) - 1$ versus the R_B -scaling and $(2R_c/2R_B) - 1$ versus the initial Alfvénic Mach number, respectively. The plotted dataset is a collection of the entries in table 3.1 that use graphite targets. Figure (b) includes trend lines associated with other characteristic cavity scalings (the equal-mass radius R_M , the primed ‘hybrid’ magnetic-mass radius R'_{BM} , and the equal-charge radius R_*) normalized to the ‘prime’ magnetic-stopping radius R'_B (equation 3.7). 63

- 3.5 A comparison between the MOIC expansion (defined by equation 3.28) and a sub-Alfvénic ($M_A \approx 0.7$), ‘weak’ ($B_{peak}/B_o \approx 1.22$) expansion from the 2011 LaPD-Phoenix campaign (Run03), as well as, the vacuum expansion from the 2013 January LaPD-Phoenix campaign (Run05). For the comparison, the plot is displayed in normalized coordinates with $X_{cav}(t)$ normalized to the maximal cavity radius R_c (equivalent to 2χ) and the expansion time time normalized to $R_c/V_{cav,o}$ (equivalent to 2τ), where $V_{cav,o}(= [\partial_t X_{cav}(t)]_{t=0})$ is the initial cavity expansion velocity. 77
- 3.6 Figures (a) and (b) show the normalized cavity expansion, $V_{cav}/V_{cav,o}$ ($= \chi_v$) versus $V_{cav,o} t/R_c$ ($= 2\tau$), for Run03 and Run04, respectively, of the 2013 January LaPD-Phoenix campaign. The MOIC expansion profile is given as the red dashed-line (equation 3.28) and the red shaded region represents the expansion profiles given the uncertainty in $V_{cav,o}$ and R_c . The blue solid-line gives the ambient-density at $X_{cav}(t)$ and the blue dashed-line does the same for $X_{ramp}(t)$ 79
- 3.7 All figures represent the magnetic field structure for a diamagnetic cavity that fully expels ($\alpha = 0$) the background magnetic field $B_o \hat{\mathbf{z}}$. Figure (a) and (b) give the compressional and shear components, respectively, for an iMS; whereas, figures (c) and (d) do the same for a normal-weighted siMS with $\sigma_c/r_c = 0.25$. The magnetic field is normalized to B_o and the spatial coordinates are normalized to the cavity radius r_c . The dash-dot line represents the magnetic field contour level of $B/B_o = 0.5$ and the dashed line gives $r = r_c$. 92

- 3.8 Plotted are some key cavity characteristics for normal-weight siMS cavities of $\alpha = 0$ versus the diamagnetic current widths σ_c/r_c . Figure (a) gives cavity locations for the compression ramp r_{ramp}/r_c , the peak magnetic compression r_{peak}/r_c , the experimentally defined cavity edge r_{cav}/r_c (where $B = 0.5B_o$), and the radial normalization for the upstream magnetic field r_{siMS}/r_c (equation 3.66). The shaded region represents the magnetization of the spheres, or diamagnetic current layer, and is defined as $\ln(-3M_n/2\mu_oB_o)$. Figure (b) gives magnetic field ratios for the peak compression B_{peak}/B_o , the magnetic field at $r = r_c$ $B(r_c)/B_o$, and the magnetic field at $r = r_c$ with respect to the peak compression $B(r_c)/B_{peak}$ 96
- 3.9 This plot compares the iMS (orange) and normal-weight siMS (light blue) models against experimental magnetic field profiles (black) from the 2011 LaPD-Phoenix campaign, Run01 in figure (a) and Run03 in figures (b) and (c). The blue curve represents the data points used to calculate α . The magnetic field is normalized to B_o and the distance from the target X_{TARGET} is normalized to the time-dependent cavity radius $r_{cav}(t) = 0.5X_{cav}(t)$. The grey shaded region represents the ambient-density. 98
- 3.10 A comparison of the magnetic field profile for Run04 of the 2013 January LaPD-Phoenix campaign (black) to the iMS (orange) and normal-weight siMS (light blue) models. The blue points represent the data of the cavity trough used to calculate α . The magnetic field is normalized to B_o and the distance from the target X_{TARGET} is normalized to the time-dependent cavity radius $r_{cav}(t) = 0.5X_{cav}(t)$. The grey shaded region represents the ambient-density. 100

3.11	Key cavity values for Run03 of the 2011 LaPD-Phoenix campaign. Figure (a) shows the cavity expansion speed $V_{cav}/V_{cav,o}$ and (red dash-line) the MOIC expansion model (§3.3). Figure (b) shows the ambient density at X_{cav} (solid) and X_{ramp} (dash). Figure (c) plots the peak experimental compression B_{peak}/B_o and (red) the iMS compression (equation 3.68). Figure (d) plots the magnetic field inside the cavity $\alpha = B_{inside}/B_o$ with the grey region representing the standard deviation of the points used for the calculation. Figure (e) gives the normalized compression ramp width (equation 3.73) and (red dash-line) the iMS width value.	106
3.12	Cavity values for Run03 of the 2013 January LaPD-Phoenix campaign. Figures (a)-(e) are the same quantities as plotted in figure 3.11. Figure (e) also plots (blue) the ratio of the local ambient-ion inertial length at X_{ramp} to the time-dependent cavity radius $(c/\omega_{pi})/r_{cav}$	108
3.13	Cavity values for Run04 of the 2013 January LaPD-Phoenix campaign. Figures (a)-(e) are same as described in figure 3.12. Figure (f) displays the normalized cavity edge to compression ramp separation (equation 3.75). The red dash-lines in figure (f) give fiducial markers for the cavity-ramp separation of the iMS model (equation 3.76) and the normal-weight siMS model with $\sigma_c/r_c = 0.20$ and 0.33	109
3.14	An illustration of the cavity magnetic field for Run17 of the 2013 October LaPD-Phoenix campaign. Plotted is a series of temporal, magnetic field line-outs stacked according to their distance from the target X_{TARGET} . Also plotted, (red) the location of the peak compression for each line-out $X_{peak}(t)$, (grey) the location in the cavity edge where the magnetic field is equal to B_o , and (blue) the location of the cavity edge $X_{cav}(t)$ (where $B = 0.5B_o$). . . .	117

- 3.15 Cavity values for Run17 of the 2013 Oct. LaPD-Phoenix campaign. Figure (a) shows the normalized cavity expansion velocity, (b) the ambient-density at X_{cav} (solid) and X_{ramp} (dash), (c) peak magnetic field compression, (d) magnetic field inside the cavity $\alpha = B_{inside}/B_o$, (e) normalized ramp width (defined in equation 3.73), and (f) normalized cavity-ramp separation Δ_{cr} (defined in equation 3.75). 119
- 3.16 Three magnetic field profiles for Run17 of the 2013 Oct. LaPD-Phoenix campaign. Each profile corresponds to a separate time frame in the expansion: early (blue), intermediate (black), and late (orange). The early time ($V_{cav,o}t/R_c = 1.06$) is just after the ‘enhanced’ deceleration phase and before the compression reaches its strongest. The intermediate time ($V_{cav,o}t/R_c = 1.56$) corresponds to when Run17 has reached its shock-like conditions just before X_{ramp} exits the high ambient-density. In the late time ($V_{cav,o}t/R_c = 2.08$) X_{ramp} has left the high ambient-density and the compression has decreased and grown broader. As a reference, the iMS magnetic profile (dash-dot) is overlaid. 121
- 4.1 A comparison of the Rayleigh/MOIC expansion model with the two expansion cases from figure 3.5 and the three datasets compared by Bonde[9] (figure 2.4 therein). The cavity radius is normalized to the maximal cavity radius R_c and the expansion time is normalized to the characteristic expansion time $1.402 R_c/V_{ro}$, where V_{ro} is the initial radial expansion velocity. For a reference, equation 4.7 is plotted in grey to represent expansions with added external pressures p_{ext} on the cavity with values of $\Gamma = 2, 5, \text{ and } 10$ 128

B.1 Figures (a) and (b) represent the inductive electric field ($\mathbf{E} = E_\phi \hat{\phi}$) for a diamagnetic cavity that fully expels ($\alpha = 0$) the background magnetic field $B_o \hat{\mathbf{z}}$. Figure (a) is for an iMS, whereas, figure (b) is for normal-weight siMS of $\sigma_c/r_c = 0.25$. The electric field is normalized to $v_c B_o$, where v_c is the cavity expansion speed, and the spatial coordinates are normalized to the cavity radius r_c . The dash-dot line represents the magnetic field contour level of $B/B_o = 0.5$ and the dashed line gives $r = r_c$ 147

B.2 All figures represent the $\mathbf{E} \times \mathbf{B}$ -drift structure for a diamagnetic cavity that fully expels ($\alpha = 0$) the background magnetic field $B_o \hat{\mathbf{z}}$. Figure (a) and (b) give the parallel and perpendicular components to \mathbf{B}_o , respectively, for an iMS; whereas, figures (c) and (d) do the same for a normal-weighted siMS with $\sigma_c/r_c = 0.25$. The $\mathbf{E} \times \mathbf{B}$ -drift is normalized to v_c and the spatial coordinates are normalized to the cavity radius r_c . The dash-dot line represents the magnetic field contour level of $B/B_o = 0.5$ and the dash line gives $r = r_c$. . . 151

LIST OF TABLES

1.1	This table compares some of the obtainable plasma parameters of the experiment with the plasma parameters of the Earth’s bow-shock, both in physical and dimensionless parameters. Even though the experiment and bow-shock have significantly varying physical parameters they still have similar dimensionless parameters, suggesting that the experiments can produce comparable conditions to astrophysical collisionless shocks.	13
1.2	The evolution of a cavity expansion has three different stages it goes through and, depending on the set plasma parameters, there are three different scenarios that can occur.	15
2.1	A timeline of the progression of the LaPD-Phoenix experiments. Each experiment marks a significant upgrade to the Phoenix laser system and/or LaPD capabilities. The steady increase in laser energy allows for stronger, larger, and, hence, longer lasting magnetic pistons. The increase in ambient-density n_e , both magnitude and volume, also provides a larger interaction scale while decreasing the Alfvén speed (effectively increasing the possible Alfvénic Mach number). LaPD’s main cathode is made from Barium-Oxide coated Nickel (BaO-Ni) and the secondary cathode is Lanthanum-Hexaboride (LaB_6). The target material is either graphite (C) or high-density polyethylene (HDPE), which is a chain structure of CH_2	23
2.2	Experimental laser configuration for each beam line in the Trident platform. There are three beam lines, of which, two are used to generating the ambient- and debris-plasma and the third is used an optical diagnostic. The diagnostic beam is configured for either Thomson scattering or proton radiography. . .	28

2.3	This table contains a summary of the dimensions and magnetic field characteristics for the pulsed Helmholtz Coil (HC) used during the 2010 Trident campaign.	30
2.4	A chart indicating the difference in key parameters between the Trident experiment and the January 2010 LaPD-Phoenix experiment. This difference leads to significant improvement in key normalized parameters and creating an environment that is more conducive for shock formation.	37
2.5	The various magnetic flux probes deployed in the LaPD-Phoenix and Trident experiments.	42
3.1	This table contains a list of accumulated experimental datasets between the Trident and LaPD-Phoenix platforms. Datasets selected contain a cavity expansion to its maximal size within the measurement range. The collection contains three vacuum expansions along with a few sub-Alfvénic expansions ($M_A < 1$), a few ‘marginally’ super-Alfvénic expansions ($M_A \sim 1$), and a few ‘highly’ super-Alfvénic expansions ($M_A > 1.5$).	60
3.2	This table compares the time and distance it takes for the compression ramp X_{ramp} of Run03 and Run04 of the 2013 January LaPD-Phoenix campaign to transverse two different sections of ambient-plasma density, $n_e \geq 0.9 [n_e]_{peak}$ and $n_e \geq 0.5 [n_e]_{peak}$	81
A.1	A list of common terms and variables used throughout this dissertation.	137

ACKNOWLEDGMENTS

I would like to thank:

My advisor, Prof. Chris Niemann, for giving me the opportunity to pursue my doctoral degree in a fascinating and difficult topic.

Dr. Carmen Constantin for dedicating countless hours to designing, building, maintaining, and operating the Phoenix Laser facility that made this dissertation possible.

Prof. Walter Gekelman, Prof. George Morales, and Prof. Christopher Russell for dedicating their time and expertise as members of my dissertation committee.

Dr. Steve Vincena, Dr. Bart Van Compernelle, and Dr. Shreekrishna Tripathi for being indispensable off-the-bench players during our experiments, continuously volunteering to stay late and come in on weekends to get the job done.

Zoltan Lucky and Marvin Drandell for sharing their knowledge of the LaPD and everything mechanical that allowed us to design and build the required infrastructure to seamlessly integrate the Phoenix Lab with the LaPD.

Dr. Patrick Pribyl, whose advice on designing and operating diagnostics is second to none. Without it, I'd probably still be chasing down why my bdot signal was always half of what I thought it should be.

Harry Lockart and the other members of the Physics and Astronomy Machine Shop for machining many tiny bdot cores and not taking their frustration out on me. They always met the tough experimental deadlines and still produced pieces that exceeded any expectations.

The local Starbucks[®] crew for always keeping me highly caffeinated and providing a frequent workspace outside the lab and home.

My fellow graduate students for putting up with my strong opinions and animated discussions. Dr. Derek Schaeffer for being just as opinionated and willing to discuss our ideas to the n^{th} degree. Dr. Anton Bondarenko for bring a perspective to the table that I would never have thought of, but always valued. Eric Clark whose is a good a brewmaster as he is

a programmer.

Dr. David Schaffner for being a trusted colleague and friend during my my graduate tenure, and beyond. I always looked forward to and valued our “coffee discussions,” from which many intriguing and humorous ideas were born.

My family for always being encouraging and understanding, even if at times it was a little backhanded. I would not have expected any less. Without their love and guidance, I would not be the person I am today.

VITA

- 2006 B.S. Physics (with Mathematics Minor)
California Polytechnic State University, San Luis Obispo
- 2006–2007 Teaching Assistant (General Physics)
Physics and Astronomy Department, UCLA.
- 2007–Present Research Assistant
Physics and Astronomy Department, UCLA.
- 2008 M.A. Physics
UCLA, Los Angeles, California
- 2009 (Fall) Teaching Assistant (Plasma Lab)
Physics and Astronomy Department, UCLA.

PUBLICATIONS

E. T. Everson, P. Pribyle, C. G. Constantin, A. Zlystra, D. Schaeffer, N. L. Kugland, and C. Niemann. “Design, construction, and calibration of a three-axis, high-frequency magnetic probe (b-dot probe) as a diagnostic for exploding plasmas.” *Review of Scientific Instruments*, 80:113505, November 2009. doi:[10.1063/1.3246785](https://doi.org/10.1063/1.3246785).

CHAPTER 1

Introduction

Collisionless shocks and their formation is a challenging topic that has caused debates for decades. They are a phenomena that occur in many astrophysical and terrestrial space environments[83] and display a wide range of physical mechanisms behind them. Most observed collisionless shocks have been of a stationary, or steady-state, type which does not allow for an investigation of the formation process. As a result, little experimental effort has been put forward to understand how a collisionless shock forms, leaving most of the investigation to theoretical efforts.[36, 50, 51, 76, 77] The recent discovery that the Earth's bow shock can reform[47] has brought new interest into the process. In an initial effort to produce laboratory collisionless shocks, the experiments discussed here set out to study and provide the initial experimental data on the processes that lead to collisionless shock formation.

Collisionless shocks are observed in the edges of supernova remnants,[79] coronal mass ejections, the solar wind, planetary bow-shocks,[26, 71] and ionospheric explosions.[24] While collisionless shocks have been studied with remote diagnostics and *in-situ* by spacecraft for decades, they are inherently difficult to diagnose by these means and there is essentially zero controllability over the parameter space. When using properly scaled dimensionless plasma parameters (see §1.2 and table 1.1), laboratory experiments can contribute to the understanding of collisionless shock physics.[23, 92] Laboratory experiments provide better control, flexibility, and reproducibility of the parameter space. They also include the transient events of the collisionless shock formation and have a more robust diagnostic capacity. This allows for a more detailed and versatile study of both the collisionless shock formation

and the physics of the formed collisionless shock. Furthermore, the experimental results can be used to compliment existing spacecraft measurements and validate computational codes.

Within the shock frame, a collisionless shock is formed when: (1) the incoming plasma flow is greater than the local magnetosonic and/or Alfvén speed, (2) the dissipation mechanism across the shock interface is sufficient enough to decelerate the incoming plasma flow, thermalize the energy of the flow, and increase entropy, and (3) this occurs over a length scale shorter than the classical ion-ion mean-free-path. The various laboratory experiments performed over the years set out to answer the dissipation question for various points within the collisionless shock parameter space. Laboratory experiments are designed around the idea of using a piston, generally a magnetosonic pulse, to couple energy and momentum into the plasma that, if conditions are sufficient enough, will cause the coupled plasma to order itself into a collisionless shock.[23], see §1.1 for more details. The “if conditions are sufficient enough” is fundamentally connected to the question of ‘what enables a collisionless shock to form?’ but is traditionally glossed over to study the shock itself.

Several experiments have been designed to access different regions in the shock parameter space, each utilizing a unique piston to shock the plasma. Early Θ -pinch experiments were successful in driving quasi-perpendicular shocks ($\theta_{Bn} = 90^\circ$ where θ_{Bn} is the angle between the background magnetic field \mathbf{B}_0 and the normal to the shock front $\hat{\mathbf{n}}$), but there was no separation between the piston and shock[20, 31, 62, 80]. A later Θ -pinch experiment had some success in producing a shock-like structure that separated from the piston[65]. V. M. Antonov *et al.* (1985)[1] had similar success with an expanding laser-produced plasma (LPP) through a magnetized background plasma. While more recent work studied collisionless shocks by combining a LPP with a Z-pinch[66] or examining at the merging of two plasma jets[53]. Other experiments studied the diamagnetic cavity generated by sub-Alfvénic LPP expansion in an external magnetic field[15, 22, 42, 70, 84].

None of the previous experiments looked at how their piston coupled to the plasma and how the shock may have formed, except for those studying the diamagnetic cavity expansion. The diamagnetic cavity studies focused on the interaction between the cavity

and surrounding plasma. These studies have correlations with the shock formation process, but they did not access a parameter space that was conducive to shock generation, i.e. the expansions were sub-Alfvénic. The experimental configuration utilized for this paper, see §1.3, utilizes the the same configuration as the diamagnetic cavity studies, but with increase laser energy and increase plasma densities that allow the experiments to achieve conditions suitable for collisionless shock generation.

To follow, section 1.1 will provide a brief overview of the types of collisionless shocks and the theory behind them. Section 1.2 will cover how an experiment can be designed to create laboratory collisionless shocks and section 1.3 will explain how the experiments utilized here satisfy that design. Before continuing on to the experimental setups (§2) and the experimental results (§3), section 1.4 will provide a scope fore this dissertation and what it sets out to achieve.

1.1 Collisionless Shocks: A Brief Review of Types

Before approaching the task of how to produce a collisionless shock in the laboratory, a brief overview of the experimentally relevant collisionless shocks is in order. For an in depth review see [72], [82], [4], [43], [11], and [83]. There is a wide range of classifications for collisionless shocks. To start, this discussion will be restricted to a classification of non-relativistic, non-radiative, and magnetized conditions. The non-relativistic condition is straight forward in requiring that all thermal speeds be much less than the speed of light $v_{th}/c \ll 1$ (for electrons this also means $k_B T_e \ll m_e c^2 \approx 0.511$ MeV) as well as the shock speed to be $v_{sh}/c \ll 1$. Non-radiative shocks require that the radiation emitted by the shocked plasma can not readily affect the upstream, un-shocked plasma. Magnetized shocks are shocks that take place in a magnetized environment and allow for the generation of currents both across and along the magnetic field. Within theses conditions there are the additional classifications of quasi-perpendicular versus quasi-parallel shocks as well as subcritical versus supercritical shocks, both discussed in more detail below.

Collisionless shocks take advantage of the plasmas ability to generate ‘anomalous collisions’ (non-classical, non-binary ‘faux’ collisions) from collective behavior between groups of particles and high-frequency field oscillations. This collective behavior generates irreversible dissipation across the shock front (Δ_{sh}) on length scales shorter than the classical mean-free-path. This irreversible dissipation, anomalous dissipation, acts to thermalize the kinetic energy of the incoming, un-shocked plasma flow as well as generate entropy. Further discussion of possible anomalous dissipation mechanism will be left to §1.1.1.

A Collisionless shock forms when a large obstacle is placed in a plasma flow in which that flow exceeds any of the characteristic electromagnetic (EM) plasma wave phase velocities in the obstacle’s frame of reference. Thus, the flow is required to decelerate on a spatial scale Δ_{sh} shorter than a classical mean-free-path. This requires the production of anomalous dissipation to thermalize the kinetic energy of the incoming plasma flow. In a magnetized plasma there are three characteristic EM plasma waves: the *fast*, *slow*, and *intermediate* (or *Alfvénic*) modes. The *intermediate* mode is the traditional Alfvén wave which has a phase velocity (Alfvén speed) of $V_A = B_o/\sqrt{\mu_o m_i n}$, where m_i is the ion mass and n is the plasma number density. The other two modes (*fast* and *slow*) are the branches of the magnetosonic waves with phase velocities given by

$$c_{ms}^2(\theta_{Bk}) = \frac{1}{2} \left\{ c_{ms}^2 \pm \left[(V_A^2 - c_s^2)^2 + 4V_A^2 c_s^2 \sin^2(\theta_{Bk}) \right]^{1/2} \right\} \quad (1.1)$$

where θ_{Bk} is the angle between the wave number \mathbf{k} and the background magnetic field \mathbf{B}_o , c_s is the sound speed, and $c_{ms}^2 = V_A^2 + c_s^2$ is the angle-independent magnetosonic sound speed. The *fast* and *slow* modes correspond to the respective phase velocities of c_{ms}^+ and c_{ms}^- . In principle, if the shock can exceed the phase velocity, then there could exist three types of shocks corresponding to each mode.

The *fast* and *slow* modes are angle-dependent with the *slow* mode disappearing for propagation across \mathbf{B}_o ($\theta_{Bk} = 90^\circ$) and the *fast* mode reducing to an Alfvén wave for propagation along \mathbf{B}_o ($\theta_{Bk} = 0^\circ$). For shocks along \mathbf{B}_o (quasi-parallel) the shock speed needs to exceed the largest EM plasma wave speed which is V_A ; hence, the shock needs

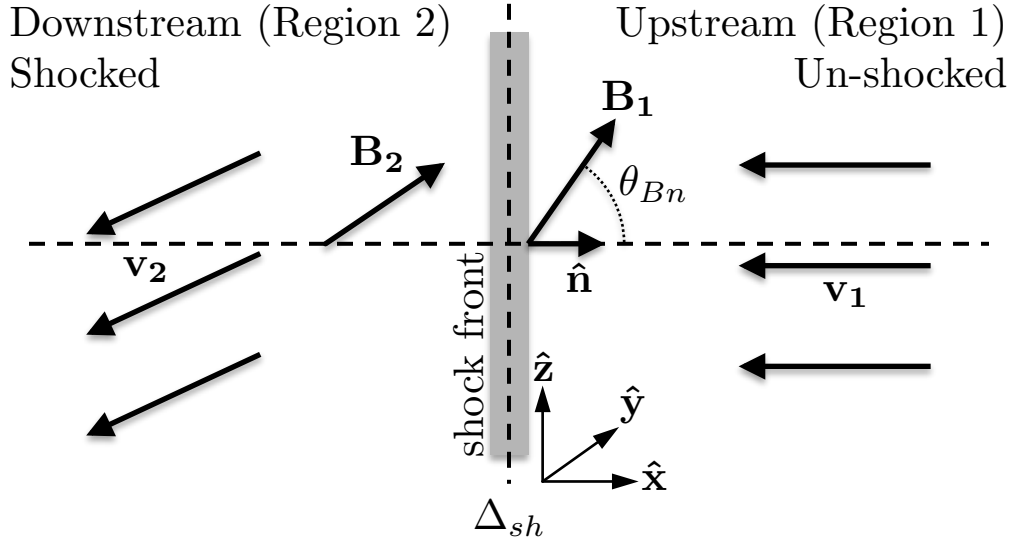


Figure 1.1: A shock frame sketch depicting the basic geometry of a thin, planar collisionless shock of thickness Δ_{sh} . Represented is a special case where the upstream plasma flow \mathbf{v}_1 is anti-parallel to the shock normal $\hat{\mathbf{n}}$. The shock is moving from left to right and values denoted with 1 correspond to upstream, un-shocked conditions and 2 correspond to downstream, shocked conditions. The magnetic field is represented by \mathbf{B} and the plasma flow velocities are represented by \mathbf{v} . Diagram is adapted from *R. A. Treumann*[83].

to be super-Alfvénic, $v_{sh}/V_A = M_A > 1$. Whereas, shocks across \mathbf{B}_0 (quasi-perpendicular) need to exceed the *fast* mode wave speed; hence, they need to be super-magnetosonic, $v_{sh}/c_{ms} = M_{ms} > 1$ ($c_{ms}^+(90^\circ) = c_{ms} = \sqrt{V_A^2 + c_s^2}$). For slow sound speeds ($c_s/V_A \ll 1$), like the experiments here, the magnetosonic speed reduces to the Alfvén speed. From here on out the use of super-magnetosonic and super-Alfvénic are considered to be interchangeable.

Figure 1.1 shows a typical shock geometry for a special case thin, planar shock where the upstream plasma flow \mathbf{v}_1 is anti-parallel to the shock normal $\hat{\mathbf{n}}$ (i.e. $\mathbf{v}_1 \times \hat{\mathbf{n}} = 0$). This is not always the case, but is the most relevant for the studies presented here. The sketch is done in the shock's reference frame and the background magnetic field \mathbf{B}_1 is at an angle θ_{Bn} to the shock normal. The shock front has a width Δ_{sh} that is less than the classical mean-free-path. The upstream, un-shocked, conditions are denoted with a 1 and the downstream, shocked, conditions are denoted with a 2. While in the shock's reference

frame, the upstream plasma flow velocity is equal to the shock speed ($v_1 = v_{sh}$). Like the magnetosonic waves in which a collisionless shock emerges from, the shock has differing behavior depending on its propagation angle to the background magnetic field. This leads to the additional classification of quasi-perpendicular shocks and quasi-parallel shocks. Quasi-perpendicular shocks have propagation angles of $\pi/2 \leq \theta_{Bn} \lesssim \pi/4$ and quasi-parallel shocks have propagation angles of $\pi/4 \lesssim \theta_{Bn} \leq 0$. The work here focuses on quasi-perpendicular collisionless shocks.

In the shock frame of reference the relationship between upstream and downstream values of density n , flow velocity normal to the shock front $|\mathbf{v} \cdot \hat{\mathbf{n}}|$, and tangential magnetic field to the shock front $|\mathbf{B} \times \hat{\mathbf{n}}|$ can be obtained using the magnetohydrodynamic (MHD) equations for a single-fluid plasma.[11, 63, 83, 93] It is assumed the shock is planar, the upstream and downstream plasmas are isotropic (allowing the fluid pressure tensor to be written as a scalar $\mathbf{P} = \nabla p$), and the plasma flow is adiabatic. This all allows the the thermal pressure to be written as a scalar with the same polytropic index (γ) perpendicular and parallel to \mathbf{B}_o , i.e. $p \propto n^\gamma$.¹ These resulting relations are known as the Rankine-Hugoniot (RH) jump conditions and they describe the global conservation of energy from the far upstream plasma to far downstream plasma, but they do not encompass the microphysics of the shock transition. For strictly perpendicular shocks ($\theta_{Bn} = \pi/2$), the jump conditions are the real solutions to the polynomial[12]

$$0 = A_2 X^2 + A_1 X + A_0 \quad (1.2)$$

$$A_2 = 1 + \gamma \quad (1.3)$$

$$A_1 = (1 - \gamma) - \gamma(1 + \beta_1)M_A^{-2} \quad (1.4)$$

$$A_0 = (\gamma - 2)M_A^{-2} \quad (1.5)$$

$$X^{-1} = \frac{n_2}{n_1} = \frac{B_2}{B_1} = \frac{v_1}{v_2} \quad (1.6)$$

¹Adiabatic means $PV^\gamma = \text{const.}$ where $P = Nk_B T/V$ is the plasma pressure, N is the total number of particles, T is the plasma temperature, and V is the system volume. Let $n = N/V$ be the particle density then $p \propto V^{-\gamma} \propto n^\gamma$.

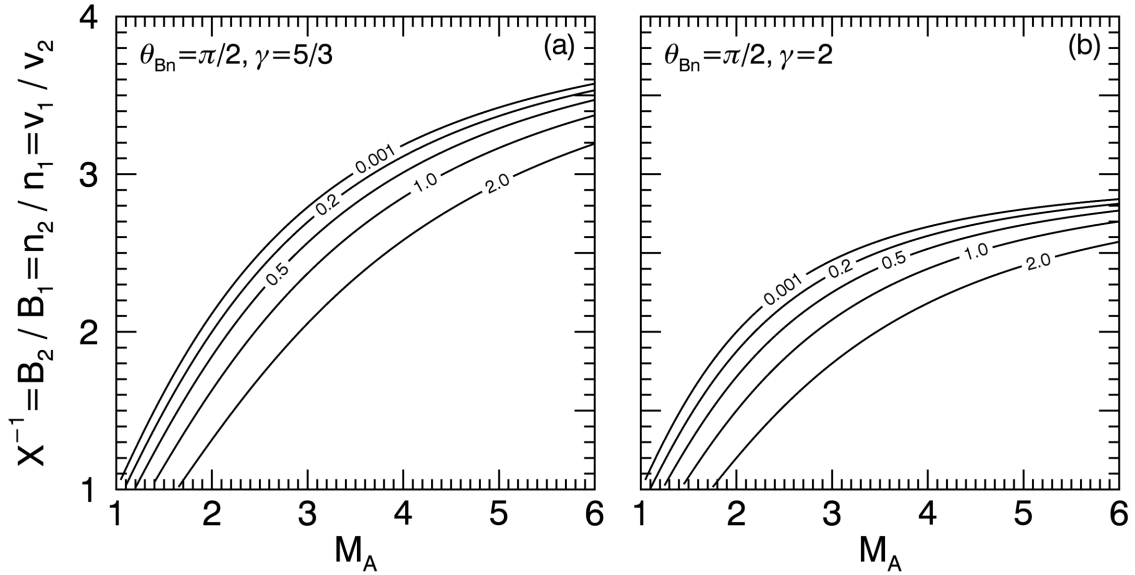


Figure 1.2: Rankine-Hugoniot jump conditions for a strictly perpendicular ($\theta_{Bn} = \pi/2$), planar collisionless shock, equation 1.7, versus the Alfvénic Mach number M_A . Each plot shows traces for fixed $\beta_1 = n_1 k_B T_1 / (B_1^2 / (2\mu_o))$ of 0.001, 0.2, 0.5, 1.0, and 2.0. Plot (a) plots the jump conditions for an adiabatic index of $\gamma = 5/3$ and plot (b) plots the jump conditions for an adiabatic index of $\gamma = 2$.

where the plasma flow velocities v_1 and v_2 are completely normal to the shock front, the upstream and downstream magnetic fields, B_1 and B_2 respectively, are completely parallel to the shock front, the shock speed equals the upstream plasma flow velocity $v_{sh} = v_1$, $M_A = v_{sh}/V_A$ is the Alfvénic Mach number for the shock, $\beta_1 = n_1 k_B T_1 / (B_1^2 / (2\mu_o))$ is the upstream plasma-beta (in mks units), and T_1 is the upstream total temperature (in mks units). Equation 1.2 has two solutions but only one real solution given by

$$\begin{aligned}
 X &= \frac{n_1}{n_2} = \frac{B_1}{B_2} = \frac{v_2}{v_1} \\
 &= \frac{\gamma - 1}{2(1 + \gamma)} \left\{ 1 + \frac{\gamma(1 + \beta_1)}{\gamma - 1} M_A^{-2} + \left[\left[1 + \frac{\gamma(1 + \beta_1)}{\gamma - 1} M_A^{-2} \right]^2 + 4 \frac{(1 + \gamma)(2 - \gamma)}{(\gamma - 1)^2} M_A^{-2} \right]^{1/2} \right\}
 \end{aligned} \tag{1.7}$$

which gives the jump conditions for a specified γ and β_1 . Figure 1.2 displays jump conditions for two adiabatic indices, $\gamma = 5/3$ for a monatomic particle with 3 degrees-of-freedom in 3D

and $\gamma = 2$ for a monatomic particle with 2 degrees-of-freedom in 2D. Each plot shows curves for five different plasma beta values ($\beta_1 = 0.001, 0.2, 0.5, 1, \text{ and } 2$) that are relevant to the experimental conditions here. As a crude approximation, it can be seen for small Alfvénic Mach numbers ($1 \leq M_A \lesssim 2$) and low plasma beta ($\beta_1 \lesssim 1$) the jump conditions scale roughly like the Alfvénic Mach number $X^{-1} = B_2/B_1 = n_2/n_1 \sim M_A$. To start, these jump conditions can initially be used as a comparable to the experiments to help confirm shock production. However, as these experiments proceed and produce more and more collisionless shock scenarios then the volume of collected data can be used to map out and validate the parameter space.

1.1.1 Shock Criticality and Dissipation

Classification of shock criticality is based on how the upstream plasma is dissipated across the shock front. Shocks are formed by a combination of nonlinear wave steepening (nonlinear dispersion) and anomalous [resistive] dissipation. A shock can be dominated by either process, but there always has to be some anomalous dissipation to generate entropy which dispersion can not do alone.[41, 46, 83] The combination of the two act to slow the upstream plasma while thermalizing it and increasing entropy. All this happens within the width Δ_{sh} of the shock front. At a certain Mach number, the critical Alfvénic Mach number M_c , the anomalous dissipation can not produce enough entropy within that Δ_{sh} to meet shock conditions. To handle the excess energy in the bulk flow that the dissipation can not thermalize, the shock must reflect a fraction of the inflowing plasma back upstream.[48] For resistive shocks (anomalous dissipation dominated) *W. Marshall* (1955)[48] was able to numerically determine the largest critical Mach number as $M_c \approx 2.76$; whereas, *J. P. Edmiston and C. F. Kennel* (1984)[25] were able to numerically solve for M_c over the parameter space spanned by θ_{Bn} and β_1 . For the experimentally relevant conditions of $\beta \lesssim 1$ and $\theta_{Bn} \sim \pi/2$, the critical Mach number is $M_c \approx 2.76$.

The experiments here focus on subcritical collisionless shocks that are dominated by anomalous dissipation, so the discussion of supercritical and dispersion dominated collision-

less shocks are beyond the scope of this paper and are left to other sources[4, 72, 82, 83]. For dissipation dominated, quasi-perpendicular subcritical collisionless shocks, figure 1.3 shows a schematic view of the theoretical workings within the shock front. The width of the shock front is typically on the order of an ion-inertial length $\Delta_{sh} \lesssim c/\omega_{pi}$ which keeps the upstream ions unmagnetized² while the electrons remain tied to the magnetic field. The upstream ions are decelerated over Δ_{sh} , but are not reflected back upstream. Consequently, there must exist an electric potential $U(x)$ across Δ_{sh} that acts to slow down the bulk flow. Since the electrons are magnetized and the ions are not, the electrons will experience an $\mathbf{E} \times \mathbf{B}$ -drift within Δ_{sh} resulting from the electric field associated with the electric potential ($E = -\partial_x U(x)$). The resulting electric current is given by

$$\mathbf{j}_e = -en \frac{\mathbf{E} \times \mathbf{B}}{B^2} \quad (1.8)$$

where n is the electron density, \mathbf{E} is the electric field associated with the electric potential, and \mathbf{B} is the magnetic field. The current flows within the shock front and perpendicular to the shock normal $\hat{\mathbf{n}}$ while simultaneously flowing perpendicular to the background magnetic field. As the current flows it acts as a free energy source to drive instabilities within the shock front. As first suggested by *R. Z. Sagdeev* (1966)[72], the anomalous dissipation arises from particle scattering of these instabilities. Such possible instabilities include the two-stream instability, ion-acoustic instability, lower-hybrid-drift instability, and the modified two-stream instability (MTSI); of which, the ion-acoustic and lower-hybrid-drift instability are thought to be favored[88, 90]. At this point, these experiments can not determine which instability is at play but will be a focus for future work.

² $c/\omega_{pi} = V_A/\Omega_{ci} = (v_{sh}/\Omega_{ci})(V_A/v_{sh}) = \rho_1/M_A$, where ω_{pi} is the upstream ion plasma frequency, c/ω_{pi} is the upstream ion-inertial length, V_A is the Alfvén speed, Ω_{ci} is the upstream ion cyclotron frequency, $\rho_1 = v_{sh}/\Omega_{ci}$ is the gyroradius of the upstream ions ($v_{sh} = v_1$), and $M_A = v_{sh}/V_A$ is the Alfvénic Mach number of the shock. Now, $\rho_1/\Delta_{sh} = (c/\omega_{pi})M_A/\Delta_{sh}$ and requiring $\Delta_{sh} \lesssim c/\omega_{pi}$ implies $\rho_1/\Delta_{sh} \gtrsim M_A$. Since $M_A \geq 1$, the upstream ions are unmagnetized with respect to the shock width $\rho_1/\Delta_{sh} \gtrsim 1$. This statement can be reversed. If it is known that the upstream ions are unmagnetized with respect to the shock front, then the shock front width has to be on the order or less than an ion-inertial length.

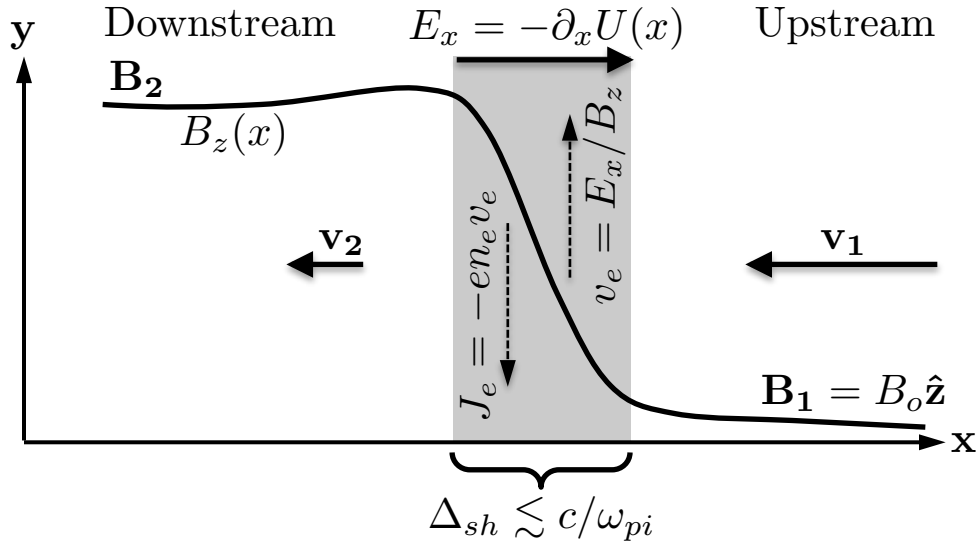


Figure 1.3: Schematic of an anomalous dissipation dominated, quasi-perpendicular, subcritical, planar collisionless shock. The upstream plasma flow \mathbf{v}_1 is decelerated as it crosses the shock front to the downstream plasma flow \mathbf{v}_2 . The deceleration comes from the electric potential $U(x)$ setup over the shock of width Δ_{sh} . A shock width of $\sim c/\omega_{pi}$ implies the ions are unmagnetized, so only the electrons will experience guiding orbit drives. The electric field from the the electric potential within the shock front causes the electrons to drift within the shock front and perpendicular to the magnetic field. This electric current behaves as a free energy source for driving anomalous dissipation within the shock front. This figure is an adaption from figure 10 and §2.1 in *R. A. Treumann (2009)*.[\[83\]](#)

1.2 Experimental Concept for Driving Collisionless Shocks

The experimental model for driving laboratory shocks is a straight forward concept on paper[\[23\]](#), but difficult to implement in practice. The model utilizes an energetic piston to act on an existing magnetized, ambient-plasma, see figure 1.4. The piston acts as a free energy source to initially couple energy and momentum into the ambient-plasma. If the piston is sufficient enough to energize the ambient-plasma into a directed flow as well as heating it, then a collisionless shock dissipation mechanism can take over and continue propagating the energized, “shocked,” ambient-plasma forward. In this scenario the “shocked”

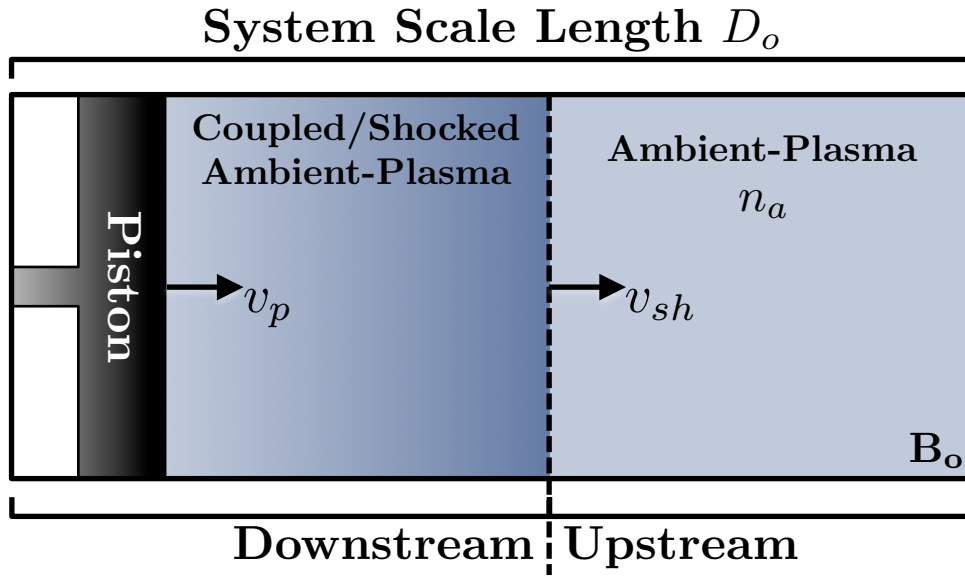


Figure 1.4: A cartoon for driving collisionless shocks in the laboratory. The background magnetic field is \mathbf{B}_o and the ambient-ion density is n_a . The piston, which is usually a strong magnetic compression, travels upstream, left to right in the figure, at a speed v_p and interacts with the ambient-plasma. As coupling occurs the piston ‘snow-plows’ the ambient-plasma creating an energized, ‘shocked,’ ambient-plasma distribution. Adapted from figure 1 in *R. P. Drake (2000). [23]*

ambient-plasma is labeled as the downstream plasma and the un-shocked ambient-plasma is labeled as the upstream plasma in figure 1.4. The difficulty in achieving success is two fold: (1) engineering an efficient piston that is able to impart sufficient momentum and energy to the existing ambient-plasma and (2) setting plasma parameters that are conducive for both collisionless shocks and coupling between the piston and ambient-plasma.

Engineering an efficient piston is specific to the experimental configuration, since not all configurations utilize the same type of piston. Understanding what makes a good piston is akin to asking what drives the piston-ambient coupling and the shock formation. The following section (§1.3), specifically §1.3.2, will discuss the importance of this coupling as it relates to the experiments presented here. The results section (§3.2-§3.6) will tackle the coupling question and shock formation based on the experimental data.

There are several necessary constraints on the plasma parameters to create conditions that are conducive to collisionless shock formation:

1. **Collisionless:** The classical mean-free-path of a shocked ambient-ion with an unshocked ambient-ion λ_{ii} must be larger than the shock features. Typically this constraint is extended to the system scale length D_o , i.e. $\lambda_{ii}/D_o > 1$.
2. **Super-Alfvénic:** The piston must drive a super-Alfvénic propagation, $M_A > 1$.
3. **Sufficient Interaction Time:** The interaction between the piston and ambient-plasma needs to be long enough for instabilities in the shock front to grow and produce significant dissipation. This implies that the time it takes for a shocked ambient-ion moving at a velocity $v(= M_A V_A)$ to transverse the experimental length ($T = D_o/v$) needs to last several gyro-periods Ω_{ci}^{-1} . This implies the shocked and unshocked ambient-ions need to be well-magnetized. $T \cdot \Omega_{ci} > 1$
4. **Sufficient Interaction Length:** The above condition also dictates the system size needs to exceed the gyroradius of the shocked ambient-ions ρ'_a ³ and, consequently, the system size must also exceed several ambient-ion inertial lengths.⁴ $D_o/\rho'_a = D_o M_A^{-1} (c/\omega_{pi})^{-1} > 1$

The last two conditions imply the ambient-ions need to be well-magnetized with respect to both the experimental volume and the piston. The later will become more apparent when the magnetic field structure of the experiment's magnetic piston is discussed in detail, see §3.4. As stated before, the constraints that make a strong piston are dependent on the type of piston utilized. For the piston used in these experiments (see §1.3), previous work attempted to set a coupling criterion that predicts when coupling is sufficient enough to drive shocks, some utilized analytical models[2, 32] and others utilized hybrid simulations[13, 60]. N. Omidi *et al.* (2002)[60] showed that the piston length scale must be larger than the

³ $\Omega_{ci}/v = \rho'_a$

⁴ $c/\omega_{pi} = V_A/\Omega_{ci} = \rho'_a/M_A$

ambient-ion inertial length, which is consistent with constraint 4 above. S. E. Clark *et al.* (2013)[13] determined that the ratio of the equal-mass radius R_M (equation 3.10) to the directed debris-ion gyroradius ρ_d must satisfy $R_M/\rho_d > 0.7$ for a H^+ ambient-plasma and C^{+4} debris-plasma.

The experiments have been able to achieve dimensionless scalable parameters that are comparable to astrophysical conditions, see table 1.1.

Plasma Parameter	Earth's Bow-Shock	Experiment
Effective Upstream Flow Speed	400 km/s	400 km/s
Ambient-Ion Density n_a	5 cm^{-3}	$5 \times 10^{13} \text{ cm}^{-3}$
Magnetic Field B_o	$5 \times 10^{-5} \text{ G}$	500 G
System Size D_o	100-1000 km	50 cm
Ambient-Ion Inertial Length c/ω_{pi}	100 km	3 cm
Debris-Ion Direction Gyroradius ρ_d	835 km	12 cm
Dimensionless Parameter		(required value)
Alfvénic Mach Number M_A	8	4 (>1)
Interaction Length $D_o (c/\omega_{pi})^{-1} > M_A$	10	10 (> 4)
Interaction Time $t \cdot \Omega_{ci}$	steady-state	3 (>1)
Collisionless λ_{ii}/D_o	10^5	$10^2 (\gg 1)$
Coupling Condition R_c/ρ_d	N/A	2 (>0.7)

Table 1.1: This table compares some of the obtainable plasma parameters of the experiment with the plasma parameters of the Earth's bow-shock, both in physical and dimensionless parameters. Even though the experiment and bow-shock have significantly varying physical parameters they still have similar dimensionless parameters, suggesting that the experiments can produce comparable conditions to astrophysical collisionless shocks.

1.3 Experimental Model

This experiment follows the rubric setup by R. P. Drake[23] by creating a LPP, referred to from here on out as the debris-plasma, to interact with a pre-existing magnetized ambient-plasma. The pre-existing magnetic field and ambient-plasma is created and allowed to reach a steady-state before the debris-plasma is generated. The interplay between the debris-plasma and background magnetic field generates the magnetic piston in Drake’s conceptual model. As the debris-plasma expands outwards it pushes the magnetic piston along with it, which in turn couples energy and momentum into the ambient-plasma. This process is referred to as the debris-piston-ambient coupling, and is interchangeably used with the terms debris-ambient coupling and piston-ambient coupling. If the coupling and plasma conditions are sufficient enough, then the necessary dissipation mechanisms are driven in the ambient-plasma, creating the collisionless shock. If successful, then the collisionless shock is a feature among the energized, or ‘shocked,’ ambient-plasma and the upstream, un-shocked, ambient-plasma. The shock itself should have a negligible to no participation from the debris-plasma.

The debris-plasma is generated from ablating a target with a high-intensity laser. At this point the largest fraction of debris-energy is contained in the debris-ions as an outward expansion. This expansion does have some directionality associated with it that is dependent on the direction of the target face surface normal. By aiming the target face at an angle to the background magnetic field then the generated piston can be roughly aimed with the directionality of the debris-plasma blow-off. This allows for the experimental investigation of both quasi-perpendicular ($45^\circ < \theta_{Bn} \leq 90^\circ$) and quasi-parallel ($0^\circ \leq \theta_{Bn} < 45^\circ$) collisionless shocks. For this paper the focus will be kept on the production of quasi-perpendicular collisionless shocks.

As the debris-plasma expands the experiment goes through three stages in its evolution. (Stage 1) At the beginning of the expansion a diamagnetic current and the resulting diamagnetic cavity are setup by the expanding debris-plasma in the background magnetic field, see

	Stage 1: Cavity Formation	Stage 2: B-Field Augmentation/ Coupling	Stage 3: B-Field Release/ Shock Breakout
No Coupling	<ul style="list-style-type: none"> • Diamagnetic Current is Driven • A fully expelled diamagnetic cavity is formed. 	<ul style="list-style-type: none"> • negligible to no coupling between the cavity and ambient-plasma • the cavity field and debris-plasma pass over the ambient-plasma unaffected • the magnetic field structure remains consistent with that of magnetized sphere 	<ul style="list-style-type: none"> • When the Cavity stops expanding the magnetic field diffuses upstream.
Weak/Moderate Coupling	<ul style="list-style-type: none"> • Diamagnetic Current is Driven • A fully expelled diamagnetic cavity is formed. 	<ul style="list-style-type: none"> • Some significant coupling occurs. • The magnetic field compression is augmented by the coupling. It increases in magnitude and has some steepening of the magnetic front. • Conditions are NOT sufficient enough to drive the necessary dissipation required for a shock. 	<ul style="list-style-type: none"> • Any coupled ambient-plasma and built up magnetic field is released upstream and allowed to diffuse when the cavity stops expanding.
Shock Production	<ul style="list-style-type: none"> • Diamagnetic Current is Driven • A fully expelled diamagnetic cavity is formed. 	<ul style="list-style-type: none"> • Strong coupling occurs. • The B-field grows and steepens to be consistent w/ the Rankine-Hugonit conditions. • An sufficient dissipation mechanism is driven in the shock front. 	<ul style="list-style-type: none"> • Shock Breakout occurs • Feature is self-consistent in the ambient-plasma • The shock feature separates from the cavity and propagates upstream as the cavity stops expanding.

Table 1.2: The evolution of a cavity expansion has three different stages it goes through and, depending on the set plasma parameters, there are three different scenarios that can occur.

§1.3.1 for details. (Stage 2) This is the coupling, or magnetic field augmentation, stage. Here the magnetic piston created in the first stage couples energy from the debris-ions into the ambient-plasma. Depending on the plasma conditions, there are several different scenarios ranging from no coupling to strong coupling that can occur here, see table 1.2 and §1.3.2 for further details. (Stage 3) This stage is marked by either a shock breakout or a diffusion of the generated field compression as the cavity stops expanding. The scenarios that occur, see table 1.3.3, depend on what occurs in stage 2. If the coupling is strong enough to drive a significant dissipation mechanism in the ambient-plasma then the formed collisionless shock will breakout as the cavity expansion comes to a stop, see §1.3.3 for further details. If not, then any built up magnetic field compression or coupled ambient-plasma will diffuse and/or advect upstream as the cavity stops expanding.

1.3.1 Stage 1: Setup of Diamagnetic Cavity

After ablation the expanding debris-plasma will form a diamagnetic cavity[16, 17, 22, 86] with a magnetic field compression (the magnetic piston) outside the cavity. The majority of the debris-energy is contained within the debris-ions. Due to the large mass discrepancies between the ions and electrons, debris-ions are unmagnetized whereas the debris-electrons are highly magnetized. This allows the debris-ions to stream radially outwards from the target while the debris-electrons are held back by the background magnetic field. The resulting space charge separation creates a radially inward electric field, see figure 1.5. This electric field provides an $\mathbf{E} \times \mathbf{B}$ -drift according to

$$\mathbf{v}_{E \times B} = \frac{\mathbf{E} \times \mathbf{B}}{B^2}. \quad (1.9)$$

Since only the debris-electrons will experience guiding orbit drifts, the debris-electrons are driven into a diamagnetic current layer while the electric field only acts to slowly pull back the expanding debris-ions. The diamagnetic current layer acts to expel the enclosed magnetic field and compress the magnetic field right outside the current layer[70, 84]. This processes is how the energy in the debris-ions is transferred into the debris-electrons, as the diamagnetic

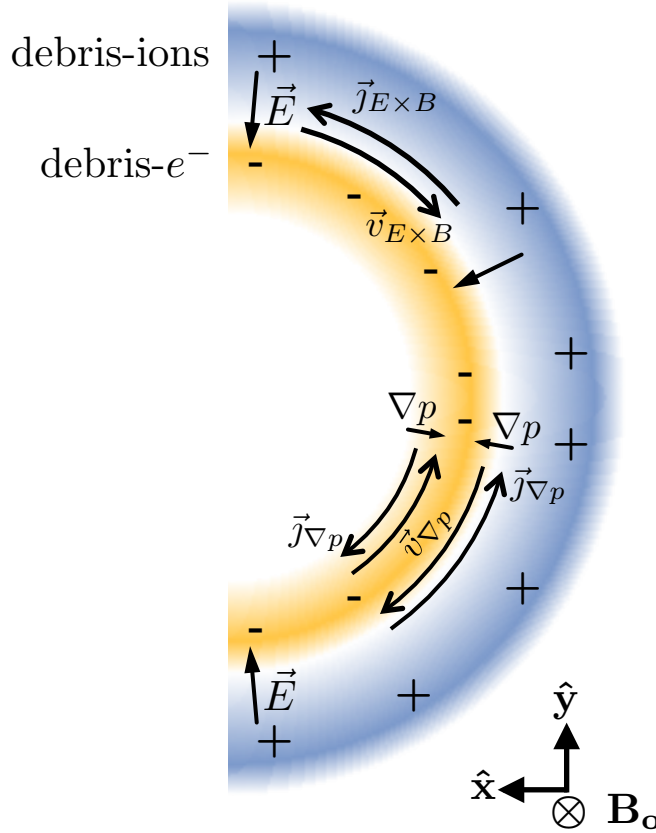


Figure 1.5: This diagram depicts how a diamagnetic current is driven to create a diamagnetic cavity. As the debris-plasma expands the highly magnetized debris-electrons (really any local electrons) will experience the guiding orbit drifts, whereas the unmagnetized debris-ions will not. The setup $\mathbf{E} \times \mathbf{B}$ -drift and $\nabla p \times \mathbf{B}$ -drift drive the diamagnetic current in the electrons.

current, which is symbolized as the energy stored in the magnetic field of the diamagnetic cavity.

This space-charge separated electric field does not act to pull the debris-electrons across the field to neutralized the expanding debris-ions. This is because the diamagnetic current is the net result of the guiding orbit in the presence of the space-charge separated electric field and \mathbf{B}_0 . For the same reason, saying the $\mathbf{J} \times \mathbf{B}_0$ force drags the electrons across the field is false. There still is a $\mathbf{J} \times \mathbf{B}$ force but it is connected to the augmented magnetic field $\delta \mathbf{B}$ created by the neighboring diamagnetic current elements. However, this $\mathbf{J} \times \delta \mathbf{B}$ acts to

squeeze the diamagnetic current layer, not drag it across \mathbf{B}_0 . Instead, as the magnetic field is expelled and an inductive electric field is generated in the polar direction $\hat{\phi}$ through the diamagnetic current layer and upstream, since the magnetic field is no longer quasi-static (i.e. $\partial_t \mathbf{B} = -\nabla \times \mathbf{E} \neq 0$). This inductive electric field generates a secondary $\mathbf{E} \times \mathbf{B}$ -drift in the radial direction that pulls the debris-electrons along at roughly the expansion speed of the debris-ions, see Appendix B.4 and figure B.2.

In addition to the $\mathbf{E} \times \mathbf{B}$ -drift there is a $\nabla p \times \mathbf{B}$ -drift, or diamagnetic drift, governed by

$$\mathbf{v}_{\nabla p} = -\frac{1}{qn} \frac{\nabla p \times \mathbf{B}}{B^2}, \quad (1.10)$$

where q is the charge of the particle experiencing the guiding orbit drift, n is the particle density of charged particle species, $p = nk_B T$ is the plasma pressure, and T is the plasma temperature. The diamagnetic drift is not a real guiding center drift because it does not cause any movement in the guiding center of a gyrating particle. Instead, it is a fluid construct resulting from the charged particles on one side of a reference area orbiting through the area more than particles orbiting through from the other side, for a given time. On the front side of the expanding debris-electrons the ∇p points radially inwards resulting in an $\nabla p \times B$ -drift in the same direction as the $\mathbf{E} \times \mathbf{B}$ -drift; thus, reinforcing the diamagnetic current. On the backside, the ∇p points a radially outwards which generates a drift that results in a non-diamagnetic current. However, the $\mathbf{E} \times \mathbf{B}$ -drift will continue driving the diamagnetic current until the enclosed magnetic field is expelled, so the backside ∇p -drift becomes negligible to the diamagnetic current on the frontside of the expanding debris-electrons.

1.3.2 Stage 2: Coupling from Piston to the Ambient-Plasma

The goal of Stage 2 is to utilize the piston generated in Stage 1 to drive the necessary dissipation required for shock formation; that is, to produce the conditions consistent with the RH jump conditions (figure 1.2) and those outlined in figure 1.3. In stage 2 the cavity has expanded to a large enough size that it can start affecting the ambient-plasma in a non-trivial manner. As listed in table 1.2, there are a few scenarios that can occur. Under sub-Alfvénic

expansion conditions the coupling becomes more of a Rayleigh-Taylor type mixing scenario from the Large Larmor Radius (LLR) instability[16, 17, 70] and/or the generalized lower-hybrid drift instability[38, 70]. Under a super-Alfvénic expansion energy can flow from the debris-ions to the magnetic piston to the ambient-plasma (debris-ambient coupling) and produce coupling that results in more of a directed flow in the ambient-plasma than of a mixing between the debris- and ambient-plasma.

When the expansion is super-Alfvénic there are three ways in which this debris-piston-ambient coupling can occur: (1) collisional coupling, (2) turbulent, or non-laminar, coupling, and (3) non-turbulent, or laminar, coupling. Collisional coupling is out since conditions have been setup to be collisionless. In turbulent coupling the energy is transferred from the debris-plasma to the ambient-plasma through the excitation of instabilities. For this experiment, the primary candidates are the modified two-stream instability and the ion-ion two-stream instability. These instabilities required $M_A \lesssim (1 + \beta_e)^{1/2}$ to grow.[52, 61] The experimental conditions have $\beta_e \ll 1$, so these instabilities are not expected to play a major roll in the coupling.

This leaves laminar coupling as the most likely method for the energy transfer. Laminar methods involve field-particle interactions through the macroscopic self-generated fields of the plasma. Previous papers[3, 7, 36, 75] have tried to address the Laminar coupling by using the electron fluid momentum equation in conjunction with Ampère’s Law to solve for the existing electric field. In this approach it is assumed the electrons are a massless fluid, there are no collisions, the plasma is quasi-neutral, and the dielectric current is negligible. The electric field is then given by [in cgs]

$$\begin{aligned} \mathbf{E} &= -\frac{1}{en_e} \nabla P_e + \frac{1}{en_e c} \mathbf{J}_e \times \mathbf{B} \\ \mathbf{E} &= -\frac{1}{en_e} \nabla P_e - \frac{1}{en_e c} \sum_s \mathbf{j}_{is} \times \mathbf{B} + \frac{1}{4\pi en_e} \mathbf{B} \times (\nabla \times \mathbf{B}), \end{aligned} \quad (1.11)$$

where n_e is the electron density, P_e is the electron plasma pressure, \mathbf{B} is the magnetic field, \mathbf{j}_{is} is the ion current of the s^{th} ion-species, and the \sum implies a sum over all the ion-species. These equations specify what the electric field should be based on known plasma conditions

(P_e , \mathbf{j}_{is} , etc.), assuming the plasma conditions are known. That is, the electric field specified by the $\mathbf{J}_e \times \mathbf{B}$ term is the field required to E×B-drift the electron fluid into that \mathbf{J}_e . Similarly, the field specified by the ∇P_e term is the field required to maintain the pressure gradient, or it corresponds to a ∇P -drift where there is an effective $\mathbf{J}_e \times \mathbf{B}$ term that makes the sum zero. Thus, this method provides good insights, but falls short since it does not give an origin story for the the electric field.

Instead of taking the above approach, this paper will attempt to provide an origin story for the field structure (E and B) based only on the existence of a diamagnetic current, and, then, infer the resulting plasma conditions and coupling mechanics within the magnetic piston. In §3.4 through §3.6 this new approach will be presented alongside comparisons to the experimental data. It will explain why the magnetic structure is shaped the way it is, how the induced and space-charge separated electric fields arise, and how the magnetic piston can fulfill the shock picture (figure 1.3).

1.3.3 Stage 3: Shock Breakout

If Stage 2 is successful at driving the necessary dissipation, then Stage 3 is where the collisionless shock separates from the diamagnetic cavity and further shock studies can be performed. If stage 2 is not successful then this stage is defined by the magnetic piston and any weakly coupling plasma diffusing and/or advecting upstream away from the diamagnetic cavity. While this stage provides a rich source of questions to be addressed and studied, it is beyond this paper and will be left to future experiments.

1.4 Scope of Dissertation

This dissertation will focuses on Stage 2 (§1.3.2) of the cavity expansion as it pertains to transferring energy from the debris-ions to the ambient-plasma through the generated magnetic piston (debris-piston-ambient coupling). This coupling studying is meant to address how the experiment can drive the shock picture (figure 1.3) for non-radiative, non-relativistic,

magnetized, quasi-perpendicular, subcritical collisionless shocks, as well as, identifying these characteristics within the experimental results. To summarize, this study sets out to:

1. Establish and validate analytical benchmarks that can be used to quantify experimental observations. These benchmarks include:
 - (a) Expansion behavior of a Magnetic Only Interacting Cavity (MOIC); that is, cavity size, expansion velocity, and deceleration versus time, see §3.3.
 - (b) Characterization of the magnetic field structure associated with a diamagnetic cavity, see §3.4.
 - (c) A maximum field compression for a MOIC, see equation 3.68 in §3.5.
 - (d) A MOIC compression ramp width, see equations 3.73 and 3.74 in §3.5.
 - (e) A separation of between the cavity edge and compression ramp, see equations 3.75 and 3.76 in §3.5
2. Establish experimental evidence of debris-piston-ambient coupling that is conducive for quasi-perpendicular, subcritical collisionless shock generation. (§3.5-§3.6)
3. Present a model, that is validated by experimental results, that explains how the magnetic piston of a MOIC can drive conditions the duplicate the collisionless shock picture, figure 1.3. (§3.5-§3.6)
4. Present further experiments that can validate/debunk additional aspects of the debris-piston-ambient coupling model.

CHAPTER 2

Experimental Platforms and Diagnostics

The data discussed in this dissertation was collected from two distinct experimental platforms: (2) the LaPD-Phoenix platform and (1) the Trident platform. Each platform was conceived to put into practice the experimental design presented in sections 1.2 and 1.3. While the platforms have their own pros and cons when it comes to the physical setup and accessible parameter space (see table 2.4), the LaPD-Phoenix platform remained the workhorse of the two platforms due to its accessibility and versatility. Both platforms utilize a LLP to form a debris-plasma and the resulting magnetic piston discussed in §1.3, but the ambient-plasma is generated from differing methods. In the Trident platform the ambient-plasma comes from the stagnation and relaxation of an expanded LLP, see section 2.2 for full details, and the LaPD-Phoenix platform uses a single or dual cold cathode discharge to generate the ambient-plasma, see section 2.1 for full details.

2.1 LaPD-Phoenix Platform

The LaPD-Phoenix platform integrates the Phoenix laser system[18] and the Large Plasma Device (LaPD)[30] at UCLA to provide a unique experimental setup. In this configuration, the LaPD provides a well-characterized ambient-plasma and magnetized environment, where the Phoenix laser system provides a well-controlled debris-plasma. Because of the high level of control between these two systems, the interaction and coupling between the debris-plasma and magnetized ambient-plasma can be meticulously investigated.

The Phoenix laser system went through several upgrades for each iteration of the exper-

LaPD-Phoenix Platform - Experiment Timeline

LaPD-Phoenix Platform - Experiment Timeline							
LaPD	BaO-Ni	$\varnothing 60$ cm $n_e \approx 2 \times 10^{12}$ cm ⁻³ H ⁺ & He ⁺					
	LaB ₆ n_e (10 ¹² cm ⁻³)		$\square 8$ cm ~ 2.0 H ⁺ , $\lesssim 6.0$ He ⁺	$\square 10$ cm $\lesssim 5.0$ H ⁺ $\lesssim 5.0$ He ⁺	$\lesssim 4.5$ He ⁺	$\square 20$ cm $\lesssim 18$ H ⁺	
Phoenix Lab	Phoenix E_{laser} (J)	$\lesssim 25$	Primary $\lesssim 35$ ~ 18.5			Diagnostic ~ 5 $\lesssim 8$	
	Raptor E_{laser} (J)			1 st Shots ~ 16	Primary $\lesssim 133$ $\lesssim 105$ $\lesssim 200$		
	PEENING				Raptor Seed		
	Target	C	C/HDPE	C	C	C/HDPE	
	Exp. Date	Aug. 2008	Jan. 2010	Jul. 2011	Jan. 2013	Jun. 2013	Oct. 2013

Table 2.1: A timeline of the progression of the LaPD-Phoenix experiments. Each experiment marks a significant upgrade to the Phoenix laser system and/or LaPD capabilities. The steady increase in laser energy allows for stronger, larger, and, hence, longer lasting magnetic pistons. The increase in ambient-density n_e , both magnitude and volume, also provides a larger interaction scale while decreasing the Alfvén speed (effectively increasing the possible Alfvénic Mach number). LaPD’s main cathode is made from Barium-Oxide coated Nickel (BaO-Ni) and the secondary cathode is Lanthanum-Hexaboride (LaB₆). The target material is either graphite (C) or high-density polyethylene (HDPE), which is a chain structure of CH₂.

iment, see table 2.1. In the beginning, the system was composed of a single beam line, the Phoenix laser, which was capable of generating up to 35 J of laser energy at a wavelength of 1064 nm in a 5 ns full-width-at-half-max (FWHM) pulse width. At its highest energies, the Phoenix laser had a repetition rate of about 10 minutes. As the necessity for larger laser energies increased (to create stronger, longer lasting magnetic pistons), the Raptor beam

line and PEENING laser were incorporated into the Phoenix laboratory. The PEENING laser operates at a wavelength of 1053 nm with a FWHM of 25 ns and energies up to 20 J. At its fastest repetition rate, the PEENING laser can operate at 6 Hz. For the experiments, the PEENING laser acted as the input seed for the Raptor laser, then the Raptor laser used a 10 cm and a 15 cm disk amplifier to increase the laser energy up to 200 J. Under Raptor operating specs, the laser pulse had a wavelength of 1053 nm with a FWHM of 25 ns and a repetition rate of 45 minutes.

The LaPD sets the ambient-plasma environment and serves as a sophisticated target vessel for the Phoenix laser system. The LaPD is a 1 m diameter by 18 m long, high vacuum ($\sim 10^{-7}$ Torr) chamber with an axial DC magnetic field, see figure 2.1. The DC magnetic field is generated by a series of independently controlled magnetic coils spaced at 32 cm intervals along the length of the machine. Utilizing this independent control, the magnetic field profile along the machine is not restricted to being continuous but can be setup to provide a variable magnetic profile (200 G to 2500 G) along the axis of the machine. This extra variability becomes a useful tool in controlling the efficiency of the plasma production and defining the ambient-plasma density.

Like the Phoenix laser system, the LaPD also went through a series of upgrades in how it produced the ambient-plasma, see table 2.1. Initially the H^+ or He^+ ambient-plasma was generated from a single cathode, the main cathode, and later was produced with a dual cathode configuration with the introduction of a secondary Lanthanum-Hexaboride[19] (LaB_6) cathode. Figure 2.1a illustrates the dual cathode setup. The two cathodes are placed facing each other at opposing ends of the machine. The main cathode is a 60 cm diameter Barium-oxide coated nickel (BaO-Ni) cathode capable of generating a steady-state, quiescent, current-free, uniformly low-density ($\sim 2 \times 10^{12}$ cm^{-3}), 60 cm diameter plasma column for a duration of 10 ms. The opposing LaB_6 cathode is capable of producing a smaller ($\lesssim 30$ cm diameter), steady-state plasma column of high-density ($\lesssim 3 \times 10^{13}$ cm^{-3}) plasma for a shorter duration of 5-7 ms. The initial incarnation of the LaB_6 cathode was an 8 cm square cathode placed about 15 m from the main cathode and was used from 2010 to the end of

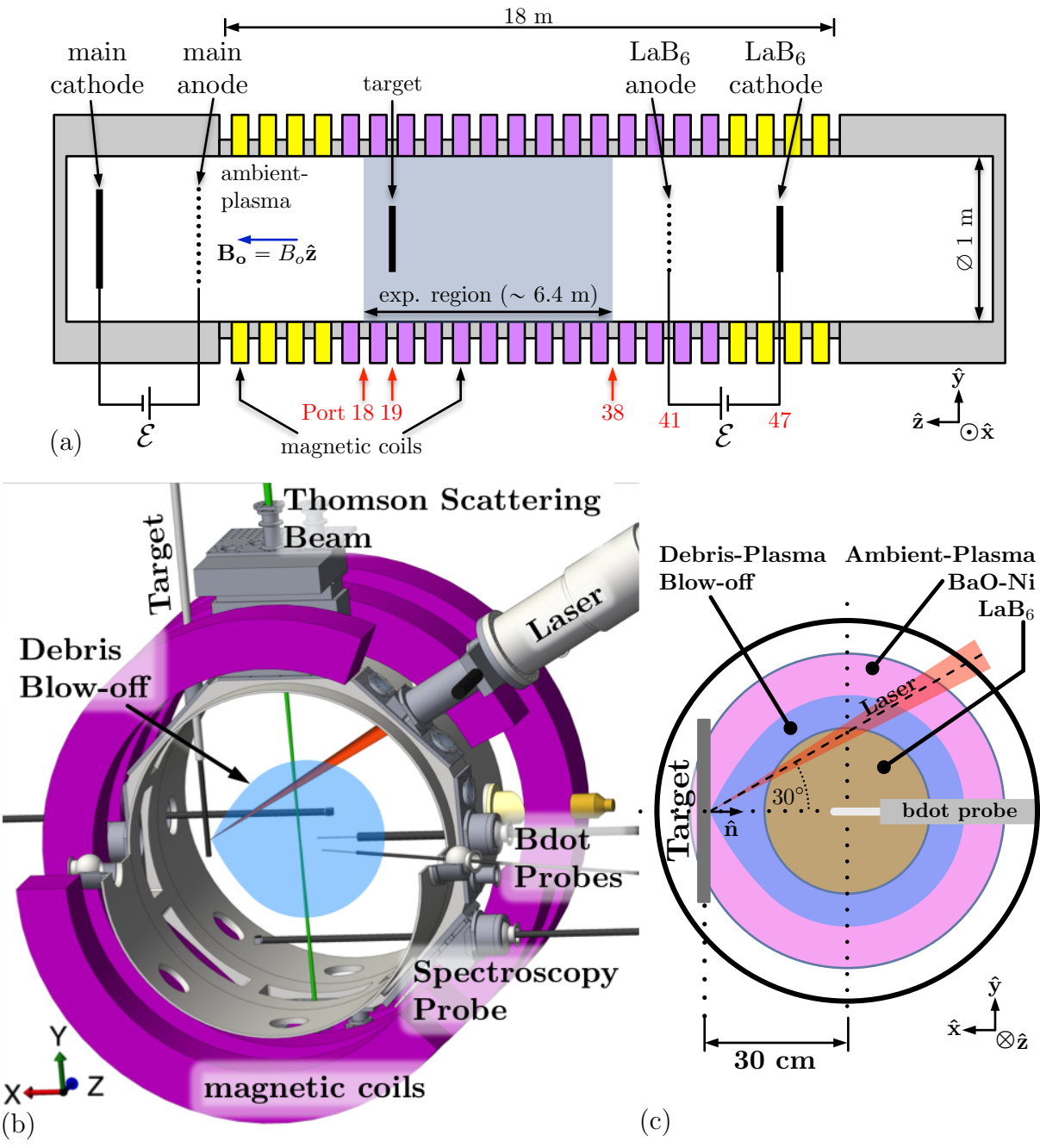


Figure 2.1: Setup of the LaPD-Phoenix experiment. Figure (a) shows a side-view of the the experiment showing the port layout for the cathodes, target (port 19), and experimental region (port 18 to 38). Figure (b) shows a 3D rendering of the target, laser, and diagnostic arrangement at port 19. Figure (c) is a simplified view of the cross-section of port 19.

2012. In 2013, the January and June experiments utilized an updated 10 cm square LaB₆ cathode and in October a larger 20 cm square LaB₆ cathode was added to the north end (opposite the main cathode) of the LaPD.

As the ambient-plasma density increases many of the variables in the parameter space become more favorable for collisionless shock formation, that is, the Alfvén speed and ion-inertial length decrease. The LaB₆ cathode was introduced to provide the density increase, but it came with a drawback of reducing the ‘favorable’ experimental volume. Since the LaB₆ cathode is smaller, it can not produce as wide of a plasma column as the main cathode can. Without an adequate system size, the expanding debris-plasma does not have sufficient time to interact and couple energy into the ambient-plasma. To mitigate this problem the axial magnetic field is increased at the cathodes, while being held low in the experiment region. This magnetic configuration has several benefits to the experiment: (1) The higher field at the cathodes helps with emission of electrons off the cathode (primary electrons) that go into ionizing the ambient-gas fill. (2) To conserve electron-flux $\Gamma = \mathbf{B} \cdot \mathbf{A}$, where \mathbf{B} is the magnetic field and \mathbf{A} is the cross-sectional area the electrons are crossing, the primary electrons must spread out as the magnetic field drops. The electrons spread out roughly like $A_{exp} = B_{cath}A_{cath}/B_o$, where A_{exp} is the cross-sectional area at the experiment region, B_o is the magnetic field at the experiment region, A_{cath} is the area of the cathode, and B_{cath} is the magnetic field at the cathode. (3) In the dual cathode configuration, the larger field at the cathodes than the experiment region creates a magnetic mirror that reflects a fraction of the primary electrons that do not ionize the gas fill on their first pass through. Thus, the primary electrons can boost the density by a small fraction from their second pass through.

The debris-plasma is generated from ablating a graphite or high-density polyethylene (HDPE) target with either the Phoenix laser or Raptor laser. In either case (carbon or HDPE target) the most energetic debris-ion species is C^{+3} or C^{+4} . The use of the two target types was an effort to find a target material that yielded a higher efficiency of laser energy to debris-ion energy. The target is located between the two LaPD cathodes at port 19 (~ 6 m from the main cathode and ~ 9 m from the LaB₆ cathode), see figure 2.1a. As seen in

figure 2.1b and 2.1c, the graphite target is offset approximately 30 cm from the LaPD axis, creating an effective experimental size of 60 cm for the expanding debris-plasma to interact with the ambient-plasma. The laser is focused through a f/10 doublet-lens and is incident at an angle of 30 degrees to the target normal. The target normal can be oriented to a specified θ_{B_n} to study quasi-perpendicular or quasi-parallel shock formation. For this series of experiments θ_{B_n} is set to 90° , allowing the blowoff to expand along the negative LaPD X-axis. The background magnetic field B_o defines the positive LaPD Z-axis, which points towards the main cathode, and the LaPD Y-axis is vertically upwards.

The LaPD-Phoenix platform uses an array of diagnostics, both optical and physical, to measure the effects of the expanding cavity on the ambient-plasma. The primary diagnostic for the experiment is a series of magnetic flux probes (a.k.a. \dot{B} or flux probes) to measure the changing magnetic field. There are several versions of flux probes used for the experiment, which depend on the application they are intended for. The design and construction of these flux probes is discussed in detail in §2.3.1. To measure the expanding cavity, a flux probe is placed opposite of the target (West side of Port 19, negative LaPD x-axis) to obtain the magnetic field profile along the the LaPD x-axis (synonymous with the axis defined by the target normal). A probe positioned here is referred to as a ‘perpendicular’ probe, since it is measuring the event directly across \mathbf{B}_o . Flux probes are also placed at various port locations along the LaPD to measure the magnetic field of any wave structures launched by the expanding cavity along the background magnetic field lines. These probes are referred to as ‘parallel’ probes.

In addition to the flux probes, Thomson scattering is utilized to measure densities and velocities of the expanding debris-plasma[75] and spectroscopy measurements are used to estimate electric fields, as well as, debris- and ambient-ion motion[5, 7], see figure 2.1b. These diagnostics and their measurements will not be discussed in detail here, but can be review in their respective sources. The results will be cited accordingly. Other non-optical based diagnostics include Langmuir probes (floating-potential and biased) and velocity analyzers were fielded but achieved little success. The strong electric currents of the system resulted in

Trident Laser Configuration

Beam	Function	λ (nm)	Pulse Width	Energy (J)	Power (GW)	Intensity 10^{11} W/cm ²
(1) Heater	creates ambient-plasma	1053	50 ns	$\lesssim 50$	1	~ 1.3
(2) Driver	creates debris-plasma	1053	5 ns	$\lesssim 250$	50	$\lesssim 64$
(3) Diagnostic	Thomson Scattering	527	0.5 ns	50	10^2	n/a
	Proton Radiography	n/a	600 fs	50	2×10^5	$10^8 - 10^9$

Table 2.2: Experimental laser configuration for each beam line in the Trident platform. There are three beam lines, of which, two are used to generating the ambient- and debris-plasma and the third is used an optical diagnostic. The diagnostic beam is configured for either Thomson scattering or proton radiography.

signals with large potentials and slew-rates that were too strong for the biasing and isolating electronics. With significant improvements to the electronics, these measurements may be possible in the future.

2.2 Trident Platform

The Trident platform differs from the LaPD-Phoenix platform in that the Trident platform uses two sequential laser pulses to create the ambient- and debris-plasma. The first LPP constitutes the ambient-plasma and the second is the debris-plasma. The background magnetic field is provided by a large ($\varnothing 56$ cm), custom built Helmholtz coil, see table 2.3 and figure 2.2. The Trident experiments were performed in July 2010 at the Trident laser facility[57] located at the Los Alamos National Laboratory (LANL). The Trident platform was conceived to access a parameter space that early versions of the LaPD-Phoenix platform (pre-2013) could not achieve, see §2.2.1. Before discussing the benefits and short comings of this platform, the Trident laser system and experimental setup need to be discussed.

The Trident laser facility offers three beam lines for experimental use, see table 2.2. The first two beams are used for generating the ambient- and debris-plasma. Beam 1, the ‘heater,’ is used to ablate a graphite or HDPE target to generate the ambient-plasma; whereas, beam 2, the ‘driver,’ is used to ablate the target, at the same spot as the ‘heater’ beam, to generate a second LPP that makes up the debris-plasma. The third beam line is used as an optical diagnostic and is configured for either Thomson scattering[74] or proton radiography measurements[73].

The ‘heater’ and ‘driver’ beams share the same wavelength, 1053 nm. The ‘heater’ is set to an energy of 50 J in a 50 ns pulse width (FWHM) and focused onto the target at an intensity of 1.3×10^{11} W/cm². The ‘driver’ can reach energies up to 250 J, but is typically configured to an energy of 200 J in a 5 ns pulse width (FWHM) and focused to an intensity of 5×10^{12} W/cm². Both beams are focused to the same spot on the target but there is a time-delay between the beams that can be varied up to 10 μ s. Typically, the time-delay is set between 7 μ s and 10 μ s to give the initial LPP enough time to expand, form a diamagnetic cavity, and allow the magnetic field to relax back to its initial state. After the magnetic field returns to its initial state, the LPP that formed the cavity becomes the ambient-plasma and fills the volume defined by the expanded diamagnetic cavity.

The magnetic field for the experiment is provided by a large, pulsed Helmholtz Coil (HC) constructed within one of the Trident high vacuum ($< 10^{-5}$ Torr) target chambers, see figure 2.2a. A summary of the HC dimensions and pulse characteristics is provided in table 2.3. At the time of the Trident experiment the LaPD-Phoenix experiments (January 2010) were achieving diamagnetic cavity sizes on the order 15 cm with 35 J of laser energy and a 600 G magnetic field. The design specs for the HC were set to achieve similar cavities sizes with the 250 J of laser energy provided by the Trident system. This institutes a HC design target for the experimental volume (HC size) and magnetic field (see equation 2.1). Firstly, the experimental volume is achieved by designing the HC with an inner radius R_{HC} of 27.9 ± 0.3 cm and a center-to-center coil spacing h_{HC} of 28.6 ± 0.3 cm ($h_{HC}/R_{HC} = 1.025 \pm 0.015$). Each coil is wound with 100 turns (5 radial by 20 axial) of AWG 10 round magnetic wire

Helmholtz Coil Dimensions & Characteristics

HC Specs		
	Value	Normalized
Inner HC Radius R_{HC}	27.9 ± 0.3 cm	
Center-to-Center Coil Spacing h_{HC}	28.6 ± 0.3 cm	$1.025 (\pm 0.015) R_{HC}$
Total Num. of Turns per Coil	100 (5 radial by 20 axial)	
Magnetic Wire	$\varnothing 0.264 (\pm 0.005)$ cm (AWG 10) Polyester A/I Topcoat Insulator (NEMA MW35C)	
Pulsed B-Field Characteristics		
Peak Magnetic Field at Center B_o	$\lesssim 1250$ G	
Rise Time t_{HCr}	22.3 ± 0.2 ms	
Duration Above $0.99B_o$ Δt_{99}	5.28 ± 0.05 ms	
Spatial Variation About HC Center $ \Delta B_z/B_o \leq 1\%$	Axial Range: ~ 16.7 cm	$\sim 0.6 R_{HC}$
	Radial Range: ~ 22.3 cm	$\sim 0.8 R_{HC}$

Table 2.3: This table contains a summary of the dimensions and magnetic field characteristics for the pulsed Helmholtz Coil (HC) used during the 2010 Trident campaign.

with a Polyester A/I Topcoat insulator. Using these HC specs, the magnetic field inside the HC can be computationally solved using the Biot-Savart Law, see in figure 2.2b. This results in a 1% magnetic field variation ($|\Delta B_z/B_o| \leq 1\%$) about the center of the HC in an axial range of $\sim 0.6R_{HC}$ (~ 16.7 cm) and a radial range of $\sim 0.8R_{HC}$ (~ 22.3 cm). For a 5% variation the range is roughly 30 cm, axially and radially.

A HC of this size presents a design challenge since the largest opening on the target chamber is $\varnothing 35.56$ cm ($\varnothing 14$ inches), nearly half the size of the HC. To accomindate this, the HC is designed to be disassembled and re-assembled inside the target chamber. Figure 2.2a shows the HC assembled inside the chamber and in the process of being wound. Each coil frame (top and bottom) that supports the windings is designed as two semi-circular

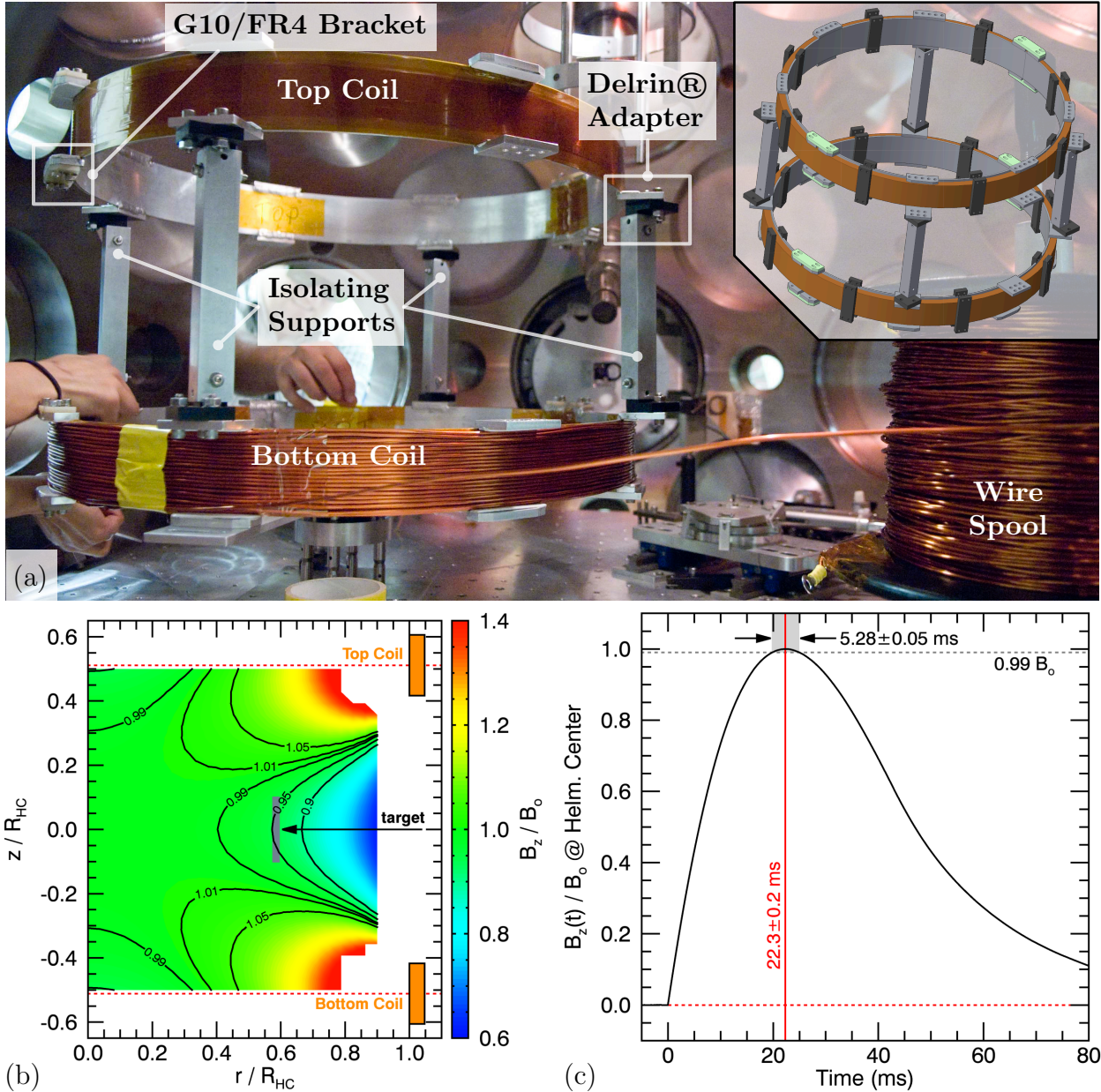


Figure 2.2: Figure (a) shows the Helmholtz Coil (HC) frame assembled in the Trident target chamber with the bottom coil being wound. The top right insert shows a 3D CAD rendering of the completely assembled HC. Figure (b) is an analytical solution of B_z (using the Biot-Savart Law) for a HC with the Trident experiment specifications. Figure (c) shows the measured time-dependent axial magnetic field $B_z(t)$ at the center of the HC for a typical discharge of the capacitor bank through the coil. The peak magnetic field occurs 22.3 ± 0.2 ms into the pulse.

halves and joined with garolite G10/FR4 brackets to keep the halves isolated and prevent any closed electrical loops. The supports between the two coil frames are also isolated using Delrin® adapters (also to prevent closed electrical loops).

The HC is pulsed by discharging a 10.5 mF capacitor bank through the HC using an insulated-gate bipolar transistor (IGBT) as a switch. The capacitor bank is rated to 900 V with a total energy storage capacity of 4.3 kJ. Once the HC is assembled inside the target chamber it is calibrated in place using a \varnothing 1 inch magnetic flux probe to determine discharge behavior and operational peak magnetic field range. It is important to do this calibration in place since the permeability of the surrounding metallic target chamber, optical bread board, and other fixtures can affect the discharge characteristics of the HC. Figure 2.2c shows the typical magnetic field pulse $B_z(t)$, normalized to the peak value B_o , as the capacitor bank is discharged through the HC. This measurement is repeated for 6 different capacitor bank voltages V_{cap} resulting in an average rise time t_{HCr} of 22.3 ± 0.2 ms. The magnetic field stays above a 99% limit ($B_z(t) \gtrsim 0.99B_o$) for a duration of $\Delta t_{99} = 5.28 \pm 0.05$ ms, which is quasi-static for the time scales of the experiment ($\Delta t_{exp} \sim 20 \mu s$).

As stated before, the target design specs for the HC have two components to it: (1) provide an experimental volume similar to the cavity sizes obtain in the January 2010 LaPD-Phoenix experiments (~ 15 cm) and (2) provide a peak magnetic field value such that the 250 J Trident laser can generated similar diamagnetic cavities sizes to the LaPD-Trident experiments. As discussed above, the HC meets the first condition. Using the scaling provided by the magnetic-stopping radius R_B (equation 3.6, discussed in §3.2) the target

magnetic field is given by

$$\begin{aligned}
\frac{[R_B^3]_{Trident}}{[R_B^3]_{LaPD}} &= 1 \\
&= \left[\frac{E_{Laser}}{B_o^2} \right]_{Trident} \left[\frac{E_{Laser}}{B_o^2} \right]_{LaPD}^{-1} \\
\Rightarrow [B_o]_{Trident} &= \left\{ \sqrt{\frac{[E_{Laser}]_{Trident}}{[E_{Laser}]_{LaPD}}} \right\} [B_o]_{LaPD} \\
&= \sqrt{\frac{250 \text{ J}}{35 \text{ J}}} (600 \text{ G}) \\
&\sim 1.6 \text{ kG}
\end{aligned} \tag{2.1}$$

where E_{Laser} is the laser energy, B_o is the background magnetic field, and brackets $[]_{Trident}$ and $[]_{LaPD}$ indicate that the enclosed quantity is in reference to the Trident values or LaPD-Phoenix values, respectively. The HC calibration yielded the following fit

$$\frac{B_o}{V_{cap}} \simeq 1.39 \pm 0.01 \text{ G/V} \tag{2.2}$$

where B_o is the peak magnetic field in Gauss and V_{cap} is the capacitor bank voltage in volts. A maximum V_{cap} of 900 V yields a maximum magnetic field of $1.25(\pm 0.01)$ kG, which is smaller than the 1.6 kG target given by equation 2.1. Using the scaling of the magnetic-stopping radius, the cavity size at 1.25 kG would be roughly 20% larger than the LaPD-Phoenix cavity sizes, resulting in a Trident cavity size of ~ 18 cm. This cavity size is still achievable within the experimental volume provided by the HC.

Figure 2.3 shows the full Trident setup with the HC positioned in the target chamber, the target in place, the ‘driver’ and ‘heater’ beam lines aligned to the target, the ‘diagnostic’ beam configured for Thomson scattering, and the array of magnetic flux probes installed. The target (either graphite or HDPE) is positioned inside the HC, on the center planed between the top and bottom coils, and offset from the HC center at a distance of $X_{tar} = 16.1 \pm 0.3$ cm ($X_{tar}/R_{HC} = 0.58 \pm 0.01$). At this position the HC magnetic field is $0.95B_o$, see figure 2.2b. The target is oriented such that its surface normal $\hat{\mathbf{n}}$ points towards the HC center, which defines the system’s $\hat{\mathbf{x}}$ -axis. The system’s $\hat{\mathbf{z}}$ -axis is defined by the HC magnetic field, which points vertically upwards (see figure 2.3c).

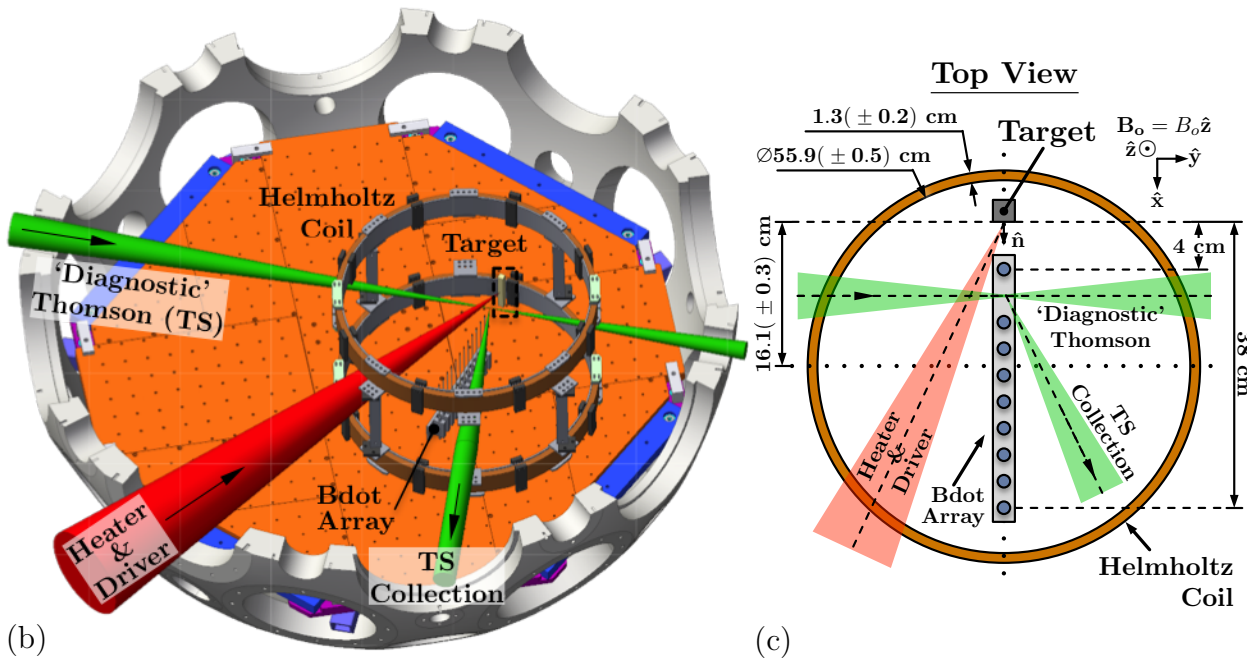
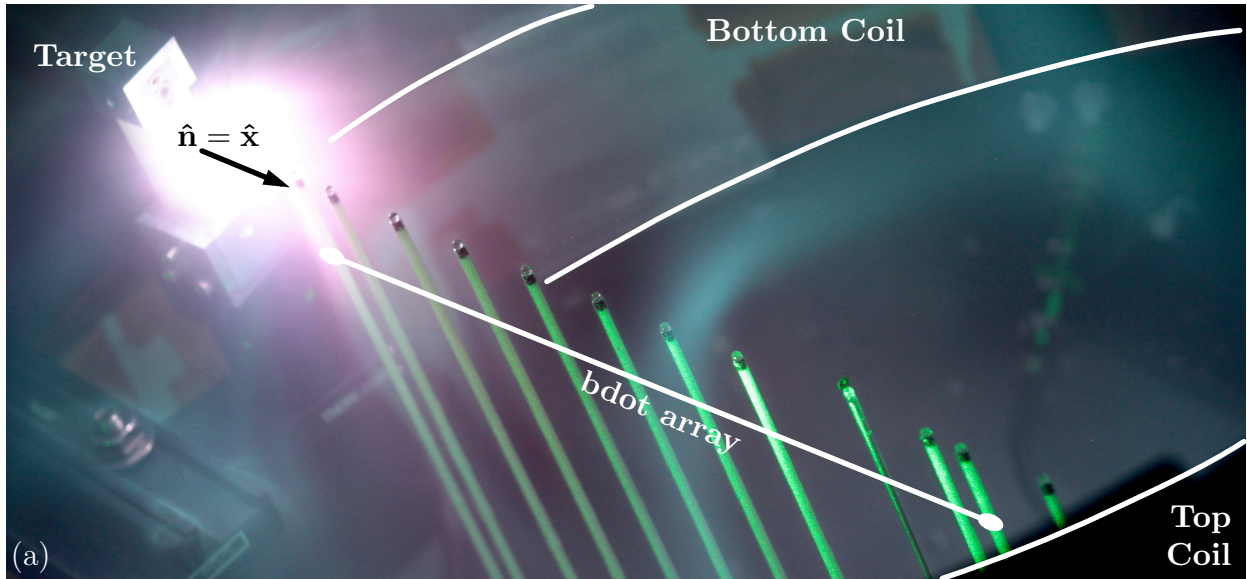


Figure 2.3: Figure (a) is a SLR photo during Trident shot 21935 of the experimental setup. The photo is taken looking down through the top coil of the HC. The green hue is due to the light scattering of the green ‘diagnostic’ beam. Figure (b) is a 3D CAD render of the experimental setup with the ‘diagnostic’ beam in green and the ‘heater’/‘driver’ beam in red. Figure (c) is a 2D schematic of the experimental setup looking from atop.

The ‘heater’ and ‘driver’ pulses share the same beam line, which comes in on the experimental xy -plane and is incident onto the target at an acute angle from $\hat{\mathbf{x}}$. Both pulses are focused to the same spot on the target, which is not optimal but is an unavoidable restriction presented by the Trident facility. Since the ‘driver’ pulse ablates the crater created by the ‘heater’ pulse, the ‘driver’ LPP has more of an angular spread in its blow-off direction. Between Trident facility shots, the target is translated or rotated to provide a fresh surface for the following facility shot.

The magnet flux probes are placed along the x-axis to measure the cavity formation and magnetic field compression of both the ‘heater’ and ‘driver’ expansions. The flux probes are wound non-differentially with a single-axis to measure $B_z(t)$ (details in §2.3.1). The probes are positioned as an array ranging from 4 cm to 38 cm from the target, see figure 2.3c. The probe position/spacing is varied depending on the distance from the target and the configuration of the ‘diagnostic’ beam. The spacing can be as small as 1 cm, but, when the ‘diagnostic’ beam is setup for Thomson scattering, a larger gap is left between the probes to keep the beam line clear. The bdot array is removed completely when the ‘diagnostic’ beam is configured for proton radiography due to the potential damage from the high proton flux and electrical noise from the short-pulse.

The ‘diagnostic’ beam enters the HC on the center plane (xy -plane) between the top and bottom coils from the left side (negative $\hat{\mathbf{y}}$ -axis). Figures 2.3b and 2.3c show the ‘diagnostic’ beam setup for Thomson scattering. Thomson scattering is configured to sample a volume of 0.04 mm^3 at a distance of 3-18 cm in front of the target (along $\hat{\mathbf{x}}$) to measure electron temperatures and densities. These measurements are used to characterize the ambient-plasma as well as the density compression generated from the expanding debris plasma. A detailed discussion of this diagnostic and its results is beyond the scope of this dissertation, so the discussion is left to [73] and [74], and will be cited when necessary. Alternatively, the ‘diagnostic’ beam is setup for proton radiography to complement the magnetic flux probes. Proton radiography measures a 2D (xz -plane) spatially-averaged cross-section of the magnetic field. Setup and operation of the proton radiography diagnostic is left for §2.3.2.

2.2.1 As Compared to pre-2013 LaPD-Phoenix Experiments

The Trident platform was conceived to overcome the disadvantages of the pre-2013 LaPD-Phoenix experiments and move into a parameter space that is more conducive to shock generation. Early LaPD-Phoenix experiments were significantly hindered by the low ambient-density and low laser energies. For example, the January 2010 LaPD-Phoenix experiments produced cavities sizes on the order of $2R_c \sim 0.7 c/\omega_{pi}$, slow expansion speeds on the order of $M_A \sim 1.4$, short expansion/interaction times on the order $\Delta t \sim 0.8\Omega_{ci}^{-1}$, and weak magnetization with respect to the cavity size $2R_c/\rho'_a \sim 0.5$.¹ As discussed in §1.1.1 and §1.2, the expansion needs to last several gyro-periods so dissipation can grow and the shock transition is on the order of an ion-inertial length.

The Trident platform looked to improve on the LaPD-Phoenix platform by increasing the achievable M_A , increasing the interaction time to several gyro-periods, and decreasing the ion-inertial length while keeping the cavity sizes the same. Table 2.4 outlines how the Trident experiment accomplishes this over the January 2010 LaPD-Phoenix experiment. Increasing the laser energy means similar cavity sizes can be produced up to 1.6 kG (equation 2.1) and the 10x increase of intensity means faster blow-off speeds can be achieved. Key improvements come from the 10x increase in ambient-density, increasing the ambient-ion mass to $m_i/m_p = 12$ over 4 for He and 1 for H, and increasing the charge state to $Z = 4$ over 1. These changes dramatically decrease the Alfvén speed which opens up the accessible Alfvénic Mach numbers. The ion-inertial length also drops by $\sim 85\%$, so, with the cavity sizes remaining the same, $2R_c/(c/\omega_{pi})$ increases by 6.7x. The ion gyro-period also decreases when compared to the He⁺ ambient-plasma. For equivalent magnetic fields between the two experiments the gyro-period decrease is by 0.75x and drops by 0.36x when the HC is operated at its max ($B_{LaPD}/B_T = 600 \text{ G}/1250 \text{ G}$). This gyro-period decrease effectively increases the normalized interaction time ($\Omega_{ci} t$) between the expanding cavity and ambient-plasma.

¹2010 January LaPD-Phoenix run parameters: ambient-ions He⁺, $E_{laser} \simeq 35 \text{ J}$, $B_o = 600 \text{ G}$, $[n_e]_{ave} \sim 4.0 \times 10^{12} \text{ cm}^{-3}$, $V_A \simeq 328 \text{ km/s}$, $f_{ci}^{-1} \simeq 4.3 \text{ } \mu\text{s}$, $c/\omega_{pi} \sim 22.7 \text{ cm}$, $V_o \simeq 450 \text{ km/s}$ ($M_A \sim 1.4$), $\rho'_a = V_o/\Omega_{ci} \simeq 31.3 \text{ cm}$, $2R_c \simeq 15 \text{ cm}$ ($\sim 0.66 c/\omega_{pi}$ or $\sim 0.48 \rho'_a$), expansion time $\Omega_{ci} t \simeq 0.8$ ($0.55 \text{ } \mu\text{s}$)

LaPD-Phoenix (Jan. 2010) versus Trident (Jul. 2010)

	LaPD-Phoenix	Trident	Change	
ambient-ion charge state Z	H +1	C +4 [†]	Z_T/Z_{LaPD}	4
	He +1			
ambient-ion mass m_i/m_p	H 1	C 12	m_T/m_{LaPD}	12
	He 4			3
ambient-ion density n_a (10^{12} cm^{-3})	H 2.0	C 50 [†]	n_T/n_{LaPD}	25
	He 6.0			8.3
laser energy E_{Laser} (J)	35	250	E_T/E_{LaPD}	7.1
laser intensity I_{Laser} (10^{11} W/cm^2)	5 – 9	62	I_T/I_{LaPD}	$\lesssim 12$
System Size D_o (cm)	60	25	D_T/D_{LaPD}	0.4

Change In Key Parameters

Alfvén Speed V_A	H $V_{A,T} / V_{A,LaPD} = 0.06 (B_T / B_{LaPD})$	
	He $V_{A,T} / V_{A,LaPD} = 0.20 (B_T / B_{LaPD})$	
ion-inertial length c/ω_{pi}	H 16 cm	$(c/\omega_{pi})_T / (c/\omega_{pi})_{LaPD} = 0.17$
	He 18 cm	$(c/\omega_{pi})_T / (c/\omega_{pi})_{LaPD} = 0.15$
ambient-ion gyro-period Ω_{ci}^{-1}	H $[\Omega_{ci}^{-1}]_T / [\Omega_{ci}^{-1}]_{LaPD} = 3.00 (B_{LaPD} / B_T)$	
	He $[\Omega_{ci}^{-1}]_T / [\Omega_{ci}^{-1}]_{LaPD} = 0.75 (B_{LaPD} / B_T)$	
ambient-ion directed Larmor radius $\rho_i = v_{sh}/\Omega_{ci} = M_A(c/\omega_{pi})$	H $[\rho_i]_T / [\rho_i]_{LaPD} = 0.17 (M_{A,T} / M_{A,LaPD})$	
	He $[\rho_i]_T / [\rho_i]_{LaPD} = 0.15 (M_{A,T} / M_{A,LaPD})$	
Relative Magnetization D_o/ρ_i	H $[D_o/\rho_i]_T / [D_o/\rho_i]_{LaPD} = 2.4 (M_{A,LaPD} / M_{A,T})$	
	He $[D_o/\rho_i]_T / [D_o/\rho_i]_{LaPD} = 2.8 (M_{A,LaPD} / M_{A,T})$	

[†] see [74] for measurement and calculation from Thomson scattering

Table 2.4: A chart indicating the difference in key parameters between the Trident experiment and the January 2010 LaPD-Phoenix experiment. This difference leads to significant improvement in key normalized parameters and creating an environment that is more conducive for shock formation.

2.3 Diagnostics

The LaPD-Phoenix and Trident platforms use an array of diagnostics to measure the expansion event. The data discussed in this dissertation is collected from magnetic flux probes (discussed in §2.3.1) and proton radiography (discussed in 2.3.2). The magnetic flux probes are the primary diagnostic in both platforms and are used to obtain a time-dependent evolution of the magnetic field at separate spatial locations, whereas, the proton radiography is used to capture a temporal snapshot of a 2D spatial image of the magnetic structure.

2.3.1 Magnetic Flux Probes (a.k.a. bdot probes)

A magnetic flux probe (a.k.a. bdot probe) is functionally straight forward, but often difficult to design for and deploy in experimental conditions. The theory, design, construction, and calibration have been covered in numerous sources[27, 39, 54, 56, 64, 68, 78, 91] with E. T. Everson *et al.* (2009)[27] outlining the design for the LaPD-Phoenix experiments. Leaving the details to these sources, this section will give a brief review of the types of magnetic flux probes used for the two experimental platforms.

A magnetic flux probe utilizes Faraday’s Law to measure the electromotive force (EMF) produced by a time varying magnetic flux through a wire loop. The basic construction of a flux probe entails winding wire about a core, typically plastic or ceramic, to create a closed electrical loop in which a changing magnetic flux can induce an EMF. The capabilities of the probe depend on how these windings are constructed on the core. The sensitivity of the probe linearly increases with the number of windings (or turns) and area per turn (see equation 2.6). Up to three winding orientations (or axes) can be built onto a single core to give flux measurements in B_x , B_y , and B_z . Lastly, a single axis can be wound with two independent loops that are grounded on opposite leads, see figure 2.4a, to create a differential winding.

Differentially winding the axes is a preferred construction method because it mitigates any electrostatic pickup between the probe and plasma, as well as, enhances the magnetic

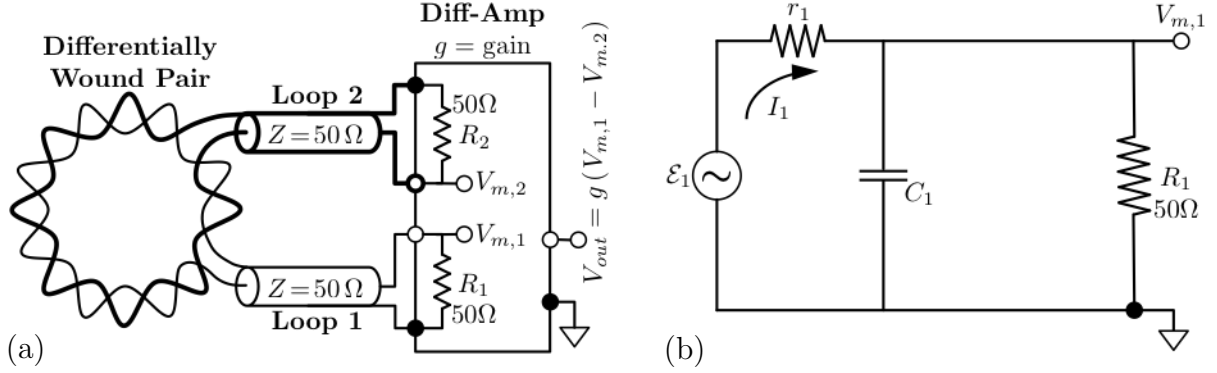


Figure 2.4: Figure (a) illustrates the the wiring of a differentially wound magnetic flux probe where the thick (normal) line represents loop 2 (loop 1) of the probe. Figure (b) shows the circuit schematic for loop 1 of the probe, where r_1 is the internal resistance of the loop, C_1 is the internal capacitance of the loop, R_1 is the load resistance attached to the loop, and I_1 is the current through the loop generated by the total EMF \mathcal{E}_1 (external magnetic flux, self-inductance L_1 , and mutual-inductance M between the two loops).

signal. When placing a flux probe in a plasma, there is a capacitive effect between the sensing element of the probe and the plasma that shows up as an identical electrostatic potential on both loops. By grounding the opposite leads of the two loops, the magnetic signal has equal magnitude on each loop, but opposite polarity. Thus, when subtracting the two signals the magnetic component is doubled and the electrostatic component is mitigated. This subtraction is performed using a differential amplifier (diff-amp) that simultaneously applies a specified gain g to the the subtracted signal.

The output signal of the diff-amp is then digitized at 100 MHz and 14-bits, 1.25 GHz and 10-bits, or 2.5 GHz and 10-bits, depending on the digital acquisition system (DAQ) available during the experiment. The 100 MHz DAQ has a ± 2.5 V range while the 1.25 GHz and 2.5 GHz have a ± 1.0 V range. The output signal of the diff-amp is kept within ± 0.8 V, since the diff-amps become non-linear near ± 1.0 V. When kept within ± 0.8 V, the linearity of the probe plus differential amplifier signal ($V_m(\omega) \propto \omega$ -- see equation 2.7) typically extends up to ~ 50 MHz.

Figure 2.4b shows the circuit schematic for the first loop of a differentially wound flux probe. The schematic for the second loop is identical. In the schematic, \mathcal{E}_1 is the EMF produced by the varying magnetic flux at the probe tip, r_1 is the the internal resistance of the loop, C_1 is the capacitance of the loop, and R_1 is the load resistance on the on the probe. The load R_1 is the 50Ω impedance of the diff-amp. The measured signal from the probe is $V_{m,1} = I_{1R}R_1$, where I_{1R} is the current through R_1 . Writing out the sum of voltages over a closed path in the circuit, the measure bdot signal and EMF can be related as

$$0 = \mathcal{E}_1 - I_1 r - I_{1R} R_1, \quad (2.3)$$

where \mathcal{E}_1 is the total EMF of the bdot loop. The total EMF is the sum of the EMF's generated by the time varying external magnetic field, the self-inductance L_1 of the loop, and the mutual-inductance M between the two loops. This total EMF is given by

$$\mathcal{E}_1 = an \frac{d}{dt} B - L_1 \frac{d}{dt} I_1 - M \frac{d}{dt} I_2, \quad (2.4)$$

where I_2 is the current through the second loop, n is the number of turns of the first loop, and a is the area per turn of the first loop. Given both loops are identical, then $I_1 = I_2$ and, after the signal is sent through the differential amplifier, $V_m = g(V_{m,1} - V_{m,2}) = 2gV_{m,1}$. Thus, the measured bdot signal V_m is relate to $\partial_t B$ by

$$aNg \frac{d}{dt} B(t) = \left\{ \left(1 + \frac{r_1}{R_1} \right) + \left(\frac{L_1 + M}{R_1} + r_1 C_1 \right) \frac{d}{dt} + (L_1 + M) C_1 \frac{d^2}{dt^2} \right\} V_m(t), \quad (2.5)$$

where N is the total number of turns between loops 1 and 2. Typically the internal resistance is negligible, $r_1/R_1 \lesssim 10^{-1} \ll 1$. In the high frequency limit $\omega R_1 C_1 \gg 1$ the capacitance acts like a short and puts a limit on the operational frequency range of the probe. In the moderate frequency range, $R_1/(L_1 + M) < \omega \ll 1/(R_1 C_1)$, the EMF from the self- and mutual-inductance of the bdot dominates the signal. As argued in E. T. Everson *et al.* (2009)[27], experiments typically operate in the low frequency range, $\omega < R_1/(L_1 + M) \ll 1/(R_1 C_1)$, which greatly simplifies equation 2.5 to

$$V_m(t) = aNg \frac{d}{dt} B(t), \quad (2.6)$$

and in frequency space

$$V_m(\omega) = i a N g \omega B(\omega). \quad (2.7)$$

Equation 2.6 can be numerically integrated to give $B(t)$ for the experiment.

Between the LaPD-Phoenix and Trident experiments, four flux probe designs were used to accommodate the various experimental restrictions, see table 2.5. The large (‘3 mm’) 3-axis, single tip probe is utilized for measuring large scale magnetic field structures along the axis of the LaPD. Its overall diameter is $\text{Ø}6.5$ mm which makes it large enough to obstruct the diamagnetic cavity features. This is why the smaller (‘1 mm’) probes were conceived. All ‘1 mm’ probes have an overall diameter of $\text{Ø}2.5$ mm. When the Raptor laser came online, the laser shot interval increase from 10 minutes to 45 minutes, so the 3-axis design was exchanged for a 5-tip, single axis design. This design mitigated the potential reduction in compressional magnetic field data from the lower laser shot rate.

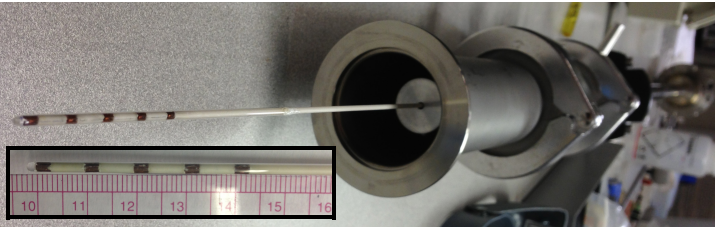
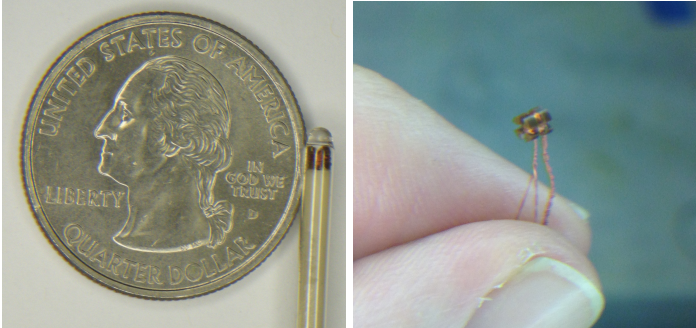
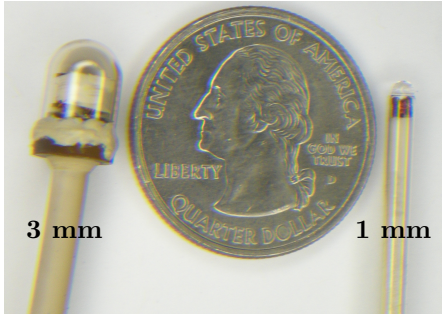

<p>5-Tip, Single Axis Probe</p> 	<p>FEATURES: 5 tips with 1 cm center-to-center spacing Single axis on each tip B_z 10 turns per axis Differentially wound area per turn $\sim 1.3 \text{ mm}^2$ Vespel[®] core ($T \lesssim 200^\circ\text{C}$)</p> <p>PLATFORM: LaPD-Phoenix</p> <p>WHY: multi-tip to compensate for low rep-rate of Raptor laser</p>
<p>3-Axis, 1 mm Probe</p> 	<p>FEATURES: Single tip 3-axis (B_x, B_y, B_z) 10 turns per axis Differentially wound area per turn $\sim 1.3 \text{ mm}^2$ Vespel[®] core ($T \lesssim 200^\circ\text{C}$)</p> <p>PLATFORM: LaPD-Phoenix</p> <p>WHY: (1) smaller than the 3 mm probe to reduce obstruction of experimental features, (2) lower self-inductance</p>
<p>3-Axis, 3 mm Probe</p> 	<p>FEATURES: Single tip 3-axis (B_x, B_y, B_z) 10-50 turns per axis Differentially wound area per turn $10\text{-}15 \text{ mm}^2$ Vespel[®] core ($T \lesssim 200^\circ\text{C}$)</p> <p>PLATFORM: LaPD-Phoenix</p> <p>WHY: (1) good for large scale, low freq. magnetic structures, (2) easier to build than 1 mm probe</p>
<p>1-Axis, 1 mm Probe</p> 	<p>FEATURES: Single tip Single axis B_z 5 turns per axis non-differential area per turn $1.5 - 1.7 \text{ mm}^2$ Delrin[®] core ($T \lesssim 80^\circ\text{C}$)</p> <p>PLATFORM: Trident</p> <p>WHY: easy to build in large numbers</p>

Table 2.5: The various magnetic flux probes deployed in the LaPD-Phoenix and Trident experiments.

2.3.2 Proton Radiography

The proton radiography diagnostic was setup as a sister diagnostic to the magnetic flux probes to provide structural measurements of the magnetic field in the Trident experiments that the magnetic flux probes can not make. Due to the experimental configuration for the proton diagnostic (figure 2.5), the addition of a short pulse laser, the two diagnostics are never fielded at the same time. Proton radiography measures the magnetic field by measuring the deflection of a proton beam as it passes through the experimental volume, which has a few advantages and disadvantages over the magnetic flux probes. Proton radiography provides a 2D temporal snapshot of the line-average magnetic field that the protons pass through. Consequently, the measurement, even though directly proportional to B and not $\partial_t B$, will be dominated by the large scale length magnetic field contributions. The proton beam is less perturbative to the the experiment than a physical probe. Since there are no electrical connections, the measurement is not susceptible to electrical noise (EMPs, ground bouncing, etc.) that the magnetic flux probes have to actively mitigate. Besides the measurement being a line-average of the magnetic field, the biggest disadvantage of this diagnostic is the lack of temporal data. In order to get a temporal evolution of the experiment, several laser shots have to be accumulated and stacked together. Still, acquiring a spatially resolved, high resolution snapshot of the magnetic field is highly advantageous for understanding the shape of the diamagnetic cavity.

The proton radiography reconfigures the Trident diagnostic beam line (see table 2.2) to create a 50 J, 600 fs short pulse beam by means of chirp pulsed amplification (CPA)[57]. As seen in figure 2.5, the CPA beam is focused onto a thick (125 μm) Cu target that is placed 3 cm from the outside of the HC frame. The CPA beam is focused to a spot size of about 10 μm on the Cu target, resulting in an intensity of $\sim 10^{19}$ W/cm² and the generation of an energetic proton beam off the backside of the Cu target. The proton beam is created by the normal sheath acceleration (TNSA) mechanism[28, 87]. The proton beam then passes through a Cu mesh with an approximate 2 mm center-to-center grid spacing, between the upper and lower HC rings, the experimental volume, and, finally, absorbed by a stack of

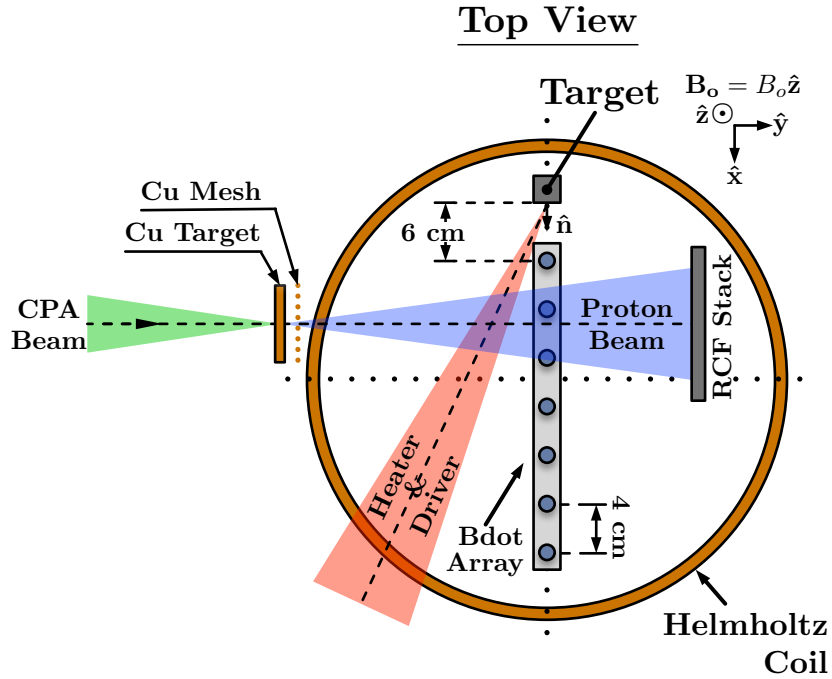


Figure 2.5: Depicted is an over top, 2D schematic of the Trident experiment when the proton radiography diagnostic is configured. The bdot array is kept in place to provide reference positions for the proton radiography, but the bdot probes do not collect data. The chirp pulse amplified (CPA) beam comes in from the left to irradiate a Cu target and produce a proton beam off the target backside (right). The proton beam then passes through a Cu mesh, then the experimental volume, and finally deposits itself on the radiochromic film (RCF) stack.

self developing radiochromic film (RCF) placed 49 cm from the Cu target. The Cu mesh is placed about 3 mm from the Cu target to create a gridded shadow/image on the RCF stack, see figure 2.6. This gridded image will serve as the means to measure the deflection of the proton beam after the beam passes through the experiment. In addition to the mesh, several bdot probes are left in the experimental volume. The bdot probes are placed along the blow-off axis \hat{n} at positions of 6, 10, 14, and 18 cm from the target so that the image captured by the RCF stack has a reference to the target.

The RCF stack is built by layering together sheets of GafchromicTM EBT2, MD-V2-55,

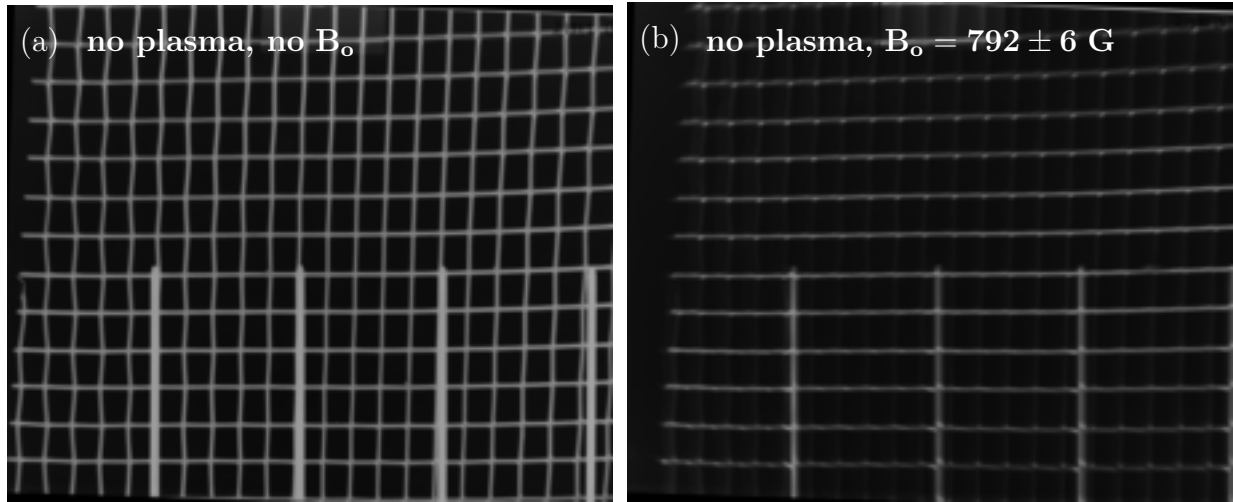


Figure 2.6: Figure (a) is an example of a proton radiograph image captured on an EBT2 RCF (Trident shot number 21971, CPA energy 45 J) with no plasma and no background magnetic field. The film darkens upon absorption of protons so the white mesh is the shadow from the Cu mesh and the bdot shadows are seen as the thicker poles emerging from the bottom of the image. The graphite target is off to the left side of the image and the left most bdot probe is 6 cm from the target. Figure (b) is the same as (a) except with a vertical background magnetic field of 792 ± 6 G (Trident 21970, CPA 51 J). The magnetic field causes the proton beam and image to be shifted to the right by 1.43 ± 0.06 cm.

and HD-810 films. To protect the film from the graphite target blow-off plasma, a thin aluminum foil of $25 \mu\text{m}$ or less is placed on the front side of the RCF stack. These dosimetry films were originally designed for detection of high energy photons, but, due to the films stopping power, they have also been calibrated for detecting high energy protons[37, 58]. Upon absorption of radiation the films darken to show an image and are then scanned at a resolution of 600 pixels-per-inch. Figure 2.6a shows an example of an image captured on EBT2 film while there is no plasma or background magnetic field (Trident facility shot number 21971) and figure 2.6b is the same but with a background field of 792 ± 6 G (Trident 21970). Comparing the two images, the vertical \mathbf{B}_0 curls the proton beam and shifts the image, as expected, by 1.43 ± 0.06 cm to the right.

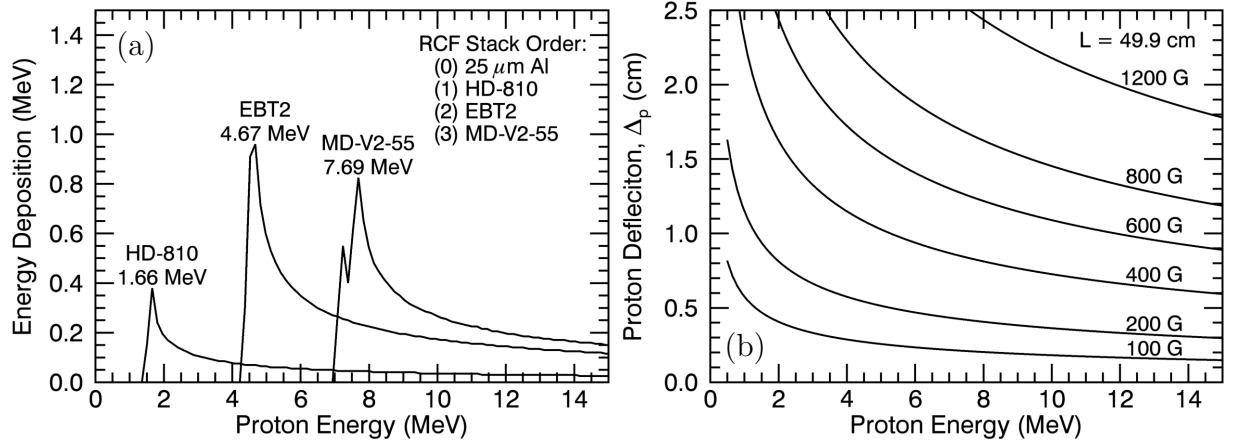


Figure 2.7: Figure (a) plots the tabulated energy deposition for a given proton energy into a layered RCF stack of 25 μm Al, 104 μm HD-810, 285 μm EBT2, and 283 μm MD-V2-55. The calculation is done using the SRIM software (www.SRIM.org)[94, 95]. Figure (b) shows the expected proton deflection Δ_p of a proton with energy E_p for various average magnetic field values over the distance $L = 49$ cm (see equation 2.11).

The generated proton beam is not monoenergetic and, thus, making it difficult to relate the proton deflection to a magnetic field value. However, the energy distribution can be approximated by the Bragg energy deposition into the RCF stack. Figure 2.7a shows an example of the calculated deposition for a RCF stack layered with a 25 μm thick Al foil, 104 μm thick HD-810 film, 285 μm thick EBT2 film, and 283 μm thick MD-V2-55 film. The proton deposition calculations are tabulated using the Stopping and Range of Ions in Matter (SRIM) software (www.SRIM.org)[94, 95]. The energy deposition for each layer initially has a sharp Bragg peak of 1.75 MeV for HD-810, 4.6 MeV for EBT2, and 7.8 MeV for MD-V2-55. Each peak has a width of ± 1 MeV which is then followed by a long tail as the proton energy increases. Consequently, the long tail will blur the captured image, but since the Bragg peak deposition is at least 2x stronger than the background, the image will still be predominantly produced by the Bragg peak protons.

Numerous approaches have been developed to analyze and interpret proton radiograph images, which are discussed in detail by N. L. Kugland *et al.* (2012)[45]. These approaches

include qualitative interpretation for inferring spatial structure of the fields, quantitative estimates based on simple scalings of the Lorentz force and assumed field scale lengths, proton ray tracing based on particle-in-cell codes to create a comparable synthetic image to experiments, and as the density increases these codes have to include slowing and scattering of the proton beam. The approach taken here will be more of a qualitative assessment of the proton images to infer the spatial magnetic structure based on some scaling assumptions of the fields.

It is assumed that the deflection of the proton beam is dominated by the large scale length magnetic field structures, since the scale length of any electrostatic electric field is far shorter than the magnetic field of the system and the force due to the inductive electric field of the expanding cavity (equation 3.78) is far weaker than that of the magnetic field (equation 3.67). For a proton velocity of v_p that is far greater than the cavity expansion speed v_c ($v_p \gg v_c$) the ratio of the magnetic force to the electric force at the equator ($\theta = \pi/2$) of a cavity that fully expels the magnetic field ($\alpha = B_{inside}/B_o = 0$) is

$$\frac{|v_p| |B|}{|E|} = \begin{cases} 0 & r < r_c \\ \frac{1}{3} \frac{v_p}{v_c} \left[2 \left(\frac{r}{r_c} \right)^2 - \frac{r_c}{r} \right] \gg 1 & r \geq r_c \end{cases}, \quad (2.8)$$

where r is the radial spatial location from the center of the cavity and r_c is the cavity radius. At this point the proton deflection distance Δ_p can be related to the average magnetic field experienced by the proton $\langle B \rangle$ when making the small deflection approximation; that is, $\Delta_p \ll L \ll \rho_p$ where L is the distance from the Cu target to the RCF stack, $\rho_p = v_p/\Omega_p$ is the proton gyro-radius, $\Omega_p = e \langle B \rangle / m_p$ is the proton gyro-frequency, and m_p is the proton mass. This also implies the proton transit time is approximately $t \approx L/v_p$. Using the particle trajectories for a charged particle in a magnetic field, the deflection Δ_p can be written as

$$\frac{y}{x} = \frac{\rho_p - \Delta_p}{L} \approx \cot \left(\Omega_p \frac{L}{v_p} \right) \approx \left(\frac{L}{\rho_p} \right)^{-1} - \frac{1}{3} \left(\frac{L}{\rho_p} \right) \quad \text{for } \frac{L}{\rho_p} \ll 1 \quad (2.9)$$

$$\implies \Delta_p \approx \frac{1}{3} \frac{L^2}{\rho_p} \quad \text{for } \Delta_p \ll L \ll \rho_p. \quad (2.10)$$

Writing the proton velocity in terms of the proton energy $v_p^2 = 2E_p/m_p$ allows equation 2.10

to be written in terms of E_p , L , and $\langle B \rangle$ to give

$$\Delta_p \approx \frac{1}{3} \langle B \rangle L^2 \left[\frac{e^2}{2E_p m_p} \right]^{1/2}. \quad (2.11)$$

Figure 2.7b gives the expected proton deflection for $L = 49$ cm, several average magnetic field values, and the expected proton energies to be absorbed by the RCF stack. Applying equation 2.11 to the $\Delta_p = 1.43 \pm 0.06$ cm shift between the RCF images in figures 2.6a and 2.6b then $\langle B \rangle \approx 558 \pm 64$ G for a 4.7 ± 1.0 MeV proton. This is less than the 792 ± 6 G of the HC B_o , but considering the HC B_z at the Cu target is near zero and about $0.8B_o$ at the RCF stack then $\langle B \rangle < B_o$ is expected.

CHAPTER 3

Discussion of Results

As outlined in §1.4, the discussion in this chapter sets out to (1) quantitatively identify and establish the existence of debris-ambient coupling within the collected datasets and (2) confirm the first production of shock-like features utilizing this experimental configuration. To achieve this an analytical model for a spherically expanding Magnetic Only Interacting Cavity (MOIC) will be developed alongside the analysis. A MOIC is an expanding cavity in which the energy contained in the debris-ions is only used to expel and compress the background magnetic field. The purpose of developing the MOIC model is to establish a set of benchmarks to which the experimental datasets can be quantitatively compared.

Previous approaches to the coupling problem, while not necessarily incorrect, took a perspective that is fairly complex and requires broad assumptions about the current structures to bring insight to the electric field structure, the magnetic field structure, and the resulting coupling behavior of the expansion event.[2, 14, 32, 36, 89] They generally ignore stage 1 of the cavity expansion (see §1.3.1) in order to jump straight ahead to stage 2 (see §1.3.2) where coupling is occurring. While stage 2 is crucial to the understanding, by glossing over stage 1 one also glosses over how the field structure evolves and grows to make stage 2 effective. The key issue with these previous approaches is that they have no origin story to the development of the field structure that drives the coupling.

The MOIC model takes a more fundamental/simplified approach to the understanding. Instead of making broad assumptions about what drives the coupling, the MOIC model starts in stage 1 and assumes no debris-ambient coupling. Regardless of if an expansion drives coupling or not, all expansions start in stage 1 where the energetics are dominated

by the diamagnetic cavity formation; that is, the debris-ion energy predominately flows into expelling/compressing the background magnetic field. Thus, every cavity starts as a MOIC; this is validated against experiments in §3.3-§3.4.

The MOIC assumption is overly simple but has two key benefits: (1) it allows for the development of analytical benchmarks that establish a baseline for experiments and (2) it gives an origin story for the electric and magnetic fields. It is understood these benchmarks will fail once coupling begins, but that is the moment that is trying to be identified. Understanding when the model agrees and when it does not is key to determining when coupling becomes non-negligible. Then, instead of making assumptions on the current structures, the MOIC model can be used to identify coupling, explain how the cavity may drive the coupling, and explain the observations made in the experimental datasets.

Before continuing it is useful to review and define some key features associated with the diamagnetic cavity. Figure 3.1 gives an example of the magnetic field generated by a diamagnetic cavity. The data depicted comes from the dataset collected during Run04 of the January 2013 LaPD-Phoenix campaign (see table 3.1 for full parameter details). Figure 3.1a shows a contour plot of the normalized magnetic field B_z/B_o as a function of time and distance from the target X_{TARGET} . There is a clear delineation between the compressed field upstream and the expelled field of the diamagnetic cavity downstream. The black contour line represents the contour level of $B_z/B_o = 1$. The contour plot does not provide much contrast for features in the compression so figure 3.1b plots the data as a series of stack plots (in X_{TARGET}) of B_z/B_o versus time that better highlights the features of the magnetic field. Here it can be seen that the compression shape and cavity edge constantly evolves as the cavity expands, going from being well-defined to smoothed out. Figure 3.1c plots a magnetic field profile (B_z/B_o versus X_{TARGET}) for a given time $t = 0.9 \mu s$. The compression region is defined when $B_z/B_o > 1$ and the expulsion region is defined when $B_z/B_o < 1$. The time-dependent cavity edge $X_{cav}(t) = 2r_c(t)$, where $r_c(t)$ is the time-dependent cavity radius, is defined to be the point where the magnetic field is expelled to $B_z/B_o = 0.5$. The trough of the cavity is defined to be the collection of points the make up lowest values of

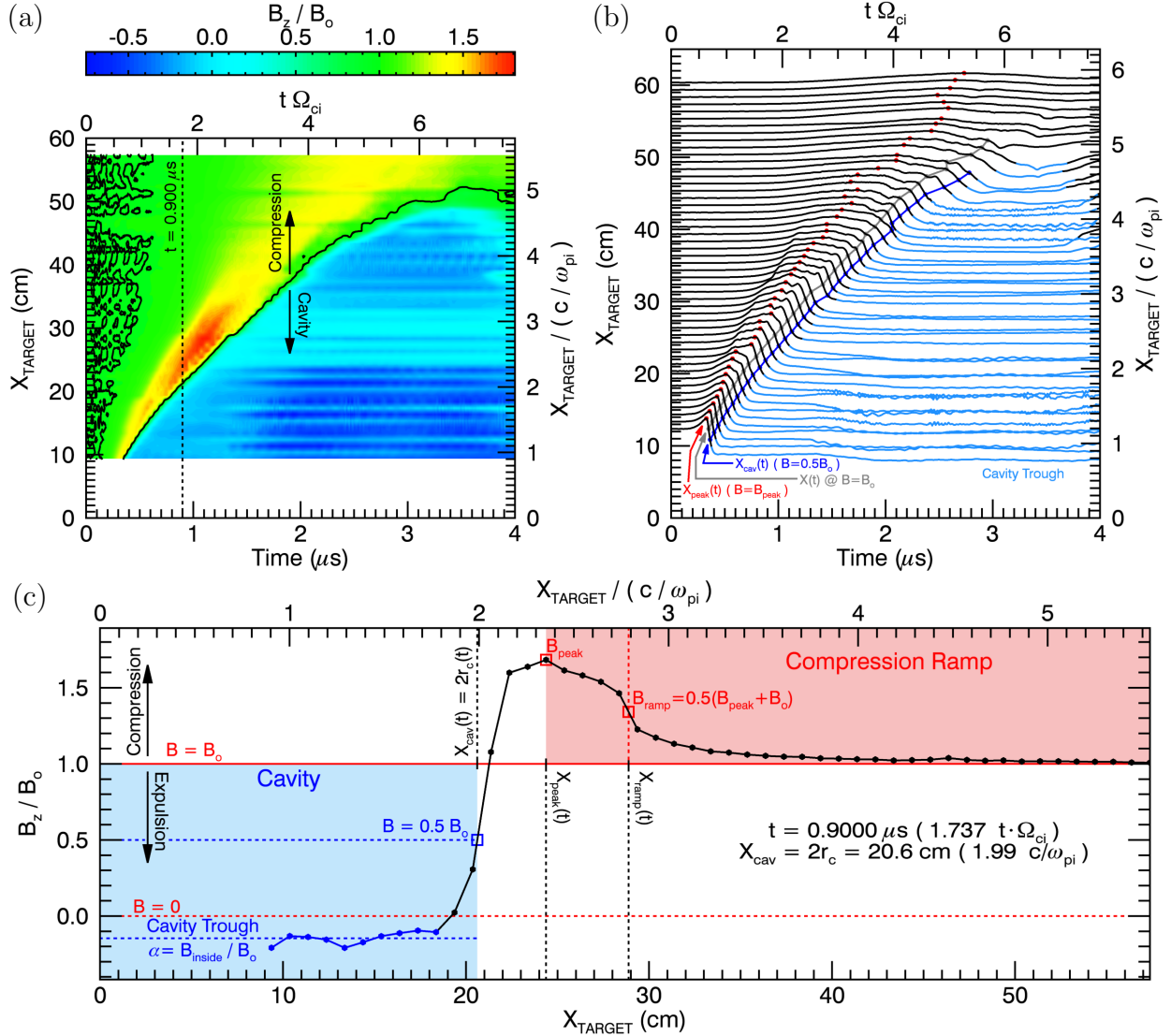


Figure 3.1: Plotted is an example of a formed diamagnetic cavity from data collected during Run04 of the 2013 January LaPD-Phoenix experiments (parameter details in table 3.1). Figure (a) shows a contour plot of the normalized magnetic field B_z/B_0 ($\mathbf{B}_0 = B_0 \hat{\mathbf{z}}$) of the diamagnetic cavity versus time and distance from the target X_{TARGET} . The data was collected along the LaPD $\hat{\mathbf{x}}$ -axis for a line out directly in front of the target. Figure (b) represents the same dataset as a series of stack plots. Figure (c) shows the magnetic field profile (B_z/B_0 versus X_{TARGET}) for a given time $t = 0.9 \mu\text{s}$ after ablation. Key cavity features (X_{cav} , X_{peak} , X_{ramp} , α , etc.) are identified and defined.

the cavity. Each point must satisfy the inequality $|B_z - B_{min}| \leq 0.1(B_o - B_{min})$ and their average value defines the magnetic field inside the cavity $\alpha = B_{inside}/B_o$. The compression ramp is defined as the region upstream of the compression peak ($X \geq X_{peak}$) and the time-dependent ramp position $X_{ramp}(t)$ is defined as the point where the compression raises to $B_z = 0.5(B_{peak} + B_o)$.

The existence of coupling does not imply the existence of a shock structure. Certain criteria need to be met for coupling to exist and then there are additional criteria for the coupling to satisfy shock conditions. The MOIC is used to help identify and satisfy these criteria. To establish the existence of debris-ambient coupling the following need to be met:

1. There must be a period of ‘enhanced’ deceleration in the cavity as compared to a cavity that expands in vacuum. The ‘enhanced’ deceleration indicates that the debris-energy is being diverted into other avenues other than just expelling the magnetic field; even though, ‘other avenues’ may not necessarily be debris-ambient coupling (e.g. slipping of debris-ions out of the cavity and upstream). (Discussed in §3.3)
2. There must be a growth of the peak magnetic field compression that can not be explained by a diamagnetic current layer. When correlated with the ‘enhanced’ deceleration, this growth distinguishes between slipping of debris-ions out of the cavity and possible debris-ambient coupling. (Discussion in §3.4 and §3.5)
3. The compression ramp must steepen and remain steep as it propagates. The steepening must bring the thickness of the compression to an order of the ambient-ion inertial length. This also distinguishes the ‘enhanced’ deceleration from being due to debris-ambient coupling or debris-ion slipping, as well as, localizing where the interaction is occurring. (Discussion in §3.4 and §3.5)

In addition to the above criteria, the following criteria need to be met in order to establish a shock structure in the data.

1. The magnetic field compression must be consistent with the Rankine-Hugoniot jump conditions. (Discussion in §1.1 and §3.6)
2. The separation between the cavity edge X_{cav} and compression ramp X_{ramp} to X_{cav} must

increase has the structure propagates while maintaining its compression and steepness, i.e. $\partial_t [(X_{ramp} - X_{cav}) X_{cav}^{-1}] > 0$. (Discussion in §3.5 and §3.6)

3.1 Proton Radiography Results

As discussed in the proton radiography diagnostic section (§2.3.2), the deflection in the proton beam Δ_p is proportional to the average magnetic field $\langle B \rangle$ experienced by the proton (equation 2.11). Due to the large path length of the proton beam (distance between the Cu target and RCF stack) and the large scale length of the HC and diamagnetic cavity magnetic field, this diagnostic configuration is insensitive to the small scale modulations. Additionally, the average magnetic field $\langle B \rangle$ will not be a good measure of the field in the xz -plane of the experiment, since the HC field varies by ΔB_o over the proton path (figure 2.2b) and the proton will have to travel through the cavity's compressed field twice as well as the expelled volume. Thus, for this discussion, the analysis of the proton deflection Δ_p will not go as far as to determining the magnetic field but will be used to capture a 2D spatial image (xz -plane) of the magnetic field structure associated with the diamagnetic cavity.

Figure 3.2b shows the deflection results for Trident shot number 21976. Shot 21976 produces a vacuum expansion in a background magnetic field of $B_o = 792 \pm 6$ G. The LPP is generated by the 'heater' beam with an energy of 217 J in a 5 ns FWHM and focused to an intensity of $3.5(\pm 1.4) \times 10^{12}$ W/cm². The proton beam is produced by a 45 J, 579 fs FWHM CPA pulse that is delayed 0.6 μ s after the 'heater' beam. To capture the proton image a RCF stack is layered with a 16 μ m thick Al filter, a 104 μ m thick HD-810 film, and 3 consecutive layers of 285 μ m thick EBT2 film. Figure 3.2a shows the proton energy deposition of this RCF stack, which is calculated using the SRIM software. The peak deposition for the first (last) EBT2 film occurs at a proton energy of 4.44 MeV (8.99 MeV).

The proton deflection in figure 3.2b is calculated between the first and last layer of EBT2 films. This is done because the original Cu mesh in the null shots 21970 and 21971 had to be replaced. However, by examining equation 2.11 and assuming $\langle B \rangle$ is approximately the

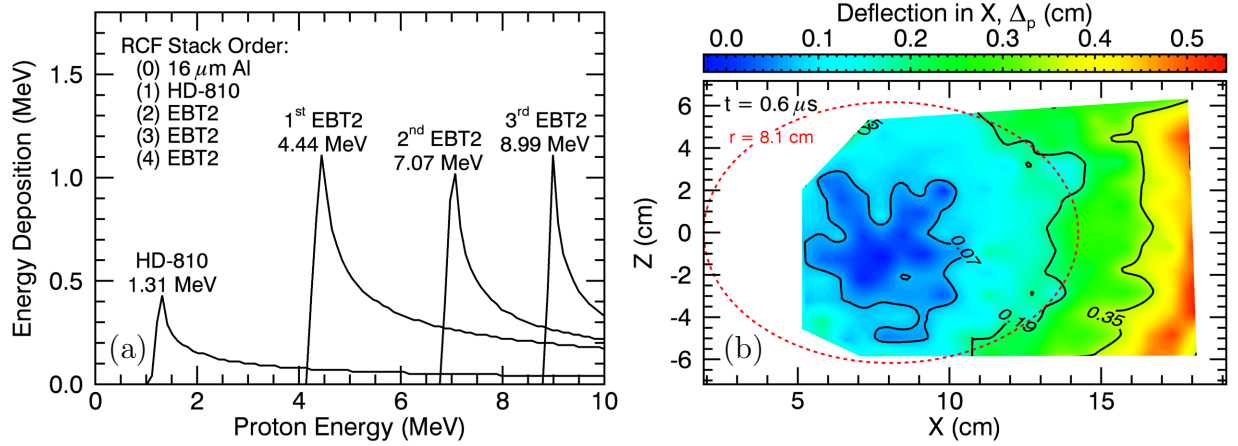


Figure 3.2: Figure (a) shows the proton energy deposition for the RCF stack used for Trident shot 21976. The RCF stack consists of five layers: 16 μm thick Al foil, 104 μm thick HD-810 film, and 3 consecutive sheets of 285 μm thick EBT2 film. Figure (b) shows horizontal proton deflection calculations made between the first and third sheet of EBT2 film. This imaged diamagnetic cavity is spherical and centered in a cavity with approximate radius of 8.1 cm and one edge still at the target surface.

same along the proton path for the peak proton energy of the two EBT2 films, then this calculation method is still proportional to $\langle B \rangle$ and gives

$$\Delta_p = \Delta_p^{(3)} - \Delta_p^{(1)} \approx \frac{1}{3} \langle B \rangle L^2 \left\{ \left[\frac{e^2}{2E_p^{(3)} m_p} \right]^{1/2} - \left[\frac{e^2}{2E_p^{(1)} m_p} \right]^{1/2} \right\} \quad (3.1)$$

where (1) and (3) indicate quantities for the first and last, respectively, EBT2 films. Calculating the deflection entails manually determining the cross-points of the Cu mesh in each image. The horizontal difference is proportional to $\langle B_z \rangle$ and is shown in figure 3.2b. Assuming the peak compression of the formed diamagnetic cavity reaches $B_{peak}/B_o = 1.5$ (see discussion in §3.4-§3.5 and equation 3.68) and fully expels the field, then the contour levels of $\Delta_p = 0.07$, 0.19, and 0.35 are chosen to approximate magnetic field values of $B = 0.2B_o$, $0.5B_o$, and B_o respectively. The resulting calculation shows that the compressed field ($\Delta_p \gtrsim 0.35$) is not strictly localized at the equator of the cavity ($z = 0$). Additionally, the formed diamagnetic cavity is spherical and centered in a circular region with an approximate radius of 8.1 cm

and one edge still at the target surface. Even though the laser blow-off is not an ideal point explosion, the cavity still resembles one as it expands out.

3.2 Scalings of the Diamagnetic Cavity Size $2R_c$

Section Highlights

1. Experimental cavity sizes trend smaller than pure vacuum cavities (the R_B -scaling) as the blow-off Alfvénic Mach number increases (figure 3.4b). For an Alfvénic Mach number of ~ 1.7 the experimental cavity size is $\sim 19\%$ smaller than that of the R_B -scaling ($2R_c/2R_B \sim 0.81$).
2. ‘Weak’ diamagnetic cavities (as defined in §3.4 as cavities with $B_{peak}/B_o \lesssim 1.4$) follow the scaling defined by the magnetic-stopping radius (the R_B -scaling), see equation 3.6 and figure 3.3.
3. The equal-mass radius R_M (equation 3.10) and the ‘hybrid’ magnetic-mass radius R_{BM} (equation 3.14) provide scalings that predict a smaller cavity size as the Alfvénic Mach number increase, but to an extent that is far greater than what is seen experimentally. These scalings indicate that energizing the ambient-ions is a reasonable (not proven) candidate for why the cavity sizes decrease with increasing Alfvénic Mach number. The scalings do overestimate how much energy gets coupled into the ambient-ions. Additionally, the scalings do not exclude the other possible energy sinks for the debris-energy:
 - (a) Ionizing the ambient neutral population
 - (b) Slipping of debris-ions upstream and out of the cavity
 - (c) Turbulent excitation leading to ambient-heating with no directed flow
 - (d) Wave excitation
4. Assuming perfect energy transfer between the debris-ions and magnetic field of the cavity, then the R_B -scaling indicates there is a Laser-to-Debris coupling efficiency of

$\alpha_{L2D} \approx 9.5(\pm 1.2)\%$ when ignoring the field compression of the cavity and $\alpha_{L2D} \approx 14.0(\pm 2.0)\%$ when including the compressed field.

This section takes a macroscopic view of the expansion event in order to develop scalings that determine the expanded/maximal radius of the diamagnetic cavity. Understanding how the initial conditions lead to the maximal cavity radius can give insight into how the debris-energy is used throughout the expansion. This in turn helps with identifying and understanding sources of debris-ambient coupling in the expansion. The discussion to follow will cover four scaling models relating the initial conditions to the maximal cavity size $2R_c$; of which, three are based on conservation of energy (the magnetic-stopping radius R_B , the equal-mass radius R_M , and the ‘hybrid’ magnetic-mass radius R_{BM}) and the fourth (the equal-charge radius R_*) comes from attempts to analytically solve the vector potential based on initial conditions.

To start, the system is initialized with a free-energy dump in the form of the ablated debris-plasma. As the debris-plasma expands there are numerous avenues for this free-energy to propagate into. These avenues depend on the set debris- and ambient-conditions and include: (1) formation of a diamagnetic current resulting in the expulsion of the background magnetic field[21, 22, 59, 69, 81], (2) excitation of wave behavior[10, 85, 86], (3) debris-ambient coupling by thermalization through excitation of turbulence[3, 79], (4) debris-ambient coupling that results in a directed flow of the ambient-ions (collisional[3] or Laminar/non-turbulent[3, 36]), and (5) debris-ions slipping out of the cavity which results in the escape of energy from participating in any of the above scenarios[36]. All expansions use some of the debris-energy to expel the background magnetic field. The MOIC model is the special case in which all of the debris-energy is used to expel the magnetic field. If the energetics fall out of favor with the MOIC model, then it can be said that one or more of the other listed physical processes are playing a non-negligible role in the energetics of the system.

The scaling from the magnetic-stopping radius R_B is based on conservation of energy

and takes the extreme MOIC scenario in which all the debris-energy goes into expelling the background magnetic field. It is also assumed that the expansion is spherical, there is no ‘progressive’ debris-ion loss during the expansion, and the energetics are dominated by a single debris-ion species. By no ‘progressive’ debris-loss it is meant that there is no rate of debris-ions slipping out of the cavity and upstream during the expansion. If there is any debris-ion loss then it all happens at $t = 0$ and the lost debris-ions are non-participants in the expansion from the beginning. In reality the debris-plasma is composed of several debris-ion species, but 2D-hybrid simulations and spectral-imaging suggest that the assumption that a single debris-ion species does all the work is a reasonable one.[6, 13]

The majority of the debris-energy is contained as the kinetic energy of the debris-ions¹ as

$$E_d = \frac{1}{2}m_d N_d V_o^2, \quad (3.2)$$

where m_d is the debris-ion mass, N_d is the number of ablated debris-ions that participate in the expansion, and V_o is the initial expansion velocity of the debris-ions. The energy of the expelled magnetic field is given by

$$E_B = \frac{B_o^2}{2\mu_o} \left(\frac{4}{3}\pi R_B^3 \right), \quad (3.3)$$

where B_o is the background magnetic field and R_B is the magnetic-stopping radius (or maximal radius of the diamagnetic cavity). The traditional derivation of the magnetic-stopping radius assumes the energy stored within the compression of the diamagnetic cavity is negligible when compared to the energy stored in the expelled magnetic field, this is equation 3.3. This is not accurate and will be discussed a little later, but for now the traditional model will be adhered to. Setting the debris-energy E_d equal to the magnetic energy E_B then the derived expression for the magnetic-stopping radius is

$$R_B = \left(\frac{3\mu_o}{4\pi} \frac{m_d N_d V_o^2}{B_o^2} \right)^{1/3}. \quad (3.4)$$

¹The kinetic energy of the debris-electrons is negligible as compared to the kinetic energy of the debris-ions, since $N_e m_e / (N_d m_d) = m_e / (Z_d m_d) \sim 10^{-3}$, where m_d is the debris-ion mass, Z_d is the debris-ion charge state, N_d is the number of ablated debris-ions, and $N_e = Z_d N_d$ is the number of ablated electrons.

For experiments N_d and V_o are not precisely known, but are dependent on the laser-energy E_{laser} . Assuming there is some coupling efficiency of the laser energy to debris-energy α_{L2D} then the debris-energy can be written as

$$E_d = \alpha_{L2D} E_{laser}. \quad (3.5)$$

It is a valid to take α_{L2D} as a constant if the target and laser conditions remain fixed, which they are during a LaPD-Phoenix campaign but not necessarily between campaigns. Under the assumption that α_{L2D} is constant, then combining equations 3.2, 3.4, and 3.5 the scaling between the magnetic-stopping radius and initial conditions is given by

$$R_B = \left(\frac{3\mu_o}{2\pi} \frac{\alpha_{L2D} E_{laser}}{B_o^2} \right)^{1/3} \propto \left(\frac{E_{laser}}{B_o^2} \right)^{1/3}. \quad (3.6)$$

This expression is referred to as the R_B -scaling and is directly comparable to experimental results.

As mentioned above, the amount of energy stored in the compressed portion of the magnetic field outside the diamagnetic cavity is not negligible. Looking ahead to discussions in §3.4 and Appendix B, an ideal diamagnetic cavity can be represented as a magnetized sphere which gives an analytical solution for the magnetic field both inside and outside the cavity, see equations 3.49, 3.50, and 3.51. Integrating over the magnetic energy density outside the diamagnetic cavity, Appendix B.3, the amount of energy stored there is equivalent to 50% of the energy contained inside the cavity. This means equation 3.3 requires an extra factor of 3/2 to account for both the energy of the cavity and compressed magnetic field. This gives a new ‘prime’ magnetic-stopping radius R'_B that shares the same scaling as the R_B -scaling but has a different nominal value given by

$$R'_B = \left(\frac{2}{3} \right)^{1/3} R_B \propto \left(\frac{E_{laser}}{B_o^2} \right)^{1/3}. \quad (3.7)$$

Table 3.1 contains a set of experimental runs, and associated parameters, that the R_B -scaling can be applied to. Run selection is restricted to datasets that contain the full cavity expansion within the measurement range. Each run is a composition of several laser shots

(“# of shots” in table 3.1) with the magnetic flux probe being placed at a unique position for each shot. It is assumed that the ambient-ions (“a-ion” in table 3.1) are singly ionized. The table also lists values for the background magnetic field B_o , the average laser energy E_{laser} for the run, the maximal cavity size $2R_c$, the initial cavity edge expansion velocity $V_{cav,o}$ (based on time-of-flight calculations), the average ambient-ion density $\langle n_a \rangle$ over the range spanned by $2R_c$, the Alfvén speed defined by the average density $V_A|_{\langle n_a \rangle}$, and the initial Alfvénic Mach number of the cavity edge expansion $M_A = V_{cav,o} / V_A|_{\langle n_a \rangle}$. The laser energy is measured for each shot with a calibrated calorimeter (Thorlabs ES111C) by detecting the 1% leak through the last turning mirror into the LaPD chamber. The maximal cavity size $2R_c$ is defined by the maximum extent the cavity edge reaches from the target (as defined in figure 3.1), given that the magnetic field is fully expelled all the way back to the target. The listed ambient-ion density is calculated from swept Langmuir probe measurements taken before and after each experimental run.

The initial debris-ion blow-off velocity V_o is approximated as the initial expansion velocity of the cavity edge $V_{cav,o}$ (i.e. $V_o \sim V_{cav,o}$). As in figure 3.1, the cavity edge X_{cav} is defined as the point where the expulsion reaches $B = 0.5B_o$. The initial cavity expansion velocity is a time-of-flight calculation based on when X_{cav} first appears in the closest measurements to the target. This approximation is an underestimate for the actual initial debris-ion blow-off velocity V_o for several reasons. First, the expansion has already slowed down a little by the time it reaches the closest probe. Second, assuming quasi-neutrality, the debris-ions span the region occupied by the diamagnetic current layer. Looking ahead to §3.4 and figure 3.8b, the center of the diamagnetic current layer is better approximated by the point where the expulsion reaches half way between B_{peak} and B_{inside} , i.e. $B = 0.5(B_{peak} + B_{inside})$. For an ideal cavity with $B_{inside}/B_o = 0$ the peak compression is given by $B_{peak}/B_o = 1.5$, so the cavity edge is better approximated by $B = 0.75B_o$. This point is ahead of X_{cav} and, thus, is expanding faster.

Using entries in table 3.1 that utilize graphite targets, figure 3.3 shows how the experimental maximal cavity size $2R_c$ trends with the R_B -scaling (equation 3.6). The R_B -scaling

Experiment	Run	a-ion	Target	# of shots	B_o (G)	E_{laser} (J)	$2R_c$ (cm)	B_{peak}/B_o	$V_{cav,o}$ (10^7 cm/s)	$V_A _{(r_a)}$ (10^7 cm/s)	M_A
Trident	35	VAC	C	1	810(± 41)	51.8(± 2.6)	13.5(± 1.5)	1.29(± 0.06)		N/A	N/A
Trident	38	VAC	C	1	1000(± 50)	97.3(± 4.9)	14.5(± 3.0)	1.27(± 0.06)		N/A	N/A
2011	1	H ⁺	C	25	275(± 6)	18.4(± 0.2)	20.4(± 1.5)	1.23(± 0.03)	4.0(± 0.9)	4.8(± 0.6)	0.8(± 0.2)
2011	2	He ⁺	C	47	275(± 6)	18.5(± 0.2)	19.3(± 1.5)	1.37(± 0.03)	3.9(± 0.8)	1.6(± 0.2)	2.5(± 0.6)
2011	3	He ⁺	C	22	600(± 12)	18.5(± 0.2)	15.0(± 1.5)	1.22(± 0.02)	3.3(± 0.8)	4.5(± 0.7)	0.7(± 0.2)
2013 Jan	1	He ⁺	C	9	275(± 6)	114.2(± 5.3)	36.9(± 1.5)	1.59(± 0.03)	2.0(± 0.2)	1.6(± 0.3)	1.2(± 0.3)
2013 Jan [†]	2	He ⁺	C	11	200(± 4)	97.0(± 8.2)	39.0(± 1.5)	1.66(± 0.03)	2.0(± 0.3)	1.2(± 0.2)	1.7(± 0.4)
2013 Jan	3	H ⁺	C	9	200(± 4)	90.2(± 2.6)	47.3(± 1.5)	1.57(± 0.03)	2.5(± 0.3)	2.8(± 0.7)	0.9(± 0.3)
2013 Jan [†]	4	H ⁺	C	11	200(± 4)	91.7(± 2.1)	49.1(± 1.5)	1.81(± 0.04)	2.6(± 0.3)	2.8(± 0.8)	0.9(± 0.3)
2013 Jan	5	VAC	C	5	200(± 4)	89.8(± 2.1)	50.0(± 3.0)	1.35(± 0.03)	2.3(± 0.1)	N/A	N/A
2013 Jun [†]	1	He ⁺	C	8	300(± 6)	99.2(± 2.6)	31.9(± 1.5)	1.44(± 0.03)	1.9(± 0.2)	1.9(± 0.5)	1.0(± 0.2)
2013 Oct [†]	17	H ⁺	HDPE	9	300(± 6)	186.2(± 7.7)	42.5(± 2.0)	2.04(± 0.04)	4.9(± 0.3)	2.3(± 0.5)	2.1(± 0.5)

[†] These cases show ‘enhanced’ deceleration in the cavity expansion speed (§3.3), as well as, some degree of augmentation of the magnetic compression (§3.5).

Table 3.1: This table contains a list of accumulated experimental datasets between the Trident and LaPD-Phoenix platforms. Datasets selected contain a cavity expansion to its maximal size within the measurement range. The collection contains three vacuum expansions along with a few sub-Alfvénic expansions ($M_A < 1$), a few ‘marginally’ super-Alfvénic expansions ($M_A \sim 1$), and a few ‘highly’ super-Alfvénic expansions ($M_A > 1.5$).

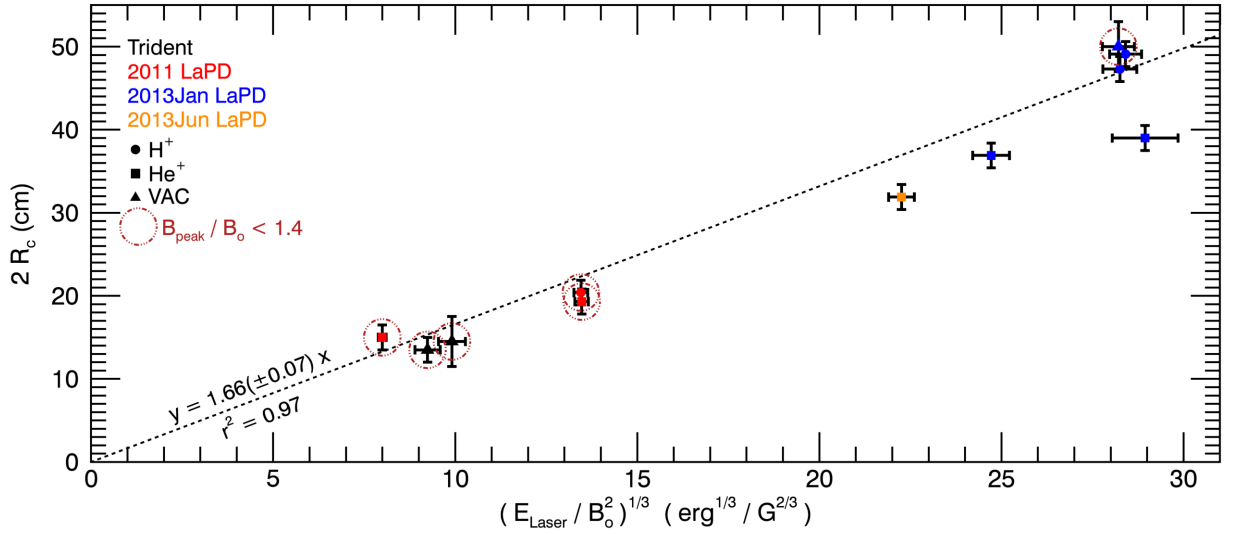


Figure 3.3: The maximal diamagnetic cavity size ($2R_c$) versus the scaling of the magnetic-stopping radius (equation 3.6) for the entries in table 3.1 using graphite targets. Each data point is color coded to its respective campaign: (black) Trident, (red) 2011 LaPD-Phoenix, (blue) 2013 January LaPD-Phoenix, and (orange) 2013 June LaPD-Phoenix. The symbols represent the ambient conditions: (circle) H^+ , (square) He^+ , (triangle) vacuum. ‘Weak’ cavities, those with $B_{peak}/B_o < 1.4$, are highlighted with a firebrick colored dash-double dot circle. The ‘weak’ cavities are used for the linear least-squares fit.

assumes negligible differences in laser-target interactions (i.e. α_{L2D} is constant), so a direct comparison between graphite and HDPE entries is not appropriate. Of the plotted data points there includes three vacuum cases, several ‘marginally’ super-Alfvénic cases ($M_A \sim 1$), and a few ‘highly’ super-Alfvénic cases ($M_A \gtrsim 1.5$). The data points are color coded to their respective campaign: black for the Trident campaign, red for the 2011 LaPD-Phoenix campaign, blue for the 2013 January LaPD-Phoenix campaign, and orange for the 2013 June LaPD-Phoenix campaign. The plotted symbol represents the ambient-ion conditions: circle for H^+ , square for He^+ , and triangle for vacuum. Those entries that are considered ‘weak’ cavities, $B_{peak}/B_o < 1.4$, are highlighted with a firebrick colored circle.

The R_B -scaling is developed for cavities that have no debris-ambient coupling, but the collection of data presented in figure 3.3 is composed of cavities formed in vacuum, as well

as, cavities that interact weakly and strongly with the ambient-plasma. Looking ahead to §3.4 and §3.5, the strongest field compression a diamagnetic current can produce when $B_{inside}/B_o = 0$ is $B_{peak}/B_o = 1.5$ (equation 3.68). A compression above 1.5 indicates generation of coupling and a compression below indicates a weak diamagnetic current and, thus, a weak magnetic piston. To prevent a fit to cavities that couple, the fit is done with cavities that have $B_{peak}/B_o < 1.4$, which includes all the vacuum cases. The linear least-squares fit suggests a strong correlation between the experiments and the R_B -scaling with an r^2 -value of 0.97. Forcing the slope through zero, the fitted slope² is $1.66(\pm 0.07) \text{ cm} \cdot \text{G}^{2/3} \cdot \text{erg}^{-1/3}$ and the resulting empirical formula (in cgs) is

$$2R_B = 1.66 \left(\frac{E_{laser}}{B_o^2} \right)^{1/3}. \quad (3.8)$$

Depending if the R_B or R'_B formulation is used, this gives a calculated laser-to-debris coupling efficiency of $\alpha_{L2D} = 9.5(\pm 1.2)\%$ and $14.0(\pm 2.0)\%$, respectively.

A good r^2 -value is not enough to establish the R_B -scaling model as a ‘good fit’ for the whole dataset, and examining a residual plot is necessary to achieve more confidence/understanding in the model. Figure 3.4a shows a normalized residual plot between the experimental data and regression fit, $(2R_c/2R_B) - 1$ versus the R_B -scaling. The residual indicates that the vacuum cavities and the majority of the ‘weak’ cavities follow the R_B -scaling within the measurement error of the experiment, but a confidence in the correlation diminishes when looking at the dataset as a whole. The ‘strong’ cavities, $B_{peak}/B_o > 1.4$, tend to have negative residues that differ beyond the measurement error, except for the two hydrogen runs (Run03 and Run04) of the 2013 January LaPD-Phoenix campaign which agree with the R_B -scaling. Additionally, the ‘weak’ cavity of Run02 of the 2011 LaPD-Phoenix campaign also differs from the R_B -scaling beyond the experimental error. These disagreements are not necessarily bad, since the R_B -scaling is expected to disagree as the cavities begin to couple with the ambient-plasma. The burden now is to determine possible causes for this disagreement.

²In mks units the slope is $7.4(\pm 0.3) \times 10^{-3} \text{ m} \cdot \text{T}^{2/3} \cdot \text{J}^{-1/3}$

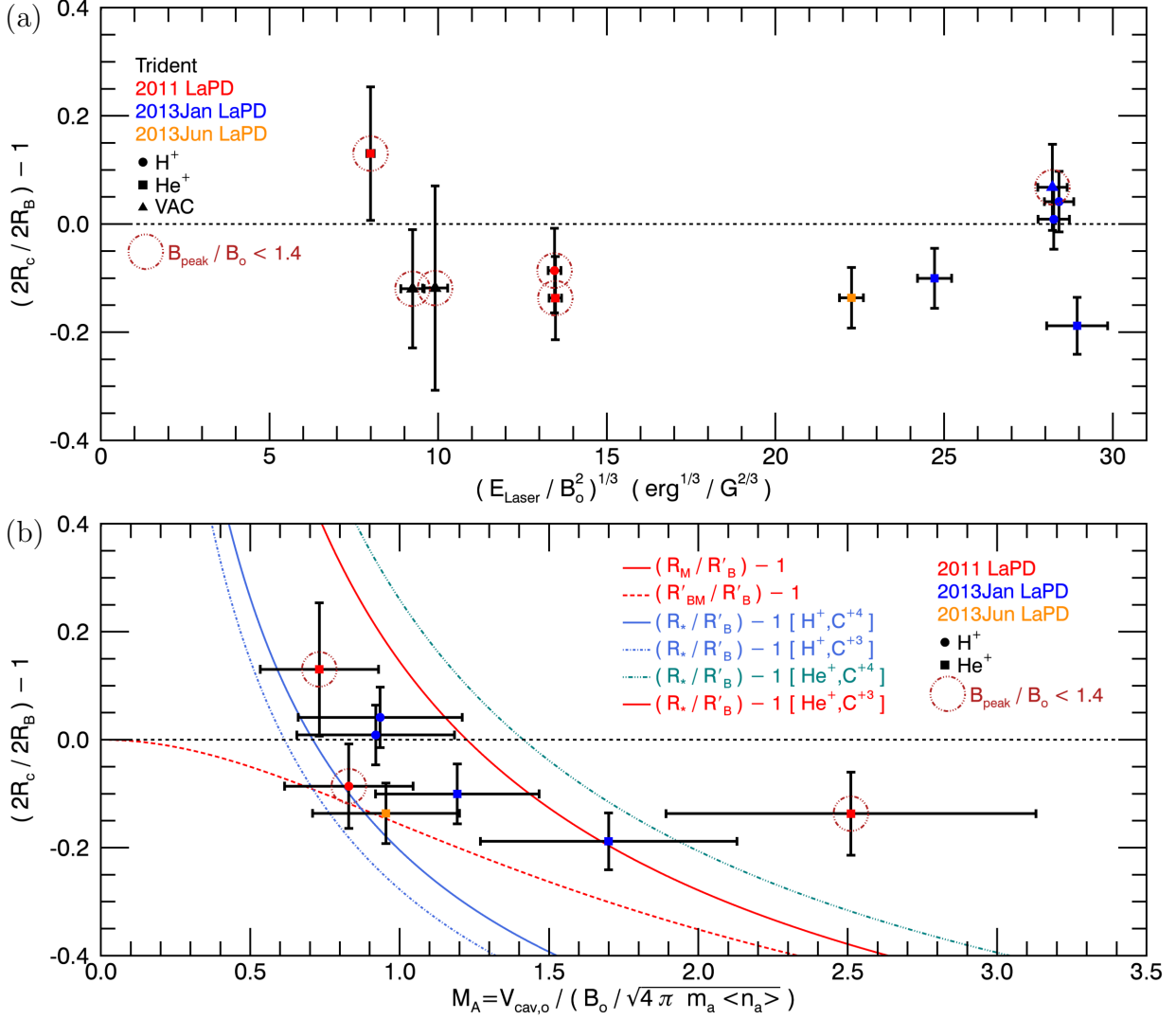


Figure 3.4: Figures (a) and (b) show a normalized residual plot between the experimental cavity size and the empirically derived cavity size $(2R_c/2R_B) - 1$ versus the R_B -scaling and $(2R_c/2R_B) - 1$ versus the initial Alfvénic Mach number, respectively. The plotted dataset is a collection of the entries in table 3.1 that use graphite targets. Figure (b) includes trend lines associated with other characteristic cavity scalings (the equal-mass radius R_M , the primed ‘hybrid’ magnetic-mass radius R'_{BM} , and the equal-charge radius R_*) normalized to the ‘prime’ magnetic-stopping radius R'_B (equation 3.7).

The R_B -scaling only has a correlation with the vacuum or ‘weak’ experimental cavities, but the variable that indicates the breakdown with the stronger cavities is not apparent in figure 3.4a. By recasting the plot from the R_B -scaling as the dependent variable to the blow-off Alfvénic Mach number, figure 3.4b shows that the residuals decrease with increasing Mach number; that is, the experimental cavity size as compared to a pure vacuum cavity trends increasingly smaller as the Mach number increases. To make sense of this trend, additional scalings (R_M , R_{BM} , and R_*) can be directly compared to the dataset on figure 3.4b.

First, the equal-mass radius R_M is based on conservation of energy, much like the magnetic-stopping radius R_B , but all the debris-energy is now considered to flow into the ambient-ions and none is consumed by augmenting the background magnetic field. This scenario envisions a ‘perfect’ debris-ambient coupling in which all of the ambient-ions that are swept over by the cavity are energized to the initial debris-ion velocity V_o . The energy of the swept ambient-ions at the end of the expansion is

$$E_a = \frac{1}{2} m_a n_a \left(\frac{4}{3} \pi R_M^3 \right) V_o^2 \quad (3.9)$$

where m_a is the ambient-ion mass, n_a is the ambient-ion number density, and R_M is the radius of the cavity created by sweeping out the ambient-ions, also known as the equal-mass radius. Setting the debris-energy E_d equal to the swept up ambient-ion energy E_a the equal-mass radius can be expressed as

$$R_M = \left(\frac{3}{4\pi} \frac{m_d N_d}{m_a n_a} \right)^{1/3}. \quad (3.10)$$

The equal-mass radius can be conveniently written in terms of either R_B or R'_B to give

$$R_M = \left(\frac{1}{M_A^2} \right)^{1/3} R_B \quad (3.11)$$

$$= \left(\frac{3}{2} \frac{1}{M_A^2} \right)^{1/3} R'_B \quad (3.12)$$

which is a form that can be plotted against the residuals between the experimental cavities and empirical- R_B (solid red line in figure 3.4b). From this relation it is seen that R_M becomes

the smaller of the two for $M_A \gg 1$, suggesting that R_M would become the dominate scale in this limit and visa-versa in the limit of $M_A \ll 1$. For marginally super-Alfvénic Mach numbers ($M_A \sim 1$) the R_B and R_M values are comparable ($M_A \sim 1.23$ for R'_B and R_M) but this is misleading when trying to determine which parameter is defining the energy partition at these conditions. Under marginally super-Alfvénic conditions the strength of the magnetic piston is not consistent from case-to-case, so the degree of debris-ambient coupling is always questionable. Thus, confidence in the R_M scaling is only reasonable for highly super-Alfvénic expansions ($M_A \gg 1$).

The ‘hybrid’ magnetic-mass radius R_{BM} attempts to build a more accurate scaling by accounting for a partition of the debris-energy into expelling the magnetic field and energizing the ambient-ions. Like the R_B -scaling, there is a primed R'_{BM} and non-primed R_{BM} version to this model. The primed ‘hybrid’ magnetic-mass radius R'_{BM} accounts for both the magnetic energy contained in the expelled and compressed portions of the diamagnetic cavity, whereas, the non-primed version R_{BM} follows the traditional approach of only considering the energy of the expelled field. It is also assumed that all the ambient-ions swept over by the cavity are energized to the initial blow-off velocity V_o . For the ‘hybrid’ magnetic-mass radius R_{BM} the energy balance goes like

$$E_d = E_a + E_B$$

$$\frac{1}{2}m_d N_d V_o^2 = \frac{1}{2}m_a n_a \left(\frac{4}{3}\pi R_{BM}^3 \right) V_o^2 + \frac{B_o^2}{2\mu_o} \left(\frac{4}{3}\pi R_{BM}^3 \right) \quad (3.13)$$

and solving for R_{BM} yields

$$R_{BM} = \left(\frac{3}{4\pi} \frac{m_d N_d}{m_a n_a} \frac{M_A^2}{1 + M_A^2} \right)^{1/3}, \quad (3.14)$$

which can be written in terms of R_B

$$R_{BM} = R_B \left(\frac{1}{1 + M_A^2} \right)^{1/3}. \quad (3.15)$$

The primed version R'_{BM} is derived in a similar manner but the definition for E_B now includes the extra factor of 3/2 to account for energy of both the expelled and compressed portions

of the diamagnetic cavity to give

$$\frac{1}{2}m_d N_d V_o^2 = \frac{1}{2}m_a n_a \left(\frac{4}{3}\pi(R'_{BM})^3 \right) V_o^2 + \frac{3}{2} \frac{B_o^2}{2\mu_o} \left(\frac{4}{3}\pi(R'_{BM})^3 \right) \quad (3.16)$$

$$\implies R'_{BM} = \left(\frac{3}{4\pi} \frac{m_d N_d}{m_a n_a} \frac{M_A^2}{3/2 + M_A^2} \right)^{1/3} \quad (3.17)$$

$$R'_{BM} = \left[\frac{1}{1 + (2/3)M_A^2} \right]^{1/3} R'_B. \quad (3.18)$$

This form is plotted against the residuals between the experimental cavities and empirical R_B as the dashed red line in figure 3.4b. The R_{BM} model asymptotically approaches the magnetic-stopping radius $R_{BM} \rightarrow R_B$ ($R'_{BM} \rightarrow R'_B$) as $M_A \rightarrow 0$ and approaches the equal-mass radius $R_{BM} \rightarrow M_A^{-2/3} R_B = R_M$ ($R'_{BM} \rightarrow \left(\frac{3}{2}\right)^{1/3} M_A^{-2/3} R'_B = R'_M$) as $M_A \rightarrow \infty$. The ratio of the ambient-ion energy E_a to the magnetic energy E_B is $E_a/E_B = M_A^2$ ($E_a/E'_B = \frac{2}{3}M_A^2$), so for marginal Mach numbers ($M_A \sim 1$) the debris-energy is evenly split between the ambient-ions and the expelled magnetic field in the traditional model, whereas, the magnetic energy is 1.5x the energy of the ambient-ions when including the compressed field.

Both the R_{BM} and R_M models envision a scenario of ‘perfect’ coupling into the ambient-ions, but do not encompass mechanisms for coupling. These scenarios are ideal and will be an overestimate for the amount of energy coupled into the ambient-ions. Therefore, the R_{BM} model is only reasonable at the limits of $M_A \ll 1$ and $M_A \gg 1$, and is considered a crude approximation for $M_A \sim 1$.

The last scaling model, the equal-charge radius R_* , arises from attempts to develop a model for the expansion event from which an analytical solution for the vector potential, and magnetic field, can be solved. Golubev *et al.* (1978)[32] presents a solution for a cylindrical expansion (2-dimensions) and Bashurin *et al.* (1983)[2] presents a solution for a spherically expanding point explosion (3-dimensions), where both solutions are based off of concepts first present by Colgate (1965)[14]. Wright (1971)[89] also presents a detailed solution for a spherical expansion. The setups in the above references impose quasi-neutrality and a ‘weakly’ interacting cavity such that the ambient-ions remain stationary during the expansion. For simplicity, it is also assumed that as the debris-ions expand they are uniformly

distributed within a radius $R_d = R_d(t)$. This allows the total electron density to be written as

$$\begin{aligned} n_e &= Z_a n_a + Z_d n_d = Z_a n_a + \frac{Z_d N_d}{\frac{4}{3}\pi R_d^3} \\ &= Z_a n_a \left[1 + \left(\frac{R_*}{R_d} \right)^3 \right] \end{aligned} \quad (3.19)$$

where R_* is the equal-charge radius and is defined as

$$R_* \equiv \left(\frac{3}{4\pi} \frac{Z_d N_d}{Z_a n_a} \right)^{1/3}. \quad (3.20)$$

The previous scalings never considered which electron population (debris or ambient) was neutralizing the debris-ions or constituting the diamagnetic current. For the R_* model, it is assumed that the debris-electrons lag behind the front of the expanding debris-ions and expand to a radius $R_{de} = R_{de}(t)$. Within R_{de} , the debris-electrons are uniformly distributed and the ambient-electrons have been pulled out to neutralize the debris-ion population that lies between R_{de} and R_d and form the diamagnetic current. The density of debris-electrons can be written as

$$n_{de} = \frac{Z_d N_d}{\frac{4}{3}\pi R_{de}^3} \quad (3.21)$$

and, since no ambient-electrons lie within R_{de} , R_{de} can be written as

$$\begin{aligned} n_{de} &= \frac{3Z_d N_d}{4\pi R_{de}^3} = Z_a n_a \left[1 + \left(\frac{R_*}{R_d} \right)^3 \right] \\ \implies \left(\frac{R_*}{R_{de}} \right)^3 &= 1 + \left(\frac{R_*}{R_d} \right)^3 \\ &= \left[1 + \left(\frac{R_{de}}{R_d} \right)^3 \right]^{-1}. \end{aligned} \quad (3.22)$$

These assumptions impose R_* as a scaling radius. Since $R_*/R_d \gtrsim 0$, $R_*/R_{de} \gtrsim 1$ and in the late time limit ($t \rightarrow \infty$) $R_d \gg R_*$ and $R_{de} \simeq R_*$. R_{de} is the inner radius to the cavity and the region spanned by R_{de} and R_d encompass the augmented magnetic field (cavity edge and magnetic compression). R_* is the largest radius in which the debris-electrons can neutralize

the stationary ambient-ions. Like the R_M and R_{BM} scalings, R_* can be written in terms of M_A and R_B (or R'_B) to give

$$R_* = \left(\frac{Z_d m_a}{Z_a m_d} \frac{1}{M_A^2} \right)^{1/3} R_B \quad (3.23)$$

$$= \left(\frac{3 Z_d m_a}{2 Z_a m_d} \frac{1}{M_A^2} \right)^{1/3} R'_B, \quad (3.24)$$

which is a form that can be plotted against the residuals between the experimental cavities and empirical- R_B in figure 3.4b (solid blue line for ambient H^+ and debris C^{+4} , dash-dot blue line for ambient H^+ and debris C^{+3} , teal dash-triple-dot teal line for ambient He^+ and debris C^{+4} , and solid red lines for ambient He^+ and debris C^{+3}).

Unlike the R_M and R_{BM} models, the R_* scaling does not include coupling of debris-energy into the ambient-ions, but provides an hypothesis for how the ambient-electrons contribute to the diamagnetic cavity formation. An agreement to this model in figure 3.4b would suggest a lack of debris-ambient coupling within the experiments and suggest an enhanced role of the ambient-electrons that is not traditionally considered. In figure 3.4b, the R_* trend lines create an envelope on the dataset with the trend lines associated with a singly-ionized hydrogen ambient-plasma providing a lower boundary line and the singly-ionized helium ambient-plasma providing the upper boundary line. However, helium data points are not associated with the upper boundary line, and visa-versa for the hydrogen data points. There is no correlation between the ambient-ion species and the R_* trend line that model expects. For this dataset, the R_* scaling does not define the behavior of the maximal cavity size.

For data points with $M_A \lesssim 1$ the residuals are clustered about zero with values ranging between ± 0.15 , indicting that the experimental cavities vary from between 15% larger than to 15% smaller than the empirical- R_B . This residual variation correlates to a significant variation in the amount of magnetic energy contained in the cavity, 1.52x the empirical- R_B based magnetic energy for a residual of +0.15 and 0.61x for a residual of -0.15. The R_M model (red line) predicts larger cavity sizes than the empirical- R_B , positive residuals, when $M_A \lesssim 1.23$, but the R_M model is only reasonable in the high Mach number limit ($M_A \gg 1$). Positive residuals are most likely a statistical variation due to variability in the the laser-to-

debris coupling efficiency α_{L2D} and/or energetic effects due to a finite diamagnetic current layer. All the scalings presented are based on a hard sphere cavity where the diamagnetic current layer is infinitely thin, but in real conditions the diamagnetic current layer has some finite thickness to it, see §3.4. A ‘soft’ sphere cavity (one with a finite thick diamagnetic current layer) of equivalent radius to a hard sphere cavity will contain less magnetic energy than the hard sphere cavity. Experimental cavities are of a ‘soft type,’ so by applying the R_B -scaling to them the amount of magnetic energy contained in them is being over reported. This has the affect of placing data points lower on the dependent axis in figure 3.3, which results in positive residuals. At this point, additional sub-Alfvénic to ‘marginal’ Mach numbers ($M_A \lesssim 1$) expansions with ‘weak’ compressions ($B_{peak}/B_o < 1.4$) need to be measured to build more statistical certainty in the R_B -scaling and incorporate the affects of finitely thick diamagnetic current layers.

For data points with $M_A > 1$, the residuals remain in a narrow, negative band with an upper limit of -0.1 and a lower limit of -0.2. The R_{BM} model, which has the best physical backing as compared to the other scalings (except for the R_B -scaling in the ‘weak’ cavity limit), encompasses the negative trend in the residuals as the Mach number increases. The R_{BM} model predicts a much smaller cavity than what is see experimentally, but that is due to an overemphasis of coupling energy into the ambient-ions. At these low Mach numbers the mechanism that couples energy into the ambient-ions is inconsistent and weak, so the assumptions of the R_{BM} model overpredicts the energy transfer into the ambient-ions. The important observation is that the experimental cavities do shrink as the compared to the vacuum case (R_B -scaling) as the Alfvénic Mach number increases.

As an example of this inconsistent coupling, the highest Mach number case (Run02 of the 2011 LaPD-Phoenix dataset) does not have a larger negative residual than the second largest Mach number data point (Run02 of the 2013 January LaPD-Phoenix dataset). This is not unexpected since conditions for this run are not favorable for coupling. The cavity size is a fraction of the ambient-ion inertial length ($0.8 c/\omega_{pi}$), the interaction/expansion time is less than a gyro-period ($\Omega_{ci} t \sim 0.75$), the magnetic piston is weak ($B_{peak}/B_o \simeq 1.37$),

and the laser energy used to drive the expansion is low (18.5 J).³ As discussed in §1.2, these conditions do not meet the criteria to provide enough interaction time or distance, as well as, not enough energy to energize the ambient-ions.

The experimental datasets show that debris-energy is being diverted from expelling the magnetic field as M_A increases, but M_A is not the only parameter that plays a role in diverting the energy. It is just one of the required conditions. There are still additional conditions at play which are not apparent at this time. Further data points need to be taken to build a better understanding of this energy diversion. Of the needed data points, there needs to be more vacuum and sub-Alfvénic ($M_A \lesssim 1$) expansions to build more confidence in the R_B -scaling, some high Mach number ($M_A > 1$), ‘strong’ ($B_{peak}/B_o > 1.5$) expansions to map out the negative drop in the residuals, and some high Mach number, ‘weak’ ($B_{peak}/B_o < 1.4$) expansions to investigate additional parameters that distinguish between the MOIC cavities and those that do work beyond expelling the magnetic field.

In summary, out of the presented scalings (R_B , R_M , R_{BM} , and R_*), the R_B -scaling and R_{BM} model make the most physical sense when compared to experiments. The R_B -scaling correlates well to the vacuum and low-Mach ($M_A \lesssim 1$), ‘weak’ ($B_{peak}/B_o < 1.4$) expansions, but does not completely encapsulate the high Mach number cases. The R_{BM} model does predict the cavity size departure from the R_B -scaling as the Mach number increases, but R_{BM} departure corresponds to a cavity size much smaller than experimentally seen. This is a result of the R_{BM} model overemphasizing how much energy is being coupled into the ambient-ions. There is also evidence of ‘other’ parameters, besides M_A , that affect how well cavities can couple energy into the ambient-ions. At this point, there is experimental evidence that debris-energy is being diverted away from expelling the magnetic field as the Alfvénic Mach number increases, but to how this is happening is still unclear. Any other avenues for this energy departure is still valid (ionizing neutrals, slipping of debris-ions, excitation of turbulence, etc.), but the comparison to the R_{BM} model suggest that energizing the ambient-ions into a directed flow is plausible. To confirm this coupling, additional evidence needs to

³For Run02 of 2011 $c/\omega_{pi} = 24$ cm, $f_{ci} = 105$ kHz, and $t_{expand} = 1.14$ μ s.

be gather, which is the focus of the following sections.

3.3 Cavity Deceleration

Section Highlights

1. The MOIC model establishes an equation-of-motion (equation 3.28) that dictates the cavity expansion for a magnetic only interacting cavity. This MOIC expansion is validated against vacuum and ‘weak’ ($B_{peak}/B_o \lesssim 1.4$) experimental cavity expansions.
2. Notable behaviors of the MOIC expansion:
 - (a) A MOIC expands in a normalized time of $V_{cav,o}t/R_c = 2.8$, where R_c is the maximal cavity radius and $V_{cav,o} = \partial_t[2r_c(t)]$ is the initial cavity diametrical expansion speed.
 - (b) During the “early phase” ($0.0 \leq V_{cav,o}t/R_c \lesssim 0.93$) of the expansion (first third), the MOIC expands to almost half of its maximal cavity size ($2r_c = 0.93R_c$), slows by 5% to $0.95V_{cav,o}$, and loses 10% of its initial debris-energy.
 - (c) In the last third of the expansion ($1.87 \lesssim V_{cav,o}t/R_c \leq 2.8$), the MOIC expands from $2r_c = 1.69R_c$ to $r_c = R_c$, loses the last 63% of its initial blow-off speed, and loses the last 40% of the initial debris-energy.
3. Some experimental runs (indicated in table 3.1) experience a period of ‘enhanced’ deceleration in the “early phase” of the expansion that is significantly stronger than the MOIC expansion. These periods of ‘enhanced’ deceleration correspond to the passage of the compression ramp X_{ramp} through the high ambient-density.
4. The experimental cases that do not experience ‘enhanced’ deceleration follow the MOIC expansion in the “early phase.”
5. The comparison between Run03 and Run04 of the 2013 January LaPD-Phoenix campaign show that having a high ambient-density is not a sufficient enough con-

dition to induce an interaction between the cavity and ambient-plasma, but the location of the density in the expansion is also crucial. To promote an interaction, it is better to place the high ambient-density towards the later half of the “early phase.”

The previous section (§3.2) established experimental evidence of debris-energy being diverted into pathways beyond expelling the magnetic field, but did not, and could not, indicate anything about how, when, or where in the expansion the initially contributing debris-ions give up their energy and/or become non-contributors. Assuming the majority of the expanding debris-ions are contained within the cavity edge, then the expansion speed of the cavity gives an indication of the total energy contained in the debris-ions and the deceleration of the cavity gives an indication of when the debris-energy is used or lost throughout the expansion. Using this axiom, the following section will attempt to characterize : (1) how these cavities decelerate and the different phases of the expansion, (2) how the expansions compare to an ideal vacuum expansion (a further evolution of the MOIC model), (3) determine if and how the expansion behavior correlates with the ambient conditions, and (4) identify any differences in the expansion behavior between the super-Alfvénic expansions and their slower counterparts. This section will achieve this by first defining how the time-dependent cavity size $2r_c(t)$ and cavity expansion speed $V_{cav}(t) = \partial_t[2r_c(t)]$ is calculated, then elaborate on the R_B -scaling from §3.2 to define an equation-of-motion for the cavity expansion to give a MOIC based theoretical trajectory for $2r_c(t)$, and then compare and contrast the two to analyze the expansion behavior.

Calculating the time-dependent experimental expansion speed of the cavity V_{cav} requires several steps. First, the cavity edge is tracked as it expands outward to give the time-dependent experimental cavity size $2r_c(t)$. As in §3.2, the cavity edge is defined to be the location where the background field is expelled by 50% ($B/B_o = 0.5$) when looking at the spatial profiles of B/B_o for a given time t . The tracking interpolates the data to calculate a $2r_c(t)$ value for each moment in time. Since the interpolation can lead to artificially erroneous

velocity calculations when calculating between adjacent time-steps, the velocity calculation will only be calculated using $2r_c$ values that match physical probe locations.

Two different bdot probe types were used to measure the cavity in the LaPD-Phoenix experiments; the 2011 campaign used a single-tip, 3-axis bdot probe while all the 2013 campaigns used a 5-tip, single-axis bdot probe. Depending on which probe was used, slightly different restrictions are imposed when calculating the expansion velocity. The 5-tip probe allows for five simultaneous measurements at five unique, 1 cm spaced positions for each laser shot. The 2013 campaigns had a 10 fold increase in laser energy (100-250 J) over the 2011 campaign, which is required to achieve the experimental goals, but has a significant drawback in that the laser energy can vary by several joules from shot-to-shot ($\pm 10\%$ of E_{ave}). This energy stability is excellent for this type of laser system, but the nominal degree of shot-to-shot energy fluctuation and non-ideal beam profile produces a significant fluctuation in the on target laser intensity. On target laser intensity affects both the amount of ablated mass and the debris-ion blow-off velocity.[34, 44, 55] The fluctuations are large enough that they produce a non-negligible variation in the initial blow-off velocity between shots for a given run. To avoid introducing error from these shot-to-shot fluctuations, the velocity calculations are only made between adjacent tips on the 5-tip probe; that is, velocity calculations for the 2013 campaigns are never performed using data from differing laser shots. In the 2011 campaign a single-tip bdot probe was deployed, so the expansion speed must be calculated using data measurements from differing laser shots. However, the significantly lower laser energy (~ 20 J) in this campaign has the upside of having a smaller variability in the shot-to-shot energy (± 1 J), resulting in imperceivable variations in the shot-to-shot datasets. Thus, the reproducibility is stable enough to generate sensible velocity calculations between laser shots, but the errors are a bit larger than those calculations made with the 5-tip bdot probe.

In the §3.2 only the initial and final energy states of the system were considered to derive the R_B -scaling, equation 3.6, but by considering the time-dependent system energy then one can develop an equation-of-motion for a MOIC expansion. This equation-of-motion can be

numerically solved to yield a comparable expansion profile to the experimental datasets. This model follows the work done by B. H. Ripin *et al.* (1983)[70] To begin, the time-dependent energy of the system for a spherical expansion is written as

$$E_{sys} = \frac{1}{2}m_d N_d [v_d(t)]^2 + \frac{B_o^2}{2\mu_o} \left\{ \frac{4}{3}\pi [r_b(t)]^3 \right\} \quad (3.25)$$

where E_{sys} is the energy of the system, $v_d(t)$ is the time-dependent debris expansion velocity ($v_d(0) = V_o$), and $r_b(t)$ is the time-dependent MOIC cavity radius (when $v_d(t_f) = 0$ then $r_b(t_f) = R_B$). Here it is taken that the debris expansion velocity is the same as the cavity edge expansion velocity ($v_d = \partial_t r_b$), since in an idealized cavity all the debris-ions are contained within the cavity edge. All physical processes are being neglected besides the expulsion of the magnetic field, the system energy remains constant throughout the expansion ($\partial_t E_{sys} = 0$). Taking the temporal-derivative of equation 3.25 yields the equation-of-motion for the cavity expansion in vacuum

$$g_{eff}(t) = -\frac{2\pi}{\mu_o m_d N_d} B_o^2 [r_b(t)]^2, \quad (3.26)$$

where $g_{eff}(t) = \partial_t^2 r_b(t)$ is the effective deceleration of the cavity caused by expelling the magnetic field. For a fixed set of initial plasma-parameters the deceleration of the cavity is solely dependent on its size and not its expansion speed. Early in the expansion the cavity pushes outward relatively unabated (a free expansion) because of the negligible deceleration resulting from the little energy required to expel the small volume of magnetic field. The cavity experiences the majority of its deceleration when it nears its maximum size because of the ever increasing amount of energy required to expel the ever increasing volume of magnetic field.

A generalized equation-of-motion is obtained by introducing a set of normalized coordi-

nates

$$\begin{aligned}
\tau &= \frac{V_o}{R_B} t \quad \rightarrow \quad \partial_\tau = \frac{R_B}{V_o} \partial_t \\
\chi &= \frac{r_b}{R_B} \\
\chi_v &= \partial_\tau \chi = \frac{1}{V_o} \partial_t r_b \\
\chi_g &= \partial_\tau^2 \chi = \frac{R_B}{V_o^2} \partial_t^2 r_b
\end{aligned} \tag{3.27}$$

which allows equation 3.26 to be rewritten as

$$\chi_g = \partial_\tau^2 \chi = -\frac{3}{2} \chi^2. \tag{3.28}$$

Under the normalized coordinates all vacuum expansions are identical and scalable by R_B and V_o . This generalized equation-of-motion is independent of whether R_B or R'_B is used for the magnetic-stopping radius. Under the R'_B framework there would be an extra factor of 3/2 out front of the second term in equation 3.25 to account for the energy in the magnetic compression, but that extra 3/2 factor is neutralized by the R'_B normalization.

Experimental expansions form spherical cavities, but the debris-plasma blow-off is more akin to a pseudo-conical expansion. In a pseudo-conical type of expansion, the debris blow-off speed is related to the cavity's diametrical expansion speed ($v_d(t) = \partial_t[2r_b(t)]$) opposed to the cavity's radial expansion speed ($v_d(t) = \partial_t[r_b(t)]$) as in the spherical model. Thus, is equation 3.28 still suitable for a pseudo-conical type expansion? Using the correct normalization, the pseudo-conical and spherical models produce the same equation-of-motion. The normalized coordinates in equation 3.27 use radial normalizations; that is, R_B is the maximal cavity radius and V_o is the initial radial expansion velocity $v_b(t = 0)$. In the pseudo-conical case, the initial radial expansion speed is now $V_o/2$ and implementing that change in the normalized coordinates gives equation 3.28 as the pseudo-conical equation-of-motion. This is true because the rate of which the magnetic energy grows

$$\frac{\partial}{\partial t} E_B(t) = \frac{2\pi}{\mu_o} B_o^2 [r_b(t)]^2 \frac{\partial}{\partial t} [r_b(t)] \tag{3.29}$$

is independent of which model is utilized.

It is straight forward to computationally solve equation 3.28 to give a vacuum (or MOIC) solution to the cavity expansion. Once the MOIC solution is validated against experimental vacuum and/or ‘weak’ cavity expansions, then the solution can act as a benchmark for all cavity expansions. This solution is useful since any deviation between it and an experimental expansion indicates the turn-on of new non-negligible physics. For example, if there is a sudden deceleration in the experimental cavity, then it is known that at that moment there is a sudden loss in the contributing debris-energy, which is not explained by the expulsion of the magnetic field. At this stage it is not known how that debris-energy is being lost (debris-ions slipping, debris-ambient coupling, etc.), but it does indicate where and when the loss is occurring. Correlating this deceleration with the ambient-plasma and/or magnetic field behavior can distinguish between whether debris-ions are slipping or if debris-ambient coupling is occurring. This will be the discussion in the following sections §3.4-§3.5

As in the validation for the R_B -scaling, the validation of the MOIC expansion is restricted to experimental cases that are not conducive for any other processes beyond expelling the magnetic field. Two experimental cases are selected for the validation: (1) a vacuum expansion in Run05 of the 2013 January LaPD-Phoenix campaign and (2) a low Mach number ($M_A \approx 0.7$), ‘weak’ ($B_{peak}/B_o \approx 1.22$) expansion in the Run03 of the 2011 LaPD-Phoenix campaign, see table 3.1 for details. The comparison is plotted in figure 3.5 using normalized coordinates, $X_{cav}(t)/R_c = 2\chi$ versus $V_{cav,o} t/R_c = 2\tau$. The MOIC expansion and experimental cases agree within the experimental uncertainty, with the MOIC model encompassing the time-dependent expansion of the cavity edge, as well as, predicting the expansion time. The MOIC model gives an expansion time of $2\tau = V_{cav,o} t/R_c = 2.8$, or $3.0 \pm 0.2 \mu s$ for Run05 and $0.6 \pm 0.2 \mu s$ for Run03. At this point it is reasonable to use the MOIC model as a benchmark against other expansion cases to identify differences from vacuum-like expansions.

In comparing the MOIC expansion profile to ‘strong’ cavity expansions ($B_{peak}/B_o \gtrsim 1.5$), two runs are selected in Run03 and Run04 of the 2013 January LaPD-Phoenix campaign. These two runs are selected because they have statistically identical laser, debris-plasma, and ambient-plasma parameters (see table 3.1), except for the placement of the high ambient-

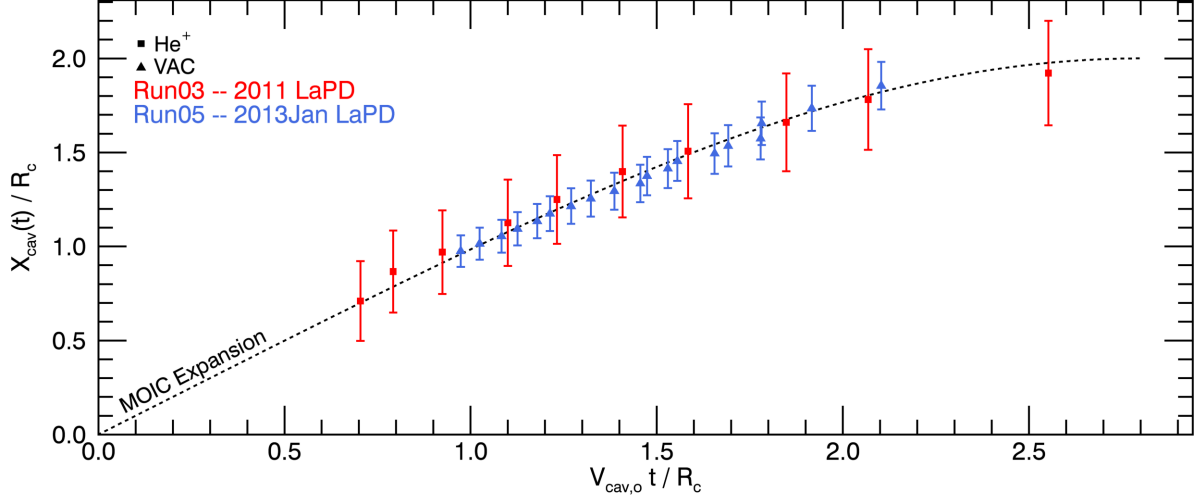


Figure 3.5: A comparison between the MOIC expansion (defined by equation 3.28) and a sub-Alfvénic ($M_A \approx 0.7$), ‘weak’ ($B_{peak}/B_o \approx 1.22$) expansion from the 2011 LaPD-Phoenix campaign (Run03), as well as, the vacuum expansion from the 2013 January LaPD-Phoenix campaign (Run05). For the comparison, the plot is displayed in normalized coordinates with $X_{cav}(t)$ normalized to the maximal cavity radius R_c (equivalent to 2χ) and the expansion time normalized to $R_c/V_{cav,o}$ (equivalent to 2τ), where $V_{cav,o}(= [\partial_t X_{cav}(t)]_{t=0})$ is the initial cavity expansion velocity.

density region with respect to the target. This placement of the high ambient-density region has a marked effect on the expansion, causing Run04 to experience an ‘enhanced’ deceleration that Run03 does not go through, see figure 3.6.

Run03 and Run04 share similar peak ambient-densities, $4.9 \times 10^{12} \text{ cm}^{-3}$ and $4.8 \times 10^{12} \text{ cm}^{-3}$ respectively, and similar average densities over $2R_c$, $2.5(\pm 0.7) \times 10^{12} \text{ cm}^{-3}$ and $2.4(\pm 0.6) \times 10^{12} \text{ cm}^{-3}$ respectively. The average Alfvén speed is also similar over $2R_c$, $3.1(\pm 1.0) \times 10^7 \text{ cm/s}$ for Run03 and $3.2(\pm 0.9) \times 10^7 \text{ cm/s}$ for Run04. The density shift in Run04 occurs from moving the LaB₆ cathode and anode 4 cm along the LaPD x-axis away from the target with respect to its position in Run03. This cathode translation causes the peak ambient-density to move 7 cm away from the target, due to the flaring of the background magnetic field between the experimental volume and the LaB₆ anode/cathode

region. The peak density shifts from 18.4 cm ($0.78R_c$) from the target in Run03 to 25.4 cm ($1.03R_c$) in Run04. The FWHM of the density profile is slightly narrower in Run04 than Run03, 19.0 cm ($0.77R_c$) versus 21.0 cm ($0.89R_c$), and the FWHM region is shifted from 9.4 – 30.4 cm ($0.40 - 1.29R_c$) in Run03 to 16.4 – 35.4 cm ($0.67 - 1.44R_c$) for Run04. In normalized coordinates, this corresponds to a shift of about a quarter of the maximal cavity radius.

Figure 3.6 shows the normalized expansion profiles for Run03 (figure 3.6a) and Run04 (figure 3.6b), $V_{cav}/V_{cav,o}$ ($= \chi_v$) versus $V_{cav,o}t/R_c$ ($= 2\tau$). The MOIC expansion profile is given as the red dashed-line and the red shaded region represents the expansion profiles given the uncertainty in $V_{cav,o}$ and R_c . Additionally, the ambient-density at locations $X_{cav}(t)$ (solid blue) and $X_{ramp}(t)$ (dashed blue) are plotted, where X_{ramp} is the location in the field compression ramp where $B = 0.5(B_{peak} + B_o)$.

Using the MOIC expansion as a reference, three time periods, or phases, can be established in attempts to make a link to the three stages of an expansion discussed in table 1.2. In table 1.2, the top row would correspond to a MOIC like expansion. A MOIC expands in a time frame of $2\tau_f = V_{cav,o}t_f/R_c = 2.8$, so dividing this expansion time into thirds the “early phase” ($0.0 \leq V_{cav,o}t/R_c \lesssim 0.93$), “intermediate phase” ($0.93 \lesssim V_{cav,o}t/R_c \lesssim 1.87$), and “late phase” ($1.87 \lesssim V_{cav,o}t/R_c \leq 2.8$) to the expansion can be defined.

In the “early phase” the MOIC expands to almost half of its maximal cavity size ($X_{cav} = 0.93R_c$), the expansion speed slows by 5% ($V_{cav} = 0.95V_{cav,o}$), and the debris-energy drops by 10% from its initial value. In this same phase Run03 slows by about 10% ($V_{cav} \simeq 0.90V_{cav,o}$), but with the experimental uncertainty this is not considered a meaningful difference over the MOIC model. However, Run04 slows considerably within this time period, going from $V_{cav} \simeq V_{cav,o}$ at $2\tau = 0.40 \pm 0.07$ ($t = 0.38 \pm 0.07 \mu s$) to $V_{cav} \simeq 0.6V_{cav,o}$ at $2\tau = 0.97 \pm 0.14$ ($t = 0.92 \pm 0.07 \mu s$). The slowing of the expansion speed is nearly linear over this ‘enhanced’

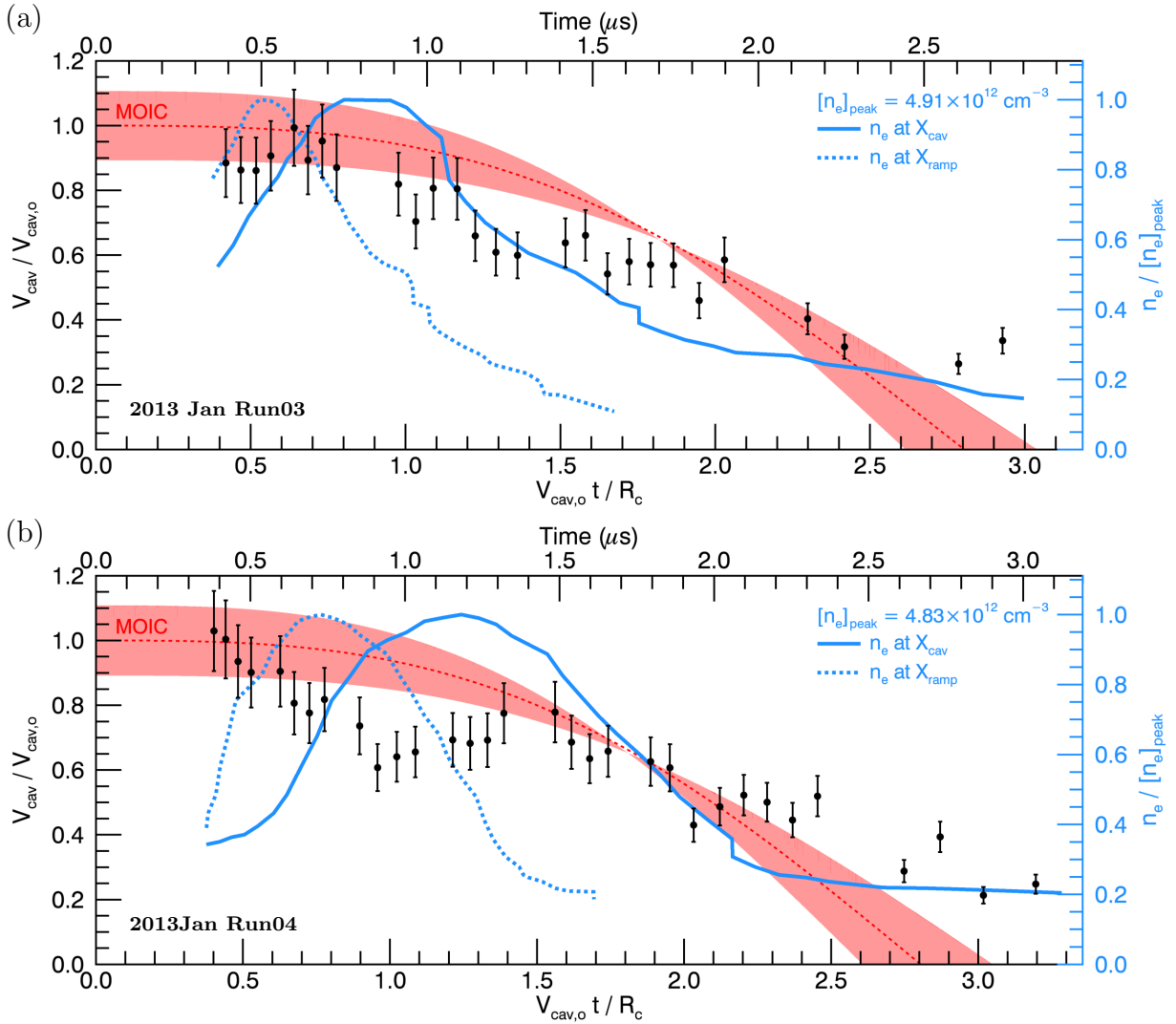


Figure 3.6: Figures (a) and (b) show the normalized cavity expansion, $V_{cav}/V_{cav,o}$ ($= \chi_v$) versus $V_{cav,o} t/R_c$ ($= 2\tau$), for Run03 and Run04, respectively, of the 2013 January LaPD-Phoenix campaign. The MOIC expansion profile is given as the red dashed-line (equation 3.28) and the red shaded region represents the expansion profiles given the uncertainty in $V_{cav,o}$ and R_c . The blue solid-line gives the ambient-density at $X_{cav}(t)$ and the blue dashed-line does the same for $X_{ramp}(t)$.

deceleration, providing an approximate normalized deceleration of

$$\begin{aligned}\chi_g &\approx \frac{\Delta\chi_v}{\Delta\tau} = \frac{\Delta(V_{cav}/V_{cav,o})}{^{1/2}\Delta(2\tau)} = \frac{2(0.6 - 1.0)}{0.97 - 0.40} \\ &\approx -1.40\end{aligned}\tag{3.30}$$

which is just over 4x stronger than the deceleration of the MOIC at the end of this phase, $(\chi_g)_{MOIC} = -1.5(0.93/2)^2 = -0.32$. In addition to Run04, this period of ‘enhanced’ deceleration is observed in several datasets, which are indicated in table 3.1. For now the discussion will remain with Run03 and Run04 of the 2013 January LaPD-Phoenix campaign, but the observations on Run04 are also seen in the other ‘enhanced’ deceleration cases to various degrees. In §3.6 the ‘enhanced’ deceleration of Run17 of the 2013 October LaPD-Phoenix campaign will be discussed.

At this point the ‘enhanced’ deceleration is only indicating that there is a rapid decrease in the expanding debris-energy that can not be contributed to expelling the magnetic field. It does not indicate what is causing this rapid energy loss. In order to connect this ‘enhanced’ deceleration with debris-ambient coupling it needs to be correlated with augmentation of the compression ramp as the cavity expands. Specifically, it needs to be correlated with steepening of the compression ramp and/or growth of the magnetic compression towards shock-like features. The following sections (§3.4-§3.5) present arguments to establish this connection, but the data in this section also provides evidence that the deceleration is likely due to an interaction with the cavity and ambient-plasma.

The ‘enhanced’ deceleration of Run04 occurs as the cavity compression passes through the high ambient-density, see figure 3.6b. The start of the ‘enhanced’ deceleration corresponds to the compression ramp X_{ramp} transitioning into the high ambient-density. The end of the ‘enhanced’ deceleration corresponds to X_{ramp} leaving the high density and the cavity edge X_{cav} entering the high density. The placement of the high density has a substantial affect on the expansion since by shifting the density two key things occur: (1) it allows the cavity and its compression to grow larger before it runs into the high density and (2) it increases the interaction time and distance between the cavity and high ambient-density.

$\Omega_{ci}/2\pi = 307 \text{ kHz}$		$n_e \geq 0.9 [n_e]_{\text{peak}} \text{ at } X_{\text{ramp}}$		$n_e \geq 0.5 [n_e]_{\text{peak}} \text{ at } X_{\text{ramp}}$	
		Run03	Run04	Run03	Run04
ΔX_{ramp}	cm	5.0	7.0	17.0	19.0
	R_c	0.21	0.29	0.72	0.77
$X_1 \rightarrow X_2$	cm	16.4 \rightarrow 21.4	21.4 \rightarrow 28.4	13.4 \rightarrow 30.4	16.4 \rightarrow 35.4
	R_c	0.69 \rightarrow 0.90	0.87 \rightarrow 1.16	0.57 \rightarrow 1.29	0.67 \rightarrow 1.44
Δt	μs	0.153	0.255	0.582	0.772
	$V_{\text{cav},o} t / R_c$	0.162	0.270	0.615	0.818
	$\Omega_{ci} t$	0.30	0.49	1.12	1.49
$t_1 \rightarrow t_2$	μs	0.448 \rightarrow 0.601	0.602 \rightarrow 0.857	0.355 \rightarrow 0.937	0.402 \rightarrow 1.174
	$V_{\text{cav},o} t / R_c$	0.474 \rightarrow 0.635	0.638 \rightarrow 0.908	0.375 \rightarrow 0.990	0.426 \rightarrow 1.243
	$\Omega_{ci} t$	0.86 \rightarrow 1.16	1.16 \rightarrow 1.65	0.68 \rightarrow 1.81	0.78 \rightarrow 2.26

Table 3.2: This table compares the time and distance it takes for the compression ramp X_{ramp} of Run03 and Run04 of the 2013 January LaPD-Phoenix campaign to transverse two different sections of ambient-plasma density, $n_e \geq 0.9 [n_e]_{\text{peak}}$ and $n_e \geq 0.5 [n_e]_{\text{peak}}$.

The MOIC expansion does not lose much energy or speed in the “early phase,” so there is not a significant penalty on the strength or speed of the magnetic piston by placing the density further away from the target, as long as the cavity still runs into the high density during this phase. Looking ahead to §3.4, the cavity’s magnetic field radial-dependence scales with the time-dependent cavity radius $r_c(t)$ like $(r_c/r)^3$ (see equations 3.55 and 3.56), where r is the radial location of interest for the magnetic field. This radial normalization implies that the magnetic field penetrates further upstream as the cavity size increases, which is consistent with experimental results. Since the density is positioned 7 cm further from the target (9.4 cm in Run03 versus 16.4 cm in Run04), the magnetic compression is allowed to penetrate about 5x $((16.4/9.4)^3 = 5.3)$ further upstream in Run04 than Run03 as the cavity edge runs into the high ambient-density. Thus, by positioning the high ambient-density further from the target, but still within the “early phase,” the compression is stronger over a larger scale length as it passes through the high density and the debris-energy is negligibly smaller.

The repositioning of the high ambient-density also makes for more favorable interaction time and length scales. At the end of the ‘enhanced’ deceleration in Run04 the ambient-density is 90% of its max value at the compression ramp X_{ramp} . Using this density value and $0.5 [n_e]_{peak}$ as references, the interaction distance and time of X_{ramp} can be compared between Run03 and Run04, see table 3.2. Looking at the FWHM of the density, X_{ramp} of both cavities take longer than a gyroperiod to transverse the density with Run04 taking 1.3x longer to do so, $1.12 \Omega_{ci} t$ for Run03 and $1.49 \Omega_{ci} t$ for Run04. Considering that $V_A \simeq 2.8 \times 10^7$ cm/s at $0.5 [n_e]_{peak}$ for both runs, the maximum possible Alfvénic Mach number is marginal ($M_A = V_{cav,o}/V_A \sim 0.9$) at this point. Moving to the density level of $0.9 [n_e]_{peak}$, the Alfvén speed drops to $\sim 2.1 \times 10^7$ cm/s, giving a maximum possible Mach number of $M_A \sim 1.2$. Here, X_{ramp} of Run04 interacts with the ambient-plasma for a time of $0.49 \Omega_{ci} t$ and a distance of $0.5 \Delta X/\rho'_a$,⁴ which is 1.6x longer and 1.4x further than Run03. These values are still not good enough to satisfy the conditions in §1.2 for shock generation, but, by slightly shifting the ambient-plasma density away from the target and later in the “early phase” of the expansion, the conditions are significantly improved over those of Run03.

In the “intermediate phase” ($0.93 \lesssim V_{cav,o} t/R_c \lesssim 1.87$) the MOIC expands to 85% of its maximal size ($X_{cav} = 1.69 R_c$), the expansion speed slows from $0.95 V_{cav,o}$ at the beginning of the phase to $0.63 V_{cav,o}$ at the end, and the debris-energy drops to 40% of its initial value. Looking at Run03, there is a similar drop in the expansion speed to the MOIC, going from $\sim 0.85 V_{cav,o}$ at the start of the phase to $\sim 0.6 V_{cav,o}$ at the end of the phase. However, the slowing does not occur in the same manner as the MOIC does. The majority of the slowing occurs as X_{cav} exits the high ambient-density region and the expansion speed remains relatively constant until the end of the phase. Looking at Run04, the expansion speed recovers a bit before it slows again. At the beginning of the phase, Run04’s expansion speed is $\sim 0.6 V_{cav,o}$ and recovers to $\sim 0.75 V_{cav,o}$ by the time $V_{cav,o} t/R_c \sim 1.4$, when X_{cav} exits the high ambient-density, and then returns to $\sim 0.6 V_{cav,o}$ by the end of the phase. Out

⁴The gyroperiod for Run03 and Run04 is $\Omega_{ci}/2\pi = 307$ kHz. The energized gyro-radius $\rho'_a = V_{cav,o}/\Omega_{ci}$ is ~ 13.0 cm for Run03 and ~ 13.5 cm for Run04.

of the cases that exhibit ‘enhanced’ deceleration, Run02 and Run04 of the 2013 January LaPD-Phoenix campaign show a recovery in the expansion speed after the deceleration, whereas, Run01 of the 2013 June and Run17 of the 2013 October LaPD-Phoenix campaigns show a constant expansion speed after the deceleration. Either a recovery in the expansion speed or a constant expansion speed in this phase suggests there is an unknown mechanism driving the cavity forward and/or some kind of geometric/dispersive effect associated with a broadening of the cavity edge, diamagnetic current, that shows a high expansion speed even though the magnetic energy is increasing. Either way, the expansion behavior of Run03 and Run04 indicated an interplay between the cavity and the high ambient-density that, while not driving a shock, is a form of debris-ambient coupling.

In the “late phase” ($1.87 \lesssim V_{cav,o} t/R_c \leq 2.8$) the MOIC reaches its maximal size and abruptly loses the last 63% of its initial expansion speed and 40% of its initial debris-energy. Both experimental cases deviate significantly from the MOIC in this case. They lose the same amount of expansion speed, going from $\sim 0.6V_{cav,o}$ to zero, but do it more slowly. It takes Run03 till $2\tau \sim 3.0$ to stop expanding and Run04 till $2\tau \sim 3.3$. This is likely due to, but unverified, geometric effects caused by dissipation of the diamagnetic current layer at the end of the expansion that the MOIC does not include. As a cavity comes to an end its diamagnetic current layer broadens due to dissipation. This causes the cavity edge to be less defined and, thus, decreases the rate in which the magnetic energy builds and weakens the deceleration. While not pertinent to shock formation, this area could be useful in understanding the collapse and dissipation of the cavity.

In summary, the MOIC model provides an equation-of-motion (equation 3.28) for a vacuum-like cavity expansion that is verified against vacuum and ‘weak’ ($B_{peak}/B_o \lesssim 1.4$) experimental cavity expansions. Using the MOIC expansion as a benchmark, it can be used to analyze the expansion behavior of ‘strong’ ($B_{peak}/B_o \gtrsim 1.5$) cavity expansions. During the “early phase” ($0.0 \leq V_{cav,o} t/R_c \lesssim 0.93$) of the cavity expansion, a handful of experimental cases (indicated in table 3.1) show a period of ‘enhanced’ deceleration that is significantly stronger than the MOIC expansion. Those that do not experience this ‘enhanced’ decelera-

tion follow the MOIC expansion. This period of ‘enhanced’ deceleration corresponds to the passage of the compression ramp X_{ramp} through the high ambient-density. The comparison between Run03 and Run04 of the 2013 January LaPD-Phoenix campaign indicates that having a high ambient-density is not a sufficient enough condition to induce an interaction between the cavity and ambient-plasma, but the density’s location in the expansion is also crucial. To promote an interaction, it is better to place the high ambient-density towards the later half of the “early phase” of the expansion. The experimental expansions are highly suggestive that the ‘enhanced’ deceleration is related to some form of debris-ambient interaction, but is not definitive. In order to connect the ‘enhanced’ deceleration with debris-ambient coupling relevant to shock formation, the period of ‘enhanced’ deceleration needs to be correlated with the augmentation of the compression as the cavity expands. The arguments associated with these correlations are present in section 3.4 to 3.5.

3.4 Cavity Magnetic Field: Models versus Experiment

Section Highlights

1. The magnetic field of a diamagnetic cavity can be represented by a single ‘ideal’ magnetized sphere (iMS) or a weighted sum of ‘ideal’ magnetized spheres (siMS). When the debris-plasma has negligible resistivity, super-conductive, then it can be modeled by an iMS. If the debris-plasma possesses some resistivity, then the diamagnetic current layer broadens out and a weighted siMS model must be used to approximate the diamagnetic current layer.
2. Since the model is developed for non-relativistic cavity expansions, the magnetic field is identical for a stationary and expanding iMS.
3. If a cavity can be modeled by only a diamagnetic current layer (no matter what the current distribution), then outside the current layer the magnetic field will decay away from the cavity like $(r_{siMS}/r)^3$ where r_{siMS} is an effective cavity radius defined by the diamagnetic current distribution (see equation 3.66).

4. For ‘weak’ cavities ($B_{peak}/B_o < (3 - \alpha)/2$ where α is the ratio of the magnetic field inside the cavity to the background), then early in the expansion the cavity can be represented by a normal-weight siMS (a sum of spheres with gaussian weighting).
5. ‘Strong’ cavities ($B_{peak}/B_o > (3 - \alpha)/2$) can not be modeled this way. They tend to have significant augmentation of the compression (growth of the peak and/or steepening of the ramp) that the iMS and siMS schemes can not duplicate.

The previous two sections (§3.2 and §3.3) approached the experiment from an energetics perspective, whereas, this section, and the following (§3.5-§3.6), will approach the experiments from a magnetics perspective. While measurements of particle trajectories and flows provide more direct understanding of the inner workings of the expansion behavior, the measurements were not a feasible endeavor at the time of these campaigns. Magnetic field measurements are the easiest to acquired, and by examining how the field structure evolves throughout the expansion one can assess when, where, and how the cavity is interacting with the ambient-plasma. To achieve this analysis, first, the MOIC model will be developed further to give an analytical solution to the electromagnetic fields of the cavity. These fields will be established as benchmarks once they are verified against ‘weak’ ($B_{peak}/B_o \lesssim 1.4$) experimental cavity expansions. Then, in comparing these benchmark fields with the ‘enhanced’ decelerated cases in table 3.1, magnetic field characteristics that deviate from a simple diamagnetic cavity can be isolated and investigated further.

In the MOIC model there are two physical interpretations for the structure of a diamagnetic cavity.

1. An infinitely thin, neutral spherical shell of radius R_c composed of both positive and negative charge carriers. One of the charge carrier species, positive or negative, is spinning at an angular frequency ω . This spinning charge species constitutes a surface current on the sphere that generates a constant magnetic field inside the sphere and an augmented field outside, see David J. Griffiths[33] example 5.11. In the experimental picture, the negative charge species, electrons, are spinning about \hat{z} to produce a

diamagnetic surface current that expels a background magnetic field $\mathbf{B}_o = B_o \hat{\mathbf{z}}$.

2. A sphere of material containing a constant magnetization \mathbf{M}_o , see David J. Griffiths[33] example 6.1 and John D. Jackson[40] §5.10-5.11. The constant magnetization \mathbf{M}_o creates a constant magnetic field inside the sphere equivalent to $\frac{2}{3}\mu_o M_o$ and an augmented field outside.

The first physical scenario represents the experiment, but both pictures produce the same analytical solution for the magnetic field. This is true since the free current of the first scenario shares the same proportionality to the spatial coordinates as the bound current for the second scenario. The free current of the first scenario looks like

$$\begin{aligned} \mathbf{J}_f &= \frac{Q\omega}{4\pi R_c} \delta(r - R_c) \sin \theta \hat{\phi} \\ &\propto \delta(r - R_c) \sin \theta \hat{\phi} \end{aligned} \quad (3.31)$$

where $\boldsymbol{\omega} = \omega \hat{\mathbf{z}}$ and Q is the total, uniformity distributed spinning charge on the shell of radius R_c ; whereas, the bound current of the second scenario is given by (equation 3.42)

$$\begin{aligned} \mathbf{J}_b &= \nabla \times \mathbf{M}_o = M_o \delta(r - R_c) \sin \theta \hat{\phi} \\ &\propto \delta(r - R_c) \sin \theta \hat{\phi} \end{aligned} \quad (3.32)$$

where $\mathbf{M}_o = M_o \hat{\mathbf{z}}$.⁵ Since it is simpler to solve the magnetized sphere (MS) problem, that is what will be done here.

Both Griffiths[33] and Jackson[40] provide solutions to the stationary MS problem. The discussion to follow will present highlights of the derivation and extrapolate it towards an expanding MS. In addition to the single ‘ideal’ magnetized sphere (iMS), a sum of ‘ideal’ magnetized spheres (siMS) will be considered to approximate non-ideal diamagnetic current layers. A full mathematical derivation of the MS is provided in Appendix B, along with the inductive electric field of an expanding iMS, the energy stored within the fields, and the

⁵A similar behavior in the diamagnetic current layer is observed by A. Collette (2010)[17], see §4 for full discussion.

$\mathbf{E} \times \mathbf{B}$ -drifts associated with the fields. It is left to the reader to go through this at his or her discretion.

The problem starts by envisioning a magnetized sphere of radius R_c and constant magnetization \mathbf{M}_o , given by

$$\mathbf{M}_o = \begin{cases} M_o \hat{\mathbf{z}} & r \leq R_c \\ 0 & r > R_c \end{cases}, \quad (3.33)$$

embedded in a constant background magnetic field of $\mathbf{B}_o = B_o \hat{\mathbf{z}}$. The derivation first solves for the magnetic field of the MS and adds in \mathbf{B}_o afterwards, since $\nabla \times \mathbf{B}_o = 0$ and $\nabla \cdot \mathbf{B}_o = 0$. Assuming negligible free current $\mathbf{J}_f = 0$ and no polarization $\mathbf{P} = 0$ (vacuum conditions), then Ampère's Law can be written as

$$\nabla \times \mathbf{B} - \mu_o \epsilon_o \frac{\partial}{\partial t} \mathbf{E} = \mu_o \mathbf{J}_b \quad (3.34)$$

where $\mathbf{J}_b = \nabla \times \mathbf{M}_o$ is the bound current associated with the MS. This form of Ampère's Law is simpler to solve by introducing the scalar potential (Φ) and vector potential (\mathbf{A}), as well as, a proper gauge for the fields. Using the potentials, the fields can be written as

$$\mathbf{B} = \nabla \times \mathbf{A} \quad (3.35)$$

$$\mathbf{E} = -\nabla \Phi - \frac{\partial}{\partial t} \mathbf{A} \quad (3.36)$$

and selecting the Lorentz gauge

$$\nabla \cdot \mathbf{A} = -\mu_o \epsilon_o \frac{\partial}{\partial t} \Phi, \quad (3.37)$$

then Ampère's Law can be written in terms of just the vector potential and bound current

$$\square^2 \mathbf{A} = [\nabla^2 - \mu_o \epsilon_o \partial_t^2] \mathbf{A} = -\mu_o \mathbf{J}_b. \quad (3.38)$$

Under the quasi-static condition ($\partial_t \rightarrow 0$) the Lorentz gauge reduces to the Coulomb gauge ($\nabla \cdot \mathbf{A} = 0$) and the displacement current goes to zero ($\partial_t \mathbf{E} \rightarrow 0$, $\partial_t^2 \mathbf{A} \rightarrow 0$). This condition represents the stationary iMS and is the problem addressed in Griffiths[33] and Jackson[40]. Without imposing the quasi-static conditions, the integral form of equation 3.38 is written as

$$\mathbf{A}(\mathbf{r}, t) = \frac{\mu_o}{4\pi} \int \frac{\mathbf{J}_b(\mathbf{r}', t_r)}{|\mathbf{r} - \mathbf{r}'|} d^3 r' \quad (3.39)$$

where \mathbf{r}' represents the integration coordinates, \mathbf{r} represents the non-integration coordinates (or points-of-interest), and $t_r \equiv t - |\mathbf{r} - \mathbf{r}'|/c$ is the retarded time. This form is valid for both a stationary and an expanding iMS. The magnetization of a stationary iMS is time-independent $\mathbf{M}_o = \mathbf{M}_o(\mathbf{r}')$ and, thus, the bound current is time-independent $\mathbf{J}_b(\mathbf{r}', t_r) = \mathbf{J}_b(\mathbf{r}') = \nabla' \times \mathbf{M}_o(\mathbf{r}')$, which is not the case for an expanding iMS. However, it can be argued that $t_r \approx t$ for the experimental conditions and, thus, eliminating the $|\mathbf{r} - \mathbf{r}'|/c$ dependence in the temporal component of the integrand. The largest experimental size is 60 cm, so the longest time for the electromagnetic fields to be communicated across the system is $|\mathbf{r} - \mathbf{r}'|/c = (60 \text{ cm})/c \sim 2 \text{ ns}$. Given that the expansion speed is highly non-relativistic $V_{cav,o}/c \sim (10^7 \text{ cm/s})/c \sim 10^{-3}$, the fields are effectively communicated instantaneously in the experiment; thus, allowing the retarded time to be approximated as the current time $t_r \approx t$. In making this approximation, the bound current of the expanding iMS becomes identical to the stationary iMS, except for replacing the time-independent cavity radius R_c with the time-dependent cavity radius $r_c = r_c(t)$. This is seen by writing the magnetization \mathbf{M}_o in terms of a Heaviside function

$$H(x) = \begin{cases} 0 & x < 0 \\ 1 & x \geq 0 \end{cases}, \quad (3.40)$$

which yields

$$\begin{aligned} \mathbf{M}_o &= M_o[1 - H(r - r_c(t))]\hat{\mathbf{z}} \\ &= M_o[1 - H(r - r_c(t))](\cos \theta \hat{\mathbf{r}} - \sin \theta \hat{\boldsymbol{\theta}}). \end{aligned} \quad (3.41)$$

The bound current of the expanding iMS is given by

$$\begin{aligned} \mathbf{J}_b(\mathbf{r}, t) &= \nabla \times \mathbf{M}_o(\mathbf{r}, t) \\ &= M_o \sin \theta \left\{ \frac{\partial}{\partial r} H(r - r_c(t)) \right\} \hat{\boldsymbol{\phi}} \\ &= M_o \sin \theta \delta(r - r_c(t)) \hat{\boldsymbol{\phi}} \\ \mathbf{J}_b(\mathbf{r}, t) &= \delta(r - r_c(t)) M_o \hat{\mathbf{z}} \times \hat{\mathbf{r}}. \end{aligned} \quad (3.42)$$

Thus, the solution to equation 3.39 is identical for both the stationary and non-relativistic expanding iMS.

Making the non-relativistic approximation $t_r \approx t$ and using equation 3.42 for the bound current, then equation 3.39 can be solved analytically (see Appendix B.1) to give a solution to the vector potential

$$\mathbf{A}(\mathbf{r}, t) = \frac{1}{3}\mu_o M_o \begin{cases} r \sin \theta \hat{\phi} & \text{for } r < r_c \\ \left(\frac{r_c(t)}{r}\right)^3 r \sin \theta \hat{\phi} & \text{for } r \geq r_c \end{cases}. \quad (3.43)$$

Using equation 3.35, the magnetic field of the iMS is

$$\mathbf{B}_{\text{MS}}(\mathbf{r}, t) = \nabla \times \mathbf{A}(\mathbf{r}, t)$$

$$B_{MS,r} = \begin{cases} \frac{2}{3}\mu_o M_o \cos \theta & r < r_c \\ \frac{2}{3}\mu_o M_o \left(\frac{r_c(t)}{r}\right)^3 \cos \theta & r \geq r_c \end{cases} \quad (3.44)$$

$$B_{MS,\theta} = \begin{cases} -\frac{2}{3}\mu_o M_o \sin \theta & r < r_c \\ \frac{1}{3}\mu_o M_o \left(\frac{r_c(t)}{r}\right)^3 \sin \theta & r \geq r_c \end{cases} \quad (3.45)$$

$$B_{MS,\phi} = 0 \quad (3.46)$$

and the total magnetic field is given by

$$\mathbf{B}(\mathbf{r}, t) = B_o \hat{\mathbf{z}} + \mathbf{B}_{\text{MS}}(\mathbf{r}, t). \quad (3.47)$$

M_o can be eliminated from \mathbf{B}_{MS} by writing it in terms of $\alpha (= B_{\text{inside}}/B_o)$ and B_o , where α is the ratio of the total magnetic field inside the MS (cavity) to the background magnetic field. This allows equation 3.47 to be written into a more convenient form for comparison to experiments. The iMS portion of the magnetic field inside the MS is $\mathbf{B}_{\text{MS}} = \frac{2}{3}\mu_o M_o \hat{\mathbf{z}}$, so M_o can be expressed in terms of α and B_o as

$$B_{\text{inside}} = \alpha B_o = B_o + \frac{2}{3}\mu_o M_o$$

$$\implies M_o = \frac{3(\alpha - 1)}{2\mu_o} B_o. \quad (3.48)$$

Using this expression for M_o , equations 3.44 and 3.45 can be written in terms of α , B_o , and $r_c(t)$ to give

$$B_r = \begin{cases} \alpha B_o \cos \theta & r < r_c \\ \left[1 + (\alpha - 1) \left(\frac{r_c(t)}{r} \right)^3 \right] B_o \cos \theta & r \geq r_c \end{cases} \quad (3.49)$$

$$B_\theta = \begin{cases} -\alpha B_o \sin \theta & r < r_c \\ - \left[1 - \frac{1}{2}(\alpha - 1) \left(\frac{r_c(t)}{r} \right)^3 \right] B_o \sin \theta & r \geq r_c \end{cases} \quad (3.50)$$

$$B_\phi = 0. \quad (3.51)$$

Experimental cavities typically fully expel the background magnetic field ($B_{inside} = 0$) which corresponds to $\alpha = 0$ and an iMS magnetic field structure of

$$\alpha = 0$$

$$B_r = \begin{cases} 0 & r < r_c \\ \left[1 - \left(\frac{r_c(t)}{r} \right)^3 \right] B_o \cos \theta & r \geq r_c \end{cases} \quad (3.52)$$

$$B_\theta = \begin{cases} 0 & r < r_c \\ - \left[1 + \frac{1}{2} \left(\frac{r_c(t)}{r} \right)^3 \right] B_o \sin \theta & r \geq r_c \end{cases} \quad (3.53)$$

$$B_\phi = 0. \quad (3.54)$$

The magnetic field can also be written in terms of the parallel and perpendicular components to the background field. The parallel component (compressional component) is defined as $B_{\parallel} = \mathbf{B} \cdot \hat{\mathbf{z}}$ and, without loss of generality due to $B_\phi = 0$, the perpendicular component (shear component) can be defined as $B_{\perp} = \mathbf{B} \cdot \hat{\mathbf{x}}$. This gives B_{\parallel} and B_{\perp} of an α -zero iMS as

$$B_{\parallel} = \mathbf{B} \cdot \hat{\mathbf{z}} = \begin{cases} 0 & r < r_c \\ \left[1 + \frac{1}{2}(1 - 3 \cos^2 \theta) \left(\frac{r_c(t)}{r} \right)^3 \right] B_o & r \geq r_c \end{cases} \quad (3.55)$$

$$B_{\perp} = \mathbf{B} \cdot \hat{\mathbf{x}} = \begin{cases} 0 & r < r_c \\ -\frac{3}{4} \sin(2\theta) \left(\frac{r_c(t)}{r} \right)^3 B_o & r \geq r_c \end{cases} \quad (3.56)$$

and showcases that the fields outside the iMS decays like $(r_c/r)^3$. The radial dependence of the magnetic field is normalized to the cavity radius r_c , causing larger cavities to produce fields that penetrate further upstream with respect to the ambient-plasma scale lengths. This increased penetration leads to larger interaction length and time scales between the cavity and the ambient-plasma.

Figures 3.7a and 3.7b, respectively, show a contour plot for the compressional and shear components of the iMS magnetic field. The dash-dot line represents the contour level of $B_z/B_o = B_{\parallel}/B_o = 0.5$, which has been the experimental definition for the location of $r_c(t)$ up to this point. In addition to the $(r_c/r)^3$ dependence for $r \geq r_c$, the iMS reaches a peak compression of $B_{peak}/B_o = 1.5$ at $r = r_c$ and $\theta = \pi/2$. The compressional component goes through a transition angle in which it goes from being compressional to expulsive and a strong shear component arises towards the poles of the cavity. The compressional transition occurs at angles for $\cos \theta = \pm 1/\sqrt{3}$ ($\theta \simeq 54.7^\circ$ and 125.3°), so B_{\parallel} is compressional near the equator of the cavity ($54.7^\circ < \theta < 125.3^\circ$) and expulsive near the poles ($0^\circ \geq \theta < 54.7^\circ$ and $125.3^\circ < \theta \leq 180^\circ$). Consequently, when determining the cavity's sphericity from the magnetic field, this expulsion at the poles gives the illusion that the cavity is oblong when in fact the diamagnetic current is spherical. The shear component is zero at the poles and equator of the cavity ($\theta = 0, \pi/2, \text{ and } \pi$) and reaches a peak value of $B/B_o = -0.75$ (0.75) at $\theta = \pi/4$ ($3\pi/4$) and $r = r_c$. The direction of the shear component changes depending on the hemisphere of the cavity, with the shear component pointing towards the cavity axis in the $+\hat{\mathbf{z}}$ hemisphere and away in the $-\hat{\mathbf{z}}$ hemisphere. The LaPD-Phoenix experiments focus on the compressional component near $\theta = \pi/2$, but the shear component of the iMS model could provide some insight for future studies on wave generation. Other studies[10, 18] have seen excitation of shear waves along B_o , of which, the iMS shear component could be a potential source.⁶

⁶The shear component has a spatial correlation with the inductive electric field (see Appendix B.2 and figure B.1) that drives $\mathbf{E} \times \mathbf{B}$ -drifts (see Appendix B.4 and figure B.2) on the ambient-electrons. The $\mathbf{E} \times \mathbf{B}$ -drift ahead of the shear magnetic field results in an electron drift along $\hat{\mathbf{z}}$ and away from the cavity.

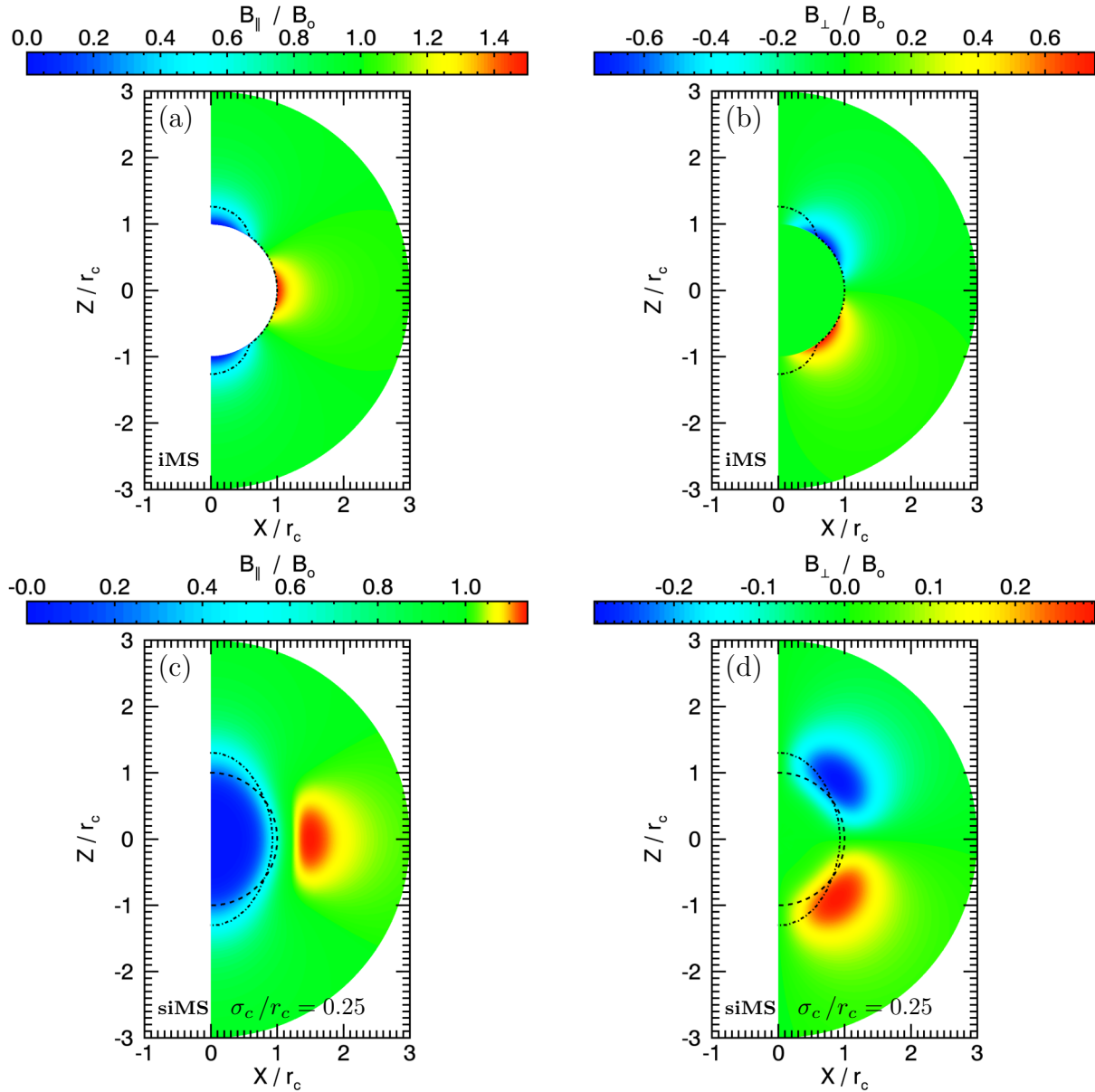


Figure 3.7: All figures represent the magnetic field structure for a diamagnetic cavity that fully expels ($\alpha = 0$) the background magnetic field $B_0 \hat{z}$. Figure (a) and (b) give the compressional and shear components, respectively, for an iMS; whereas, figures (c) and (d) do the same for a normal-weighted siMS with $\sigma_c/r_c = 0.25$. The magnetic field is normalized to B_0 and the spatial coordinates are normalized to the cavity radius r_c . The dash-dot line represents the magnetic field contour level of $B/B_0 = 0.5$ and the dashed line gives $r = r_c$.

The iMS is a best case, ideal scenario for the diamagnetic cavity. In reality the diamagnetic current layer is not infinitely thin, but possesses some radial distribution. In attempts to model this distribution, the cavity can be assumed to be composed of several magnetized spheres, or a sum of ‘ideal’ magnetized spheres (siMS). From equation 3.42 it can be seen that the magnetization of each sphere represents the strength of the diamagnetic current; thus, the distribution of the diamagnetic current layer can be modeled by controlling the magnetization of each sphere in the siMS. Without knowing details of an experimental diamagnetic current distribution, two simple models can be used as a starting point. First, an equal weighting of all the spheres and, secondly, a normal weighting (gaussian distribution) to the spheres. The equal-weight siMS represents a diamagnetic current layer of constant value over some radial width w_c centered about r_c . However, this provides a very discrete magnetic profile (B versus X) that does not represent the softer transitions of the cavity edge seen in figure 3.1c, whereas the normal-weight siMS scheme can.

The normal-weight siMS models the diamagnetic current layer by adding together N_S magnetized spheres that are evenly distributed over the range $r_c - 3\sigma_c \leq r \leq r_c + 3\sigma_c$, where r_c is the central radius to the normal distribution and σ_c is the standard deviation to the normal distribution. It is imposed that all the current must lie within $3\sigma_c$ about r_c , which constrains σ_c to be less than or equal to $r_c/3$ ($0 \leq \sigma_c/r_c \leq 1/3$). The magnetization of the n^{th} sphere in the distribution is given by

$$\begin{aligned} M_n &= \frac{1}{\mathcal{Z}} \exp \left\{ -\frac{(r_n - r_c)^2}{2\sigma_c^2} \right\} \\ &= \frac{1}{\mathcal{Z}} \exp \left\{ -\frac{9}{2} \left[\frac{2n}{N_S - 1} - 1 \right]^2 \right\} \end{aligned} \quad (3.57)$$

where $n \in [0, 1, \dots, N_S - 1]$, \mathcal{Z} is a normalization constant for the distribution, and r_n is the

radial location of the n^{th} sphere given by

$$\begin{aligned}
r_n &= n \cdot \Delta r + r_{min} \\
&= n \left(\frac{6\sigma_c}{N_S - 1} \right) + (r_c - 3\sigma_c) \\
&= r_c \left[1 + 3 \left(\frac{\sigma_c}{r_c} \right) \left(\frac{2n}{N_S - 1} - 1 \right) \right].
\end{aligned} \tag{3.58}$$

Going back to equation 3.48, the normalization constant can be defined in terms of the cavity expulsion factor α . Inside the cavity ($r < r_c - 3\sigma_c$) the total magnetic field is written as

$$\alpha B_o = B_o + \sum_{n=0}^{N_S-1} \frac{2}{3} \mu_o M_n \tag{3.59}$$

which allows the normalization constant to be written as follows

$$\mathcal{Z} = \frac{2\mu_o}{3(\alpha - 1)B_o} \mathcal{S}(N_S) \tag{3.60}$$

where

$$\mathcal{S}(N_S) = \sum_{n=0}^{N_S-1} \exp \left\{ -\frac{9}{2} \left[\frac{2n}{N_S - 1} - 1 \right]^2 \right\}. \tag{3.61}$$

This gives the magnetization of the n^{th} sphere,

$$M_n = \frac{3}{2\mu_o} \frac{(\alpha - 1)B_o}{\mathcal{S}(N_S)} \exp \left\{ -\frac{9}{2} \left[\frac{2n}{N_S - 1} - 1 \right]^2 \right\}, \tag{3.62}$$

in terms of B_o , α , and the sum over the exponential factors $\mathcal{S}(N_S)$. There is no clean form for the magnetic field inside the current layer ($r_c - 3\sigma_c \leq r \leq r_c + 3\sigma_c$), but a clean expression can be obtained for the region outside the current layer ($r \geq r_c + 3\sigma_c$). For $r \geq r_c + 3\sigma_c$ the

normal-weight siMS magnetic field components (without B_o) are written as

$$\begin{aligned} B_{siMS,r} &= \sum_{n=0}^{N_S-1} \frac{2}{3} \mu_o M_n \left(\frac{r_n}{r} \right)^3 \cos \theta \\ &= (\alpha - 1) \frac{B_o \cos \theta}{r^3} \left[\frac{1}{\mathcal{S}(N_S)} \sum_{n=0}^{N_S-1} r_n^3 \exp \left\{ -\frac{(r_n - r_c)^2}{2\sigma_c^2} \right\} \right] \end{aligned} \quad (3.63)$$

$$\begin{aligned} B_{siMS,\theta} &= \sum_{n=0}^{N_S-1} \frac{1}{3} \mu_o M_n \left(\frac{r_n}{r} \right)^3 \sin \theta \\ &= \frac{1}{2} (\alpha - 1) \frac{B_o \sin \theta}{r^3} \left[\frac{1}{\mathcal{S}(N_S)} \sum_{n=0}^{N_S-1} r_n^3 \exp \left\{ -\frac{(r_n - r_c)^2}{2\sigma_c^2} \right\} \right] \end{aligned} \quad (3.64)$$

$$B_{siMS,\phi} = 0. \quad (3.65)$$

Outside the current layer the siMS still exhibits the $1/r^3$ decay seen in the iMS model, but the radial normalization is no longer r_c but some effective cavity radius r_{siMS} . Examining equations 3.63 and 3.64, this $1/r^3$ decay behavior is independent of the siMS model since $1/r^3$ will always be factored out of the sum. Meaning, any cavity whose current structure is dominated by a spherical diamagnetic current (or paramagnetic current) will show a $1/r^3$ decay of the magnetic field outside the current structure, and its radial normalization will be some effective cavity radius that is dependent on the current distribution. For the normal-weight siMS, the effective cavity radius is given as

$$\begin{aligned} r_{siMS}^3 &= \frac{1}{\mathcal{S}(N_S)} \sum_{n=0}^{N_S-1} r_n^3 \exp \left\{ -\frac{(r_n - r_c)^2}{2\sigma_c^2} \right\} \\ &= \frac{r_c^3}{\mathcal{S}(N_S)} \sum_{n=0}^{N_S-1} \left[1 + 3 \left(\frac{\sigma_c}{r_c} \right) \left(\frac{2n}{N_S - 1} - 1 \right) \right]^3 \exp \left\{ -\frac{9}{2} \left(\frac{2n}{N_S - 1} - 1 \right)^2 \right\} \end{aligned} \quad (3.66)$$

where $r_{siMS} \rightarrow r_c$ when $\sigma_c/r_c \ll 1$.

Figures 3.7c and 3.7d, respectively, show the compressional and shear components of a normal-weight siMS with $\sigma_c/r_c = 0.25$, a relatively wide diamagnetic current layer. Again, the dash line corresponds to $r = r_c$ and the dash-dot line corresponds to the compressional level of $B_{\parallel}/B_o = B_z/B_o = 0.5$. The normal-weight siMS model exhibits a similar magnetic field structure to the iMS model, with the same angular transition points for the compressional and shear components. The widening of the current layer effectively decreases the

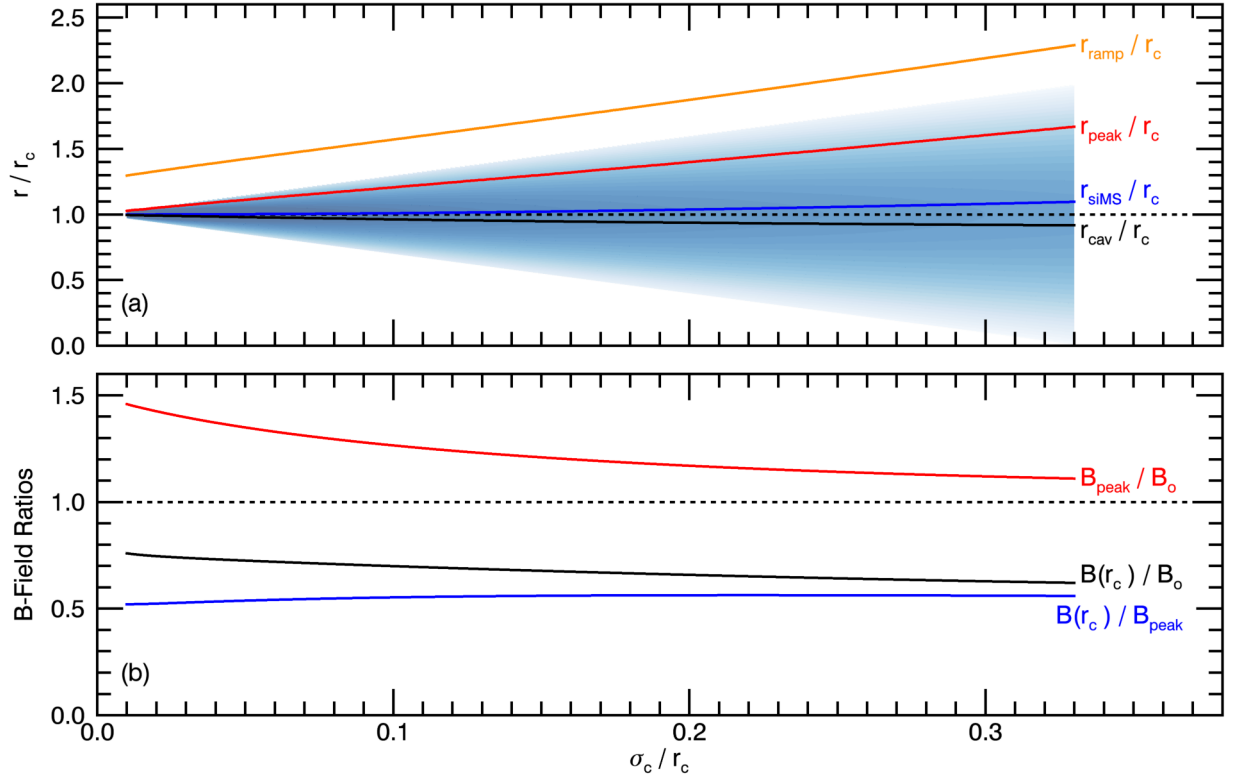


Figure 3.8: Plotted are some key cavity characteristics for normal-weight siMS cavities of $\alpha = 0$ versus the diamagnetic current widths σ_c/r_c . Figure (a) gives cavity locations for the compression ramp r_{ramp}/r_c , the peak magnetic compression r_{peak}/r_c , the experimentally defined cavity edge r_{cav}/r_c (where $B = 0.5B_o$), and the radial normalization for the upstream magnetic field r_{siMS}/r_c (equation 3.66). The shaded region represents the magnetization of the spheres, or diamagnetic current layer, and is defined as $\ln(-3M_n/2\mu_oB_o)$. Figure (b) gives magnetic field ratios for the peak compression B_{peak}/B_o , the magnetic field at $r = r_c$ $B(r_c)/B_o$, and the magnetic field at $r = r_c$ with respect to the peak compression $B(r_c)/B_{peak}$.

strength of the magnetic field (see figure 3.8b) and the larger radial normalization $r_{siMS} > r_c$ (see figure 3.8a) pushes the field structure upstream and spreads it out over the volume. The ‘faux’ elongation of the cavity is more apparent in the siMS model, with r_{cav} (location of $B_{||}/B_o = 0.5$) being $0.93r_c$ at $\theta = \pi/2$ (opposed to r_c for the iMS) and $1.30r_c$ at $\theta = 0$ and π (opposed to $1.26r_c$ for the iMS).

As seen in figure 3.8b, the peak magnetic compression decreases as the diamagnetic current layer increases in width (σ_c/r_c increases) for a given expulsion α . The peak compression of $B_{peak}/B_o = 1.5$ only happens for a thin current layer associated with an iMS. This reduction in the peak compression is a result of distancing current elements from the point of interest, effectively sampling the generated magnetic field further from said current element. Thus, for an $\alpha = 0$ diamagnetic cavity the maximum possible compression is $B_{peak}/B_o = 1.5$.

The magnetic field at $r = r_c$ is not $B/B_o = 0.5$ as previously defined (for r_{cav}), but is closer to $B/B_o \sim 0.75$ for $\sigma_c/r_c \ll 1$ and asymptotically decreases to $B/B_o \rightarrow 0.6$ as $\sigma_c/r_c \rightarrow 1/3$, see figure 3.8b. At the same time $r_{cav} \rightarrow 0.9 r_c$ as $\sigma_c/r_c \rightarrow 1/3$ (figure 3.8a), slightly behind the center of the diamagnetic current layer. The peak compression gets pushed upstream to $r_{peak} \rightarrow 1.7 r_c$, but remains within the diamagnetic current layer.

Both the iMS and normal-weight siMS models are compared to the experiments in figure 3.9. These models are suppose to work best when compared to cavities with conditions that minimize coupling into the ambient-plasma and debris-ion slipping upstream. Such scenarios correlate best to early stages of a sub-Alfvénic, ‘weak’ ($B_{peak}/B_o \lesssim 1.4$) cavity expansion. The first comparison is made to an early time-frame of Run01 of the 2011 LaPD-Phoenix experiment (figure 3.9a), since it has the earliest magnetic field profile in normalized expansion time $V_{cav,o} t/R_c = 0.55$. The next two comparisons (figures 3.9b and 3.9c) are made with Run03 of the 2011 LaPD-Phoenix experiments to be consistent with the deceleration analysis made in §3.3. To fit the iMS model, r_c is defined using the experimental $r_{cav} = 0.5X_{cav}$ and α is assumed to be 0.02 for Run01 and calculated based on data points in the cavity trough for Run03. The assumption $\alpha = 0.02$ is taken for Run01 since the time-frame is too early to have cavity trough points for the calculation, but later time-frames put $\alpha \approx 0.02$. In fitting the siMS model α and B_{peak} are defined from the experiment and σ_c/r_c is selected to satisfy those conditions. Then r_c for the siMS is scaled such that the location for $B/B_o = 0.5$ lines up with the experimental cavity.

In all three time frames the iMS model clearly overpredicts the compression and does not resolve the cavity edge, which is expected since the model is the most ideal scenario.

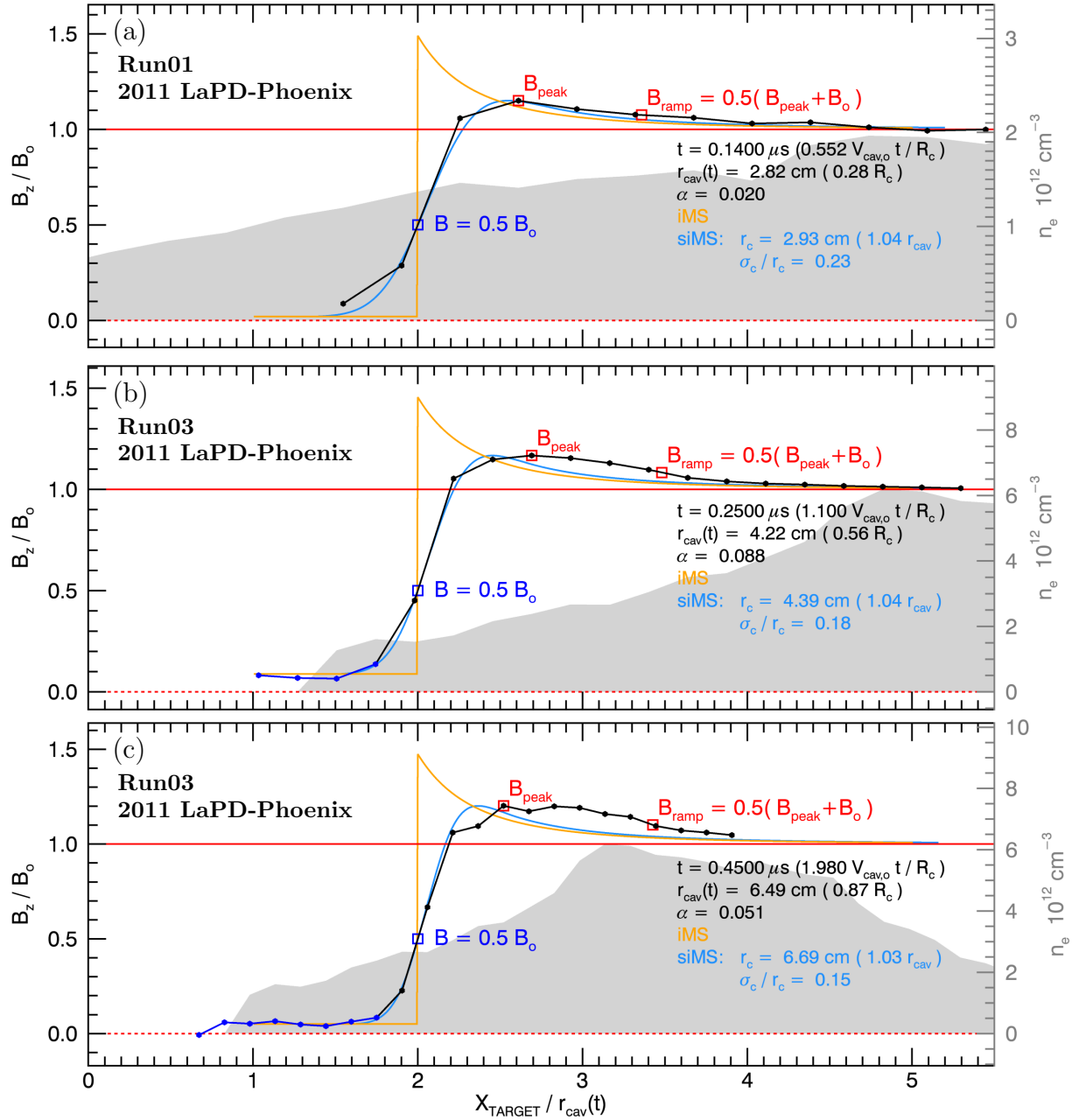


Figure 3.9: This plot compares the iMS (orange) and normal-weight siMS (light blue) models against experimental magnetic field profiles (black) from the 2011 LaPD-Phoenix campaign, Run01 in figure (a) and Run03 in figures (b) and (c). The blue curve represents the data points used to calculate α . The magnetic field is normalized to B_0 and the distance from the target X_{TARGET} is normalized to the time-dependent cavity radius $r_{cav}(t) = 0.5X_{cav}(t)$. The grey shaded region represents the ambient-density.

On the other hand, the normal-weight siMS does well in predicting the cavity edge but the upstream field compression differs as the cavity evolves later into its expansion. In the earliest time frame $V_{cav,o} t/R_c = 0.55$ (figure 3.9a) the siMS current layer width is relatively thick $\sigma_c/r_c = 0.23$, with respect to the central radius of the current distribution. When examining the later time frames $V_{cav,o} t/R_c = 1.10$ (figure 3.9b) and $V_{cav,o} t/R_c = 1.98$ (figure 3.9c) the siMS normalized thickness decreases to $\sigma_c/r_c = 0.18$ and 0.15 , respectively. Since the cavity is expanding, these normalized thicknesses translate to wider current layers in physical space, $\sigma_c \approx 0.79$ cm and 1.00 cm respectively. The experimental and normal-weight siMS compression are in good agreement in the earliest time frame, indicating that the experimental compression does follow the $1/r^3$ decay. In later frames the experimental compression is stronger in the upstream compression ramp than the siMS model. There is no steepening of the compression ramp, just an overall stronger compression. This strengthening of the compression occurs as the compression ramp runs into the higher ambient-density, so this strengthening could be early indications of a weak interaction with the ambient. Slipping of debris-ions out of the cavity can also cause a mild, broad enhancement of the compression upstream.[36] At this point, either case is just as likely.

Extending the comparison to a ‘strong’ cavity ($B_{peak}/B_o \gtrsim 1.5$) that exhibits ‘enhanced’ deceleration, then there are marked differences between the models and experiment. Using the same case study as in §3.3, the comparison is made to Run04 of the 2013 January LaPD-Phoenix campaign at a time of $V_{cav,o} t/R_c = 0.95$, see figure 3.10. This is right at the end of the ‘enhanced’ deceleration phase, see figure 3.6b. The experimental profile reverses the background magnetic field inside the cavity with $\alpha = -0.13$ and produces a peak compression of $B_{peak}/B_o = 1.68$. The iMS and siMS models can not produce a peak compression above $B_{peak}/B_o = (3 - \alpha)/2 = 1.565$. When looking ahead another $0.25 \mu\text{s}$ the experimental compression continues to grow to ~ 1.8 , see figure 3.13c. Examining the compression ramp from upstream to downstream, the ramp starts by closely following the $1/r^3$ behavior, but deviates over the region spanned by the high ambient-density. Within the high density region the compression ramp abruptly steepens at $X_{TARGET}/r_{cav}(t) \sim 2.8$ and

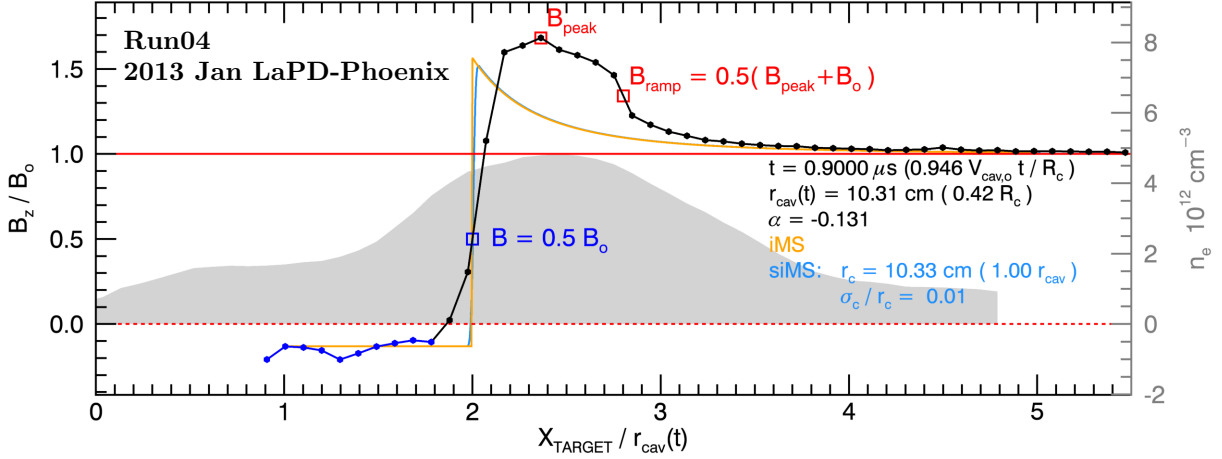


Figure 3.10: A comparison of the magnetic field profile for Run04 of the 2013 January LaPD-Phoenix campaign (black) to the iMS (orange) and normal-weight siMS (light blue) models. The blue points represent the data of the cavity trough used to calculate α . The magnetic field is normalized to B_o and the distance from the target X_{TARGET} is normalized to the time-dependent cavity radius $r_{cav}(t) = 0.5X_{cav}(t)$. The grey shaded region represents the ambient-density.

remains high and relatively flat until the cavity edge. Since the iMS and normal-weight siMS can not duplicate the compression within the high ambient-density, this cavity can not be modeled by a diamagnetic current distribution. What this implies is left for the discussion in the following section (§3.5).

To briefly summarize, the iMS and siMS comparison indicate that: (1) for a ‘weak’ cavity ($B_{peak}/B_o \lesssim 1.4$) the normal-weight siMS can duplicate the magnetic profile early in the expansion, (2) weak cavities have peak compressions significantly lower than an iMS due to the larger width of the diamagnetic current layer, (3) a cavity that can be modeled solely by a diamagnetic current layer will exhibit a $1/r^3$ decay in the field compression outside the diamagnetic current layer that is normalized to some effective cavity radius r_{siMS} (equation 3.66 for a normal-weight siMS), (4) a strong cavity ($B_{peak}/B_o \gtrsim 1.5$) can achieve peak compressions above an iMS, and (5) for a strong cavity neither the iMS nor siMS can duplicate the cavity’s magnetic profile (peak compression and compression ramp). Simply

put, the compression profile of a weak cavity can still be modeled by a simple diamagnetic current layer, but as the cavity gets stronger the experimental profiles differ from the iMS and siMS model profiles. The agreement with ‘weak’ cavities allows for the iMS and normal-weight siMS models to be used as benchmarks, or a comparison point, for stronger cavities. Knowing the manner in which the experimental magnetic field profiles differ (growth of the peak compression and steepening of the compression ramp) over the iMS will help quantify the behavior of the compression. The implication of these differences will be discussed in the following section.

3.5 Cavity Compression Analysis & Debris-Ambient Coupling

Section Highlights

1. The iMS and normal-weight siMS models of the previous section (§3.4) give several key benchmarks for the cavity compression features.
 - (a) A scaling of the peak magnetic field compression B_{peak}/B_o for a given field expulsion $\alpha = B_{inside}/B_o$, see equation 3.68.
 - (b) A normalized compression ramp width w_{ramp}/r_{cav} , see equations 3.73 and 3.74. An iMS gives a ramp width of $w_{ramp}/r_c \approx 0.63$; whereas, a normal-weight siMS of $\sigma_c/r_c = 0.20$ and 0.33 give ramp widths of 0.94 and 1.16 , respectively.
 - (c) A normalized cavity edge to compression ramp separation Δ_{cr} , defined in equation 3.75. An iMS gives a $\Delta_{cr} \approx 0.26$; whereas, a normal-weight siMS of $\sigma_c/r_c = 0.20$ and 0.33 give Δ_{cr} of 0.87 and 1.29 , respectively. More importantly, if Δ_{cr} is constant, then $X_{ramp} \propto X_{cav}$ and the compression ramp and cavity edge are still tied together. If $\partial_t \Delta_{cr} > 0$ (< 0) then $V_{ramp} > V_{cav}$ ($V_{ramp} < V_{cav}$) and $X_{ramp} \not\propto X_{cav}$.
2. Run04 of the 2013 January LaPD-Phoenix campaign shows first experimental evidence of coupling debris-energy into the ambient-plasma in a manner that is con-

ductive to shock formation, but has yet to reach shock conditions.

- The experimental compression grows to a strength of $B_{peak}/B_o = 1.81$, which is about 16% stronger than the iMS model.
- The experimental compression ramp steepens to a width of $w_{ramp}/r_{cav} = 0.33$, which is 1.9x steeper than the iMS model ($w_{ramp}/r_{cav} = 0.63$).
- The compression growth and steepening occurs during the ‘enhanced’ deceleration phase of the cavity (see §3.3 and figure 3.6b) and as the compression ramp passes through the high ambient-density.
- This run does not meet shock conditions since the cavity-ramp separation is constant ($\Delta_{cr} = \text{const.}$), indicating the compression ramp is still tied to the cavity.
- Compression growth and steepening indicate the generation of additional current structures within the compression ramp and the correlation with the ‘enhanced’ deceleration indicate that the energy to drive the current comes from the energy stored in the debris-plasma.

3. Experimental data falls short of determining the debris-ambient coupling mechanism, but the iMS model provides a plausible mechanism that fulfills the shock picture in figure 1.3.

- An expanding cavity generates an inductive electric field in the compression ramp that produces a radial $E \times B$ -drift on the electrons, while leaving the unmagnetized ambient-ions unaffected.
- The electrons drift upstream creating a space-charge separated electric field that acts to drag the ambient-ions forward and produces a secondary $E \times B$ -drift on the electrons.
- The secondary $E \times B$ -drift drives the electrons into a non-diamagnetic current that serves to steepen the compression ramp and strengthen the downstream

magnetic field.

- The downstream magnetic field enhancement serves to increase the effective background magnetic field inside the cavity, which the diamagnetic current then needs to expel to keep $\alpha = 0$. This causes the ‘enhanced’ deceleration of the cavity.

In the previous section, the iMS (equations 3.49-3.51) and normal-weight siMS (equations 3.63-3.65) models were validated against ‘weak’ experimental cavities. The normal-weight siMS was established as a reasonable model for describing the magnetic field of cavities that only act to expel the background magnetic field; whereas, the iMS is the best case scenario for any type of MOIC. This allows the iMS to act as a benchmark to quantify experimental cavities, giving markers to identify features in the magnetic field compression that can not be described by a spherical diamagnetic current. Describing these differences gives insight into the onset of debris-ambient coupling.

Figure 3.10 shows an example of how an experimental cavity can differ from the iMS model. Two key features are seen in the comparison: (1) the peak experimental compression grew larger than the possible compression of the iMS and (2) the experimental compression ramp steepened as compared to the $1/r^3$ decay behavior of the iMS and siMS models. These are important behaviors because it tells that the total magnetic field is no longer the sum of \mathbf{B}_o and \mathbf{B}_{MS} (equations 3.44-3.46), but there is now an additional ‘other’ magnetic field component \mathbf{B}_{other} . By equation 3.35, the presence of \mathbf{B}_{other} implies there is an ‘other’ vector-potential \mathbf{A}_{other} and, by equation 3.38, this means an additional current is driven. Since the compression growth and steepening occurs upstream in the compression ramp while the debris-ions are contained in the cavity, this driven current must occur within the ambient-plasma.

The experimental compression growth and steepening need to be significantly greater than the iMS or siMS models in order to infer the occurrence of debris-ambient coupling. As seen in figures 3.9b and 3.9c, a subtle growth in the upstream compression ramp can

also be reasoned to be the cause of debris-ions slipping upstream, not just an interaction with the ambient-plasma. Additionally, reflected ambient-ions can create a shallow foot to the compression ramp, but all experimental cavities expand well below the critical Alfvénic Mach number ($M_A < 2.67$) and reflected ambient-ions only occur for Mach numbers larger than the critical Mach number.[25, 48, 83]

To set the first iMS benchmark, the peak field compression can be derived from equation 3.49-3.51. The iMS compressional magnetic field is

$$\frac{\mathbf{B} \cdot \hat{\mathbf{z}}}{B_o} = \begin{cases} \alpha & r < r_c \\ \left[1 + \frac{\alpha-1}{2}(1 - 3 \cos^2 \theta) \left(\frac{r_c(t)}{r} \right)^3 \right] B_o & r \geq r_c \end{cases} \quad (3.67)$$

and the peak compression occurs at $\theta = \pi/2$ and $r = r_c$ to give

$$\left[\frac{\mathbf{B} \cdot \hat{\mathbf{z}}}{B_o} \right]_{peak} = \frac{3 - \alpha}{2}, \quad (3.68)$$

which is only dependent on the magnetic field inside the cavity α . The peak iMS compression is the same regardless of how large the cavity is or how fast it is expanding. Any siMS model will have a compression less than equation 3.68. Thus, if an experimental cavity achieves a compression larger than an iMS, then that compression can not be the result of the spherical diamagnetic current layer. That compression has to be the result of a secondary, driven current within the compression.

To create a benchmark for the steepness of the compression ramp across B_o ($\theta = \pi/2$), a “width” of the ramp w_{ramp} is defined to be the region in which the ramp grows from $B = 0.2(B_{peak} - B_o) + B_o$ to $B = 0.8(B_{peak} - B_o) + B_o$. In the iMS model the radial location for $B = 0.2(B_{peak} - B_o) + B_o$ is

$$\frac{\mathbf{B}(r_{0.2}, \pi/2) \cdot \hat{\mathbf{z}}}{B_o} = 0.2 \left[\frac{3 - \alpha}{2} - 1 \right] + 1 = 1 - \frac{1}{2}(\alpha - 1) \left(\frac{r_c}{r_{0.2}} \right)^3 \quad (3.69)$$

$$\implies r_{0.2} = 5^{1/3} r_c \quad (3.70)$$

and the radial location for $B = 0.8(B_{peak} - B_o) + B_o$ is

$$\frac{\mathbf{B}(r_{0.8}, \pi/2) \cdot \hat{\mathbf{z}}}{B_o} = 0.8 \left[\frac{3 - \alpha}{2} - 1 \right] + 1 = 1 - \frac{1}{2}(\alpha - 1) \left(\frac{r_c}{r_{0.8}} \right)^3 \quad (3.71)$$

$$\implies r_{0.8} = \left(\frac{5}{4} \right)^{1/3} r_c, \quad (3.72)$$

which gives the iMS compression ramp width as

$$\frac{w_{ramp}}{r_c} \equiv \frac{r_{0.2} - r_{0.8}}{r_c} \quad (3.73)$$

$$= 5^{1/3} - \left(\frac{5}{4} \right)^{1/3} \approx 0.63. \quad (3.74)$$

The ramp width w_{ramp} is independent of α and the cavity expansion speed, but dependent of the cavity size r_c . If a cavity has a $w_{ramp}/r_c < 0.63$, then steepening is occurring. As a reference, $w_{ramp}/r_c \approx 0.94$ for a normal-weight siMS of $\sigma_c/r_c = 0.2$, and increases to $w_{ramp}/r_c \approx 1.16$ when $\sigma_c/r_c = 1/3$

Figures 3.11, 3.12, and 3.13, respectively, plot the compression values for Run03 of the 2011, Run03 of the 2013 January, and Run04 of the 2013 January LaPD-Phoenix campaigns (the same runs compared in §3.3). Run03 of the 2011 LaPD-Phoenix campaign is one of the ‘weak’ cavities that is consistent with the normal-weight siMS (see figures 3.9b and 3.9c). Figure 3.11 re-enforces this consistency with the siMS model, with figure 3.11a showing that the experimental expansion is consistent with the MOIC model (§3.3), figure 3.11c showing that the peak compression remains below the iMS model $B_{peak}/B_o - (3 - \alpha)/2 \sim -0.3$, and figure 3.11e shows that the compression ramp width remains greater than the iMS model $w_{ramp}/r_{cav} > 0.63$. The ramp width stabilizes at $w_{ramp}/r_{cav} \sim 0.85$ which is consistent with the normal-weight siMS fitted to the run in figure 3.9c ($w_{ramp}/r_c = 0.87$ for $\sigma_c/r_c = 0.15$ and $\alpha = 0.05$).

Run03 and Run04 of the 2013 January LaPD-Phoenix campaigns are ‘strong’ cavities in that their peak compressions reach values of $B_{peak}/B_o \gtrsim (3 - \alpha)/2$. Recall from §3.3, these two runs are statistically identical except for the placement of the high ambient-density, and Run04 experiences a phase of ‘enhanced’ deceleration in the cavity expansion that Run03

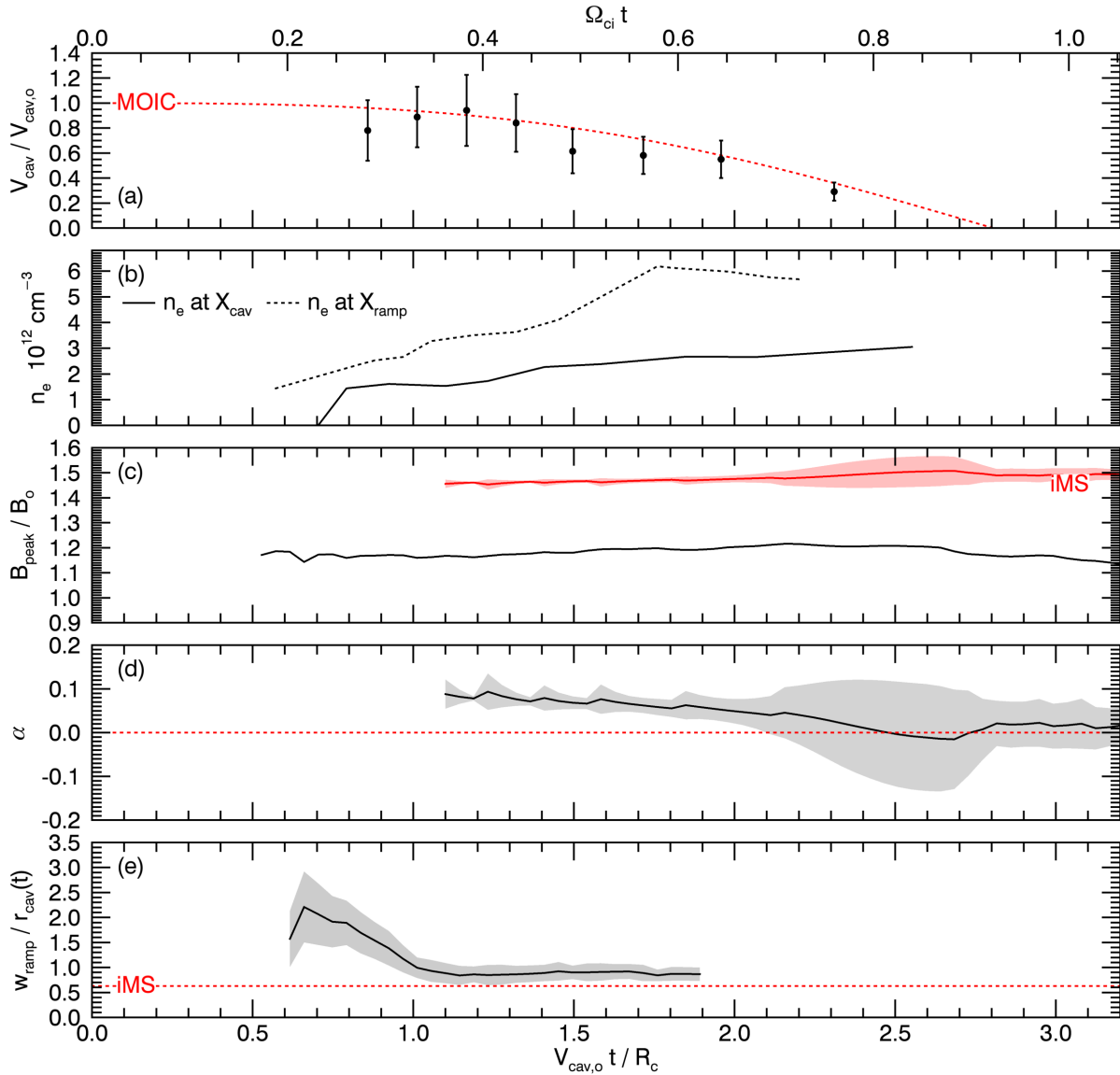


Figure 3.11: Key cavity values for Run03 of the 2011 LaPD-Phoenix campaign. Figure (a) shows the cavity expansion speed $V_{cav}/V_{cav,o}$ and (red dash-line) the MOIC expansion model (§3.3). Figure (b) shows the ambient density at X_{cav} (solid) and X_{ramp} (dash). Figure (c) plots the peak experimental compression B_{peak}/B_o and (red) the iMS compression (equation 3.68). Figure (d) plots the magnetic field inside the cavity $\alpha = B_{inside}/B_o$ with the grey region representing the standard deviation of the points used for the calculation. Figure (e) gives the normalized compression ramp width (equation 3.73) and (red dash-line) the iMS width value.

does not. By comparing figure 3.12 and 3.13, this ‘enhanced’ deceleration is not the only marked difference between the two runs. Run04 also shows considerable growth of the peak compression (figure 3.13c) and steepening of the compression ramp (figure 3.13e) as compared to Run03 and the iMS model.

First, looking at Run03 the peak compression remains at the iMS level until the cavity edge X_{cav} exits the high ambient-density and, then, the compression begins to slowly drop, see figures 3.12b and 3.12c. While the compression ramp X_{ramp} of Run03 transverses the high ambient-density, the steepness of the ramp is consistent with the iMS model, only showing a slight steepening just before X_{ramp} leaves the high density, see figures 3.12b and 3.12e. Once X_{ramp} leaves the high density, the ramp width immediately begins to grow, indicating that the diamagnetic current is getting broader and/or whatever plasma that was built up in the compression is being released upstream.

In Run04 the ‘enhanced’ deceleration phase lasts till $V_{cav,o} t/R_c \approx 0.95$ when the compression ramp X_{ramp} leaves the peak of the high ambient-density region, see figures 3.13a and 3.13b. During this deceleration phase the ramp width steepens to $w_{ramp}/r_{cav} = 0.33$ at $V_{cav,o} t/R_c = 0.88$ (see figure 3.13e), which is 1.9x steeper than the iMS model. Upon the end of the deceleration phase, the ramp width begins to grow, surpassing the iMS width at $V_{cav,o} t/R_c = 1.17$ and reaching a width that is about 2x broader than the iMS model. The compression growth correlates with the ‘enhanced’ deceleration phase and steepening of the ramp. At the beginning of the deceleration phase the peak compression starts at the iMS level, but begins to grow above that level at $V_{cav,o} t/R_c = 0.78$. The growth continues past the deceleration phase, reaching its largest compression of $B_{peak}/B_o = 1.81$ at $V_{cav,o} t/R_c = 1.18$. Then the peak compression promptly begins to decay at the same moment that the ramp width exceeds the iMS width $w_{ramp}/r_{cav} \geq 0.63$. The time of $V_{cav,o} t/R_c \sim 1.2$ is also the moment when X_{ramp} enters the low density region of $n_e \lesssim [n_e]_{peak}$ and X_{cav} is just reaching the peak ambient-density. The peak compression falls back below the iMS level at $V_{cav,o} t/R_c = 1.4$.

As compared to the iMS metrics, the degree to which the Run04 compression ramp

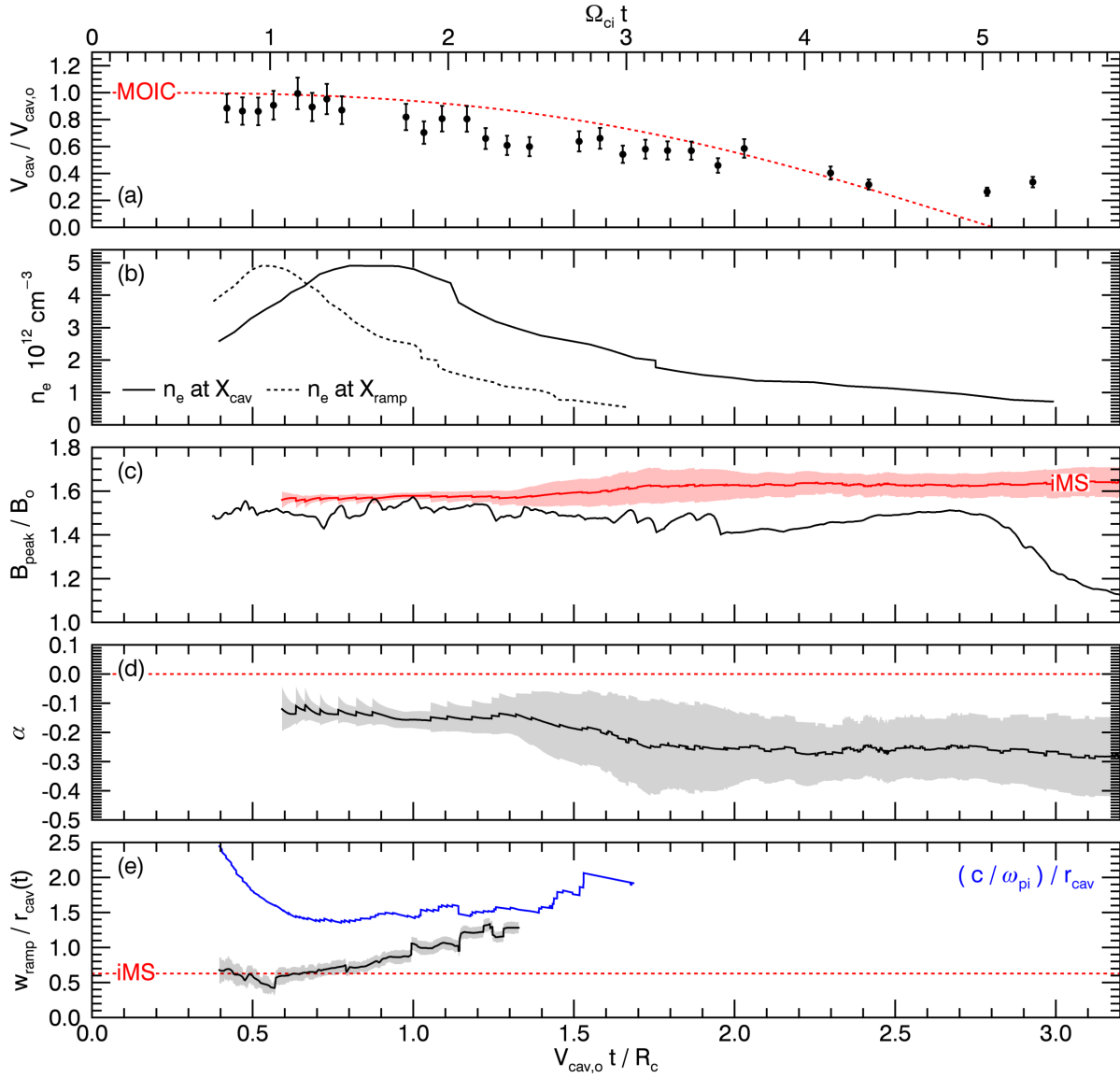


Figure 3.12: Cavity values for Run03 of the 2013 January LaPD-Phoenix campaign. Figures (a)-(e) are the same quantities as plotted in figure 3.11. Figure (e) also plots (blue) the ratio of the local ambient-ion inertial length at X_{ramp} to the time-dependent cavity radius $(c/\omega_{pi})/r_{\text{cav}}$.

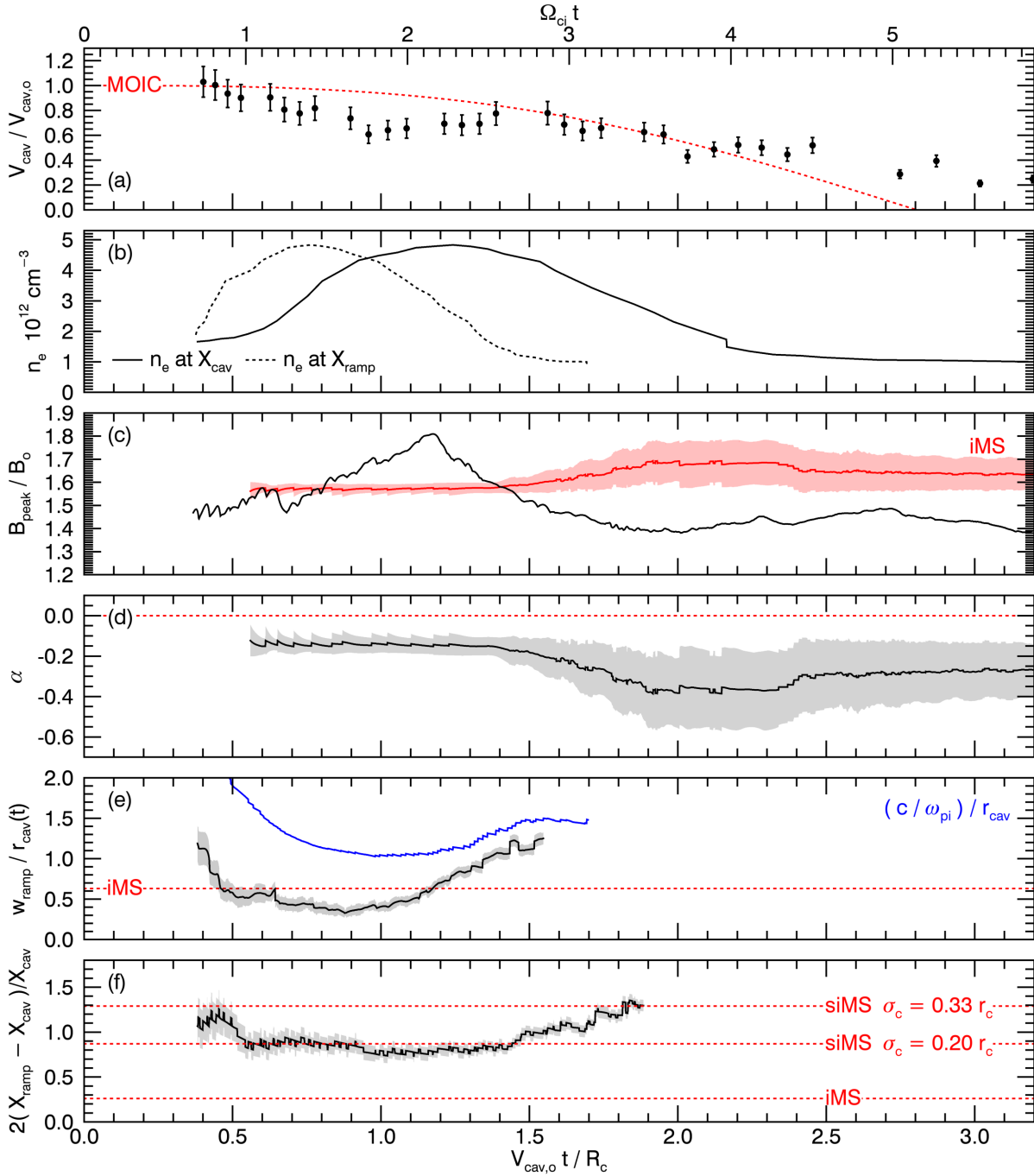


Figure 3.13: Cavity values for Run04 of the 2013 January LaPD-Phoenix campaign. Figures (a)-(e) are same as described in figure 3.12. Figure (f) displays the normalized cavity edge to compression ramp separation (equation 3.75). The red dash-lines in figure (f) give fiducial markers for the cavity-ramp separation of the iMS model (equation 3.76) and the normal-weight siMS model with $\sigma_c/r_c = 0.20$ and 0.33 .

steepens and peak compression grows, in correlation with the ‘enhanced’ deceleration of the cavity, is a clear indicator of driving debris-ambient coupling. This conclusion is bolstered by the fact that all three behaviors occur when the compression ramp passes through the high ambient-density, and ends once X_{ramp} leaves the density. These behaviors also disappear when the high density is moved too close to the target, as seen in Run03 of the 2013 January LaPD-Phoenix campaign. The ‘enhanced’ deceleration indicates that the debris-ions are losing energy at a rate quicker than a pure vacuum expansion. The compression growth and steepening indicate that the magnetic field is no longer solely driven by the diamagnetic current. In order to create this new field structure, new current features have to be driven within the compression ramp (by equations 3.35 and 3.38). Since the debris-ions are unmagnetized and contained within the cavity, these additionally driven current structures must involve the ambient-plasma. The correlation between the compression features and ‘enhanced’ deceleration imply that the energy to drive the additional current features in the compression ramp comes from the energy contained in the debris-ions. However, the mechanism by which this happens is not apparent through the experimental measurements.

Even though there is evidence of debris-ambient coupling in Run04, the conditions have not reached shock-like values. At the end of the deceleration phase, the compression ramp is expanding at a local Alfvénic Mach number of $M_A \approx 1.1$. The Rankine-Hugoniot jump conditions would dictate a compression jump of $B_{peak}/B_o \approx M_A \approx 1.1$ (see figure 1.2), which is far below the experimental B_{peak}/B_o of 1.8. The ramp width has steepened to $w_{ramp}/r_{cav} = 0.33$ ($w_{ramp} = 0.30 c/\omega_{pi}$), which is consistent with an expected shock width $\Delta_{sh} \lesssim c/\omega_{pi}$ for a subcritical, quasi-perpendicular, dissipation dominated collisionless shock discussed in §1.1.1. However, experimental data (figure 3.13f) shows that the compression ramp is not separating from the cavity (discussed below). A separation is needed to indicate a transition from coupling physics into shock physics that allows the compression jump to become a self-consistent feature that propagates forward without the push from the cavity.

Figure 3.13f shows the normalized separation between the cavity edge and compression

ramp, which is defined as

$$\Delta_{cr} \equiv \frac{X_{ramp} - X_{cav}}{0.5X_{cav}}. \quad (3.75)$$

A normalized definition is chosen since the ramp position for the iMS and siMS models is proportional to the cavity radius; thus, giving a constant Δ_{cr} . For an iMS this definition gives a cavity-ramp separation value of

$$[\Delta_{cr}]_{iMS} = \frac{(2^{1/3}r_c + r_c) - 2r_c}{r_c} \approx 0.26, \quad (3.76)$$

which is about 0.29x smaller than what is measure experimentally. A normal-weight siMS with σ_c/r_c of 0.20 and 0.33, respectively, give Δ_{cr} of 0.87 and 1.29. The power of this definition comes from examining $\partial_t[\Delta_{cr}]$. If $\partial_t[\Delta_{cr}] = 0$ ($\Delta_{cr} = \text{const.}$) then $X_{ramp} \propto X_{cav}$, implying that the cavity edge and compression ramp are still tied together. Any iMS or siMS models share this proportionality. If $\partial_t[\Delta_{cr}] > 0$ (< 0) then $V_{ramp} > V_{cav}$ ($V_{ramp} < V_{cav}$), since $X_{ramp} > X_{cav}$. Assuming the normalized spatial parameters to the diamagnetic current distribution remain constant, then $\partial_t[\Delta_{cr}] \neq 0$ also implies that the compression ramp is no longer tied to the cavity edge. In figure 3.13f, Δ_{cr} remains constant during the deceleration and steepening phase. This indicates that even though debris-ambient coupling is being driven, not enough energy has been transferred to the ambient-plasma to allow the compression jump to separate from the cavity and form a shock.

Even though current experimental measurements give evidence of debris-ambient coupling, they fall short of being able to directly show how the magnetic piston couples energy into the ambient-plasma. This is due to the experimental limitations and probe design feasibility at the time of execution. The low shot rate of the laser system prevented collection of volumetric magnetic field data, which could be used to estimate current systems in the compression; as well as, correlation data to investigate the existence of turbulence in the compression and/or cavity edge. The large electric currents of the cavity were beyond the biasing ability of the hardware (strength and slew-rate) for existing Langmuir probes. The design of emissive probes for measuring the plasma potential and the electrostatic electric field on the LaPD were in their infancy.[49] However, the iMS model does provide a coupling

mechanism that explains the compression growth, the compression ramp steepening, and the ‘enhanced’ deceleration of the cavity expansion. This model can guide future investigations, along with upgrades to current diagnostics, the introduction of emissive probes, and the launch of a high repetition rate laser system.

The iMS coupling mechanism is similar to how the diamagnetic current of the cavity is driven, discussed in §1.3.1, and sets up the shock picture in figure 1.3, discussed in §1.1.1. The rationale for the iMS coupling mechanism is similar to the argument for the MOIC model, start with what is known (the diamagnetic cavity) and then add on the higher order complexity based on what the zero order solution suggests. The first interaction point between the ambient-plasma and cavity occurs upstream in the compression ramp. This is confirmed by the fact that the steepening of the ramp in Run04 occurs about one full cavity radius ahead of the cavity edge $r_{ramp} \sim 2r_{cav}$, see figure 3.13f. Thus, the ambient-plasma interacts with the magnetic and electric fields of the cavity compression ramp before coming into contact with the debris-plasma that makes up the cavity. Knowing, and validating, this field structure is key to understanding the coupling mechanism provided by the iMS model.

Validating the iMS magnetic field against experiments consequently validates the vector-potential \mathbf{A} and the resulting inductive electric field of the expanding cavity ($\mathbf{E} = -\partial_t \mathbf{A}$). However, it says nothing about possible electrostatic electric fields ($\mathbf{E} = -\nabla \Phi$). Since the cavity is expanding, the magnetic field is not stationary $\partial_t \mathbf{B} \neq 0$ and, thus, an inductive electric field exists. By combining equations 3.43 and 3.48, the iMS vector-potential can be written in terms of α , $r_c(t)$, and B_o to give

$$\mathbf{A}(\mathbf{r}, t) = \frac{1}{2} (\alpha - 1) B_o \begin{cases} r \sin \theta \hat{\phi} & \text{for } r < r_c \\ \left(\frac{r_c(t)}{r}\right)^3 r \sin \theta \hat{\phi} & \text{for } r \geq r_c \end{cases}. \quad (3.77)$$

Using equation 3.36 and assuming α is constant, the iMS inductive electric field is written as (see Appendix B.2 for complete details)

$$\mathbf{E}(\mathbf{r}, t) = -\frac{3}{2} (\alpha - 1) B_o \sin \theta \begin{cases} 0 & \text{for } r < r_c \\ \left(\frac{r_c(t)}{r}\right)^2 v_c(t) \hat{\phi} & \text{for } r \geq r_c \end{cases}, \quad (3.78)$$

where $v_c = \partial_t r_c$ is the time-dependent cavity expansion velocity. The radial-dependence of the inductive electric field is normalized to the cavity radius r_c (like the magnetic field), but decays like $(r_c/r)^2$. The field is also proportional to the background magnetic field B_o and the cavity expansion velocity $v_c(t)$. This inductive electric field then gives rise to an $\mathbf{E} \times \mathbf{B}$ -drift everywhere outside the cavity, see Appendix B.4. Keeping focused on the expansion across \mathbf{B}_o , the $\mathbf{E} \times \mathbf{B}$ -drift at $\theta = \pi/2$ is

$$\mathbf{U}(r, \pi/2, t) = -\frac{E_\phi}{B_\theta} \hat{\mathbf{r}} \quad (3.79)$$

$$U_r(r, \pi/2, t) = \frac{3(\alpha - 1)(r_c/r)^2}{(\alpha - 1)(r_c/r)^3 - 2} v_c \quad \text{for } r \geq r_c, \quad (3.80)$$

where E_ϕ is given in equation 3.78 and B_θ is given in equation 3.50. The resulting radial drift is independent of B_o and only depends on how strongly the cavity is expelled α , the expansion speed of the cavity v_c , and the test particle's location in the compression ramp. The radial drift asymptotically approaches zero as $r \rightarrow \infty$ and, for $\alpha \geq -3$, the maximum drift of $U_r = v_c$ occurs at $r = r_c$. Only a particle that is highly magnetized with respect to the cavity will experience this $\mathbf{E} \times \mathbf{B}$ -drift. For Run04, at the time the compression ramp reaches its steepest value an ambient-ion has only gone through roughly a quarter of its gyro-orbit $\Omega_{ci} t / 2\pi \sim 0.28$. So, the ambient-ions are considered to be unmagnetized while the ambient-electrons are highly magnetized, since $\Omega_{ce} / \Omega_{ci} = m_i / m_e \sim 10^3$. In this scenario, the ambient-electrons will receive a radial $\mathbf{E} \times \mathbf{B}$ -drift that will push the electrons upstream and create a radially outward space-charge separated electric field. This space-charge electric field gives rise to the potential jump across the compression ramp that acts to accelerate the ambient-ions and is synonymous with the potential jump across Δ_{sh} in figure 1.3. This electric field also generates a 2^{nd} order $\mathbf{E} \times \mathbf{B}$ -drift that drives the electrons in a non-diamagnetic current. This results in the electric current that flows perpendicular to \mathbf{B}_o and the expansion $\hat{\mathbf{n}}$ in figure 1.3.

Driving this electric current acts to steepen the compression ramp, grow the compression, and cause the cavity to decelerate. Steepening is achieved since the electric current forms a ring around the cavity that reduces the magnetic field upstream and enhances the field

downstream. This downstream enhancement adds compression to the magnetic field and alters the background field inside the cavity from \mathbf{B}_o to $\mathbf{B}_o + \delta\mathbf{B}$, where $\delta\mathbf{B}$ is the added compression from the driven electric current. Since the total ‘background field’ in the cavity is now $\mathbf{B}_o + \delta\mathbf{B}$, the diamagnetic current of the cavity has to be driven harder to keep $\alpha = 0$. The energy to drive the diamagnetic current comes from the debris-energy and, thus, causing the expanding debris-ions to experience the ‘enhanced’ deceleration. Driving a stronger diamagnetic current also adds to the field compression, even though experimentally the cavity field remains as $\alpha = 0$.

The iMS coupling mechanism provides a process that duplicates the expected shock front schematic, figure 1.3, but falls short of predicting conditions in which the coupling will succeed. The model and experiment need to evolve to better understand the formation of the space-charge separated electric field and the resulting cross-field electric current. In the experiment, this is where volumetric magnetic field data and emissive probe data will be illuminating. An approximate calculation of the current structures can be made from the volumetric magnetic field data. While correlating emissive probe measurements of the plasma potential with the steepening of the compression ramp can confirm or refute the growth of the electrostatic field within the steepened compression ramp.

In summary, the experiments have achieved first evidence of coupling debris-energy into the ambient-plasma in a manner that is conducive for shock formation, but has yet to reach shock conditions. This is achieved from comparing experiments to established benchmarks from the MOIC model and correlating cavity behavior with the ambient-plasma conditions. Run04 of the 2013 January LaPD-Phoenix campaign shows a compression growth that is about 16% stronger than the iMS model and a compression ramp steepening that is 1.9x steeper than the iMS model. Both these features occur during the ‘enhanced’ deceleration phase of the cavity expansion (figure 3.6b) and as the compression ramp passes through the high ambient-density. This correlation indicates the driving of a cross-field current in the compression ramp and that the energy to drive the current comes from slowing the debris-ions. The experimental data falls short of indicating the coupling mechanism between the

cavity and ambient-plasma, but the iMS model does provide a mechanism that is in agreement with the shock model in figure 1.3. In order to understand the coupling mechanism, further experiments need to be performed that gather detailed volumetric magnetic field data and volumetric plasma potential data from emissive probes. Doing so will allow for a correlation between the plasma potential and steepening of the compression ramp that will confirm or refute the growth of an electrostatic electric field within the compression ramp.

3.6 Run17: A Shock-Like Event

Section Highlights

1. Run17 of the 2013 October LaPD-Phoenix campaign shows the same debris-ambient coupling indicators as observed in Ru04 of the 2013 January LaPD-Phoenix campaign.
 - There is an ‘enhanced’ deceleration phase that is 8.8x stronger than the MOIC model and 1.6x stronger than Run04.
 - The peak compression grows to $B_{peak}/B_o = 2.04$, about $0.5B_o$ stronger than the iMS predicted compression.
 - The compression ramp steepens to $w_{ramp}/r_{cav} = 0.18$ ($w_{ramp} = 0.30 c/\omega_{pi}$) which is 3.5x steeper than the iMS model and 1.8x steeper than Run04.
2. Run17 also exhibits shock-like conditions.
 - There is a weak decoupling between the compression ramp and cavity edge, since there is weak growth in the normalized cavity-ramp separation $\partial_t \Delta_{cr} > 0$, see equation 3.75 and figure 3.15f.
 - The experiment is consistent with the Rankine-Hugoniot jump conditions with the compression front expanding with a local Alfvénic Mach number of $M_A = 2.0(\pm 0.1)$ and providing a compression jump of $B_{peak}/B_o = 2.0$.

3. Run17 is the only experimental case in which the ambient-ion inertial length is less than the scale length of the iMS compression ramp, $(c/\omega_{pi})/r_{cav} = 0.5 < 0.63$. This criterion for generating shocks is consistent with similar criterion based on hybrid simulations[13, 60].

The previous section defined benchmarks to identifying the occurrence of debris-ambient coupling in experiments, but the case study for the section (Run04 of the 2013 January LaPD-Phoenix campaign) did not reach shock-like conditions. Advancements in the LaPD-Phoenix infrastructure (see table 2.1) improved the plasma conditions for the 2013 October LaPD-Phoenix campaign. Using Run17 as the case study for this section (see table 3.1), the laser energy has doubled to produce a larger blow-off velocity of $V_{cav,o} = 4.9(\pm 0.3) \times 10^7$ cm/s (versus $V_{cav,o} = 2.6(\pm 0.3) \times 10^7$ cm/s for Run04). The target material for the debris-plasma was changed from graphite to HDPE, since HDPE produced less backscatter and appeared to provide better energy coupling between the laser energy and debris-plasma. The upgraded LaB₆ cathode increased the peak ambient-density by 2.4x over the Run04 peak, to 11.7×10^{12} cm⁻³, and provided a larger density FWHM, 27 cm for Run17 as compared to 19 cm for Run04. The background magnetic field was increased from 200 G to 300 G, which, with the density increase, kept the minimum Alfvén speed approximately the same. These changes created an event in Run17 that exhibits debris-ambient coupling, satisfies the Rankine-Hugoniot jump conditions, and shows a weak decoupling between the compression ramp expansion and cavity expansion.

Figure 3.14 shows a series of magnetic field line-outs (B vs. t) stacked according to their location from the target. This representation better illustrates the features of the magnetic compression and cavity edge. The plotted dataset is generated by combining data take from 9 laser shots. Every five sequential line-outs correspond to one laser shot and the the 5 bdot tips (discussed in §2.3.1). This plot does show signs that the probe is beginning to affect the magnetic field and that laser energy/intensity variation is causing some variation in the stitched together dataset. There is a jump in the cavity edge between positions 23.4 cm

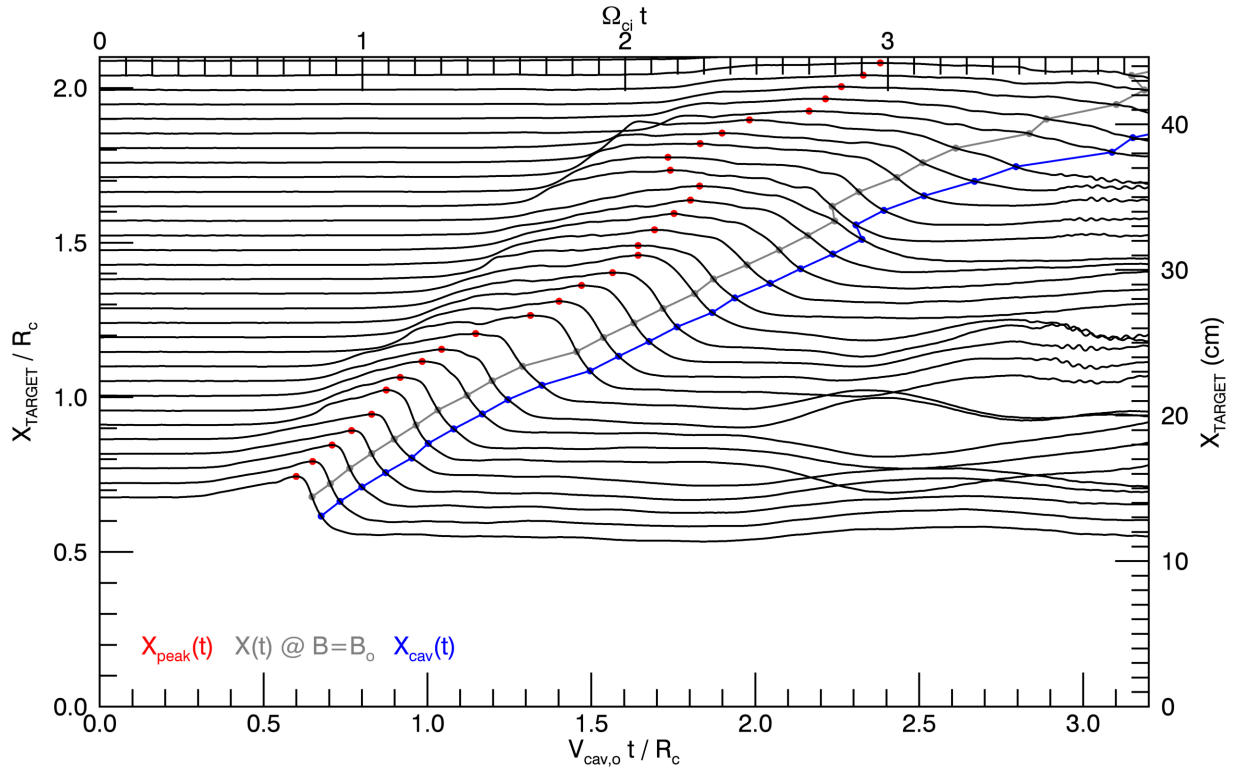


Figure 3.14: An illustration of the cavity magnetic field for Run17 of the 2013 October LaPD-Phoenix campaign. Plotted is a series of temporal, magnetic field line-outs stacked according to their distance from the target X_{TARGET} . Also plotted, (red) the location of the peak compression for each line-out $X_{peak}(t)$, (grey) the location in the cavity edge where the magnetic field is equal to B_o , and (blue) the location of the cavity edge $X_{cav}(t)$ (where $B = 0.5B_o$).

($1.10R_c$) and 24.4 cm ($1.15R_c$), as well as, 33.4 cm ($1.57R_c$) and 34.4 cm ($1.62R_c$). This is primarily due to the variation of the laser intensity on target, since the laser intensity dictates the blow-off velocity of the debris-plasma. This stitching error is considered when discussing the cavity features and is clearly labeled in figures 3.15e and 3.15f. It does not affect the calculated expansion speed since speeds are not calculated between different laser shots (§3.3).

The probe's affect on the magnetic field is seen in two ways. First, when looking at the 5 sequential line-outs for a given shot, the closest line-out to the target has the temporally

steepest compression front and then broadens slightly out to the fifth line-out. Then the first line-out in the next laser shot is steep again. This suggests that the probe tip, though small at $\varnothing 2.5$ mm and 240 mm long, is locally disrupting the driven cross-field current in the compression front. Secondly, inside the cavity the magnetic field varies wildly for $V_{cav,o}t/R_c \gtrsim 2.0$. This variation is due to the generation of a large EMP caused by arching along the probe shaft and/or the target surface. Arching is observed on the target surface in time-integrated SLR images and on the metallic probe shaft as arching footprints on the shaft surface. This arching is also evidence of strong electric fields in the diamagnetic current layer and/or compression front.

Looking to figure 3.15, Run17 shows the same debris-ambient coupling indicators as seen for Run04 of the 2013 January LaPD-Phoenix campaign; ‘enhanced’ deceleration, growth of magnetic compression, and steepening of compression ramp. The cavity expansion exhibits an ‘enhanced’ deceleration that ends at $V_{cav,o}t/R_c \sim 0.9$ (see figure 3.15a). It is likely that the ‘enhanced’ deceleration started before the closest data point, since the ‘instantaneous’ expansion velocity at $V_{cav,o}t/R_c = 0.71$ ($0.304 \mu s$) and $X_{cav} = 0.70R_c$ (14.9 cm) is 18% slower than the time-of-flight blow-off velocity, $V_{cav} = 0.82V_{cav,o}$. This is especially so when considering that the time-of-flight value $V_{cav,o}$ is an underestimate for the actual blow-off velocity. During the observed deceleration period, the cavity expansion velocity slows to $V_{cav} = 0.59V_{cav,o}$ at $2\tau = V_{cav,o}t/R_c = 0.91$. This gives a normalized deceleration of

$$\begin{aligned} \chi_g &\approx \frac{\Delta\chi_v}{\Delta\tau} = \frac{\Delta(V_{cav}/V_{cav,o})}{\frac{1}{2}\Delta(2\tau)} = \frac{2(0.59 - 0.82)}{0.91 - 0.71} \\ &\approx -2.3, \end{aligned} \tag{3.81}$$

which is 8.8x stronger than the deceleration of the MOIC model (equation 3.28) at the end of this phase, where $X_{cav} = 0.84R_c$ and $(\chi_g)_{MOIC} = -1.5(0.84/2)^2 = -0.26$. It is also 1.6x stronger than the ‘enhanced’ deceleration experienced by Run04 of the 2013 January LaPD-Phoenix campaign, see equation 3.30.

During the ‘enhanced’ deceleration phase the peak magnetic field compression grows from $B_{peak}/B_o = 1.58$ to 1.9 (figure 3.15c). The largest compression value is $B_{peak}/B_o = 2.04$,

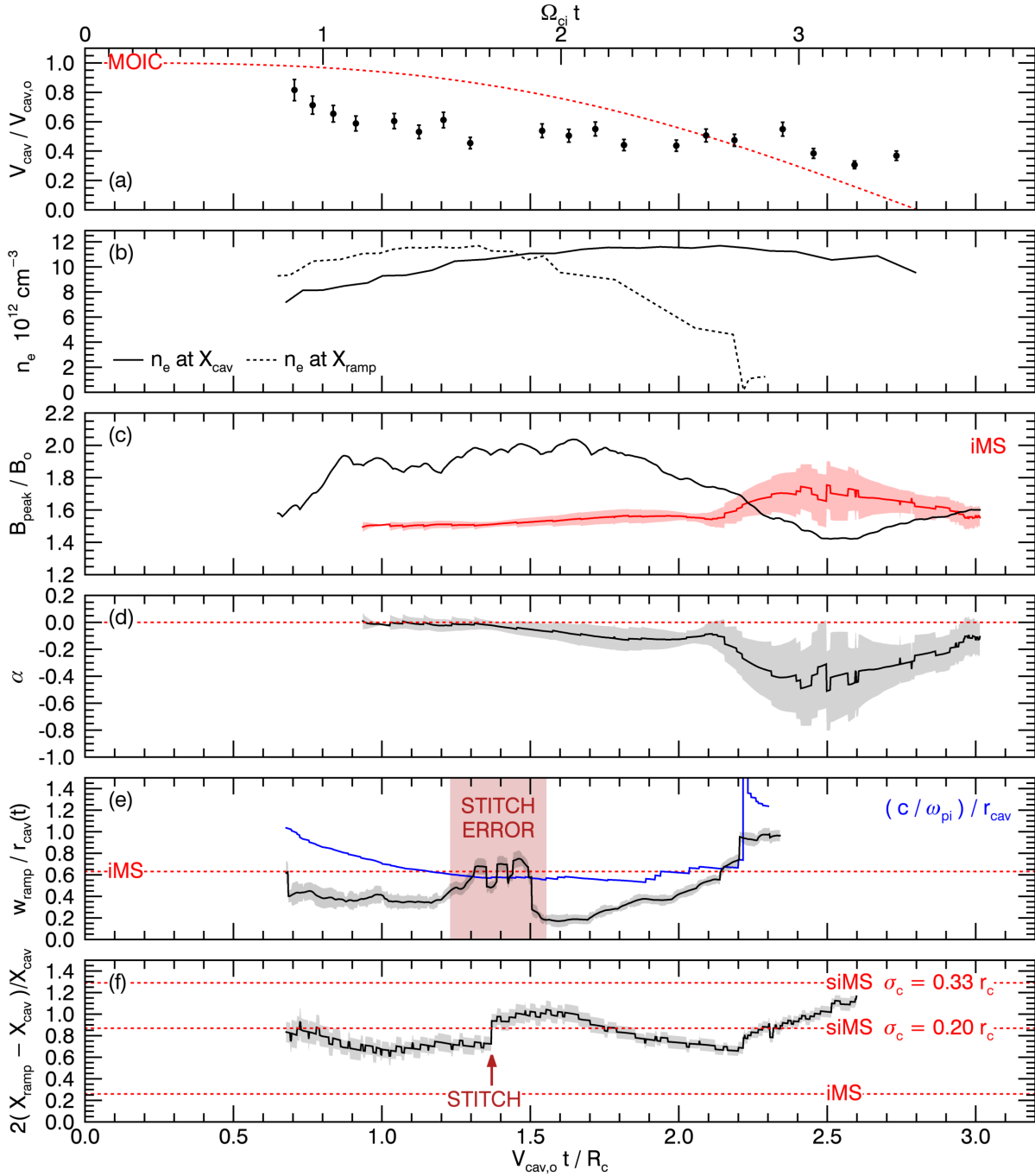


Figure 3.15: Cavity values for Run17 of the 2013 Oct. LaPD-Phoenix campaign. Figure (a) shows the normalized cavity expansion velocity, (b) the ambient-density at X_{cav} (solid) and X_{ramp} (dash), (c) peak magnetic field compression, (d) magnetic field inside the cavity $\alpha = B_{inside}/B_o$, (e) normalized ramp width (defined in equation 3.73), and (f) normalized cavity-ramp separation Δ_{cr} (defined in equation 3.75).

which is reached when $V_{cav,o} t/R_c = 1.64$ ($0.708 \mu\text{s}$) and the cavity edge is $X_{cav} = 1.22R_c$ (25.9 cm). After the cavity achieves its largest compression, the compression promptly decays as the compression ramp X_{ramp} leaves the high ambient-density region, see figure 3.15b. When the compression is near its strongest, $V_{cav,o} t/R_c \approx 0.9$ to 1.7, the background field is compressed by $0.4B_o$ to $0.5B_o$ over the iMS predicted peak compression.

Over the deceleration phase and during the high field compression ($V_{cav,o} t/R_c \lesssim 1.7$), the compression ramp width remains significantly steeper than the predicted iMS width (figure 3.15e). Unlike Run04 of the 2013 January LaPD-Phoenix campaign (figure 3.13e), the compression ramp for Run17 has already begun steepening by the time it reached the closest measurement location; again, giving credence to the idea that the ‘enhanced’ deceleration started before the first measurement. Run17 produces the steepest compression ramp of all the experimental datasets, achieving $w_{ramp}/r_{cav} = 0.18$ ($w_{ramp} = 0.30 c/\omega_{pi}$) over $1.55 \lesssim V_{cav,o} t/R_c \lesssim 1.70$. This is 3.5x steeper than the iMS ramp width and 1.8x steeper than the ramp width achieved by Run04 of the 2013 January LaPD-Phoenix campaign. The ramp width also begins to grow when the compression begins to decay ($V_{cav,o} t/R_c \gtrsim 1.7$), or as X_{ramp} leaves the high ambient-density.

To give a reference to the compression ramp growth and steepening, figure 3.16 plots three magnetic field profiles, each for a separate time-frame of $V_{cav,o} t/R_c = 1.06$ (blue), 1.56 (black), and 2.08 (orange). All three profiles have similar magnetic fields inside the cavity ($-0.1 \lesssim \alpha \lesssim 0.0$) and similar normalized cavity edge (diamagnetic current layer) widths. The early and late time-frames share similar peak compressions and compression ramps, which are still weaker and broader than the intermediate time-frame but stronger and steeper than the iMS model (dash-dot). The intermediate time-frame is an example of the cavity profile when the compression is near its strongest and steepest. In this time-frame, the compression quickly grows to $B_{peak}/B_o \approx 1.9$ over $w_{ramp}/r_{cav} = 0.18$ and stays highly compressed until the cavity edge, a spanned distance of $\sim r_{cav}$. The observed dip in the compression is from the stitching of data between probe locations 33.4 cm ($1.57R_c$) and 34.3 cm ($1.62R_c$). The weaker compression values of positions 30.4 cm ($1.43R_c$), 31.4 cm

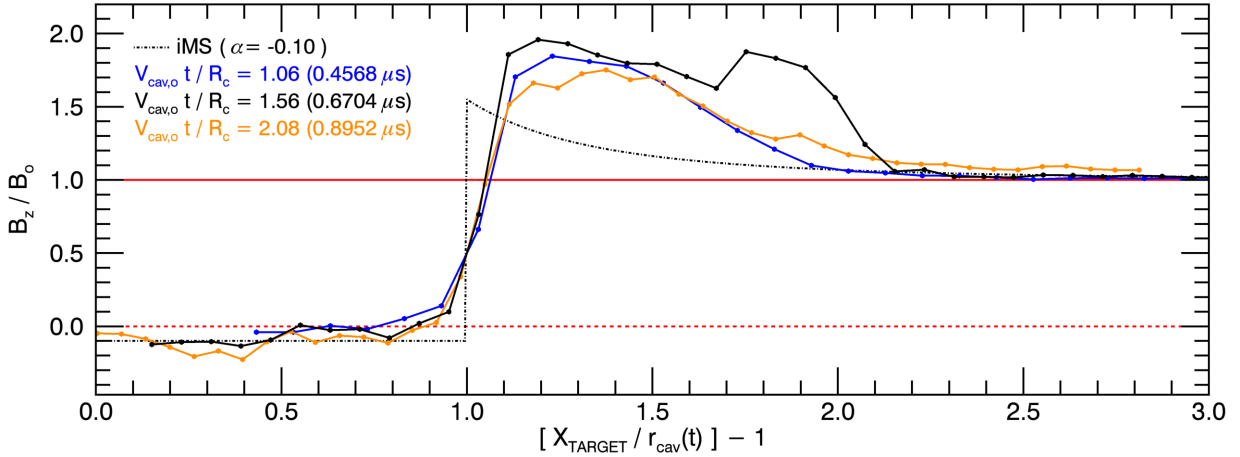


Figure 3.16: Three magnetic field profiles for Run17 of the 2013 Oct. LaPD-Phoenix campaign. Each profile corresponds to a separate time frame in the expansion: early (blue), intermediate (black), and late (orange). The early time ($V_{cav,o}t/R_c = 1.06$) is just after the ‘enhanced’ deceleration phase and before the compression reaches its strongest. The intermediate time ($V_{cav,o}t/R_c = 1.56$) corresponds to when Run17 has reached its shock-like conditions just before X_{ramp} exits the high ambient-density. In the late time ($V_{cav,o}t/R_c = 2.08$) X_{ramp} has left the high ambient-density and the compression has decreased and grown broader. As a reference, the iMS magnetic profile (dash-dot) is overlayed.

($1.48R_c$), 32.4 cm ($1.52R_c$), and 33.4 cm ($1.57R_c$) are a consequence of the probe shadowing.

The correlation of the deceleration, compression growth, and compression steepening features with each other and with the passage of X_{ramp} through the high ambient-density indicates a debris-ambient coupling. This coupling serves to drive a cross-field current in the compression ramp (see discussion in §3.5), but is not sufficient proof for shock generation. Run04 of the 2013 January campaign did not satisfy shock conditions because it did not meet the Rankine-Hugoniot jump condition and did not show evidence of separating from the cavity. This is not the case for Run17. Firstly, the compression front does show a weak growth of the cavity-ramp separation Δ_{cr} (equation 3.75), see figure 3.15f. Recall, a constant Δ_{cr} means $X_{ramp} \propto X_{cav}$ and the compression ramp is still connected to the cavity; whereas, a $\partial_t \Delta_{cr} \neq 0$ means the compression ramp is expanding independently from X_{cav} (assuming

the normalized diamagnetic current layer remains constant). Looking to figure 3.16, this assumption on the diamagnetic current width is reasonable for Run17. Before the stitch jump ($1.0 \lesssim V_{cav,o}t/R_c < 1.37$) and after the stitch jump ($1.37 < V_{cav,o}t/R_c \lesssim 1.6$) there is a weak growth in Δ_{cr} , growing from $\Delta_{cr} = 0.61$ to 0.76 before the stitch and $\Delta_{cr} = 0.93$ to 1.04 after the stitch. That is a 25% increase in the cavity-ramp separation before the stitch and a 12% increase afterwards. After $V_{cav,o}t/R_c \sim 1.6$ the cavity-ramp separation begins to decrease as the compression front loses its strength and the cavity edge begins to catch up.

Secondly, Run17 has to be consistent with the Rankine-Hugoniot jump conditions, discussed in §1.1. When Run17 is at its steepest ($1.55 \lesssim V_{cav,o}t/R_c \lesssim 1.70$), the compression ramp X_{ramp} is expanding at $V_{ramp} = 4.1(\pm 0.2) \times 10^7$ cm/s with a local Alfvénic Mach number of $M_A = 2.0(\pm 0.1)$; whereas, the cavity edge X_{cav} is expanding at $V_{cav} = 2.7(\pm 0.2) \times 10^7$ cm/s with a local Mach number of $M_A = 1.3(\pm 0.1)$. For low β and M_A shocks, the Rankine-Hugoniot jump conditions dictate the compress goes like M_A ($B_{peak}/B_o \sim M_A$), see figure 1.2. Run17 is consistent with the jump conditions, since the observed compression front is expanding at $M_A = 2.0(\pm 0.1)$ and the the compression jump is $B_{peak}/B_o \approx 2.0$. Thus, Run17 also satisfies the conditions for a quasi-perpendicular, resistive, sub-critical collisionless shock.

Examining all the case studies thus far (Run03 of the 2011, Run03 and Run04 of the 2013 January, and Run17 of the 2013 October LaPD-Phoenix campaign), there is a trend of improved coupling as $(c/\omega_{pi})/r_{cav}$ decreases. In Run03 of 2011 the lowest value for $(c/\omega_{pi})/r_{cav}$ is 2.8 as compared to 1.4 for Run03 of 2013 January, 1.0 for Run04 of 2013 January, and 0.5 for Run17 of 2013 October. Run17 is the only case that reached shock-like conditions and is the only case in which the ambient-ion inertial length is less than the scale length of the iMS piston, $(c/\omega_{pi})/r_{cav} = 0.5 < 0.63$. More case studies need to be performed to verify this trend, but the trend is consistent with the findings made by N. Omidi *et al.* (2002)[60] on their hybrid simulations of the interaction between the solar wind and magnetized asteroids.

Requiring the ambient-ion inertial length c/ω_{pi} to be less than the scale length of the

iMS compression ramp

$$\frac{c/\omega_{pi}}{r_{cav}} < 0.63 \quad (3.82)$$

is consistent with the shock criterion discussed by S. E. Clark *et al.*(2013)[13] that requires $R_M/\rho_d > 0.7$ for a H^+ ambient-plasma and C^{+4} debris-plasma. Through specific parameter ratios $r_{cav}/(c/\omega_{pi})$ and R_M/ρ_d can be related to each other. First, let $\delta = r_{cav}/R_c$, $R_c = R'_B = (2/3)^{1/3}M_A^{2/3}R_M$ (equation 3.12), and

$$c/\omega_{pi} = \frac{V_A}{\Omega_{ca}} = \frac{\rho_d}{M_A} \left(\frac{m_a}{m_d} \right) \left(\frac{Z_d}{Z_a} \right), \quad (3.83)$$

where $M_A = V_{cav,o}/V_A$, $\rho_d = V_{cav,o}/\Omega_{cd}$, a represents an ambient-ion value, and d represent a debris-ion value. Then equation 3.82 can be rewritten as

$$\frac{r_{cav}}{c/\omega_{pi}} = \frac{R_M}{\rho_d} \left\{ \left(\frac{m_d}{m_a} \right) \left(\frac{Z_a}{Z_d} \right) \delta \left(\frac{2}{3} \right)^{1/3} M_A^{5/3} \right\} > 1.59 \quad (3.84)$$

$$\implies \frac{R_M}{\rho_d} > \frac{1.82}{\delta} \left(\frac{m_a}{m_d} \right) \left(\frac{Z_d}{Z_a} \right) M_A^{-5/3}. \quad (3.85)$$

To establish an upper limit for the inequality let $M_A = 1$. For a H^+ ambient and C^{+4} debris $(m_a/m_d)(Z_d/Z_a) = 1/3$ and equation 3.85 yields

$$\frac{R_M}{\rho_d} > \frac{0.61}{\delta}. \quad (3.86)$$

Imposing that the condition has to occur by the end of the expansion ($\delta = 1$) then the criterion gives $R_M/\rho_d > 0.61$, which is roughly in line with the findings by S. E. Clark *et al.*(2013).[13] However, the experimentally the best coupling occurred when $V_{cav,o}t/R_c \sim 1.6$ and $X_{cav} \sim 1.2R_c$ which gives $\delta \sim 0.6$ and $R_M/\rho_d > 1.02$. At the moment the physical implications of the condition $(c/\omega_{pi})/r_{cav} < 0.63$ is unknown, but the ratio is consistent with simulation based criterion[13, 60].

In summary, Run17 is the first experimental case to exhibit debris-ambient coupling characteristics as well as satisfying collisionless shock conditions. There is a period of ‘enhanced’ deceleration that is 8.8x stronger than a similar vacuum (MOIC) expansion. The peak compression grows to $B_{peak}/B_o = 2.0$, a nearly $0.5B_o$ compression above the iMS prediction. At the same time the compression ramp steepens to $w_{ramp}/r_{cav} = 0.18$ ($w_{ramp} = 0.30 c/\omega_{pi}$),

which is 3.5x steeper than the iMS model. To satisfy shock conditions, the compression ramp exhibits a weak decoupling from the cavity with a mild growth in the normalized cavity-ramp separation $\partial_t \Delta_{cr} > 0$, as well as, satisfying the Rankine-Hugoniot jump conditions with $B_{peak}/B_o = 2.0$ when $M_A = 2.0(\pm 0.1)$. Additional datasets need to be acquired to confirm the trend, but current experiments suggest that debris-ambient coupling will not be sufficient enough to drive a shock until the ambient-ion inertial length is less than the characteristic scale length of the iMS compression ramp, $(c/\omega_{pi})/r_{cav} < 0.63$. This observation is consistent with findings from hybrid simulations[13, 60].

CHAPTER 4

Comparison to Recent Experiments

In recent years, several experiments at UCLA have investigated the collisionless interaction between an expanding LPP and the ambient-plasma of the LaPD[5, 7–9, 13, 15–17, 75]. These investigations have been able to observe, build on, and report concepts discussed within this dissertation. Utilizing high repetition rate (1 Hz) laser systems, they have been able to make volumetric measurements of the magnetic field and the electrostatic component of the electric field (electrostatic field) associated with the cavity. Doing so allows for approximate calculations of the current structures associated with the cavity. The following section will briefly compare the work in this dissertation to these other works.

In J. Bonde (2016)[9] (doctoral dissertation) datasets are compared to an equation-of-motion derived by Lord Rayleigh[67] and found to be in good agreement; same as the comparison done with the LaPD-Phoenix experiments and the MOIC equation-of-motion in figure 3.5. To follow, it is shown that the MOIC equation-of-motion is the same as the one utilized by Bonde[9] (Lord Rayleigh’s equation-of-motion). The equation-of-motion used by Bonde is

$$\partial_{\tilde{\tau}}\tilde{R} = \sqrt{1 - \frac{1}{\beta}(\tilde{R}^3 - 1)}, \quad (4.1)$$

where

$$\beta \equiv \frac{C}{D} \frac{\frac{1}{2}N_d m_d V_o^2}{(B_o^2/2\mu_o) (\frac{4}{3}\pi R_o^3)} = \frac{C}{D} \left(\frac{R_B}{R_o}\right)^3 = \frac{\text{initial directed radial energy density}}{\text{magnetic field energy density}}, \quad (4.2)$$

$\tilde{\tau} = t/t_o$, t_o is some time during the cavity expansion, $\tilde{R} = r/R_o$, $R_o = r(t_o)$ is the cavity radius at time t_o , R_B is the magnetic-stopping radius (equation 3.4), $V_o = v(t_o)$ is the cavity expansion velocity at time t_o , N_d is the number of debris-ions, m_d is the debris-ion mass,

and C and D are correction constants for the profile-averaged values of the cross-field kinetic energy and magnetic field energy, respectively (this is clearer in equation 4.3). The Rayleigh equation-of-motion is derived from the following time-dependent system energy

$$E_{sys} = \frac{C}{2} N_d m_d [\partial_t r(t)]^2 + D \frac{B_o^2}{2\mu_o} \left\{ \frac{4}{3} \pi [r(t)]^3 \right\}, \quad (4.3)$$

where $r(t)$ is the time-dependent cavity radius and $\partial_t r(t)$ is the time-dependent cavity radial expansion velocity. When comparing to datasets, Bonde utilizes $\beta = (R_B/R_o)^3$ and, thus, imposes that $C = D = 1$. With $C = D = 1$, equation 4.3 is the time-dependent system energy that is used by the MOIC scheme (equation 3.25). Since both models use the same time-dependent system energy, they produced the same equation-of-motion for the cavity expansion.

The Rayleigh equation-of-motion (equation 4.1) and the MOIC equation-of-motion (see footnote¹) appear different for two reasons: (1) the choice of normalizations and (2) the point in the expansion when the constant system energy E_o is defined. These two factors do not fundamentally change the equation-of-motion. The Rayleigh scheme allows for the constant system energy to be defined at any time t_o in the cavity expansion,

$$\begin{aligned} E_o = E_{sys}(t = t_o) &= \frac{C}{2} N_d m_d V_o^2 + D \frac{B_o^2}{2\mu_o} \left\{ \frac{4}{3} \pi R_o^3 \right\} \\ &= \frac{C}{2} N_d m_d V_o^2 (1 + \beta^{-1}) \end{aligned} \quad (4.4)$$

where $V_o = \partial_t r(t)|_{t_o}$ and $R_o = r(t_o)$. The MOIC scheme specifically uses $t_o = 0$ as the point in time to define E_o , which corresponds to values of $R_o = 0$ and $\beta^{-1} = 0$. The Rayleigh equation-of-motion results from subtracting equation 4.4 and 4.3 and imposing Bonde's normalizations to give equation 4.1. Instead of taking $t_o = 0$, Bonde uses the laser pulse width to define $t_o (= 1.93 \text{ ns})$ and the spot size to define $R_o (= 250 \text{ } \mu\text{m})$, and empirical scaling relations[29, 34, 35, 55] to define V_o and N_d . This results in a $\beta \sim 6 \times 10^5$, which

¹The MOIC equation-of-motion (§3.3, equation 3.28 -- $\partial_\tau^2 \chi = -\frac{3}{2} \chi^2$) can be reduced to a non-linear 1st-order partial differential equation by means of separation of variables. This results in $(\partial_\tau \chi)^2 = 1 - \chi^3$, where $\partial_\tau \chi = 1$ and $\chi = 0$ when $\tau = 0$.

means $1 + \beta^{-1} \approx 1$ and equation 4.4 reduces to $E_o = E_{sys}(t = 0)$. As a result, equation 4.1 can be written as

$$\begin{aligned}
\partial_{\tilde{\tau}} \tilde{R} &= \sqrt{1 - \frac{1}{\beta} (\tilde{R}^3 - 1)} \\
&= \sqrt{1 + \beta^{-1} - \beta^{-1} \tilde{R}^3} \\
&\approx \sqrt{1 - \beta^{-1} \tilde{R}^3} \\
\frac{\partial t}{\partial \tilde{\tau}} \frac{\partial}{\partial t} \left(\frac{r}{R_o} \right) &\approx \sqrt{1 - \left(\frac{R_o}{R_B} \right)^3 \left(\frac{r}{R_o} \right)^3} \\
t_o \frac{\partial}{\partial t} \left(\frac{r}{R_o} \right) &\approx \sqrt{1 - \left(\frac{r}{R_B} \right)^3} \\
\frac{\partial_t r}{V_o} &\approx \sqrt{1 - \left(\frac{r}{R_B} \right)^3} \tag{4.5}
\end{aligned}$$

and imposing the MOIC normalization (equation set 3.27) gives the MOIC equation-of-motion,

$$\partial_{\tau} \chi = \sqrt{1 - \chi^3}. \tag{4.6}$$

Thus, the MOIC equation-of-motion is the case of Rayleigh's expression when V_o and R_o are defined at $t_o = 0$, and the comparison by Bonde[9] and in figure 3.5 adds further validation of the Rayleigh/MOIC equation-of-motion as a model for the cavity expansion.

Bonde[9] also examines the effect of an additional external pressure on the cavity expansion. This external pressure p_{ext} is considered to act in the same way as the magnetic pressure p_B (i.e. $p_{ext} \propto r^3$). Implementing p_{ext} , Rayleigh's equation-of-motion can be augmented to give

$$\partial_{\tilde{\tau}} \tilde{R} = \sqrt{1 - \frac{1 + \Gamma}{\beta} (\tilde{R}^3 - 1)} \tag{4.7}$$

where $\Gamma = p_{ext}/p_B$. Here $\Gamma = 0$ returns the Rayleigh equation-of-motion and $\Gamma = -1$ is a free expansion. The data compared by Bonde[9] (figure 2.4 therein) is collected from Bonde's work, Collette[17] (figure 3.13a therein), and Dimonte[22] (figure 3a therein). This data and the two case from the LaPD-Phoenix experiments (figure 3.5) are plotted in figure

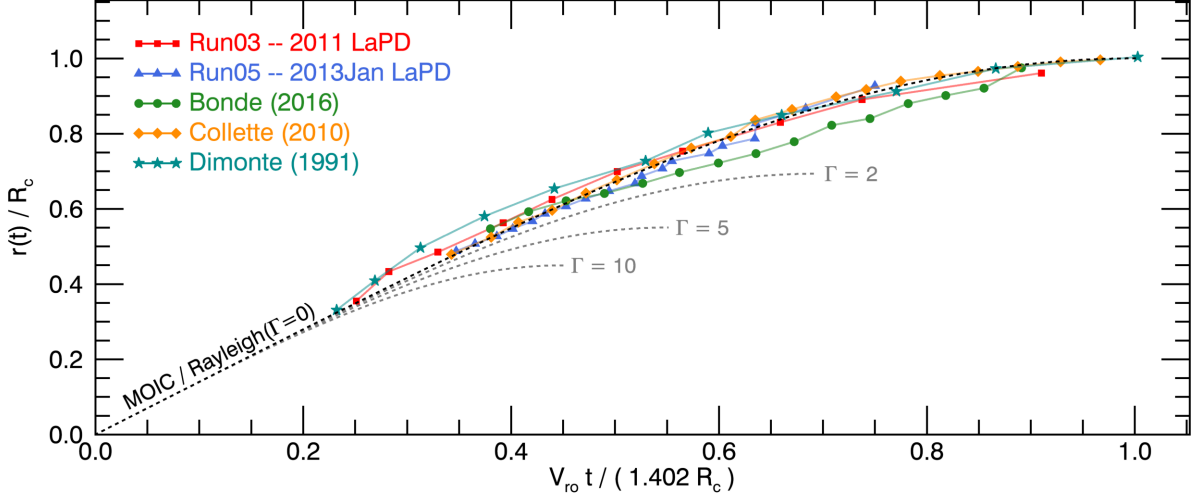


Figure 4.1: A comparison of the Rayleigh/MOIC expansion model with the two expansion cases from figure 3.5 and the three datasets compared by Bonde[9] (figure 2.4 therein). The cavity radius is normalized to the maximal cavity radius R_c and the expansion time is normalized to the characteristic expansion time $1.402 R_c/V_{ro}$, where V_{ro} is the initial radial expansion velocity. For a reference, equation 4.7 is plotted in grey to represent expansions with added external pressures p_{ext} on the cavity with values of $\Gamma = 2, 5,$ and 10 .

4.1 along with several values for Γ . For these vacuum-like expansions, the Rayleigh/MOIC equation-of-motion ($\Gamma = 0$) depicts the cavity expansion well and any p_{ext} is negligible.

The iMS and siMS models prescribe a single azimuthal diamagnetic current layer for a spherical cavity that is proportional to $\sin \theta$ ($J_\phi \propto \sin \theta$ as in equation 3.42 of §3.4). This specifies that the magnitude of the diamagnetic current will decrease towards the poles of the cavity, or in xy -planes with larger z -values. This same behavior, while not directly compared against $\sin \theta$, is observed by Collette *et al.*[15–17] (figure 3.9a in Collette[17]) for a quasi-perpendicular, sub-Alfvénic expansion produced by a 1.2 J laser pulse. The reduced current density at the poles of the cavity is most likely a geometric effect resulting from the decreasing enclosed area of the diamagnetic current loop. However, not encompassed by the iMS or siMS models, Collette also observes a J_z component to the current density that transitions from $-\hat{z}$ in the cavity trough to $+\hat{z}$ when the diamagnetic current is at its

strongest and then back to $-\hat{\mathbf{z}}$ just outside the cavity (see figure 3.9b in [17], figure 5 in [15], and figure 5 in [16]). This results in a diamagnetic current layer that, in the $-\hat{\mathbf{z}}$ hemisphere of the cavity, twists towards the cavity pole inside the cavity and twists towards the cavity equator on the edge of the cavity. Thus, while the azimuthal current J_ϕ of the MOIC model and experimental cavity are consistent, the model does not encompass the axial current J_z observed by Collette *et al.*[15–17]. The origin for this this complex current structure is not well understood.

Bonde *et al.*[8, 9] collected volumetric measurements of the magnetic field and plasma potential (from emissive probes) for a quasi-parallel, ‘marginally’ Alfvénic cavity expansion ($v_{exp} \sim V_A$) that was produced from a 1 J Nd:YAG laser. For the first time, the electrostatic field is deduced from the plasma potential and compared to the magnetic structure. In this dataset, no steepening of the magnetic compression is reported, but the cavity does produce a strong radially-inward electric field inside the cavity and, a weaker, outward electric field outside the cavity (figure 2 in [8] and figure 4.11 in [9]). The flip in the electric field direction from $-\hat{\mathbf{r}}$ to $+\hat{\mathbf{r}}$ occurs across the peak of the magnetic compression. The electric field inside the cavity corresponds to the space-charge electric field that forms the diamagnetic current. The upstream electric field persists as the cavity expands but rapidly diminishes when the cavity stagnates. This result is consistent with the iMS coupling hypothesis (discussed at the end of §3.5), where the radial $\mathbf{E} \times \mathbf{B}$ -drift on the electrons will cause a space-charge separation in the compression ramp that results in a radially-outward electric field. This $\mathbf{E} \times \mathbf{B}$ -drift is proportional to the expansion speed of the cavity (equation 3.80), so when the cavity stagnates the driver for the space-charge separation also stagnates.

Bondarenko *et al.*[5, 7] identified debris-ambient coupling in a quasi-perpendicular cavity expansion and computed an electric field that is consistent with the iMS inductive electric field. The data was collected in a LaPD-Phoenix experiment with a $B_o = 710$ G and a cavity expansion of $v_{exp} \sim 10^7$ cm/s. Bondarenko used emission spectroscopy to measure a Doppler broadening of an ambient-ion spectral line (He II, 468.6 nm) as the cavity passed over the ambient-plasma. The diagnostic was aligned to collect light along a $+\hat{\mathbf{y}}$ line-of-sight. The

observed asymmetric broadening corresponds to an asymmetric acceleration of the He II ions that is perpendicular to \mathbf{B}_o and the expansion of the cavity $\hat{\mathbf{n}}$. According to the Doppler broadening, the He II ions gained velocity components that are 10^2 times larger than the root-mean-square velocity of the unperturbed ambient-ions. Bondarenko calculated this acceleration to be consistent with an unmagnetized He II ion in an azimuthal-like electric field on the order of 10^2 V/cm. The iMS model provides an azimuthal inductive electric field (equation 3.78), which, given the experimental B_o and v_{exp} , predicts a maximum field strength on the order of 10^2 V/cm.

Clark *et al.* has provided 2D-hybrid simulations for the LaPD-Phoenix experiments[13] that are consistent with the analytical models within the MOIC scheme. The simulation performed by Clark represents a LaPD-Phoenix experiment with $M_A \sim 2$, $V_o \sim 2.5 \times 10^7$ cm/s, $n_i = n_o \sim 10^{13}$ cm $^{-3}$, and $B_o \sim 200$ G. Figure 2 within Clark *et al.*[13] shows an expansion event that expands to a maximal radius $R_c \sim 4.3 c/\omega_{pi}$ in a time period of $t_{exp} \sim 3.1 \Omega_{ci}^{-1}$. In the MOIC normalized coordinates (equation set 3.27), this corresponds to an expansion time of $\tau_{exp} = V_o t_{exp} / R_c \sim 1.4$, which is the MOIC expansion time. Additionally, the simulated electric field structure is azimuthal-like except at the cavity edge and steepened magnetic compression (figure 3 in [13]). At these locations the radial component dominates the electric field. This is consistent with the iMS model and coupling hypothesis, since the azimuthal field corresponds to the inductive electric field and the strong radial electric fields are associated with driving the diamagnetic current and the shock-front current. The simulated radial electric field also follows the observations of Bonde *et al.*[8, 9], in which the field points in the $-\hat{\mathbf{r}}$ direction inside the cavity and the $+\hat{\mathbf{r}}$ direction in the magnetic compression. These consistences help bolster confidence in the simulations.

The findings and coupling hypothesis of the MOIC model presented in this dissertation are consistent with recent experiments. This is a valuable agreement, because the MOIC model provides a straightforward methodology for identifying and quantifying debris-ambient coupling within the experiment (discussed in §3.5) and explains how the field structure arises and evolves throughout the expansion. Whereas past experiments utilized complex

diagnostics (emissive probe and emission spectroscopy) to identify debris-ambient coupling, the methodology of the MOIC model is a simple and quick way of determining coupling from just flux probe measurements. This is an invaluable tool when it comes to the LaPD-Phoenix type experiments where the collected data is limited.

The most notable agreement with past works and this dissertation is with Bonde *et al.*[8]. Bonde succeeded in measuring and correlating the magnetic field and electrostatic field of an expanding cavity. This was achievable since Bonde's experiment was not limited by a low repetition-rate laser. Though the findings are consistent with the iMS coupling hypothesis, the cavity produced is 'marginally' Alfvénic ($M_A \sim 1$) and shows no signs of steepening in the magnetic profile. These measurements still need to be collected for a super-Alfvénic expanding cavity that exhibits shock-like features in the magnetic compression, similar to Run17 conditions (discussed in §3.6).

CHAPTER 5

Conclusion

The goal of this dissertation was to produce, identify, and quantify the magnetic characteristics associated with coupling of energy and momentum from a LPP (debris-plasma) into a magnetized ambient-plasma with the use of a driven magnetic piston (debris-ambient coupling). Understanding the coupling mechanism is key to developing the knowledge behind the physics associated with driving a resistive, quasi-perpendicular magnetized collisionless shock. To achieve this goal a simple analytical model was developed to characterize the behavior of a “magnetic-only interacting cavity” (MOIC), that is, a diamagnetic cavity that only interacts with the background magnetic field. The MOIC model includes a scaling for the maximal cavity radius (§3.2), an equation-of-motion that predicts the trajectory of the cavity expansion (§3.3), as well as, the magnetic and electric field structure for a diamagnetic cavity with an infinitely thin diamagnetic current layer and a diamagnetic cavity with a radial distribution (§3.4). All these models are validated against experimental cases that satisfy the assumptions of the models and, thus, allowing for the development of benchmarks to quantify the behavior of all experimental cavities and the strength of their magnetic piston (§3.5). With these benchmarks the advent of debris-ambient coupling can be identified and quantified.

Auxiliary goals for the dissertation included: (1) to drive and identify a subcritical, quasi-perpendicular collisionless shock and (2) use the MOIC model to develop a physical picture for the coupling and guide future experiments. Though the experimental shock-like event only had a weak decoupling from the cavity expansion, it did satisfy the necessary Rankine-Hugoniot jump conditions.

The principal findings of this dissertation include:

- Proton deflection measurements from the Trident campaign indicate that, even though the LPP is not an ideal point explosion, the diamagnetic cavity resembles a point explosion as it expands with one edge still residing at the target surface.
- ‘Weak’ experimental cavities, those with $B_{peak}/B_o \lesssim 1.4$, trend with the scaling of the magnetic-stopping radius R_B (equation 3.6) to give an empirical formula (equation 3.8) relating the cavity size to the laser energy and background magnetic field. If the magnetic energy of the cavity compression is taken into account, then this empirical formula yields a laser energy to debris-energy coupling efficiency of 14.0 ± 2.0 %. Cavities with super-Alfvénic Mach numbers ($M_A \gtrsim 1$) and strong compressions ($B_{peak}/B_o \gtrsim 1.5$) fall off the trend of the R_B -scaling. This indicates that a few experimental runs have had some of their debris-energy diverted from expelling the magnetic field.
- The MOIC model provides four key expansion and magnetic compression characteristics for a diamagnetic cavity. These parameters agree with ‘weak’ and vacuum experimental cavities, which allows them to be used as baseline values for future observations. The MOIC benchmarks are as follows:
 1. An equation-of-motion (equation 3.28) that predicts the trajectory of the cavity expansion. It accurately predicts the expansion time of a MOIC-like (vacuum) cavity to be $V_{cav,o} t / R_c = 2.8$. Any deceleration stronger than this model indicates that the debris-plasma is losing energy into ‘other channels’ besides expelling the background magnetic field.
 2. The maximum magnetic compression a diamagnetic cavity can produce is modeled by an ‘ideal’ magnetized sphere (iMS) and is only dependent on the expulsion value of the background field (equation 3.68). Spreading out the diamagnetic current only serves to weaken the compression. For a cavity that fully expels the background field ($\alpha = B_{inside}/B_o = 0$), this peak compression is $B_{peak}/B_o = 1.5$. Any observed

compression above this value, without additional expulsion, indicates the generation of additional current structures beyond the diamagnetic current.

3. The compression ramp of a diamagnetic cavity is always normalized to an effective cavity radius to give an upstream field decay of $(r_c/r)^3$. Here, only the normalizing radius is dependent on the diamagnetic current distribution. Defining the width of this ramp as in equation 3.73, the iMS model has a constant normalized width of $w_{ramp}/r_c \approx 0.63$. Similar to the peak compression, a steepening of the compression ramp (i.e. $w_{ramp}/r_c < 0.63$) indicates the generation of additional current structures, but this current has to be driven where the steepening occurs.
 4. The distance between the center of the compression ramp X_{ramp} (where $B = 0.5(B_{peak} + B_o)$) and the cavity edge is normalized to the cavity radius. With the cavity-ramp separation Δ_{cr} defined as in equation 3.75, the iMS separation is constant at $\Delta_{cr} \approx 0.26$. Using this definition, the compression front is tied to the cavity ($X_{ramp} \propto X_{cav}$) if $\Delta_{cr} = \text{constant}$ and begins to diverge when $\partial_t \Delta_{cr} > 0$.
- Exceeding the first three MOIC benchmarks, indicates that the cavity is driving current upstream in the compression ramp that is both perpendicular to the expansion and \mathbf{B}_o , but is not necessarily strong enough to form a shock. When experiments exceed the first three benchmarks, they happen in correlation with each other and in correlation with the compression ramp passing through the high ambient-density. This means that as the upstream current is being driven in the compression front, the debris is losing energy at an expedited rate.
 - Run04 of the 2013 January LaPD-Phoenix campaign exhibits debris-ambient coupling but does not reach shock-like conditions. It experiences an ‘enhanced’ deceleration that is 4x stronger than the MOIC, has a compression growth up to $B_{peak}/B_o = 1.81$ that is 16% stronger than the iMS model, and a steepening to $w_{ramp}/r_{cav} = 0.33$ that is 1.9x steeper than the iMS model. However, the cavity-ramp separation Δ_{cr} remains constant.

- Run17 of the 2013 October LaPD-Phoenix campaign exhibits debris-ambient coupling and satisfies shock conditions, albeit with only a weak separation from the cavity. It experiences an ‘enhanced’ deceleration that is 8.8x stronger than the MOIC, has a compression growth up to $B_{peak}/B_o = 2.0$ that is $0.5B_o$ stronger than the iMS model, and a steepening to $w_{ramp}/r_{cav} = 0.18$ that is 3.5x steeper than the iMS model. There is a weak growth in the cavity-ramp separation when the compression front is at its steepest and the magnetic jump across the compression ramp satisfies the Rankine-Hugoniot jump conditions, $B_{peak}/B_0 = 2.0 \sim M_A$ when the local Alfvénic Mach number of the compression front is $M_A = 2.0 \pm 0.1$.
- Previous work on hybrid simulations[13, 60] attempted to develop a criterion for generating shocks. S. E. Clark *et al.* (2013)[13] set the criterion of $R_M/\rho_d > 0.7$ for a H^+ ambient-plasma and a C^{+4} debris-plasma, which, through some parameter ratios, is equivalent to the results of N. Omidi *et al.* (2002)[60], namely that the ambient-ion inertial length must be less than the scale length of the piston. Further work needs to be done, but experiments do agree with these conditions. As $(c/\omega_{pi})/r_{cav}$ decreases, the strength of the debris-ambient coupling increases. Run17 is the only case that meets the shock-like conditions and is the only case in which the ambient-ion inertial length is less than the scale length of the iMS compression, $(c/\omega_{pi})/r_{cav} = 0.5 < 0.63$.
- The MOIC model does provide a coupling mechanism that explains all the observed coupling indicators and sets up the subcritical, quasi-perpendicular collisionless shock picture (figure 1.3). However, additional experiments are needed to explore the mechanism. The theorized mechanism is similar to how the diamagnetic current is driven. As the cavity expands an azimuthal inductive electric field is created upstream in the compression ramp. Since the ambient-ions are unmagnetized, the electrons experience a radial $E \times B$ -drift that pushes them upstream. This creates a radial space-charge electric field that serves to pull the ambient-ions forward and produce a secondary $E \times B$ -drift on the electrons. This secondary $E \times B$ -drift drives an electric current in a non-diamagnetic manner that is perpendicular to the expansion and \mathbf{B}_o . The resulting

electric current reduces the magnetic field upstream and strengthens it downstream, resulting in steepening and compression growth. The downstream compression growth increases the total ‘background field’ inside the cavity by $\delta\mathbf{B}$ to $\mathbf{B}_0 + \delta\mathbf{B}$. A diamagnetic cavity always works to fully expel the background field, so the diamagnetic current is driven harder to expel $\delta\mathbf{B}$ and does so by slowing the expanding debris-ions.

This is the point where the MOIC model needs to evolve to include a 1st-order interaction between the cavity and ambient-plasma, and experiments need to study the compression steepening in more detail. They specifically investigate the setup of the space-charge electric field that is crucial for driving the cross-field electric current. Experiments should correlate emissive probe measurements of the plasma potential with steepening of the compression ramp to check if the two correlate and to determine if the correlation has a ‘turn-on’ when $(c/\omega_{pi})/r_{cav} < 0.63$. Integrating a 1st-order interaction into the MOIC model that attempts to predict the strength of the space-charge electric field and electric current also has the potential to explain the $(c/\omega_{pi})/r_{cav} < 0.63$ criterion.

APPENDIX A

List of Key Terms/Variables

Table A.1: A list of common terms and variables used throughout this dissertation.

Term/Variable	Description
$\alpha = B_{inside}/B_o$	the ratio of the magnetic field inside a cavity to the background magnetic field
α_{L2D}	the laser energy to debris-energy coupling efficiency.
α -zero iMS/siMS	refers to any iMS or siMS that fully expels the background magnetic field (i.e. $\alpha = 0$)
BaO-NI	Barium-Oxide coated Nickel cathode. The main LaPD cathode.
B_{inside}	the magnetic field inside the diamagnetic cavity. Also referred to as the magnetic field of the cavity trough.
$\mathbf{B}_o = B_o \hat{\mathbf{z}}$	the background magnetic field
B_{peak}	the peak compression associated with the diamagnetic cavity
$\chi = r_b/R_B$	the normalized cavity radius for the MOIC equation-of-motion
$\chi_v = \partial_\tau \chi$	the normalized cavity expansion velocity for the MOIC equation-of-motion
$\chi_g = \partial_\tau^2 \chi$	the normalized effective deceleration of the cavity expansion for the MOIC equation-of-motion
c_{ms}	the angle-independent magnetosonic sound speed
c_{ms}^+	the <i>fast</i> mode phase velocity
c_{ms}^-	the <i>slow</i> mode phase velocity

compression ramp	the upstream region outside the cavity where the magnetic compression growth from B_o to B_{peak} .
CPA	chirp-pulsed-amplification. This is the configuration for the ‘diagnostic’ beam in the Trident experiment when proton radiography is used.
c_s	the sound speed
D_o	experimental system size, or scale length
debris-ambient coupling	see <i>debris-piston-ambient coupling</i>
debris-piston-ambient coupling	refers to the process in which energy is transferred from the expanding LPP debris-ions to the magnetic piston of the diamagnetic cavity and then to the ambient-plasma
Δ_{cr}	the spatial separation between the cavity edge X_{cav} and compression ramp X_{ramp} as defined in equation 3.75 (iMS value in equation 3.76).
Δ_p	the proton radiography deflection of a proton beam through a magnetic field.
Δ_{sh}	the shock-front width
‘diagnostic’ beam	this refers to the third beam line in the Trident experiment that was setup as a diagnostic. It was use for either Thomson scattering or proton radiography.
‘driver’ beam	this refers to the second beam in the Trident platform that generates the debris-plasma
empirical- R_B	this refers to the empirical formula (equation 3.8) relating the experimental cavity radius to the R_B -scaling
HC	Helmholtz Coil

HDPE	high-density polyethylene. A type of plastic polymer composed of a chain of CH ₂ molecules. The material was used as a laser target in both the Trident and LaPD-Phoenix experiments.
‘heater’ beam	this refers to the first beam in the Trident platform that generates the ambient-plasma
iMS	‘ideal’ magnetized sphere. Specifically, a single MS that models a diamagnetic cavity infinitely thin current layer.
LaB ₆	Lanthanum-Hexaboride cathode. The secondary cathode in the LaPD to increase the ambient-plasma density.
λ_{ii}	classical mean-free-path between a coupled, ‘shocked,’ ambient-ion and an upstream ambient-ion
LaPD	Large Plasma Device
LLP	Laser-Produced Plasma
M_c	the critical Alfvénic Mach number in which ion reflection off the shock front starts to occur. For low- β , quasi-perpendicular collisionless shocks this is ~ 2.76 .
M_A	the Alfvénic Mach number
MOIC	Magnetic Only Interacting Cavity. This is a diamagnetic cavity that only works to expel and compress the background magnetic field.
MOIC model	refers to the collection of analytical models that describe a MOIC (the R_B -scaling, the equation-of-motion for an expansion, the iMS model, and the siMS model)
MS	magnetized sphere
MTSI	modified two-stream instability
$\hat{\mathbf{n}}$	the surface normal to the shock/compression front
Ω_{ci}	the ambient-ion cyclotron frequency (in rads/s)

PEENING	the high repetition rate laser used as a seed for the Raptor laser in the Phoenix Lab.
Phoenix laser	the first laser in the Phoenix Lab.
piston-ambient coupling	see <i>debris-piston-ambient coupling</i>
Raptor	the high energy, low repetition rate laser in the Phoenix Lab.
$r_b = r_b(t)$	the time-dependent cavity radius used in MOIC expansion equation-of-motion, see equation 3.25. At the end of the expansion event t_f then $r_b(t_f) = R_B$.
R_B	magnetic-stopping radius, see equations 3.4 and 3.6
R'_B	magnetic-stopping radius that accounts for the energy stored in the compression of the diamagnetic cavity, see equation 3.7
R_B -scaling	refers to the proportionality between the cavity's maximal size $2R_c$ and the set debris- and ambient-parameters for a MOIC, equation 3.6
R_{BM}	the 'hybrid' magnetic-mass radius (see equation 3.14)
R'_{BM}	the 'hybrid' magnetic-mass radius that accounts for the energy in the compressed magnetic field (see equation 3.17)
RCF	radiochromic film
$r_c = r_c(t)$	the time-dependent cavity radius of an expanding iMS or siMS
$r_{cav} = r_{cav}(t)$	the time-dependent cavity radius for an expanding experimental cavity as defined by the magnetic field value of $B = 0.5B_o$. Similar to $r_c(t)$, but the <i>cav</i> label distinguishes the quantity as an experimental one.
R_c	The maximal cavity radius obtained by the experimental cavity or expanding iMS. Also, the MS radius when working in the stationary iMS model.
R_M	equal-mass radius (equation 3.10)

$r_{peak} = X_{peak} - r_{cav}$	see X_{peak}
$r_{ramp} = X_{ramp} - r_{cav}$	see X_{ramp}
RH	Rankine-Hugoniot
ρ_d	directed debris-ion gyroradius
ρ_a	un-shocked ambient-ion gyroradius
ρ'_a	shocked, or coupled, ambient-ion gyroradius
r_{siMS}	the effective cavity radius for a normal-weight siMS, see equation 3.66.
R_*	the equal-charge radius (see equation 3.20)
$\tau = V_o t / R_B$	the normalized time for the MOIC equation-of-motion
σ_c	The standard deviation that defines the width to the normal-weight siMS distribution, see §3.4, and in doing so it defines the width of the diamagnetic current.
siMS	sum of iMS's. This is a sum of of iMS's with some kind of weighted distribution to model a cavity with a finite width to the diamagnetic current layer. The primary siMS model used here is one that applies a radial normal-distribution to the magnetizations of the MS's.
'strong' cavity	an experimental cavity with a peak compression of $B_{peak}/B_o \gtrsim 1.5$
θ_{Bn}	the angle between the background magnetic field \mathbf{B}_o and the shock front surface normal $\hat{\mathbf{n}}$
V_A	the Alfvén velocity
$v_c = v_c(t) = \partial_t r_c$	the time-dependent expansion velocity of the cavity
$V_{cav} = \partial_t X_{cav}$	the experimental time-dependent expansion velocity of the cavity edge (a diametrical expansion velocity)

$V_{cav,o}$	the experimental initial expansion velocity of the cavity. This is calculated with the time-of-flight measurement based on when the cavity edge level of $B = 0.5B_o$ reaches the first bdot probe.
$v_d = v_d(t)$	the time-dependent debris-ion expansion velocity for the MOIC equation-of-motion
V_o	The initial expansion speed of the debris-ions in the MOIC models.
v_p	(1) The piston velocity in <i>R. P. Drake</i> (2000)[23] conceptual model for driving a collisionless shock in the laboratory. (2) the proton velocity for proton radiography
v_{sh}	The collisionless shock velocity in <i>R. P. Drake</i> (2000)[23] conceptual model for driving a collisionless shock in the laboratory.
w_{ramp}/r_c	the normalized width of the compression ramp as defined in equation 3.73 (iMS value in equation 3.74).
‘weak’ cavity	an experimental cavity with a peak compression of $B_{peak}/B_o \lesssim 1.4$
$X_{cav}(t) = 2r_{cav}(t)$	an experimental quantity referring the time-dependent distance from the laser target to the cavity edge where $B = 0.5B_o$. For the experiment, this is the same as the the cavity diameter.
X_{peak}	the distance from the laser target to B_{peak}
X_{ramp}	the distance from the laser target to half way up the compression ramp (where $B = 0.5(B_{peak} + B_o)$)
X_{TARGET}	the distance from the laser target to the point of interest.

APPENDIX B

Magnetized Sphere Derivation

B.1 The Magnetic Field

As discussed in the lead-in of §3.4, a diamagnetic cavity can be represented as a magnetized sphere (MS) of magnetization $\mathbf{M}_o = M_o \hat{\mathbf{z}}$ placed in a background magnetic field of $\mathbf{B}_o = B_o \hat{\mathbf{z}}$. The magnetic field solution for the MS problem is outline by David J. Griffiths[33] (example 6.1 therein) and John D. Jackson[40] (§5.10-5.11 therein). In the MS model the diamagnetic current is represented by the bound current of the MS (equation 3.42). Section 3.4 also argues that the magnetic field solution for a non-relativistic expanding MS is identical to the field solution for a stationary MS. This section will provide the math for MS magnetic field solution picking up form equation 3.39.

The MS solution starts by first solving for the vector potential of the MS, then determining the MS magnetic field, and, finally, adding \mathbf{B}_o to get the full field solution. The generalized vector potential is

$$\mathbf{A}(\mathbf{r}, t) = \frac{\mu_o}{4\pi} \int \frac{\mathbf{J}_b(\mathbf{r}', t)}{|\mathbf{r} - \mathbf{r}'|} d^3r' \quad (\text{B.1})$$

where \mathbf{r}' represents the integration coordinates, \mathbf{r} represents the non-integration coordinates (or points-of-interest), and $\mathbf{J}_b = \nabla \times \mathbf{M}_o$ is the bound current of the MS . The bound current is given by equation 3.42 and plugging it into the above equation reduces the volume integral into a surface integral along the bounding surface of the MS,

$$\begin{aligned} \mathbf{A}(\mathbf{r}, t) &= \frac{\mu_o}{4\pi} \int_V \frac{\delta(r' - r_c(t)) \mathbf{M}_o \times \hat{\mathbf{r}}'}{|\mathbf{r}' - \mathbf{r}|} r'^2 \sin \theta' dr' d\theta' d\phi' \\ &= \frac{\mu_o}{4\pi} \int_S \frac{M_o \sin \theta' \hat{\boldsymbol{\phi}}'}{|r_c \hat{\mathbf{r}}' - \mathbf{r}|} [r_c(t)]^2 \sin \theta' d\theta' d\phi', \end{aligned} \quad (\text{B.2})$$

where $r_c = r_c(t)$ is the time-dependent radius of the MS. This integral becomes significantly easier when writing the integrand in terms of the associated Legendre Functions in Spherical Harmonics $Y_{lm}(\theta, \phi)$. The denominator of equation B.2 can be written as (see equation 3.70 in Jackson[40])

$$\frac{1}{|r_c \hat{\mathbf{r}}' - \mathbf{r}|} = 4\pi \sum_{l=0}^{\infty} \sum_{m=-l}^l \frac{1}{2l+1} \frac{r_{<}^l}{r_{>}^{l+1}} Y_{lm}^*(\theta, \phi) Y_{lm}(\theta', \phi') \quad (\text{B.3})$$

where $r_{<}$ ($r_{>}$) is the smaller (greater) of r_c and r . The numerator of equation B.2 can be written in terms of the Y_{11} ($l = 1, m = 1$) and $Y_{1,-1}$ ($l = 1, m = -1$) Legendre functions,

$$Y_{11}(\theta, \phi) = -\sqrt{\frac{3}{8\pi}} \sin \theta e^{i\phi} \quad (\text{B.4})$$

$$Y_{1,-1}(\theta, \phi) = -Y_{11}^*(\theta, \phi), \quad (\text{B.5})$$

to give

$$\begin{aligned} \sin \theta' \hat{\phi}' &= \sin \theta' (-\sin \phi' \hat{\mathbf{x}} + \cos \phi' \hat{\mathbf{y}}) \\ &= -\sin \theta' \frac{e^{i\phi'} - e^{-i\phi'}}{2i} \hat{\mathbf{x}} + \sin \theta' \frac{e^{i\phi'} + e^{-i\phi'}}{2} \hat{\mathbf{y}} \\ &= -\frac{1}{2i} \left(-\sqrt{\frac{8\pi}{3}} \right) [Y_{11}(\theta', \phi') - Y_{11}^*(\theta', \phi')] \hat{\mathbf{x}} + \frac{1}{2} \left(-\sqrt{\frac{8\pi}{3}} \right) [Y_{11}(\theta', \phi') + Y_{11}^*(\theta', \phi')] \hat{\mathbf{y}} \\ &= \frac{1}{2} \sqrt{\frac{8\pi}{3}} [Y_{1,-1}^*(\theta', \phi')(i\hat{\mathbf{x}} + \hat{\mathbf{y}}) + Y_{11}^*(\theta', \phi')(i\hat{\mathbf{x}} - \hat{\mathbf{y}})]. \end{aligned} \quad (\text{B.6})$$

The prime notation is dropped on the cartesian unit vectors ($\hat{\mathbf{x}}$, $\hat{\mathbf{y}}$, and $\hat{\mathbf{z}}$) because they are identical for the prime and non-prime coordinate systems. With these two expressions

(equations B.3 and B.6) the surface integral (equation B.2) reduces to

$$\begin{aligned}
\mathbf{A}(\mathbf{r}, t) &= \frac{\mu_o M_o r_c^2}{4\pi} \int_S \left\{ 4\pi \sum_{l=0}^{\infty} \sum_{m=-l}^l \frac{1}{2l+1} \frac{r_{<}^l}{r_{>}^{l+1}} Y_{lm}^*(\theta, \phi) Y_{lm}(\theta', \phi') \right\} \\
&\quad \left\{ \frac{1}{2} \sqrt{\frac{8\pi}{3}} [Y_{1,-1}^*(\theta', \phi')(i\hat{\mathbf{x}}' + \hat{\mathbf{y}}') + Y_{11}^*(\theta', \phi')(i\hat{\mathbf{x}} - \hat{\mathbf{y}})] \right\} \sin \theta' d\theta' d\phi' \\
&= \mu_o M_o r_c^2 \sqrt{\frac{2\pi}{3}} \sum_{l=0}^{\infty} \sum_{m=-l}^l \frac{1}{2l+1} \frac{r_{<}^l}{r_{>}^{l+1}} Y_{lm}^*(\theta, \phi) \\
&\quad \int_0^{\pi} \int_0^{2\pi} \{ Y_{lm}(\theta', \phi') Y_{1,-1}^*(\theta', \phi')(i\hat{\mathbf{x}} + \hat{\mathbf{y}}) + Y_{lm}(\theta', \phi') Y_{11}^*(\theta', \phi')(i\hat{\mathbf{x}} - \hat{\mathbf{y}}) \} \sin \theta' d\theta' d\phi' \\
&= \mu_o M_o r_c^2 \sqrt{\frac{2\pi}{3}} \sum_{l=0}^{\infty} \sum_{m=-l}^l \frac{1}{2l+1} \left(\frac{r_{<}^l}{r_{>}^{l+1}} \right) Y_{lm}^*(\theta, \phi) [\delta_{l,1} \delta_{m,-1} (i\hat{\mathbf{x}} + \hat{\mathbf{y}}) + \delta_{l,1} \delta_{m,1} (i\hat{\mathbf{x}} - \hat{\mathbf{y}})] \\
&= \frac{1}{3} \mu_o M_o r_c^2 \left(\frac{r_{<}}{r_{>}^2} \right) \sin \theta [-\sin \phi \hat{\mathbf{x}} + \cos \phi \hat{\mathbf{y}}] \\
\mathbf{A}(\mathbf{r}, t) &= \frac{1}{3} \mu_o M_o r_c^2 \left(\frac{r_{<}}{r_{>}^2} \right) \sin \theta \hat{\boldsymbol{\phi}}. \tag{B.7}
\end{aligned}$$

Writing equation B.7 piecewise yields

$$\mathbf{A}(\mathbf{r}, t) = \frac{1}{3} \mu_o M_o \begin{cases} r \sin \theta \hat{\boldsymbol{\phi}} & \text{for } r < r_c \\ \left(\frac{r_c(t)}{r} \right)^3 r \sin \theta \hat{\boldsymbol{\phi}} & \text{for } r \geq r_c \end{cases}. \tag{B.8}$$

At this point the magnetic field derivation is straightforward and outline from equation 3.43 to equations 3.49-3.51. For completeness, the magnetic field solution is

$$B_r = \begin{cases} \alpha B_o \cos \theta & r < r_c \\ \left[1 + (\alpha - 1) \left(\frac{r_c(t)}{r} \right)^3 \right] B_o \cos \theta & r \geq r_c \end{cases} \tag{B.9}$$

$$B_{\theta} = \begin{cases} -\alpha B_o \sin \theta & r < r_c \\ - \left[1 - \frac{1}{2}(\alpha - 1) \left(\frac{r_c(t)}{r} \right)^3 \right] B_o \sin \theta & r \geq r_c \end{cases} \tag{B.10}$$

$$B_{\phi} = 0, \tag{B.11}$$

where $\alpha = B_{inside}/B_o$ is the total magnetic field inside the MS (or cavity). Contour plots of the field structure are given in figure 3.7.

B.2 The Inductive Electric Field

An expanding iMS produces an inductive electric field ($\mathbf{E} = -\partial_t \mathbf{A}$) due to the time varying magnetic field. The vector potential for a MS with magnetization $\mathbf{M}_o = M_o \hat{\mathbf{z}}$ is given in equation B.8. There is an additional component to \mathbf{A} from \mathbf{B}_o ($\mathbf{A} = \frac{1}{2} B_o r \hat{\mathbf{r}} \times \hat{\mathbf{z}}$), but this term is zero under the temporal derivative and, thus, does not contribute to the inductive electric field. Using a Heaviside step function (equation 3.40) the the vector potential can be written as

$$\mathbf{A}(\mathbf{r}, t) = \frac{1}{3} \mu_o M_o r \sin \theta \left\{ 1 + \left[\left(\frac{r_c}{r} \right)^3 - 1 \right] H(r - r_c) \right\} \hat{\phi}. \quad (\text{B.12})$$

Assuming M_o remains constant throughout the expansion, the the inductive electric field is

$$\begin{aligned} \mathbf{E} &= -\frac{\partial}{\partial t} \mathbf{A} \\ &= -\frac{1}{3} \mu_o M_o r \sin \theta \left\{ 3 \frac{r_c^2}{r^3} v_c H(r - r_c) + \left[\left(\frac{r_c}{r} \right)^3 - 1 \right] v_c \delta(r - r_c) \right\} \hat{\phi} \\ &= -\mu_o M_o \sin \theta \left(\frac{r_c}{r} \right)^2 v_c H(r - r_c) \hat{\phi}, \end{aligned} \quad (\text{B.13})$$

where $v_c = \partial_t r_c$ is the radial expansion speed. For the iMS model with the magnetization $M_o = 3(\alpha - 1)B_o/(2\mu_o)$ (equation 3.48) the field is

$$\mathbf{E}(\mathbf{r}, t) = -\frac{3}{2} (\alpha - 1) B_o \sin \theta \begin{cases} 0 & \text{for } r < r_c \\ \left(\frac{r_c}{r} \right)^2 v_c \hat{\phi} & \text{for } r \geq r_c \end{cases}. \quad (\text{B.14})$$

Like the magnetic field, the radial dependence of the inductive field is normalized to the cavity radius r_c , but decays upstream like $(r_c/r)^2$, opposed to $(r_c/r)^3$. The field is also proportional to the expansion speed of the cavity. A contour plot is given in figure B.1a.

The normal-weight siMS scheme discussed in §3.4 can also be applied to the inductive electric field. In doing so, the sum must first be applied to the vector potential. For a location outside the largest sphere ($r \geq r_c + 3\sigma_c$) the vector potential is

$$\mathbf{A} = \frac{1}{3} \mu_o \sum_{n=0}^{N_S-1} M_n \frac{r_n^3}{r^2} \sin \theta \hat{\phi}, \quad (\text{B.15})$$

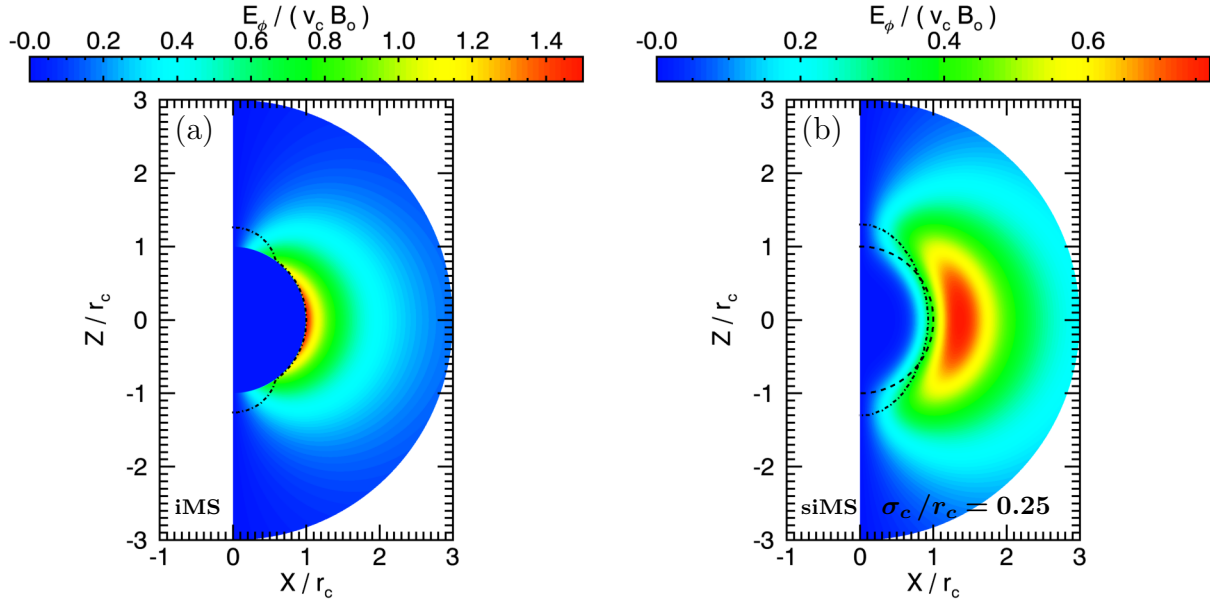


Figure B.1: Figures (a) and (b) represent the inductive electric field ($\mathbf{E} = E_\phi \hat{\phi}$) for a diamagnetic cavity that fully expels ($\alpha = 0$) the background magnetic field $B_o \hat{\mathbf{z}}$. Figure (a) is for an iMS, whereas, figure (b) is for normal-weight siMS of $\sigma_c/r_c = 0.25$. The electric field is normalized to $v_c B_o$, where v_c is the cavity expansion speed, and the spatial coordinates are normalized to the cavity radius r_c . The dash-dot line represents the magnetic field contour level of $B/B_o = 0.5$ and the dashed line gives $r = r_c$.

where N_S is the number of magnetized spheres in the sum, M_n is the magnetization of the n^{th} sphere (equation 3.62), and r_n is the radial location of the n^{th} sphere (equation 3.58). The magnetization does not depend on time, so applying the temporal derivative gives an inductive electric field of

$$\mathbf{E} = -\mu_o \sum_{n=0}^{N_S-1} M_n \left(\frac{r_n}{r}\right)^2 v_n \sin \theta \hat{\phi}, \quad (\text{B.16})$$

where $v_n = \partial_t r_n$ is the expansion velocity of the n^{th} sphere. Assuming the normalized diamagnetic current distribution remains constant (i.e. $\sigma_c/r_c = \text{constant}$), then the expansion velocity of the n^{th} sphere is

$$v_n = v_c \left[1 + 3 \left(\frac{\sigma_c}{r_c}\right) \left(\frac{2n}{N_S - 1} - 1\right) \right], \quad (\text{B.17})$$

and the inductive field can be written as

$$\mathbf{E} = -\frac{3}{2}(\alpha - 1)B_o \sin \theta \left(\frac{r_{siMS}}{r_c}\right)^3 \left(\frac{r_c}{r}\right)^2 v_c \hat{\phi} \quad (\text{B.18})$$

where r_{siMS} the the siMS normalizing radius (equation 3.66). For the normal-weight siMS scheme, the upstream inductive electric field keeps the same proportionality to r and v_c as the iMS model, but the radial normalization is now $r_c(r_{siMS}/r_c)^{3/2}$. Since σ_c/r_c is assumed to be constant, $(r_{siMS}/r_c)^{3/2} = \text{constant} \geq 1$. Figure B.1b shows the inductive electric field for a normal-weight siMS of $\sigma_c/r_c = 0.25$. Much like the effect on the magnetic field contour (figure 3.7), the broadening of the diamagnetic current layer decreases the peak strength of the electric field and spreads the structure out.

B.3 Energy of the Fields

Traditionally it has been said that the magnetic energy of the expelled field far out weighs the magnetic energy of the compressed field outside the cavity. This is not true. The iMS model indicates that the magnetic energy of the compression is equivalent to 50% of the energy in the expelled field. This will be shown below along with the energy of the inductive electric field.

Inside the cavity the magnetic energy is given by

$$E_{B,inside} = \frac{[(\alpha - 1)B_o]^2}{2\mu_o} \left(\frac{4}{3}\pi r_c^3\right) \quad (\text{B.19})$$

where B_o is the background field, r_c is the cavity radius, and $\alpha = B_{inside}/B_o$ is the magnetic field inside the cavity ($\alpha = 0$ for a fully expelled cavity). Combining equations 3.44-3.46 and 3.48 then the magnetic field outside the cavity ($r \geq r_c$) is

$$B_{MS,r} = (\alpha - 1)B_o \left(\frac{r_c}{r}\right)^3 \cos \theta \quad (\text{B.20})$$

$$B_{MS,\theta} = \frac{1}{2}(\alpha - 1)B_o \left(\frac{r_c}{r}\right)^3 \sin \theta \quad (\text{B.21})$$

$$B_{MS,\phi} = 0 \quad (\text{B.22})$$

$$B_{MS}^2 = \left[\frac{1}{2}(\alpha - 1) \left(\frac{r_c}{r}\right)^3 B_o\right]^2 (1 + 3 \cos^2 \theta) \quad (\text{B.23})$$

and the energy stored in this region is

$$\begin{aligned}
E_{B,outside} &= \int_{r_c}^{\infty} \int_0^{\pi} \int_0^{2\pi} \frac{B_{MS}^2}{2\mu_o} r^2 \sin \theta \, dr \, d\theta \, d\phi \\
&= \frac{1}{2\mu_o} \left[\frac{1}{2}(\alpha - 1)r_c^3 B_o \right]^2 \int_{r_c}^{\infty} \frac{1}{r^4} \, dr \int_0^{\pi} (1 + 3 \cos^2 \theta) \sin \theta \, d\theta \int_0^{2\pi} d\phi \\
&= \frac{1}{2} \left\{ \frac{[(\alpha - 1)B_o]^2}{2\mu_o} \left(\frac{4}{3}\pi r_c^3 \right) \right\} \\
E_{B,outside} &= \frac{1}{2} E_{B,inside}. \tag{B.24}
\end{aligned}$$

Thus, the energy stored in the compression of the cavity is equivalent to 50% of the energy of the expulsion. This relation is independent of how well the cavity expels the background magnetic field. The total magnetic energy of the magnetized sphere is

$$\begin{aligned}
E_B &= \frac{3}{2} E_{B,inside} \\
&= \frac{3}{2} \left\{ \frac{[(\alpha - 1)B_o]^2}{2\mu_o} \left(\frac{4}{3}\pi r_c^3 \right) \right\}. \tag{B.25}
\end{aligned}$$

which is the formulation used for the ‘primed’ magnetic-stopping radius R'_B , equation 3.7.

The energy of the inductive electric field can be calculated in a similar way using

$$E_E = \int_V \frac{1}{2} \epsilon_o E_{MS}^2 \, d^3r \tag{B.26}$$

where E_{MS} is the inductive electric field given by equation B.14. Thus, the energy of the inductive field goes like

$$\begin{aligned}
E_E &= \frac{1}{2} \epsilon_o \int_{r_c}^{\infty} \int_0^{\pi} \int_0^{2\pi} \left[-\frac{3}{2}(\alpha - 1)B_o \left(\frac{r_c}{r} \right)^2 v_c \sin \theta \right]^2 r^2 \sin \theta \, dr \, d\theta \, d\phi \\
&= \frac{1}{2} \epsilon_o \left[\frac{3}{2}(\alpha - 1)r_c^2 v_c B_o \right]^2 (2\pi) \int_{r_c}^{\infty} \frac{1}{r^2} \, dr \int_0^{\pi} \sin^3 \theta \, d\theta \\
&= \pi \epsilon_o \left[\frac{3}{2}(\alpha - 1)r_c^2 v_c B_o \right]^2 \left(\frac{1}{r_c} \right) \left(\frac{4}{3} \right) \\
E_E &= 3\pi \epsilon_o [(\alpha - 1)B_o]^2 r_c^3 v_c^2 \tag{B.27} \\
&= 3\epsilon_o \mu_o v_c^2 \left\{ \frac{3}{2} \frac{[(1 - \alpha)B_o]^2}{2\mu_o} \left(\frac{4}{3}\pi r_c^3 \right) \right\}
\end{aligned}$$

$$E_E = 3 \left(\frac{v_c}{c} \right)^2 E_B. \tag{B.28}$$

Since this formulation is for highly non-relativistic expansions ($v_c/c \ll 1$), the amount of energy contained in the inductive field is negligible compared to the energy stored in the magnetic field. Consequently, the inductive energy has a negligible effect on the cavity scalings discussed in §3.2 and the cavity deceleration discussed in §3.3.

B.4 $\mathbf{E} \times \mathbf{B}$ -Drifts

The existence of an inductive electric field and magnetic field for an iMS implies the existence of an $\mathbf{E} \times \mathbf{B}$ -drift structure about the cavity. The first point of interaction for an ambient-plasma with a diamagnetic cavity is with the upstream fields. Knowing the field structure and the resulting $\mathbf{E} \times \mathbf{B}$ -drift structure can give an idea of what this interaction may look like. The end of §3.5 gives an hypothesis of how this interaction may look at the equator of the cavity ($\theta = \pi/2$).

Of course the iMS field structure is not uniform, so there are higher order corrections to the $\mathbf{E} \times \mathbf{B}$ -drift. For the experiments discussed in this dissertation, the ambient-ions are unmagnetized and the electrons are highly magnetized. Thus, the $\mathbf{E} \times \mathbf{B}$ -drifts will have a negligible effect on the ions, whereas, the electrons will experience the drift. Considering the electron gyro-radius is less than the scale length of the field structure, this $\mathbf{E} \times \mathbf{B}$ -drift is a decent zeroth-order approximation for the electron drift.

The $\mathbf{E} \times \mathbf{B}$ -drift is given by

$$\mathbf{U}_{E \times B} = \frac{\mathbf{E} \times \mathbf{B}}{B^2}, \quad (\text{B.29})$$

from which the iMS $\mathbf{E} \times \mathbf{B}$ -drift can be calculated using equation B.14 for the inductive electric field and equations B.9-B.11 for the magnetic field. For an iMS that fully expels B_o ($\alpha = 0$), figure B.2a plots the drift parallel to \mathbf{B}_o and B.2b plots the drift perpendicular to \mathbf{B}_o . Similarly, the $\mathbf{E} \times \mathbf{B}$ -drift structure is calculated for an $\alpha = 0$ normal-weight siMS of $\sigma_c/r_c = 0.25$ and plotted in figure B.2c for the drift parallel to \mathbf{B}_o and figure B.2d for the drift perpendicular to \mathbf{B}_o . In these plots the dash line represents $r = r_c$ and the dash-dot line represents where the magnetic field is expelled to $B/B_o = 0.5$. The perpendicular

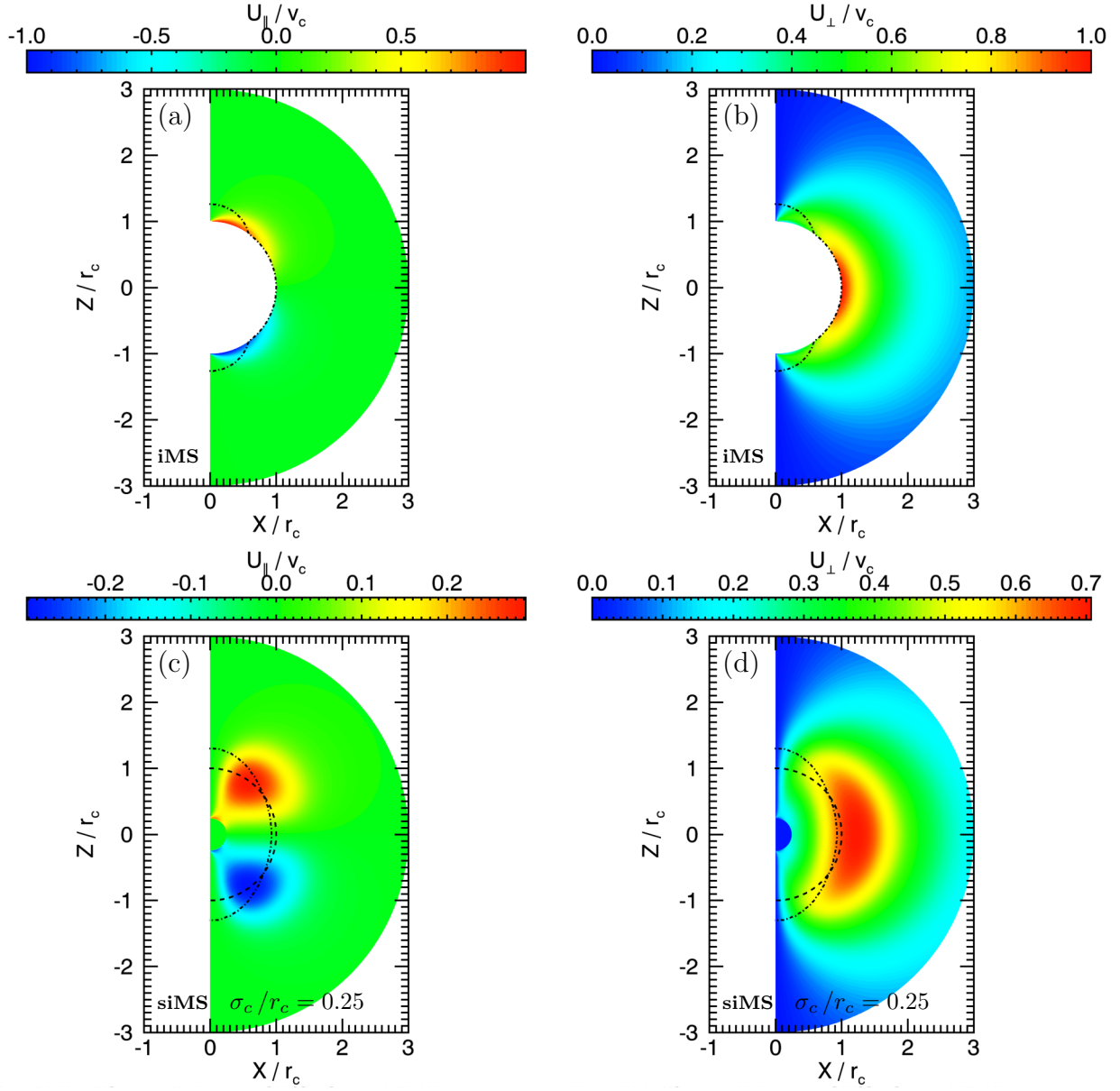


Figure B.2: All figures represent the $E \times B$ -drift structure for a diamagnetic cavity that fully expels ($\alpha = 0$) the background magnetic field $B_o \hat{\mathbf{z}}$. Figure (a) and (b) give the parallel and perpendicular components to \mathbf{B}_o , respectively, for an iMS; whereas, figures (c) and (d) do the same for a normal-weighted siMS with $\sigma_c/r_c = 0.25$. The $E \times B$ -drift is normalized to v_c and the spatial coordinates are normalized to the cavity radius r_c . The dash-dot line represents the magnetic field contour level of $B/B_o = 0.5$ and the dash line gives $r = r_c$.

drift is not localized to the equator of the cavity; it remains above 50% of its peak value inside roughly $\pm 70^\circ$ about the equator. The perpendicular drift also exists throughout the diamagnetic current layer (figure B.2d) and acts to pull that layer across \mathbf{B}_0 as the cavity expands. There is also a drift component parallel to \mathbf{B}_0 that acts to drift electrons in the $+\hat{\mathbf{z}}$ direction in the $+\hat{\mathbf{z}}$ hemisphere of the cavity and in the $-\hat{\mathbf{z}}$ direction in the $-\hat{\mathbf{z}}$ hemisphere. This parallel drift component correlates with the location of the shear component of the magnetic field (figures 3.7b and 3.7d).

BIBLIOGRAPHY

- [1] V. M. Antonov, V. P. Bashurin, A. I. Golubev, V. A. Zhmailo, Yu. P. Zakharov, A. M. Orishich, A. G. Ponomarenko, V. G. Posukh, and V. N. Snytnikov. “A study of the collisionless interaction of interpenetrating super-Alfvén plasma flows.” *Journal of Applied Mechanics and Technical Physics*, **26**(6):757–763, November 1985. ISSN 1573-8620. doi:[10.1007/BF00919519](https://doi.org/10.1007/BF00919519).
- [2] V.P. Bashurin, A.I. Golubev, and V.A. Terekhin. “The collisionless deceleration of an ionized cloud dispersing in a uniform plasma in a magnetic field.” *Journal of Applied Mechanics and Technical Physics*, **24**(5):614–620, September 1983. doi:[10.1007/BF00905870](https://doi.org/10.1007/BF00905870).
- [3] Yu A. Berezin, G. I. Dudnikova, M. P. Fedoruk, and V. A. Vshivkov. “Explosion Phenomena in Collisionless Plasmas at Super-Alfvénic Speed.” *International Journal of Computational Fluid Dynamics*, **10**(2):112–126, January 1998. doi:[10.1080/10618569808961678](https://doi.org/10.1080/10618569808961678).
- [4] D. Biskamp. “Collisionless shock waves in plasmas.” *Nuclear Fusion*, **13**(5):719, 1973. URL <http://stacks.iop.org/0029-5515/13/i=5/a=010>.
- [5] A. S. Bondarenko. *Collision-less Coupling between Explosive Debris Plasma and Magnetized Ambient Plasma*. PhD thesis, UCLA, 2015. URL <http://escholarship.org/uc/item/09n3185f>.
- [6] A. S. Bondarenko, D. B. Schaeffer, E. T. Everson, C. G. Constantin, S. E. Clark, and C. Niemann. “Feasibility of characterizing laser-ablated carbon plasmas via planar laser induced fluorescence.” *Review of Scientific Instruments*, **83**(10), 2012. doi:[10.1063/1.4733562](https://doi.org/10.1063/1.4733562).
- [7] A. S. Bondarenko, D. B. Schaeffer, E. T. Everson, S. E. Clark, C. G. Constantin, and C. Niemann. “Spectroscopic measurement of high-frequency electric fields in the

- interaction of explosive debris plasma with magnetized background plasma.” *Physics of Plasmas*, **21**(12):122112, 2014. doi:[10.1063/1.4904374](https://doi.org/10.1063/1.4904374).
- [8] Jeffrey Bonde, Stephen Vincena, and Walter Gekelman. “Electrostatic structure of a magnetized laser-produced plasma.” *Phys. Rev. E*, 92:051102, Nov 2015. doi:[10.1103/PhysRevE.92.051102](https://doi.org/10.1103/PhysRevE.92.051102).
- [9] Jeffrey D. Bonde. *Collisionless Energy and Momentum Coupling of a High-Beta Expansion to an Ambient Plasma*. PhD thesis, UCLA, 2016. URL <http://search.proquest.com/docview/1811598238>.
- [10] Stephen H. Brecht, Dennis W. Hewett, and David J. Larson. “A magnetized, spherical plasma expansion in an inhomogeneous plasma: Transition from super- to sub-Alfvénic.” *Geophysical Research Letters*, **36**(15), 2009. ISSN 1944-8007. doi:[10.1029/2009GL038393](https://doi.org/10.1029/2009GL038393). L15105.
- [11] D. Burgess. *Introduction to Space Physics*, pages 129–163. Cambridge University Press, New York, 1995.
- [12] Iver H. Cairns and Crockett L. Grabbe. “Towards an MHD theory for the standoff distance of Earth’s bow shock.” *Geophysical Research Letters*, **21**(25):2781–2784, 1994. ISSN 1944-8007. doi:[10.1029/94GL02551](https://doi.org/10.1029/94GL02551).
- [13] S. E. Clark, D. Winske, D. B. Schaeffer, E. T. Everson, A. S. Bondarenko, C. G. Constantin, and C. Niemann. “Hybrid simulation of shock formation for super-Alfvénic expansion of laser ablated debris through an ambient, magnetized plasma.” *Physics of Plasmas (1994-present)*, **20**(8):082129, 2013. doi:[10.1063/1.4819251](https://doi.org/10.1063/1.4819251).
- [14] Stirling A. Colgate. “The phenomenology of the mass motion of a high altitude nuclear explosion.” *Journal of Geophysical Research*, **70**(13):3161–3173, 1965. ISSN 2156-2202. doi:[10.1029/JZ070i013p03161](https://doi.org/10.1029/JZ070i013p03161).

- [15] A. Collette and W. Gekelman. “Structure of an Exploding Laser-Produced Plasma.” *Physical Review Letters*, **105**(195003), November 2010. doi:[10.1103/PhysRevLett.105.195003](https://doi.org/10.1103/PhysRevLett.105.195003).
- [16] A. Collette and W. Gekelman. “Structure of an exploding laser-produced plasma.” *Physics of Plasmas*, **18**(055705), April 2011. doi:[10.1063/1.3567525](https://doi.org/10.1063/1.3567525).
- [17] Andrew Collette. *Structure of an Expanding Laser-Produced Plasma*. PhD thesis, UCLA, 2010. URL <http://search.proquest.com/docview/861924186>.
- [18] C. Constantin, W. Gekelman, P. Pribyl, E. Everson, D. Schaeffer, N. Kugland, R. Presura, S. Neff, C. Plechaty, S. Vincena, A. Collette, S. Tripathi, M. Villagram Muniz, and C. Niemann. “Collisionless Interaction of an Energetic Laser Produced Plasma with a Large Magnetoplasma.” *Astrophysics and Space Science*, **322**(1):155–159, 2009. ISSN 1572-946X. doi:[10.1007/s10509-009-0012-z](https://doi.org/10.1007/s10509-009-0012-z).
- [19] C. M. Cooper, W. Gekelman, P. Pribyl, and Z. Lucky. “A new large area lanthanum hexaboride plasma source.” *Review of Scientific Instruments*, **81**(8):083503, 2010. doi:[10.1063/1.3471917](https://doi.org/10.1063/1.3471917).
- [20] A. W. DeSilva and J. A. Stamper. “Observation of Anomalous Electron Heating in Plasma Shock Waves.” *Phys. Rev. Lett.*, 19:1027–1030, Oct 1967. doi:[10.1103/PhysRevLett.19.1027](https://doi.org/10.1103/PhysRevLett.19.1027).
- [21] H. Dickinson, W. H. Bostick, J. N. DiMarco, and S. Koslov. “Experimental Study of Rayleigh-Taylor Instability in Plasma.” *The Physics of Fluids*, **5**(9):1048–1056, September 1962. doi:[10.1063/1.1724472](https://doi.org/10.1063/1.1724472).
- [22] Guy Dimonte and L. G. Wiley. “Dynamics of Exploding Plasmas in a Magnetic Field.” *Physical Review Letters*, 67:1755–1758, September 1991. doi:[10.1103/PhysRevLett.67.1755](https://doi.org/10.1103/PhysRevLett.67.1755).

- [23] R. P. Drake. “The Design of Laboratory Experiments to Produce Collisionless Shocks of Cosmic Relevance.” *Physics of Plasmas*, **7**(11):4690–4698, 2000. doi:[10.1063/1.1314625](https://doi.org/10.1063/1.1314625).
- [24] Palmer Dyal. “Particle and Field Measurements of the Starfish Diamagnetic Cavity.” *Journal of Geophysical Research*, **111**(A12211), December 2006. doi:[10.1029/2006JA011827](https://doi.org/10.1029/2006JA011827).
- [25] J. P. Edmiston and C. F. Kennel. “A parametric survey of the first critical Mach number for a fast MHD shock.” *Journal of Plasma Physics*, **32**(3):429–441, December 1984. doi:[10.1017/S002237780000218X](https://doi.org/10.1017/S002237780000218X).
- [26] C. P. Escoubet, M. Fehringer, and M. Goldstein. “The Cluster mission.” *Annales Geophysicae*, **19**(10/12):1197–1200, 2001. doi:[10.5194/angeo-19-1197-2001](https://doi.org/10.5194/angeo-19-1197-2001).
- [27] E. T. Everson, P. Pribyle, C. G. Constantin, A. Zlystra, D. Schaeffer, N. L. Kugland, and C. Niemann. “Design, construction, and calibration of a three-axis, high-frequency magnetic probe (B-dot probe) as a diagnostic for exploding plasmas.” *Review of Scientific Instruments*, 80:113505, November 2009. doi:[10.1063/1.3246785](https://doi.org/10.1063/1.3246785).
- [28] K. A. Flippo, J. Workman, D. C. Gautier, S. Letzring, R. P. Johnson, and T. Shimada. “Scaling laws for energetic ions from the commissioning of the new Los Alamos National Laboratory 200 TW Trident laser.” *Review of Scientific Instruments*, **79**(10), 2008. doi:[10.1063/1.2987678](https://doi.org/10.1063/1.2987678).
- [29] D. W. Forslund, J. M. Kindel, Kenneth Lee, E. L. Lindman, and R. L. Morse. “Theory and simulation of resonant absorption in a hot plasma.” *Physical Review A*, 11:679–683, February 1975. doi:[10.1103/PhysRevA.11.679](https://doi.org/10.1103/PhysRevA.11.679).
- [30] W. Gekelman, H. Pfister, Z. Lucky, J. Bamber, D. Leneman, and J. Maggs. “Design, Construction, and Properties of the Large Plasma Research Device - The LAPD at UCLA.” *Review of Scientific Instruments*, **62**(12):2875–2883, December 1991. doi:[10.1063/1.1142175](https://doi.org/10.1063/1.1142175).

- [31] George C. Goldenbaum. “Experimental Study of Collision-Free Shock Waves and Anomalous Electron Heating.” *Physics of Fluids (1958-1988)*, **10**(9):1897–1904, 1967. doi:[10.1063/1.1762385](https://doi.org/10.1063/1.1762385).
- [32] A. I. Golubev and A. A. Solov’ev. “Collisionless dispersion of an ionized cloud into a homogeneous magnetized plasma.” *Journal of Applied Mechanics and Technical Physics*, **19**(5):602–609, 1978. doi:[10.1007/BF00850600](https://doi.org/10.1007/BF00850600).
- [33] David J. Griffiths. *Introduction to Electrodynamics*. Prentice Hall, Upper Saddle River, NJ, third edition, 1999. ISBN 0-13-805326-X.
- [34] J. Grun, R. Decoste, B. H. Ripin, and J. Gardner. “Characteristics of ablation plasma from planar, laser-driven targets.” *Applied Physics Letters*, **39**(7):545–547, 1981. doi:[10.1063/1.92788](https://doi.org/10.1063/1.92788).
- [35] J. Grun, S. P. Obenschain, B. H. Ripin, R. R. Whitlock, E. A. McLean, J. Gardner, M. J. Herbst, and J. A. Stamper. “Ablative acceleration of planar targets to high velocities.” *Physics of Fluids*, **26**(2):588–597, 1983. doi:[10.1063/1.864145](https://doi.org/10.1063/1.864145).
- [36] Dennis W. Hewett, Stephen H. Brecht, and David J. Larson. “The physics of ion decoupling in magnetized plasma expansions.” *Journal of Geophysical Research: Space Physics*, **116**(A11), November 2011. ISSN 2156-2202. doi:[10.1029/2011JA016904](https://doi.org/10.1029/2011JA016904). A11310.
- [37] D. S. Hey, M. H. Key, A. J. Mackinnon, A. G. MacPhee, P. K. Patel, R. R. Freeman, L. D. Van Woerkom, and C. M. Castaneda. “Use of GafChromic film to diagnose laser generated proton beams.” *Review of Scientific Instruments*, **79**(5):053501, 2008. doi:[10.1063/1.2901603](https://doi.org/10.1063/1.2901603).
- [38] J. D. Huba, A. B. Hassam, and D. Winske. “Stability of sub-Alfvénic plasma expansions.” *Physics of Fluids B: Plasma Physics (1989-1993)*, **2**(7):1676–1697, 1990. doi:[10.1063/1.859441](https://doi.org/10.1063/1.859441).

- [39] I. H. Hutchinson. *Principles of Plasma Diagnostics*. Cambridge University Press, 2nd edition, 2002. ISBN 9780511613630. doi:[10.1017/CBO9780511613630](https://doi.org/10.1017/CBO9780511613630).
- [40] John D. Jackson. *Classical Electrodynamics*. John Wiley & Sons, Inc., New York, third edition, 1999. ISBN 0-471-30932-X.
- [41] Frank C. Jones and Donald C. Ellison. “The Plasma Physics of Shock Acceleration.” *Space Science Reviews*, **58**(1):259–346, 1991. ISSN 1572-9672. doi:[10.1007/BF01206003](https://doi.org/10.1007/BF01206003).
- [42] S. Kacenjar, M. Hausman, M. Keskinen, A. W. Ali, J. Grun, C. K. Manka, E. A. McLean, and B. H. Ripin. “Magnetic Field Compression and Evolution in Laser-Produced Plasma Expansions.” *Physics of Fluids*, **29**(6):2007–2012, 1986. doi:[10.1063/1.865578](https://doi.org/10.1063/1.865578).
- [43] C. F. Kennel, J. P. Edmiston, and T. Hada. *A Quarter Century of Collisionless Shock Research*, volume 34, pages 1–36. American Geophysical Union, January 1985. ISBN 9781118664032. URL <http://onlinelibrary.wiley.com/doi/10.1029/GM034p0001/summary>.
- [44] M. H. Key, W. T. Toner, T. J. Goldsack, J. D. Kilkenny, S. A. Veats, P. F. Cunningham, and C. L. S. Lewis. “A study of ablation by laser irradiation of plane targets at wavelengths 1.05, 0.53, and 0.35 μm .” *Physics of Fluids*, **26**(7):2011–2026, July 1983. doi:[10.1063/1.864348](https://doi.org/10.1063/1.864348).
- [45] N. L. Kugland, D. D. Ryutov, C. Plechaty, J. S. Ross, and H.-S. Park. “Invited Article: Relation between electric and magnetic field structures and their proton-beam images.” *Review of Scientific Instruments*, **83**(10):101301, 2012. doi:[10.1063/1.4750234](https://doi.org/10.1063/1.4750234).
- [46] B. Lembege, J. Giacalone, M. Scholer, T. Hada, M. Hoshino, V. Krasnoselskikh, H. Kucharek, P. Savoini, and T. Terasawa. “Selected Problems in Collisionless-Shock Physics.” *Space Science Reviews*, **110**(3):161–226, 2004. ISSN 1572-9672. doi:[10.1023/B:SPAC.0000023372.12232.b7](https://doi.org/10.1023/B:SPAC.0000023372.12232.b7).

- [47] V. V. Lobzin, V. V. Krasnoselskikh, J.-M. Bosqued, J.-L. Pinçon, S. J. Schwartz, and M. Dunlop. “Nonstationarity and reformation of high-Mach-number quasiperpendicular shocks: Cluster observations.” *Geophysical Research Letters*, **34**(5):n/a–n/a, 2007. ISSN 1944-8007. doi:[10.1029/2006GL029095](https://doi.org/10.1029/2006GL029095). L05107.
- [48] W. Marshall. “The Structure of Magneto-Hydrodynamic Shock Waves.” *Proceedings of the Royal Society of London A: Mathematical, Physical and Engineering Sciences*, **233**(1194):367–376, 1955. ISSN 0080-4630. doi:[10.1098/rspa.1955.0272](https://doi.org/10.1098/rspa.1955.0272).
- [49] M. J. Martin, J. Bonde, W. Gekelman, and P. Pribyl. “A resistively heated CeB6 emissive probe.” *Review of Scientific Instruments*, **86**(5):053507, 2015. doi:[10.1063/1.4921838](https://doi.org/10.1063/1.4921838).
- [50] S. Matsukiyo and M. Scholer. “Modified two-stream instability in the foot of high Mach number quasi-perpendicular shocks.” *Journal of Geophysical Research: Space Physics*, **108**(A12):SMP 19–1–SMP 19–10, 2003. ISSN 2156-2202. doi:[10.1029/2003JA010080](https://doi.org/10.1029/2003JA010080).
- [51] S. Matsukiyo and M. Scholer. “On microinstabilities in the foot of high Mach number perpendicular shocks.” *Journal of Geophysical Research: Space Physics*, **111**(A6):n/a–n/a, 2006. ISSN 2156-2202. doi:[10.1029/2005JA011409](https://doi.org/10.1029/2005JA011409). A06104.
- [52] J.B. McBride and E. Ott. “Electromagnetic and finite β_e effects on the modified two stream instability.” *Physics Letters A*, **39**(5):363 – 364, 1972. ISSN 0375-9601. doi:[10.1016/0375-9601\(72\)90096-5](https://doi.org/10.1016/0375-9601(72)90096-5).
- [53] E. C. Merritt, A. L. Moser, S. C. Hsu, J. Loverich, and M. Gilmore. “Experimental Characterization of the Stagnation Layer between Two Obliquely Merging Supersonic Plasma Jets.” *Phys. Rev. Lett.*, 111:085003, Aug 2013. doi:[10.1103/PhysRevLett.111.085003](https://doi.org/10.1103/PhysRevLett.111.085003).
- [54] S. Messer, D. D. Blackwell, W. E. Amatucci, and D. N. Walker. “Broadband calibration of radio-frequency magnetic induction probes.” *Review of Scientific Instruments*, **77**(11):115104, November 2006. doi:[10.1063/1.2387880](https://doi.org/10.1063/1.2387880).

- [55] B. Meyer and G. Thiell. “Experimental scaling laws for ablation parameters in plane target–laser interaction with 1.06 μm and 0.35 μm laser wavelengths.” *Physics of Fluids*, **27**(1):302–311, January 1984. doi:[10.1063/1.864483](https://doi.org/10.1063/1.864483).
- [56] Paul A. Miller, Edward V. Barnat, Gregory A. Hebner, Alex M. Paterson, and John P. Holland. “Spatial and frequency dependence of plasma currents in a 300 mm capacitively coupled plasma reactor.” *Plasma Sources Science and Technology*, **15**(4):889–899, October 2006. doi:[10.1088/0963-0252/15/4/036](https://doi.org/10.1088/0963-0252/15/4/036).
- [57] N. K. Moncur, R. P. Johnson, R. G. Watt, and R. B. Gibson. “Trident: a versatile high-power Nd:glass laser facility for inertial confinement fusion experiments.” *Applied Optics*, **34**(21):4274–4283, July 1995. doi:[10.1364/AO.34.004274](https://doi.org/10.1364/AO.34.004274).
- [58] F. Nürnberg, M. Schollmeier, E. Brambrink, A. Blažević, D. C. Carroll, K. Flippo, D. C. Gautier, M. Geißel, K. Harres, B. M. Hegelich, O. Lundh, K. Markey, P. McKenna, D. Neely, J. Schreiber, and M. Roth. “Radiochromic film imaging spectroscopy of laser-accelerated proton beams.” *Review of Scientific Instruments*, **80**(3):033301, 2009. doi:[10.1063/1.3086424](https://doi.org/10.1063/1.3086424).
- [59] Shigefumi Okada, Kohnosuke Sato, and Tadashi Sekiguchi. “Behaviour of Laser-Produced Plasma in a Uniform Magnetic Field-Plasma Instabilities.” *Japanese Journal of Applied Physics*, **20**(1):157–165, January 1981. URL <http://stacks.iop.org/1347-4065/20/i=1/a=157>.
- [60] N. Omidi, X. Glanco-Cano, C. T. Russell, H. Karimabadi, and M. Acuna. “Hybrid simulations of solar wind interaction with magnetized asteroids: General characteristics.” *Journal of Geophysical Research*, **107**(A12):1487, 2002. doi:[10.1029/2002JA009441](https://doi.org/10.1029/2002JA009441).
- [61] K. Papadopoulos, R. C. Davidson, J. M. Dawson, I. Haber, D. A. Hammer, N. A. Krall, and R. Shanny. “Heating of Counterstreaming Ion Beams in an External Magnetic Field.” *Physics of Fluids*, **14**(4):849–857, April 1971. doi:[10.1063/1.1693520](https://doi.org/10.1063/1.1693520).

- [62] J. W. M. Paul, G. C. Goldenbaum, A. Iiyoshi, L. S. Holmes, and R. A. Hardcastle. “Measurement of Electron Temperatures produced by Collisionless Shock Waves in a Magnetized Plasma.” *Nature*, **216**(5113):363–364, 10 1967. doi:[10.1038/216363a0](https://doi.org/10.1038/216363a0).
- [63] S. M. Petrinec and C. T. Russell. “Hydrodynamic and MHD Equations Across the Bow Shock and Along the Surfaces of Planetary Obstacles.” *Space Science Reviews*, **79**(3):757–791, 1997. ISSN 1572-9672. doi:[10.1023/A:1004938724300](https://doi.org/10.1023/A:1004938724300).
- [64] R. C. Phillips and E. B. Turner. “Construction and Calibration Techniques of High Frequency Magnetic Probes.” *The Review of Scientific Instruments*, **36**(12):1822–1825, December 1965. doi:[10.1063/1.1719473](https://doi.org/10.1063/1.1719473).
- [65] I. M. Podgorny. “Collisionless shocks: Simulation and laboratory experiments.” *Il Nuovo Cimento C*, **2**(6):834–853, 1979. doi:[10.1007/BF02558135](https://doi.org/10.1007/BF02558135).
- [66] Radu Presura, Stephan Neff, and Lucas Wanex. “Experimental Design for the Laboratory Simulation of Magnetized Astrophysical Jets.” *Astrophysics and Space Science*, **307**(1-3):93–98, 2007. doi:[10.1007/s10509-006-9286-6](https://doi.org/10.1007/s10509-006-9286-6).
- [67] Lord Rayleigh. “VIII. On the pressure developed in a liquid during the collapse of a spherical cavity.” *Philosophical Magazine Series 6*, **34**(200):94–98, 1917. doi:[10.1080/14786440808635681](https://doi.org/10.1080/14786440808635681).
- [68] Michael P. Reilly, William Lewis, and George H. Miley. “Magnetic field probes for us in radio frequency plasma.” *Review of Scientific Instruments*, **80**(5):053508, May 2009. doi:[10.1063/1.3136907](https://doi.org/10.1063/1.3136907).
- [69] B. H. Ripin, E. A. McLean, C. K. Manka, C. Pawley, J. A. Stamper, T. A. Peyser, A. N. Mostovych, J. Grun, A. B. Hassam, and J. Huba. “Large-Larmor-Radius Interchange Instability.” *Physical Review Letters*, 59:2299–2303, November 1987. doi:[10.1103/PhysRevLett.59.2299](https://doi.org/10.1103/PhysRevLett.59.2299).

- [70] B. H. Ripin, J. D. Huba, E. A. McLean, C. K. Manka, T. Peyser, H. R. Burris, and J. Grun. “Sub-Alfvénic Plasma Expansion.” *Physics of Fluids B*, **5**(10):3491–3506, October 1993. doi:[10.1063/1.860825](https://doi.org/10.1063/1.860825).
- [71] C. T. Russell and E. W. Greenstadt. “Initial ISEE Magnetometer Results: Shock Observation.” *Space Science Reviews*, **23**(1):3–37, March 1979. ISSN 1572-9672. doi:[10.1007/BF00174109](https://doi.org/10.1007/BF00174109).
- [72] R. Z. Sagdeev. “Cooperative Phenomena and Shock Waves in Collisionless Plasmas.” *Reviews of Plasma Physics*, 4:23–91, 1966. URL <http://adsabs.harvard.edu/abs/1966RvPP....4...23S>.
- [73] D. B. Schaeffer, E. T. Everson, D. Winske, C. G. Constantin, A. S. Bondarenko, L. A. Morton, K. A. Flippo, D. S. Montgomery, S. A. Gaillard, and C. Niemann. “Generation of magnetized collisionless shocks by a novel, laser-driven magnetic piston.” *Physics of Plasmas*, **19**(7):070702, 2012. doi:[10.1063/1.4736846](https://doi.org/10.1063/1.4736846).
- [74] D B Schaeffer, D S Montgomery, A S Bondarenko, L A Morton, R P Johnson, T Shimada, C G Constantin, E T Everson, S A Letzring, S A Gaillard, K A Flippo, S H Glenzer, and C Niemann. “Thomson Scattering Measurements of Temperature and Density in a Low-Density, Laser-Driven Magnetized Plasma.” *Journal of Instrumentation*, **7**(02):P02002, 2012. URL <http://stacks.iop.org/1748-0221/7/i=02/a=P02002>.
- [75] Derek Schaeffer. *Generation of Quasi-Perpendicular Collisionless Shocks by a Laser-Driven Magnetic Piston*. PhD thesis, UCLA, January 2014. URL <http://www.escholarship.org/uc/item/4xw9d45t>.
- [76] M. Scholer and S. Matsukiyo. “Nonstationarity of quasi-perpendicular shocks: a comparison of full particle simulations with different ion to electron mass ratio.” *Annales Geophysicae*, **22**(7):2345–2353, 2004. doi:[10.5194/angeo-22-2345-2004](https://doi.org/10.5194/angeo-22-2345-2004).
- [77] M. Scholer, I. Shinohara, and S. Matsukiyo. “Quasi-perpendicular shocks: Length scale of the cross-shock potential, shock reformation, and implication for shock surfing.” *Jour-*

- nal of Geophysical Research: Space Physics*, **108**(A1):SSH 4–1–SSH 4–11, 2003. ISSN 2156-2202. doi:[10.1029/2002JA009515](https://doi.org/10.1029/2002JA009515).
- [78] R. S. Shaw, J. H. Booske, and M. J. McCarrick. “Broadband calibration for magnetic probes for use in the Maryland spheromak.” *Review of Scientific Instruments*, **58**(7): 1204–1210, July 1987. doi:[10.1063/1.1139440](https://doi.org/10.1063/1.1139440).
- [79] D. S. Spicer, R. W. Clark, and S. P. Maran. “A Model of the Pre-Sedov Expansion Phase of Supernova Remnant-Ambient Plasma Coupling and X-Ray Emission from SN 1987A.” *The Astrophysical Journal*, 356:549–571, June 1990. doi:[10.1086/168862](https://doi.org/10.1086/168862).
- [80] J. A. Stamper and A. W. DeSilva. “Experimental Study of the Structure of Plasma Shock Waves in a Fast θ Pinch.” *Physics of Fluids*, **12**(7):1435–1440, 1969. doi:[10.1063/1.1692685](https://doi.org/10.1063/1.1692685).
- [81] M. F. Thomsen, J. T. Gosling, S. A. Fuselier, S. J. Bame, and C. T. Russell. “Hot, Diamagnetic Cavities Upstream from the Earth’s Bow Shock.” *Journal of Geophysical Research: Space Physics*, **91**(A3):2961–2973, March 1986. ISSN 2156-2202. doi:[10.1029/JA091iA03p02961](https://doi.org/10.1029/JA091iA03p02961).
- [82] D. A. Tidman and N. A. Krall. *Shock Waves in Collisionless Plasmas*. Wiley series in plasma physics. Wiley-Interscience, New York, 1971. ISBN 0471867853.
- [83] R. A. Treumann. “Fundamentals of collisionless shocks for astrophysical application, 1. Non-relativistic shocks.” *Astronomy and Astrophysics Review*, 17:409–535, September 2009. doi:[10.1007/s00159-009-0024-2](https://doi.org/10.1007/s00159-009-0024-2).
- [84] M. Van Zeeland and W. Gekelman. “Laser-Plasma Diamagnetism in the Presence of an Ambient Magnetized Plasma.” *Physics of Plasmas*, **11**(1):320–323, January 2004. doi:[10.1063/1.1628233](https://doi.org/10.1063/1.1628233).
- [85] M. Van Zeeland, W. Gekelman, S. Vincena, and G. Dimonte. “Production of Alfvén

- Waves by a Rapidly Expanding Dense Plasma.” *Physical Review Letters*, **87**(10): 105001, September 2001. doi:[10.1103/PhysRevLett.87.105001](https://doi.org/10.1103/PhysRevLett.87.105001).
- [86] Michael Anthony Van Zeeland. *Generation of shear Alfvén waves by expanding plasmas*. PhD thesis, UCLA, 2003. URL <http://search.proquest.com/docview/305350367>.
- [87] S. C. Wilks, A. B. Langdon, T. E. Cowan, M. Roth, M. Singh, S. Hatchett, M. H. Key, D. Pennington, A. MacKinnon, and R. A. Snavely. “Energetic proton generation in ultra-intense laser–solid interactions.” *Physics of Plasmas*, **8**(2):542–549, 2001. doi:[10.1063/1.1333697](https://doi.org/10.1063/1.1333697).
- [88] D. Winske, J. Giacalone, M. F. Thomsen, and M. M. Mellott. “A Comparative Study of Plasma Heating by Ion Acoustic and Modified Two-Stream Instabilities at Subcritical Quasi-Perpendicular Shocks.” *Journal of Geophysical Research: Space Physics*, **92** (A5):4411–4422, May 1987. ISSN 2156-2202. doi:[10.1029/JA092iA05p04411](https://doi.org/10.1029/JA092iA05p04411).
- [89] Thomas P. Wright. “Early-Time Model of Laser Plasma Expansion.” *Physics of Fluids*, **14**(9):1905–1910, September 1971. doi:[10.1063/1.1693699](https://doi.org/10.1063/1.1693699).
- [90] C.S. Wu, D. Winske, Y.M. Zhou, S.T. Tsai, P. Rodriguez, M. Tanaka, K. Papadopoulos, K. Akimoto, C.S. Lin, M.M. Leroy, and C.C. Goodrich. “Microinstabilities associated with a high Mach number, perpendicular bow shock.” *Space Science Reviews*, **37**(1-2): 63–109, 1984. ISSN 0038-6308. doi:[10.1007/BF00213958](https://doi.org/10.1007/BF00213958).
- [91] J. G. Yang, J. H. Choi, B. C. Kim, N. S. Yoon, and S. M. Hwang. “A Calibration Method of a Radio Frequency Magnetic Probe.” *Review of Scientific Instruments*, **70** (9):3774–3775, September 1999. doi:[10.1063/1.1149951](https://doi.org/10.1063/1.1149951).
- [92] Yuri P. Zakharov. “Collisionless Laboratory Astrophysics with Lasers.” *IEEE Transactions on Plasma Science*, **31**(6):1243–1251, December 2003. ISSN 0093-3813. doi:[10.1109/TPS.2003.820957](https://doi.org/10.1109/TPS.2003.820957).

- [93] H. C. Zhuang and C. T. Russell. “An analytic treatment of the structure of the bow shock and magnetosheath.” *Journal of Geophysical Research: Space Physics*, **86**(A4): 2191–2205, 1981. ISSN 2156-2202. doi:[10.1029/JA086iA04p02191](https://doi.org/10.1029/JA086iA04p02191).
- [94] J. F. Ziegler, J. P. Biersack, and M. D. Ziegler. *SRIM - The Stopping and Range of Ions in Matter*. 15th edition, 2015. URL <http://www.srim.org/>.
- [95] James F. Ziegler. “SRIM-2003.” *Nuclear Instruments and Methods in Physics Research Section B: Beam Interactions with Materials and Atoms*, 219–220:1027 – 1036, 2004. ISSN 0168-583X. doi:[10.1016/j.nimb.2004.01.208](https://doi.org/10.1016/j.nimb.2004.01.208). Proceedings of the Sixteenth International Conference on Ion Beam Analysis.